Dissertation
submitted to the
Combined Faculties for the Natural Sciences and for Mathematics
of the Ruperto-Carola University of Heidelberg, Germany
for the degree of
Doctor of Natural Sciences

Presented by
Diplom-Physicist: Markus Jehle
born in: Bad Säckingen

Oral examination: 20.12.2006

Spatio-Temporal Analysis of
Flows Close to Free Water Surfaces

Referees: Prof. Dr.   Bernd Jähne
                Prof. Dr.   Christoph Cremer

Zusammenfassung

Für Untersuchungen des Gasaustausches zwischen Atmosphäre und Ozean werden Kenntnisse über das Strömungsfeld in und unter der wasserseitigen viskosen Grenzschicht benötigt. Hierfür wurde eine neuartige Messtechnik zur raumzeitlichen Analyse von Strömungen nah an der Wasseroberfläche entwickelt.

Ein Flüssigkeitsvolumen wird von LEDs durchleuchtet. Kleine sphärische Teilchen werden der Flüssigkeit beigemengt und dienen als Tracerpartikel. Eine Kamera, die von oben auf die Wasseroberfläche gerichtet ist, nimmt Bildsequenzen auf. Der Abstand einer Kugel zur Wasseroberfläche wird durch einen Licht absorbierenden Farbstoff kodiert. Indem man LEDs zweier verschiedener Wellenlängen benutzt, wird es möglich, Tracerpartikel verschiedener Größe zu verwenden.

Die drei Geschwindigkeitskomponenten der Strömung erhält man, indem man eine Erweiterung der Methode des optischen Flusses verwendet, bei der die vertikale Geschwindigkeitskomponente aus der zeitlichen Helligkeitsänderung bestimmt wird. Indem dreidimensionale parametrische Bewegungsmodelle verwendet werden, kann die Schubspannung direkt, also ohne vorherige Berechnung der Geschwindigkeitsfelder, bestimmt werden.

Hardware und Algorithmik werden auf verschiedene Arten getestet. Eine laminare Rieselfilmströmung dient als Referenz. Das vorhergesagte parabolische Profil dieser stationären Strömung kann mit hoher Genauigkeit rekonstruiert werden. Konvektive Turbulenz dient als Beispiel einer von Natur aus instationären dreidimensionalen Strömung. Aus Sequenzen, die aus der Biofluidmechanik stammen, wird direkt die Wandscherrate bestimmt, wobei eine wesentliche Verbesserung gegenüber konventionellen Methoden deutlich wird.

Abstract

In order to examine the air-water gas exchange, a detailed knowledge is needed about the flow field within and beneath the water-side viscous boundary layer. Therefore a novel measurement technique is developed for the spatio-temporal analysis of flows close to free water surfaces.

A fluid volume is illuminated by LEDs. Small spherical particles are added to the fluid, functioning as a tracer. A camera pointing to the water surface from above records the image sequences. The distance of the spheres to the surface is coded by means of a supplemented dye, which absorbs the light of the LEDs. By using LEDs flashing with two different wavelengths, it is possible to use particles variable in size.

The velocity vectors are obtained by using an extension of the method of optical flow. The vertical velocity component is computed from the temporal change of brightness. Using 3D parametric motion models the shear stress at surfaces can be estimated directly, without previous calculation of the vector fields.

Hardware and algorithmics are tested in several ways: A laminar falling film serves as reference flow. The predicted parabolic profile of this stationary flow can be reproduced very well. Buoyant convective turbulence acts as an example for an instationary inherently 3D flow. The direct estimation of the wall shear rate is applied to sequences recorded in the context of biofluidmechanics, revealing a substantial improvement compared to conventional techniques.

Contents

Contents

1 Introduction

1.1 Motivation

During the last two centuries the atmospheric carbon dioxide concentration has increased by 100 ppm to the today's value of 380 ppm. However, the carbon dioxide stemming from the burning of fossil fuel exceeds this amount by about 100%. The results of [Sabine et al., 2004] show, that the oceans store a large fraction of the anthropogenic carbon dioxide. [Le Quéré et al., 2003] quantifies the global ocean sinks for the last two decades using recent atmospheric inversions and ocean models (see Fig. 1.1). For the 1990s the mean global oceanic sink is $1.9 \, \mathrm{Pg\,C\,yr^{-1}}$, but an uncertainty on the mean value of the order of $\pm 0.7 \, \mathrm{Pg\,C\,yr^{-1}}$ remains[1]. The high variations in the predictions of the models are partly caused by insufficient understanding of the mechanics of air-sea gas exchange.
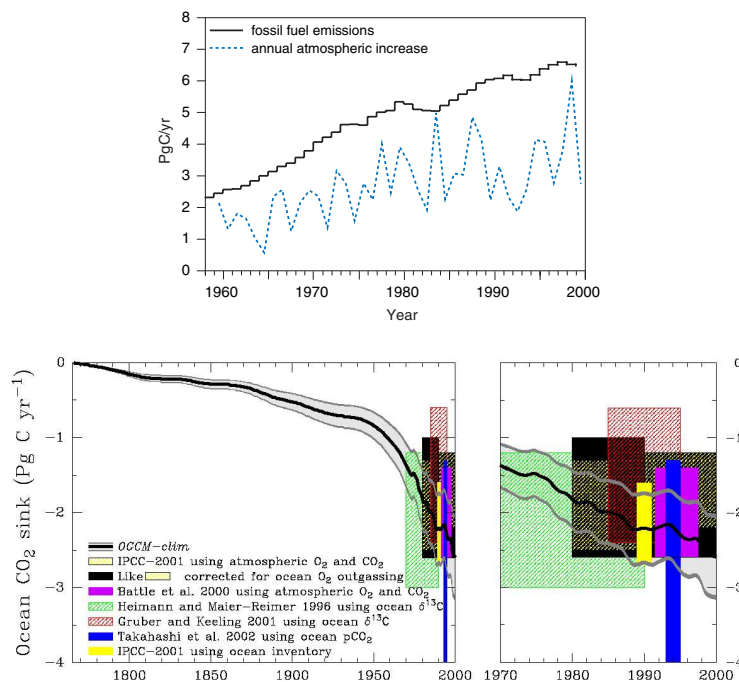
Figure 1.1: *Top: Annual fossil fuel emissions (solid line) and annual increase of atmospheric carbon dioxide (dotted line). Bottom: Global oceanic CO$_2$ sink computed using different models. The central ocean model estimate was forced with atmospheric CO$_2$ concentration from ice cores before 1970 and from direct measurements after 1970, where an error of 20% is assumed. The coloured boxes represent estimates by various researchers using differing methods (from [IPCC, 2001] (top) and from [Le Quéré et al., 2003] (bottom))*
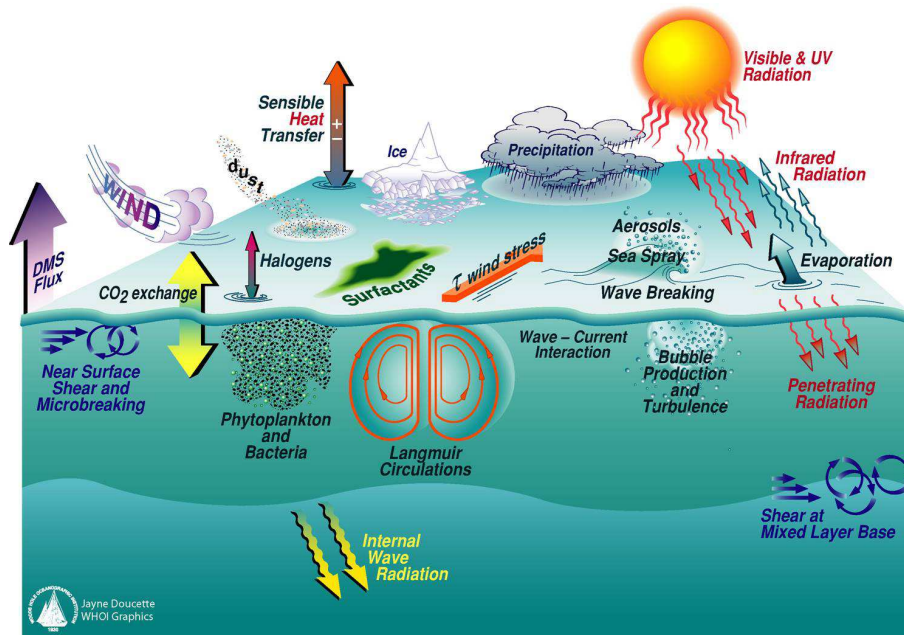
Figure 1.2: *Air-sea interaction is governed by physical, chemical and biological mechanisms. Hydrodynamical processes at or near the surface include momentum transport by wind stress, wave formation and -breaking and Langmuir circulations (from SOLAS[2]).*

The air-water interface is the "bottleneck" for the gas transfer between oceans and atmosphere. Many relevant gases (like carbon dioxide or methane) are of low solubility in water, so that their transfer resistance resides in the water-side. The transfer resistance, or its inverse, the transfer velocity characterises the rate of gas exchange. In order to model the world-wide annual gas flux there has to be chosen a parametrisation, which relates the transfer velocity k to meteorologically accessible quantities like wind speed or slope of the water surface. The experiments of [Jähne, 1985] yield as a suitable parameterisation:

$$k = \beta^{-1} u_* Sc^{-n}, \tag{1.1}$$

where β is a nondimensional scaling factor, u_* is the friction velocity, which is a measure for the momentum transported by the wind into the water bulk, and $Sc = \nu/D$ is the nondimensional Schmidt-number, which quantifies a certain substance according to the ratio of its viscosity ν to its diffusivity D. The Schmidt-number exponent n characterises the state of the water surface. It turns out, that the presence of a smooth surface implies $n = 2/3$ whereas a wavy surface requires $n = 1/2$. Waviness can be characterised by the mean square slope of the water surface (which is accessible by radar backscattering methods on a global scale) much better than by the average wave speed.

In order to find out the physical processes for this interrelationship, one has to consider the hydrodynamics of the water-side flow. Whereas in large scales mass, heat or momentum are

---

[1]1 Pg are 10^{12} kg

[2]Surface Ocean - Lower Atmosphere Study; http://www.uea.ac.uk/env/solas/

transported by turbulent eddies much more efficiently than by molecular diffusion, in the small scale of the viscous boundary layer transport by diffusion is the dominant process. One critical parameter for this transport is the boundary layer thickness, which may be variable in space and time. Some models propose, that this variability is affected by surface convergences and divergences, which in turn are induced by subsurface turbulence generated by wind stress, (micro) breaking waves or (micro) Langmuir circulations. In extreme cases, the whole surface may be renewed. Today it is generally accepted, that all of these models yield the correct Schmidt-number dependency in Eq. (1.1), although they differ in the vertical profiles of concentration and momentum.

During the last two decades image based velocity measurement methods have been developed, which are capable to analyse the surface flow and parts of the internal flow structure of the viscous boundary layer and of surface waves. Most of these methods are restricted to a two-dimensional plane, which typically is aligned into streamwise direction. Because both turbulence, waves and Langmuir circulations are inherently three-dimensional phenomena, clearly a two-dimensional setup is insufficient. Furthermore, we are interested in the flow very close to the boundary, which may be embedded in a wavy surface. The presence of a phase interface poses a further great challenge to flow measurement.

1.2 Own Contribution

In this thesis a novel method for the spatio-temporal analysis of flows close to the water surface is developed. Following new contributions are presented:

Measurement in 3D-space We adapt the idea of [Debaene, 2005], which is suited for measuring the wall-near flow in the context of biofluidmechanics, and generalise it for the use of polydisperse seeding particles. Thus we are able to locate the depth of a tracer particle.

Measurement of 3C-velocities Using extended optical-flow based methods, we are capable to extract all three components of the Eulerian velocity vector field. Furthermore by implementing particle tracking (PTV), we obtain its Lagrangian representation [Jehle and Jähne, 2006b,c].

Direct estimation of the wall shear rate The water-side wall shear rate, which together with the viscosity characterises the stress at the interface, can be estimated directly without previous computation of the velocity vector field [Jehle and Jähne, 2006a].

Both, measurement setup and algorithmics are tested in several ways: By applying the technique to a well known laminar flow its accuracy could be evaluated. Adopting it to the more complicated case of heat-driven turbulence, its feasibility for the application in instationary inherently 3D flows could be demonstrated. The direct estimation of the wall shear rate was applied to sequences recorded in the context of biofluidmechanics.

1.3 Thesis Outline

The thesis is structured into seven major chapters. Chapter 2 is concerned with summarizing the physical foundations required for understanding the transport of mass and momentum at the air-water interface. Apart from classical fluid dynamics, some transport models are sketched

and microscale wave breaking and Langmuir circulations are described. Previous attempts to visualise these phenomena are reviewed.

Chapter 3 presents the techniques to measure physical quantities in fluid. Special attention is drawn onto velocity measurement, such like thermoelectric, optical, acoustic and image-based methods. PIV and PTV belong to the latter ones; they are explained in more detail.

Another method, which has become of interest in fluid flow measurement during the last years is the optical-flow based approach presented in chapter 4. Optical-flow methods can be classified in differential, frequency-based and tensor-based techniques. Naive application often leads to difficulties. We will sketch some approaches to overcome them. The chapter closes with a literature review concerning the application of optical-flow based techniques to hydromechanical problems. This chapter is a shortened version of [Jehle et al., in preparation].

Chapter 5 describes the "heart" of the measurement technique, presented in this thesis: The reconstruction of a fluid particle's 3D-position exploiting Beer-Lambert's law and illuminating with light of two wavelengths. The errors of this technique are investigated.

The hardware components are characterised in detail in chapter 6. A proper selection of tracer particles, dye and light emitting diodes is essential in particular for the measurement method presented here. Like in all quantitative fluid visualisation techniques, optics and cameras have to be adjusted to the experiment.

We make extensive use of image processing techniques. Chapter 7 explains the various steps, the raw image sequences have to pass until the Eulerian or Lagrangian flow field respectively the wall shear rate can be extracted. The determination of both the three-component velocity vector field and the wall shear rate relies on the tensor-based methods, which have been introduced in chapter 4.

Experimental results are given in chapter 8. Two methods of calibrating the determination of a particle's depth are investigated. Both, measurements in a falling film and in a convection tank were conducted. Moreover our method of direct determination of the wall shear rate is applied to sequences recorded in the context of biofluidmechanics. To each of the experiments a short introduction to the theory and a summary of the experimental setup is given.

2 Transport of Mass and Momentum at the Air-Water Interface

2.1 Kinematics of Fluids

In this section we will address some issues regarding the kinematics of fluids, which will be relevant for our analysis. Kinematics is known as the branch of mechanics that deals with quantities involving space and time only. In contrast to dynamics, kinematics *describes* motion, it does not try to *explain* it (by forces for instance).

2.1.1 Lagrangian and Eulerian Perspective

There are two alternative representations of fluid motion: The Eulerian description gives information about what happens at a fixed spatial point in space; the Lagrangian description follows an individual fluid particle on its way through space.

The Eulerian perspective

A scalar-, vector- or tensor-valued quantity F, like temperature, velocity or the diffusion tensor, is measured (or calculated) at a fixed position $\boldsymbol{x}$ at a given time t: $F(\boldsymbol{x}, t)$.

The partial derivative

$$\frac{\partial F(\boldsymbol{x}, t)}{\partial t} \tag{2.1}$$

yields the local rate of change of the quantity at a point $\boldsymbol{x}$ and at a time t and gives *not* the total rate of change as seen by the fluid particle.

We define the quantity $\boldsymbol{u} = \partial \boldsymbol{x}/\partial t$ to be the *Eulerian velocity field*. The tangents to the Eulerian vectors are called *streamlines*.

The Lagrangian perspective

Here an individual fluid particle is followed, which is located at the position $\boldsymbol{x}_0$ at the time $t = 0$. Thus the value of an arbitrary quantity can be specified by $F(\boldsymbol{x}_0, t)$ for $t > 0$. The time t can be considered as the parameter of a trajectory, which forms the *pathline* of the fluid particle.

We can calculate the total rate of change of the quantity along its way on the trajectory by using the chain rule:

$$\frac{\mathrm{d}F(\boldsymbol{x}, t)}{\mathrm{d}t} = \frac{\partial F(\boldsymbol{x}, t)}{\partial t} + \frac{\mathrm{d}\boldsymbol{x}}{\mathrm{d}t} \nabla F. \tag{2.2}$$

Literally speaking, this total rate of change (material derivative, substantial derivative, particle derivative) of a quantity F is composed of two parts:

- The local rate of change of F at a given point $\boldsymbol{x}$ and the

- *advective* derivative of the quantity as a result of its motion $\boldsymbol{u}\nabla F$, which is a product of the spatial gradient of the quantity ∇F and the velocity $\boldsymbol{u} = \mathrm{d}\boldsymbol{x}/\mathrm{d}t$ of the fluid particle.

Thus, a quantity, say temperature, of a fluid particle can change, because the whole temperature field is changing, or it can change, because it is just moving around (maybe it moves into a hotter region). For the latter, Eq. (2.1) may be zero but Eq. (2.2) is different from zero, because both, the gradient of the temperature and the fluid particle's velocity are not zero.

2.1.2 The Helmholtz Theorem

We can extend the infinitesimal velocity vector $\boldsymbol{u} = (u_1, u_2, u_3)^T$ of a fluid element, which is located at the position $\boldsymbol{x} = (x_1, x_2, x_3)$, up to first order by expanding it into a Taylor series:

$$u_i(x_j, t) \approx u_i(x_{j,0}) + \frac{\partial u_i}{\partial x_j} x_j + \frac{\partial u_i}{\partial t} t \quad \text{with} \quad i, j = 1 \ldots 3.$$

Here $u_i(x_j, 0)$ is its translation, $(\gamma_{ij}) = \partial u_i/\partial x_j$ is known as the velocity gradient tensor, and $\partial u_i/\partial t$ is its acceleration.

The velocity gradient tensor can be decomposed into a symmetrical (s_{ij}) and an antisymmetrical (a_{ij}) part:

$$\gamma_{ij} = \frac{1}{2}(\gamma_{ij} + \gamma_{ji}) + \frac{1}{2}(\gamma_{ij} - \gamma_{ji}) \equiv s_{ij} + a_{ij},$$

which reads in matrix-notation:

$$(\gamma_{ij}) = \begin{pmatrix} 0 & -a_{21} & a_{13} \\ a_{21} & 0 & -a_{32} \\ -a_{13} & a_{32} & 0 \end{pmatrix} + \begin{pmatrix} \partial u_1/\partial x_1 & s_{12} & s_{13} \\ s_{12} & \partial u_2/\partial x_2 & s_{23} \\ s_{13} & s_{23} & \partial u_3/\partial x_3 \end{pmatrix}. \qquad (2.3)$$

The different parts of (γ_{ij}) can be identified with different types of affine transformations:

Rotation The first matrix in Eq. (2.3) is a rotation matrix - their components can be identified with half of the rotation vector:

$$\boldsymbol{\omega} = (\nabla \times \boldsymbol{u}) = (\partial/\partial x_1, \partial/\partial x_2, \partial/\partial x_3)^T \times \boldsymbol{u} \equiv 2(a_{32}, a_{13}, a_{21})^T.$$

Dilation The trace of the second matrix in Eq. (2.3) represents the volume dilation Θ_V, which is the divergence of the vector field

$$\Theta_V = \partial u_1/\partial x_1 + \partial u_2/\partial x_2 + \partial u_3/\partial x_3 = \nabla \cdot \boldsymbol{u}.$$

Shear: The non-diagonal elements of the second matrix in Eq. (2.3) are half of the shear strain rates, which are defined by the rates of decrease of the angle formed by two mutually perpendicular lines on the element.

We have shown, that every infinitesimal motion of a fluid volume element can be decomposed into a translation, a rotation and a deformation. The latter consists of dilation and shearing of the element. This is know as the *Helmholtz theorem* ([Helmholtz, 1858]).

2.2 Dynamics of Fluids

2.2.1 Forces in Fluid Dynamics

The forces acting on a fluid element can be divided into three classes: body forces, surface forces, and line forces.

Body forces: Body forces result from the medium being placed in a force field. Examples are the gravitational or electric force. They have in common, that they are proportional to the mass of the body, they act on. An example is the gravitational force $\boldsymbol{F}$:

$$\boldsymbol{F} = m\boldsymbol{g} \quad \text{resp.} \quad \boldsymbol{f} = \rho\boldsymbol{g},$$

with $\boldsymbol{g}$ being the gravitational constant. The introduction of a force density $\boldsymbol{f}$, i. e. force per unit volume, is appropriate in continuum mechanics.

Surface forces: Surface forces are proportional to the area, they act on. They can be resolved into components normal and tangential to the area. The i-component of the surface force per unit volume of an element is

$$\partial\tau_{ij}/\partial x_j,$$

where (τ_{ij}) is the stress tensor. The first index of this symmetric tensor i indicates the direction of the normal to the surface on which the stress is considered, and the second index j indicates the direction in which the stress acts. The diagonal elements $(i = j)$ of the stress tensor are the normal stresses, and the off-diagonal elements are the tangential or shear stresses.

The relation of the stress and the deformation in a continuum is called a constitutive equation. In the case of a Newtonian, incompressible fluid, the stress is related to the pressure p and the strain $s_{ij} = 1/2(\partial u_i/\partial x_j + \partial u_j/\partial x_i)$ according to

$$\tau_{ij} = -p\delta_{ij} + 2\mu s_{ij}, \tag{2.4}$$

where μ is the dynamical viscosity.

Line forces: Line forces are proportional to the extent of the line they act along. An example is the surface tension force. This kind of force does not appear directly in the equations of motion, but enters in the boundary conditions.

2.2.2 Basic Equations

All fluid mechanics is based on the conservation laws for mass, momentum and energy. In the following, we will present these laws in differential form.

Conservation of mass - continuity equation

Conservation of mass is expressed by the continuity equation, which reads in its general form:

$$\frac{\partial\rho}{\partial t} + \nabla \cdot (\rho\boldsymbol{u}) = 0. \tag{2.5}$$

For incompressible fluids (i. e. for liquids and gases with speeds considerably smaller than the speed of sound), we can regard ρ as constant, so that the continuity equation becomes:

$$\nabla \cdot \boldsymbol{u} = 0.$$

Conservation of momentum - Navier-Stokes equation

Newton's law is applied to an infinitesimal fluid element:

$$\rho \frac{\mathrm{d}u_i}{\mathrm{d}t} = \rho g_i + \frac{\partial \tau_{ij}}{\partial x_j}.$$

By inserting the constitutive equation Eq. (2.4), we obtain the Navier-Stokes equation, which reads in matrix-vector notation:

$$\rho \frac{\mathrm{d}\boldsymbol{u}}{\mathrm{d}t} = \frac{\partial \boldsymbol{u}}{\partial t} + \boldsymbol{u}\nabla\boldsymbol{u} = \rho\boldsymbol{g} - \nabla p + \mu\nabla^2\boldsymbol{u}. \tag{2.6}$$

We can rewrite the Navier-Stokes equation by introducing non-dimensional quantities $\tilde{\boldsymbol{u}} = \boldsymbol{u}/V_0$, $\tilde{\boldsymbol{x}} = \boldsymbol{x}/L_0$, $\tilde{t} = tV_0/L_0$ and $\tilde{p} = p/(\rho V_0^2)$ using a typical velocity scale V_0 and a typical length scale L_0

$$\frac{\mathrm{d}\tilde{\boldsymbol{u}}}{\mathrm{d}\tilde{t}} = \frac{1}{\mathrm{Fr}^2}\boldsymbol{g}/g - \tilde{\nabla}\tilde{p} + \frac{1}{\mathrm{Re}}\tilde{\nabla}^2\tilde{\boldsymbol{u}},$$

where we have introduced the Reynolds-number $\mathrm{Re} = V_0 L_0 \nu^{-1}$, which characterises the relative strength of inertial and viscous forces, and the Froude-number $\mathrm{Fr} = V_0(L_0 g)^{-1/2}$, which quantifies the relative importance of inertia and gravity forces.

In the following two limits of the Navier-Stokes equation will be discussed:

Viscous flow (Re $\ll$ 1): The inertia term in Eq. (2.6) is negligible compared to the viscous term. This results in the Stokes equation:

$$\rho \frac{\partial \boldsymbol{u}}{\partial t} = \rho\boldsymbol{g} - \nabla p + \mu\nabla^2\boldsymbol{u}.$$

Inviscid flow (Re $\gg$ 1): The viscous term can be neglected in Eq. (2.6). This results in the Euler equation:

$$\rho \frac{\mathrm{d}\boldsymbol{u}}{\mathrm{d}t} = \rho\boldsymbol{g} - \nabla p.$$

We can derive a mechanical energy equation directly from the momentum equation (see [Kundu, 1990]).

Conservation of thermal energy - Heat equation

Under several restrictions including that in which the flow speeds are small compared to the speed of sound and in which the temperature differences in the flow are small, the heat equation becomes

$$\frac{\mathrm{d}T}{\mathrm{d}t} = D_H\nabla^2 T,$$

with D_H being the thermal diffusion.

2.3 Transport in Fluids

In this section we will consider the transport of any *substantial addition* in fluids. Such an addition can be *mass* (for example a trace gas like carbon dioxide), *momentum* or *heat*. In the following formulas we will denote the addition by the symbol c, which represents the concentration, the momentum (here c is vector-valued) or the heat.

2.3.1 Molecular Transport: Diffusion

Diffusion in gases can be considered as a result of the Brownian motion of molecules. Mathematically stationary diffusion can be described by *Fick's first law*:

$$\boldsymbol{j} = -D\nabla c, \tag{2.7}$$

where $\boldsymbol{j}$ is the flux density and D is the diffusion constant. In order to fulfill stationarity it is assumed, that the concentration of mass, heat or momentum in the reservoirs is sufficiently large, so that it stays constant over the regarded time interval.

For instationary processes, we have to take care, that we satisfy the continuity equation $\partial c/\partial t + \nabla \boldsymbol{j} = 0$. Combining this with Eq. (2.7), we arrive at *Fick's second law*:

$$\frac{\partial c}{\partial t} = D\nabla^2 c. \tag{2.8}$$

Here we assumed homogeneous, isotropic diffusion. In the general case D is a tensor of second order, so that Equation (2.8) has to be rewritten to:

$$\frac{\partial c}{\partial t} = \nabla(\boldsymbol{D}\nabla c).$$

Until now we didn't specify the type of tracer, which is represented by the symbol c:

- The mass transport can be described by the flux-density

$$\boldsymbol{j}_m = -D\nabla c,$$

  here c is the concentration of the material inside the fluid, which can be specified in mol/l for instance. D is the diffusion constant (with units $\mathrm{m^2 s^{-1}}$), a specific property of the considered material.

- Heat transport can be described by the flux-density

$$\boldsymbol{j}_H = -D_H\nabla(\rho c_P T) = -\lambda\nabla T,$$

  here the concentration is replaced by $\rho c_P T$. If we regard the density ρ and the specific heat c_P as independent from position, we see, that the flux density is proportional to the temperature gradient. The proportionality constant is the diffusion constant for heat, which depends on the coefficient of thermal conductivity λ in the way $D_H = \lambda(\rho c_P)^{-1}$. Again this diffusion constant has units $\mathrm{m^2 s^{-1}}$.

- Momentum transport can be described by the flux-density

$$\boldsymbol{j}_p = -\nu\nabla(\boldsymbol{u}),$$

  where the flux-density is related to the shear stress $\boldsymbol{\tau}$ via $\boldsymbol{j} = \boldsymbol{\tau}/\rho$ and the diffusion constant for momentum is the kinematic viscosity ν. Thus for incompressible media (with constant ρ) the shear stress is proportional to the velocity gradient. Here the kinematic viscosity has units $\mathrm{m^2 s^{-1}}$, too.

2.3.2 Turbulent Transport

Now we consider, that tracers can be transported both by diffusion and convection. In order to do so, we have to regard the total differential of the concentration change (here again "concentration" stands for mass, heat and momentum):

$$\frac{\mathrm{d}c}{\mathrm{d}t} = \frac{\partial c}{\partial t} + \boldsymbol{u}\nabla c = D\nabla^2 c \tag{2.9}$$

Fick's second law Equation (2.8) becomes the *general transport equation*, which is linear in c if the diffusion constant D is not a function of concentration. The only unknown in Equation (2.9) is the velocity vector field $\boldsymbol{u}$, which can be obtained by solving the Navier-Stokes-equation Eq. (2.6).

Reynolds decomposition

From now on we move over to turbulent flows, which are the norm, rather than the exception in environmental fluid dynamics (consider the atmosphere or the ocean, for instance). We perform the Reynolds decomposition of the velocity and concentration fields into mean (uppercase letters) and fluctuating (primed lowercase letters) quantities:

$$\boldsymbol{u} = \boldsymbol{U} + \boldsymbol{u}' \quad \text{and} \quad c = C + c'.$$

We average the whole transport equation Eq. (2.9):

$$\overline{\partial/\partial t(C + c') + (\boldsymbol{U} + \boldsymbol{u}')\nabla(C + c')} = \overline{D\nabla^2(C + c')},$$

which becomes (using Einstein's summation convention)

$$\frac{\partial C}{\partial t} + \frac{\partial}{\partial x_i}\left(CU_i + \overline{c'u_i'}\right) = D\frac{\partial^2}{\partial x_i^2}C,$$

where we introduced the *Reynolds stress* $\overline{c'u_i'}$ which is essentially the covariance between c' and u_i'. In the case of simple parallel shear flow with a positive mean velocity- and concentration gradient $\partial U(z)/\partial z > 0$ and $\partial C(z)/\partial z > 0$, the velocity fluctuations tend to balance the flow in the way, that the concentration gradient is flattened, i.e. we have $\overline{c'w'} < 0$ in this case.

1D-case

We will consider the 1D-case of a homogeneous flow $U = U(z)$, where we have a mean velocity field $(U, 0, 0)$ and a fluctuating velocity field (u', v', w'). From the assumption of homogeneity it follows, that $\overline{c'u'} = \overline{c'v'} = 0$, so that the Reynolds-averaged transport equation becomes:

$$\frac{\partial C}{\partial t} + \frac{\partial}{\partial x_i}(CU_i) + \frac{\partial}{\partial z}\overline{c'w'} = D\frac{\partial^2}{\partial z^2}C.$$

Because of homogeneity we can set $\partial/\partial x_i(CU_i)$ to zero, so that we arrive at

$$\frac{\partial C}{\partial t} = \frac{\partial}{\partial z}\left(D\frac{\partial C}{\partial z} - \overline{c'w'}\right) \tag{2.10}$$

for concentration (general) and

$$\frac{\partial U}{\partial t} = \frac{\partial}{\partial z}\left(\nu\frac{\partial U}{\partial z} - \overline{u'w'}\right) \tag{2.11}$$

for momentum (in particular). The latter is known as Reynolds-equation in the literature.

Linear-logarithmic velocity profile

Now we will consider a stationary 1D solution. The transport term in Eq. (2.11) becomes a constant flux density for momentum:

$$j_p = \nu\frac{\partial U}{\partial z} - \overline{u'w'} = \frac{\partial U}{\partial z}(\nu + K_t) = j_{\text{diff}} + j_{\text{turb}}. \tag{2.12}$$

Here the first term $\nu\partial U/\partial z$ is due to the molecular transport and may be described using a (molecular) diffusive flux density and the second term $\overline{u'w'}$ is due to turbulence and may be described using a turbulent flux density, which can be expressed using a turbulent diffusion constant for momentum K_t.

There have to be fulfilled two assumptions for the turbulent diffusion constant approach:

1. The size of the eddies has to be small compared to the dimensions of the system, and

2. turbulence has to be homogeneous and isotropic.

Clearly the first assumption is not fulfilled, because the eddy-size (which is a measure for the mean free path in turbulence) can reach the dimensions of the system. Now the big question is: Which eddys are relevant to the process, great ones, or small ones?

To find an expression for the velocity profile $U(z)$, we have to rearrange Equation (2.12), and integrate:

$$\frac{\partial U}{\partial z} = -\frac{j_p}{\rho(\nu + K_t(z))} \Rightarrow U(z) = -\frac{\tau}{\rho}\int_0^z\frac{\mathrm{d}z'}{\nu + K_t(z')} \quad \text{where} \quad U(0) = 0. \tag{2.13}$$

Based on intuition we have (unlike the case of molecular diffusion) a clear spatial dependency of K_t. Using the definition of the friction velocity $\tau = \rho u_*^2$, we can split the integral into two parts: one outside the boundary layer (where $K_t \gg \nu$) and one inside the boundary layer (where $\nu \gg K_t$). The integral outside the boundary layer reads:

$$U(z_1) - U(z_0) = u_*^2\int_{z_0}^{z_1}\frac{\mathrm{d}z'}{K_t(z')} \tag{2.14}$$

A guess for spatial dependency of the turbulent diffusion constant *outside* of the viscous boundary layer would be

$$K_t(z) = \kappa u_* z, \tag{2.15}$$

with the von Karman constant $\kappa \approx 0.41$. Here the turbulent diffusion constant is directly proportional to the distance to the wall z. By plugging this into Equation (2.14) we get

$$U(z_1) - U(z_0) = \frac{u_*}{\kappa}\int_{z_0}^{z_1}\frac{\mathrm{d}z'}{z'} = \frac{u_*}{\kappa}(\ln z_1 - \ln z_0).$$

This is the logarithmic profile, which can be made nondimensional in the dependent and independent variables by applying the transformations

$$u_+ \leftarrow U(z)/u_* \quad \text{and} \quad z_+ \leftarrow u_* z/\nu,$$

so that we arrive at

$$u_+ = (\ln z_+)/\kappa + \text{const.} \tag{2.16}$$

To obtain an expression for the profile near the wall, we use the definitions of shear stress (near the wall) and friction velocity:

$$\left[\frac{\partial U}{\partial z}\right]_{z=0} = \frac{\tau}{\rho\nu} = \frac{u_*^2}{\nu} \Rightarrow U = \frac{u_*^2 z}{\nu} \Rightarrow u_+ = z_+. \tag{2.17}$$

We see, that the profile in the viscous sublayer (where the viscosity is large compared to the turbulent diffusion) becomes linear. The universal law of the wall is plotted in Fig. 2.1.

Implications on gas transfer

Until now we have addressed the transport of momentum. What are the implications for the transport of mass, for example? We have (similar to Equation (2.13)) an expression for the mean mass-concentration C depending on the wall-distance z:

$$C(z) = j \int_0^z \frac{\mathrm{d}z'}{D + K_c(z')} + C_0, \tag{2.18}$$

where we used the turbulent diffusion for concentration K_c, which depends on z, too. Here we introduce the transfer velocity $k \equiv j/\Delta c$, which is known as the "piston velocity": Visually, k specifies the velocity, concentration is pushed through the boundary layer into the under- resp. overlying bulk region.

2.4 Transport Models

2.4.1 Film Models

Film models (e. g. in [Liss and Slater, 1974]) are based on the assumption, that there is no turbulence in the viscous boundary layer. Contrary to that, outside of the boundary layer there is high mixing, so that there is no concentration gradient.

We can define a typical thickness for the boundary layer z_* by intersecting the linear velocity profile Eq. (2.17) and the logarithmic velocity profile Eq. (2.16). We find $z_+ \approx 11$, i. e. $z_* \approx 11\nu/u_*$. By plugging this into Fick's first law Eq. (2.7), we get an expression for the mass flux density, which depends on the concentration difference and on the boundary layer thickness:

$$j_m = -D\frac{\partial c}{\partial z} = -D\frac{\Delta c}{z_*}.$$

In order to get an expression for the transfer velocity, we divide the flux density by the concentration difference:

$$k = \frac{j_m}{\Delta c} = \frac{D}{z_*} = \frac{Du_*}{11\nu} = \frac{1}{11}Sc^{-1}u_*. \tag{2.19}$$
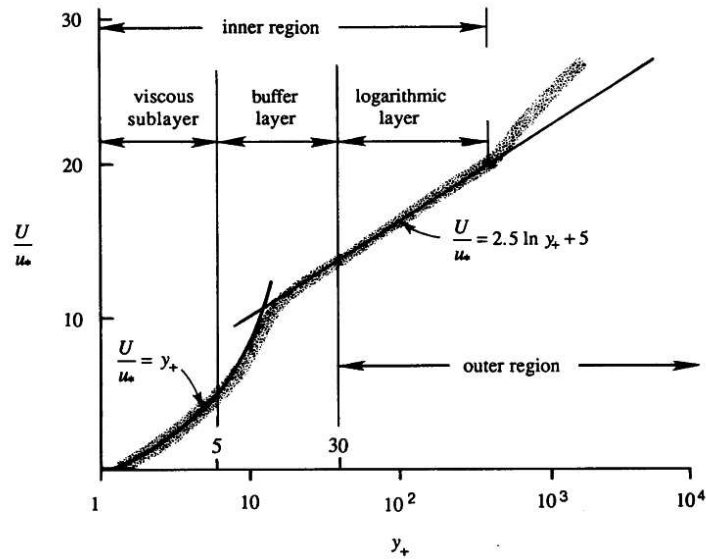
Figure 2.1: *Universal law of the wall. The non-dimensional velocity $u_+ = U/u_*$ is plotted semilogarithmically relative to the non-dimensional wall distance $z_+ = u_* z/\nu$. For small distances ($z_+ < O(5)$), there is a linear, for larger distances ($z_+ > O(30)$) there is a logarithmic dependence. From [Kundu, 1990]*

Recapulitating: If the concentration profile is known, so the boundary layer thickness is known, so the transfer velocity is known (with known diffusion constant).

In the last step of Eq. (2.19) we used the definition of the nondimensional Schmidt-Number for gases, which is viscosity of the fluid divided by molecular diffusion constant: $Sc = \nu/D$. For most gases, Sc is in the range of 200 to 3000. Experiments show, that the film model is totally unreal, because the measured transfer velocities exceed the theoretically derived by orders of magnitude.

2.4.2 Surface Renewal Models

A completely different approach is made in the surface renewal models (see [Danckwerts, 1951; Higbie, 1935]). Here the basic idea is, that large eddies rebuild the boundary layer in a statistical sense. We can incorporate that by assuming the divergence of the Reynolds stress for concentrations $\partial/\partial z(\overline{c'w'})$ in Eq. (2.10) to be directly proportional to the concentration itself. Dimensional reasoning shows, that the proportionality constant has to be an inverse time, which is called renewal rate τ^{-1}. Then the stationary transport equation reads

$$D\frac{\partial^2 c}{\partial z^2} - \tau^{-1}c = 0, \tag{2.20}$$

which is a second order ordinary differential equation, and can be solved by the ansatz $c = c_0 \exp(-z/z_*)$. We get for the boundary layer thickness $z_* = \sqrt{D\tau}$.

13
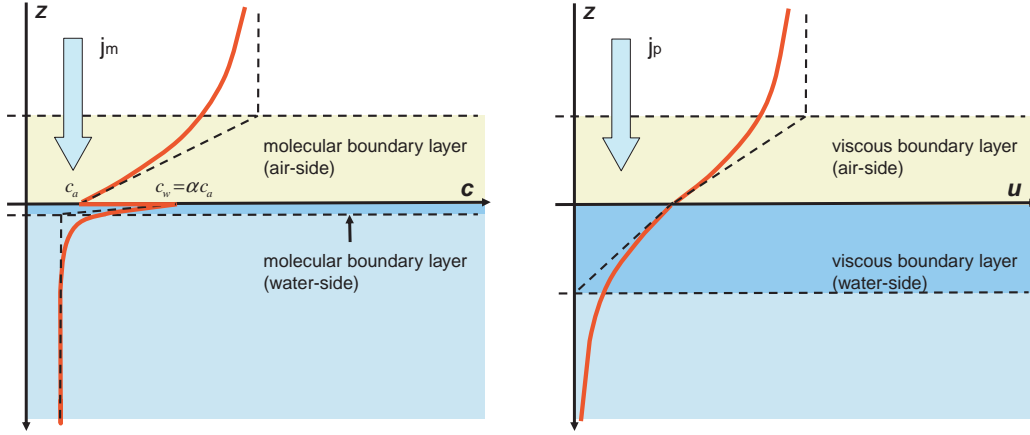
Figure 2.2: *Schematical illustration of boundary layers at the water surface. Left: Because the solubility of a gas in water is not equal to unity, there exists a discontinuity of the concentration profile. Right: The velocity profile is continuous. The thickness of the molecular boundary layer is O(100 μm), the thickness of the viscous boundary layer is O(1 mm) (from [Degreif, 2006]).*

Because τ merely can depend on the viscosity and on the friction velocity, we have by dimensional reasoning:

$$\tau(u_*, \nu) = \beta^2 \frac{\nu}{u_*^2},$$

where we have introduced the proportionality constant β^2. We can plug that into the nondimensional form of Eq. (2.20):

$$D\frac{\partial^2 c}{\partial z^2}\frac{u_*^2}{\nu^2} - \frac{cu_*^2}{\beta^2\nu} = 0 \Rightarrow \frac{\partial^2 c}{\partial z_+^2} - \frac{Sc}{\beta^2}c = 0,$$

where we have used the nondimensional wall distance $z_+ = zu_*/\nu$. By fitting the solution of this equation $c = c_0 \exp(-Scz_+/\beta)$ to the universal velocity profile, we get $\beta \approx 16$, so that we can determine expression for the transfer velocity:

$$k = \frac{D}{z_*} = \sqrt{\frac{D}{\tau}} = \frac{u_*}{\beta}\sqrt{\frac{D}{\nu}} = \frac{1}{16}Sc^{-1/2}u_*.$$

Considering Schmidt numbers of order 1000 we see, that the surface renewal model yields much higher transfer velocities than the film model, because the Schmidt number exponent is only 1/2, in contrast to the film model, where it is unity.

2.4.3 Turbulent Diffusion Models

In contrast to the previous models, where heuristic assumptions were made, turbulent diffusion models and surface divergence models are hydrodynamically more founded. Here we will sketch the derivation of [Coantic, 1986].

Starting point of the turbulent diffusion models is the solution of the 1D-stationary Reynolds-averaged transport equation Eq. (2.18)). To integrate this equation, we have to find an expression for the turbulent diffusion constant containing z. The turbulent diffusion constant is by definition (Eq. (2.12)) proportional to the Reynolds stress $K_t \propto \overline{u'w'}$, where the proportionality constant is $-(\partial U/\partial z)^{-1}$.

Now we expand the Reynolds stress into a Taylor series for small distances z from the surface:

$$\overline{u'w'} \approx 0 + \left[\frac{\partial}{\partial z}\overline{u'w'}\right]_{z=0} z + \left[\frac{\partial^2}{\partial z^2}\overline{u'w'}\right]_{z=0} z^2.$$

For the first derivative of the Reynolds stress at the surface we have

$$\left[\frac{\partial}{\partial z}\overline{u'w'}\right]_{z=0} = \overline{\frac{\partial u'}{\partial z}w'} + \overline{u'\frac{\partial w'}{\partial z}}.$$

Because $w' = 0$ the first term vanishes. The second term vanishes at a rigid surface, too, because there u' is zero, also. At a free surface, we have $u' \neq 0$ and $w' \neq 0$ in general, but we may have $\partial w'/\partial z = 0$. This is exactly the case, if the 2D-continuity $\partial u'/\partial x + \partial v'/\partial y = 0$ holds. If we calculate the second derivative of the Reynolds stress:

$$\left[\frac{\partial^2}{\partial z^2}\overline{u'w'}\right]_{z=0} = \overline{\frac{\partial u'}{\partial z}\frac{\partial w'}{\partial z}} + \overline{u'\frac{\partial^2 w'}{\partial z^2}},$$

we find, that both, first and second term vanishes in the rigid surface case (because, there $\partial w'/\partial z = u' = 0$), but surely this not happens in the free surface case, because there both u' and $\partial^2 w'/\partial z^2$ are definitely not zero.

Recapitulating, in the rigid surface case we require, that the second derivative of the Reynolds stress has to vanish, so that we have for the turbulent diffusion constant:

$$K_t(z) = \alpha_3 z^3 + O(z^4) \quad \text{for a rigid surface.}$$

In the free-surface-case the second derivative does not disappear, so we can apply:

$$K_t(z) = \alpha_2 z^2 + O(z^3) \quad \text{for a free surface.}$$

Because the resistance for gas transfer resides mainly in the boundary layer, we let z go to infinity, so that the transfer velocity becomes

$$k = \frac{j_m}{C - C_0} \left(\int_0^\infty \frac{\mathrm{d}z'}{D + \alpha_n z'^p}\right)^{-1},$$

where we plugged in the expressions for the turbulent diffusion constants for the free-surface-case ($p = 2$), and the solid-surface-case ($p = 3$). After nondimensionalising and some simple manipulations, we get

$$k = \frac{u_*}{Sc} \left(\int_0^\infty \frac{\mathrm{d}z'_+}{1 + \alpha_n z'^p_+/D}\right)^{-1},$$

which can be integrated to

$$k = \beta_p^{-1} Sc^{\frac{1}{p}-1} u_*$$

which holds exactly for $Sc \to \infty$. In particular we find

$$
\begin{aligned}
k &= \beta_2^{-1} Sc^{-1/2} u_* \qquad \text{for a free surface } (p = 2), \text{ and} \\
k &= \beta_3^{-1} Sc^{-2/3} u_* \qquad \text{for a solid surface } (p = 3)
\end{aligned}
$$

The free-surface case is reproduced by the surface renewal model $k = 1/16 Sc^{-1/2} u_*$, whereas the Schmidt number exponent forecasted by the film model $k = 1/11 Sc^{-1} u_*$ is even to low to match with the turbulent-diffusion model for a solid surface.

[Deacon, 1977] integrated Eq. (2.18) numerically using an analytical expression for $K_t(z_+)$ (given by [Reichardt, 1951]) to obtain more exact expressions for the transfer velocity, which depend on the magnitude of the Schmidt number.

2.4.4 Surface Divergence Models

Surface divergence models relate hydrodynamical quantities (i.e. surface divergence) to the boundary layer thickness and to the transfer velocity. Their attraction originates from the fact, that surface divergences can be measured directly or can be related to phenomena like microscale wave breaking.

From the continuity equation it follows at the surface:

$$w = -z \left(\frac{\partial u}{\partial x} + \frac{\partial v}{\partial y} \right),$$

where we have assumed u and v being constant in the thin mass boundary layer. Where the horizontal flow is divergent, the vertical velocity is upward, so that the mass boundary layer is squeezed by advection. In the region of surface convergence, the vertical velocity is downward, and the mass boundary layer is pulled down. Thus the thickness of the mass boundary layer, and thus the transfer velocity is controlled by the surface divergences.

Free surface stagnation point flow

In the following we will discuss the model for a simple free-surface stagnation point flow, which can be described by

$$u = ax, \quad v = -ax,$$

where a is the divergence of the horizontal velocity field. The stationary transport equation (Eq. (2.9)) reads (for simplicity, we consider only one horizontal dimension)

$$u \frac{\partial c}{\partial x} + w \frac{\partial c}{\partial z} = D \left(\frac{\partial^2 c}{\partial x^2} + \frac{\partial^2 c}{\partial y^2} \right).$$

There is no horizontal concentration gradient at the surface $\partial c / \partial x = 0$, and the horizontal diffusion is negligible $\partial^2 c / \partial x^2 = 0$, so that the concentration profile is determined by

$$c(z) = c_0 \text{erfc} \left(z \sqrt{\frac{a}{2D}} \right).$$

The transfer velocity at the surface is given by

$$k = \frac{j_0}{c_0} = \frac{D \left[\dfrac{\partial c}{\partial z} \right]_{z=0}}{c_0} = \sqrt{\frac{2aD}{\pi}} = 0.623 u_* \frac{Sc^{-1/2}}{\sqrt{Re}},$$

with the Reynolds number $Re = u_*^2/a\nu$.

Rigid surface stagnation point flow

Having the boundary condition of a rigid surface, the 2D-flow field becomes

$$u = \frac{\partial u}{\partial x} = \frac{\partial w}{\partial z} = 0, \quad w = w_{BL}\Phi(\eta),$$

with $w_{BL} = \sqrt{nua}$. Here $\Phi(\eta)$ is a function describing the "Hiemez flow", the flow field around s stagnation point in the rigid-surface case [Schlichting, 1960]. In the case of large Schmidt-numbers, we can solve the transport equation, yielding the transfer velocity at the surface:

$$k = 0.66 u_* \frac{Sc^{-2/3}}{\sqrt{Re}}.$$

Evidently, these very idealised assumptions lead to the correct Schmidt-number-exponents. [Csanady, 1990] elaborated an extension to this model, applying results of measurements in short wind waves (see section 2.5.2).

2.5 Microscale Wave Breaking and Langmuir Circulations

Unless now we only considered extremely simplified models of transport of mass and momentum through a free surface. The major difficulty is the presence of a free-surface boundary condition. In interaction with the wind stress this can lead to the formation of shear flow, (breaking) waves and Langmuir circulations. All of these nonlinear phenomena generate turbulence, which is responsible for creating surface divergences, and thus for thinning or renewing the mass boundary layer, which affects the resistance for the gas transfer. While the surface of the waves is measurable relatively easy (see for example [Balschbach et al., 2001; Jähne et al., 2005]), it is considerable more difficult to obtain quantitative information about their internal flow field. In this section we will recapitulate some facts about linear and nonlinear wave theory, have a closer look to microscale wave breaking and Langmuir circulations and have a tour through historical and current attempts to obtain knowledge about the near-surface flow. Regarding the dynamics of surface waves we suggest reading [Phillips, 1969]; for an overview over the basic mechanisms of the interaction of atmosphere and ocean see [Kraus and Businger, 1994].

2.5.1 Definition and Theory

Linearised wave theory

The *linearised wave theory* assumes a sine-shaped boundary condition at the air-water interface:

$$\eta = a\cos(kx - \omega t),$$

with a functional interrelation between the wave frequency ω and the wave number k, called dispersion relation, which reads

$$\omega = \sqrt{gk \tanh(kH)},$$

depending on the water depth H. In its deep-water approximation the linearised wave theory predicts particle orbits describing circles, whose size is damped exponentially with increasing distance from the surface. The applicability of linear wave theory requires $a \ll H$ and $ka \ll 1$. The latter implies, that the slope of the sea-surface is small.

Stokes theory

In a dispersive system, like in deep water, an accumulation of linear waves is prevented, because the different Fourier components propagate at different speeds and become separated from each other. *Nonlinear* steepening could cancel out the dispersive spreading, resulting in finite amplitude waves of constant form.

[Stokes, 1847] showed, that periodic waves of finite amplitude are possible in deep water. The surface elevation of irrotational waves in deep water is given by a power series of the small parameter ak, the wave steepness:

$$\eta = a \left(\cos k(x - ct) + \frac{1}{2}ka \cos 2k(x - ct) + \frac{3}{8}(ka)^2 \cos 3k(x - ct) + \dots \right),$$

with the dispersion relation

$$\omega = \sqrt{gk(1 + (ka)^2)}.$$

Unlike in the linear approximation, in the Stokes solution the fluid elements don't move in circles exactly but move in orbits, whose average motion is slowly in the direction of the waves. This is due to the fact, that the particles move faster forward (when they are at the top of the trajectory) than backward (when they are at the bottom of the orbit). This Stokes drift is

$$u_S = a^2 \omega k \exp 2kz_0,$$

where z_0 is the particle's initial vertical position.

It turns out, that these waves become instable, if the maximum amplitude exceeds 0.07 times the wavelength, so that the crest becomes a sharp 120°angle. This is the classical Stokes criterion.

Wave breaking

There is no generally accepted definition of wave breaking. One way to define this phenomenon would be to demand air entrainment as necessary concomitant to wave breaking [Cokelet, 1977]. The resulting characteristic "whitecaps" are easily detectable. Due to the accompanying bubble formation, the rate of gas transfer is further increased.

Air entrainment and bubble formation may not be the only criteria for wave breaking; several researchers have found a characteristic change of the internal flow structure of breaking waves like break-down of the subsurface flow and the generation of turbulence with enhanced diffusion and dissipation, possibly accompanied by flow separation. [Banner and Phillips, 1974] define breaking waves as those, in which certain fluid elements at the free surface (near the wave crest) are moving forward at a speed greater than the propagation speed of the wave profile as a whole.

In deep water the fluid elements slide down the leading slope. This results in air entrainment at large scales of breaking, but not necessarily at smaller scales. Thus the term *microscale wave breaking* was created to distinguish this behaviour from the bubbles-producing mechanism. One characteristic of such a breaking wave is the existence of a stagnation point in the mean flow, because the mean flow reverses near the crest.

Parasitic capillaries

Moderately short gravity waves exhibit "parasitic capillaries" on the leeward face. These capillary waves have the same phase speed like the gravity waves, which becomes possible due to the different dispersion relations. [Longuet-Higgins, 1992] conjectures, that the parasitic capillaries are the source of vorticity, because their orbital frequency is much greater than the orbital frequency of the gravity waves. Thus the mean vorticity, which is a measure for turbulence, depends both on the wave slope ak of the gravity waves and on the orbital frequency of the capillaries. The two kinds of waves constitute a symbiotic system, a "capillary roller" - the energy of the gravity waves is pumped into the capillary waves, which would otherwise be damped away. Together with microscale wave breaking due to wind-induced shear stress, the vorticity production by parasitic capillaries may be the major reason for the rapid increase of the gas transfer rate, once waves have formated (i. e. the transition of the Schmidt number exponent from -2/3 to -1/2, which was reported by [Jähne et al., 1987]).

Small-scale Langmuir circulations

Langmuir circulations are streamwise vortices near the surface accompanied by regions of surface convergence and divergence (Fig. 2.3). [Melville et al., 1998] presented laboratory measurements of the generation and evolution of micro-Langmuir circulations as an instability of a wind-driven surface shear layer using the 2D-PIV-technique. [Veron and Melville, 2001] found that the heat and gas transfer velocities are increased by a factor of 1.7 to 2 by the small-scale Langmuir circulations using the controlled flux technique. As opposed to micro-breakers, which renew only a fraction of the surface layer, these circulations rapidly renew the whole surface. Observations show, that length and time scales associated with the generation of surface waves and micro-Langmuir circulations are comparable. This suggests a clear coupling of of the Langmuir cells with the surface waves and the subsequent cross-wind 3D-modulation of the wave field. According to the results of the experiments and field-measurements of [Veron and Melville, 2001] even the early stages of wind-wave evolution cannot be completely understood without the inclusion of the small-scale Langmuir circulations and wave-current interactions.

2.5.2 Experiments

Visualisation via bubble-lines and polysterene beads

[Okuda, 1982] used a specially designed hydrogene bubble-line technique to visualise the 2D-velocity vector field $(u(x,z), w(x,z))^T$ in short wind waves. The bubble lines were produced intermittently by the electrolysis of water. Flow measurement was feasible except in the highly turbulent flow a little leeward of the crest to a short distance on the windward side. A vorticity field was calculated via $\omega = \partial v/\partial z - \partial w/\partial x$. It was found, that the surface vorticity layer is
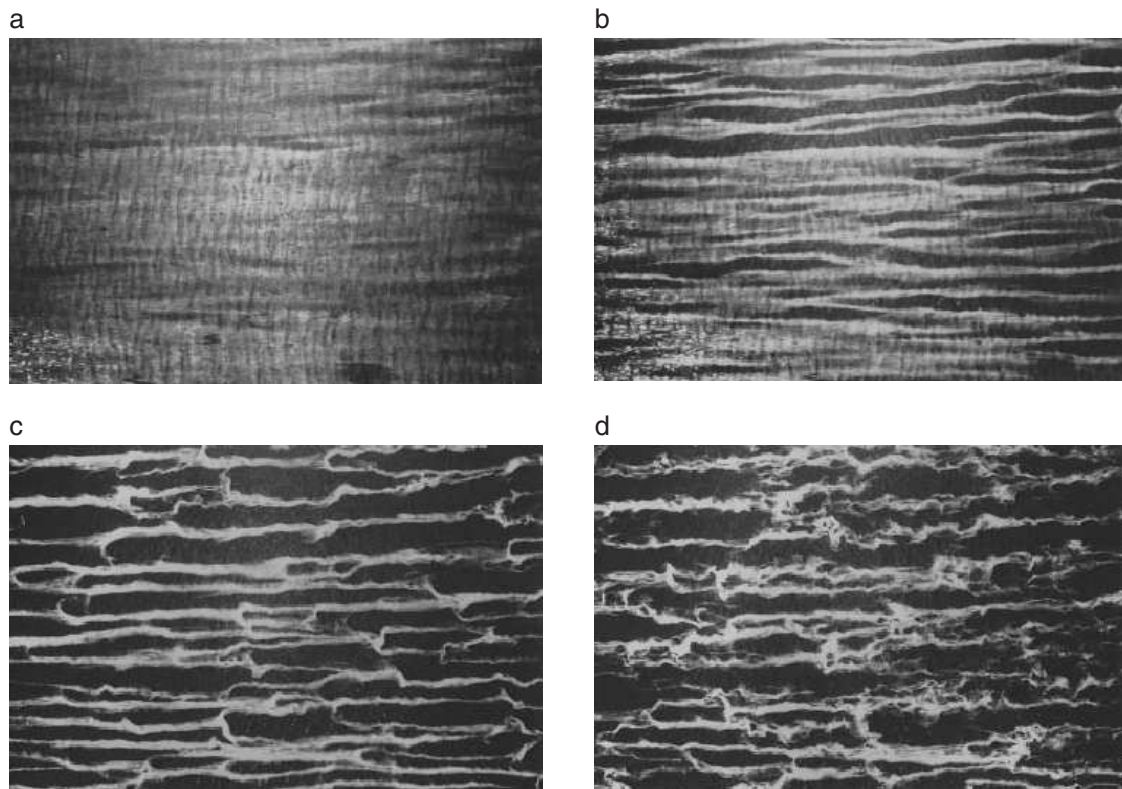
Figure 2.3: *Flow visualisation of the surface by seeding with small slightly buoyant glass hollow spheres. The images are taken at time 21.5 s (**a**), 22.5 s (**b**), 23.5 s (**c**), 24.5 s (**d**) after turning on the wind. The waves travel in the direction of the wind from left to right and appear as crosswind (vertical) structures in the images. At the beginning, the Langmuir circulations appear as streamwise streaks, but soon undergo bifurcations, so that the flow becomes 3D and turbulent (from [Melville et al., 1998]).*

greatly thickened at the crest especially in steep waves. It may happen, that the surface velocity exceeds the phase speed ("excess flow"), which leads to a downward intrusion of water elements characterising microscale wave breaking. From the bubble lines it was possible to deduce the water-side tangential stress, whose magnitude is in a small region at the crest about five times higher than the mean wind stress. These stress peaks were made responsible for the occurrence of the excess flow and the development of turbulence.

Using floating polysterene beads of different sizes, whose centers of gravity are located at different distances from the surface, it was possible to measure the characteristics of the flow just below the water surface near the crest. These investigations confirm the presence of the excess flow even there, where no downward intrusion occurs.

[Csanady, 1990] constructs a model of a "roller", which is based on the experimental results of [Okuda, 1982]. The roller may be envisaged as a two-dimensional flow structure, whose intense internal vorticity originates from the viscous boundary layer on the upwind side of a wavelet, where a shear-stress spike is exerted by the wind. From this model the correct Schmidt-number

dependence

$$k = \beta^{-1} u_* S c^{-1/2}$$

at a free surface can be derived. Unlike in the case discussed in section 2.4.4, here $k_+ = k/u_*$ exhibits no Reynolds number-dependency, which is approved by [Jähne et al., 1987] experimentally.

PIV measurements

Both, PIV- and PTV-techniques were applied to measurements in a wind-induced wavy shear flow [Dieter and Jähne, 1994; Hering et al., 1995b]. Here we will restrict ourselves to the experiments of [Banner and Peirson, 1998; Peirson and Banner, 2003].

[Banner, 1990] concluded from aerodynamic measurements, that the *form drag* (i. e. the momentum flux from the wind to the waves resulting from normal stress coherent with the wave slope) and not the tangential stress is the major contribution to the total wind stress.

[Banner and Peirson, 1998] criticise the measurements of [Okuda, 1982] in several ways: Their method is intrusive due the presence of the hydrogene wire and the characteristics of the bubbles (size, rise velocity, impact on the water surface).

The surface tangential stress is measured by [Banner and Peirson, 1998] using a 2D-PIV technique, recording particles located in a laser-light-sheet aligned in flow direction. In order to obtain the shear stress, the difference of the in-stream-velocities of two particles has to be divided by the vertical particle separation: $\tau_{\text{tang}} = \mu \Delta u / \Delta y$. The measured tangential stress levels on the water side are significantly lower, than those obtained by [Okuda, 1982] and are in correspondence to the total wind stress measurements and form drag measurements: $\tau_{\text{tang}}/\tau_{\text{total}} = O(0.3)$.

[Peirson and Banner, 2003] found using a similar 2D-PIV setup, that the spilling region downward of the crest generally remains locally compact, with a strong convergence of surface fluid at the toe and relatively weak divergence near the crest and the upwind face of the wave. This observation is in contrast to the suggestions of [Okuda, 1982] that the viscous sublayer on the windward face of microscale breaking waves flows over the crest and feeds into the spilling region (see also Fig. 2.4).

Combined PIV and thermographic measurements

Using infrared thermography one can detect turbulent wakes of microscale-breaking waves. [Zappa et al., 2004] applied the active controlled flux technique (developed by [Jähne et al., 1989] and [Haussecker et al., 1995]) to measure the local transfer velocities in and outside of these wakes and found that on average the transfer velocity was enhanced by a factor of 3.5 inside of the wakes. They also estimated that up to 75% of the transfer across the air-water interface was contributed by microscale wave breaking. They concluded, that in their laboratory experiments microscale wave breaking was the dominant process controlling the gas transfer rate at low to moderate wind speeds. They also noted that at low windspeeds apart from the microscale breaking waves a secondary mechanism may be of importance in determining air-water transfer velocities. A promising candidate is the occurence of small-scale Langmuir-circulations (see section 2.5.1).

[Siddiqui et al., 2001] used PIV to observe the velocity field beneath the microscale breaking waves, which were detected by infrared thermography. Because the measurements were relatively

a

Wind →

Envisaged site of separated airflow reattachment and consequent shear stress spike driving wind drift current over crest

Wind-induced tangential stress generating strong surface vorticity diffusing to interior

Parasitic capillaries

Trough sheltered from wind

Trough sheltered from wind

12 ∞m resolution image window

35 ∞m resolution image window

Spilling region occupies entire crest

Vorticity generated by spilling or parasitic capillaries dispersing to the interior

~175 mm

b

Wind →

Airflow reattachment point position (varies), with no large shear stress spike

Wind-induced tangential stress generates surface vorticity ~200 s‡ and surface divergence <10 s‡

Parasitic capillaries

Trough sheltered from wind

Surface wind-induced drift velocity ~$0.3u_*^a \pm 0.1u_*^a$ opposes rearward transport relative to the moving wave

Intense vorticity (>1000 s‡) and surface convergence (100 s‡)

Figure 2.4: *Kinematic behaviour of microscale breaking waves.* **a** *As proposed by [Okuda, 1982]: In a frame of reference moving with the wave, transport is rearward except within the wave crest, where the surface velocity excesses the phase speed. Strong surface tangential stresses from the point of airflow reattachment induce transport up to the windward face and over the crest and are responsible for the generation of vorticity to a large fraction. Furthermore the PIV window sizes used for the investigation of [Peirson and Banner, 2003] are indicated.* **b** *As proposed by [Banner and Peirson, 1998; Peirson and Banner, 2003]: The contribution of the tangential stresses is comparably small. The spilling region is compact with a strong convergence of surface fluid at the toe and weak divergence near the crest (figure from [Peirson and Banner, 2003]).*

large-scale (measurement area about 8×6 cm^2 at a spatial resolution of about 2×2 mm^2), it was not possible to resolve the viscous boundary layer, but to quantify the subsurface vorticity and thus the turbulence produced by the microbreakers. They found that the air-water heat transfer velocity was correlated with the magnitude of the near-surface vorticity, which was responsible for enhancing the air-water heat transfer rates. [Siddiqui et al., 2004] quantified the coherent structures generated beneath laboratory wind waves.

3 Fluid Flow Analysis

As this thesis is concerned with developing a novel fluid flow measurement technique, here an overview is presented over the various approaches which have been introduced and partly are still in progress of being developed.

In this chapter we will go through the subject in a coarse-to-fine-manner outlined in Fig. 3.1: We will start with an overview over the relevant quantities and technologies, then we will be concerned about the measurement of velocity in particular. During the last 20 years image based techniques have become common in velocity field measurement. Optical-flow based velocity analysis has become recently of interest for the experimental fluid mechanics community, although it was introduced in the context of computer vision much earlier. Chapter 4 is devoted to optical flow methods in fluid flow analysis.
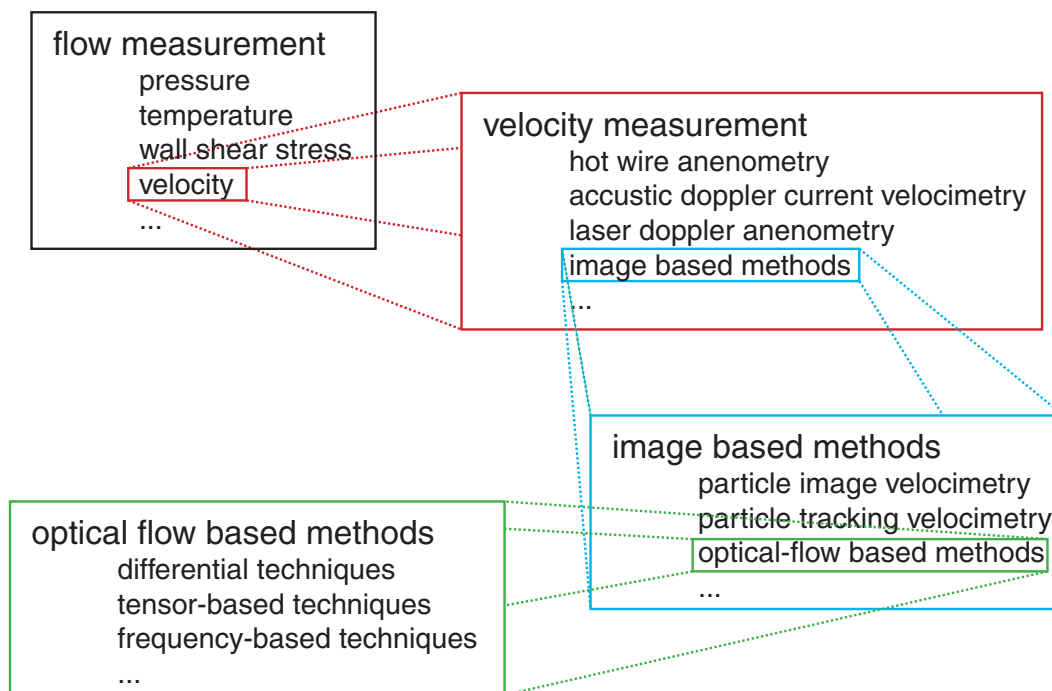
Figure 3.1: *Overview over the task of fluid flow analysis like it is presented in this chapter. Gradually we will dive deeper into the subject.*

3.1 Measurement Technology for Quantities Related to Flows

There are various possibilities to categorise flow measurement techniques. We can classify them regarding the way, how they work (e. g. mechanical, electronic, optical, etc. – like this was done in [Eckelmann, 1997]), or we can sort them according to the measured quantities (e. g. pressure, wall friction, temperature, velocity, etc. – like in [Nitsche, 1994; Tropea et al., in preparation]). In this section we will use the first categorisation; in the following we will give an overview over important quantities related to flows and how to measure them.

Pressure From the pressure distribution around a body, we can compute both, its drag and its lift, which play an important role in aerodynamics. Moreover, we can get information about the flow field itself, like mean flow velocities or local wall shear stresses.

According to Bernoulli's equation the total pressure splits into static pressure, dynamic pressure and hydrostatic pressure:

$$p_{\text{tot}} = p_{\text{static}} + \frac{\rho}{2} u^2 + \rho g h = \text{const.} \tag{3.1}$$

Directly only the static pressure at the wall is measurable, for example by placing small boreholes into the wall and connecting them to a pressure transmitter via a hose connection. Examples for pressure transmitters are manometers or electromechanic sensors, like strain gauges or piezo elements. Because of their compact size, the latter are appropriate for the measurement of fluctuations of the static pressure (see [Detert et al., 2004]). In order to measure spatial distributions of surface pressure non-intrusively, pressure (oxygen) sensitive paints have become available [McLachlan and Bell, 1995].

In order to measure the total pressure, it is common to use pitot tubes (1D-case). The concept of a pitot-tube can be generalised to three dimensions by using sensors with many bores at once.

The dynamic pressure can be measured by exploiting Eq. (3.1) and subtracting the static pressure from the total pressure. For this task there exist apparati, like Prandtl's pitot tube.

Temperature and heat flux Because most of the flow-properties are temperature-dependent, often simultaneous measurement of temperature and other quantities is necessary.

Liquid crystals allow a simultaneous measurement of both the temperature and velocity fields [Hiller et al., 1993]. The visualization of temperature using thermochromic liquid crystals is based on their temperature-dependent refractivity at the wavelengths of visible light.

Thermography can be used to measure spatially distributed and time resolved temperature fields and heat fluxes [Garbe et al., 2003].

Especially for the investigation of temperature fields in combustion processes laser methods are appropriate. If the pressure remains constant during a temperature change the absorber density will be modified by the temperature, which can be detected by a spectrometer [Wolfrum et al., 2000].

Wall shear stress Because the wall friction is responsible for the viscosity-dependent flow resistance, it might be important to measure this quantity globally. On the other hand, a local analysis of the wall shear stress gives insight into the boundary layer flow. An overview over some of the methods is given by [Fernholz et al., 1996].

Primarily in the high speed- (and thus high shear stress-) section, mechanical techniques like balances are used.
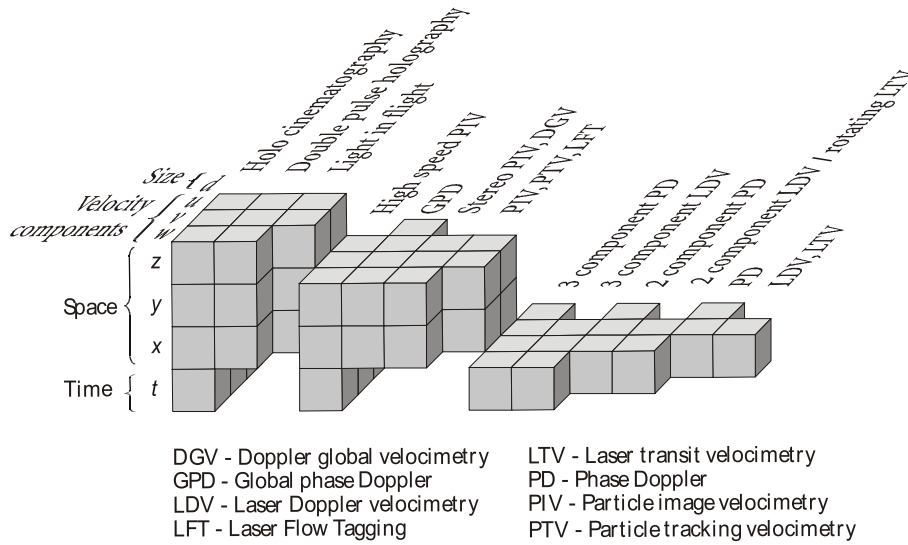
Figure 3.2: *Classification of velocity measurement methods according to the number of measured components and dimensionality of the underlying spatial domain[1]*

Thermoelectric methods to measure the wall friction are techniques using hot films, momentum wires and hot wires at the surface. These methods have in common, that the local wall shear stress is measured by forced convection in a thermoelectric heated wall sensor (hot film) or using the measured near-wall velocity (momentum wires and hot wires). Because none of these techniques measures the wall shear stress directly, calibration is an especially important issue.

Pressure sensors also can be used to measure the wall shear stress. For example a pitot tube can slighty be modified to measure wall friction. Another technique is using a surface fence, where the pressure difference up- and downstream of an edge is measured. All of these sensor-based methods are more or less invasive.

Because Laser Doppler anemometry (see section 3.2.2) is capable to measure velocities very precisely and high resolved, it can be used to measure the velocity profile near a wall and thus the wall shear stress. Like the previous methods, LDA is only a point measurement method. Examples of spatial measurements methods are oil film interferometry [Monson et al., 1993] and infrared thermography [Mayer et al., 1998].

Velocity Again pressure sensors can be used to measure velocity using Bernoulli's equation Eq. (3.1). Predominantly point measurement methods are thermoelectric techniques (hot-wire-anemometry, momentum-wire-anemometry), acoustic techniques (acoustic Doppler velocimetry) and optical techniques (laser Doppler anemometry). Spatial methods are the image-based techniques. In the next section we will have a closer look to some of these methods.

---

[1]Figure from http://www.sla.tu-darmstadt.de/lehre/smt.ger.htm/lecture-das_experiment_b.pdf (Tropea et al.).

3.2 Measurement of Velocity

The velocity field is one of the most basic quantities in continuum mechanics. Other kinematical quantities (like vorticity or strain rate) can be derived by the velocity field and its spatial and temporal derivatives. The Navier-Stokes-Equation or the continuity equation, are formulated in terms of velocity as unknown parameter.

This section is concerned about measuring the velocity, which can be interpreted as a spatio-temporal vector field, i.e. at every point in the fluid (which is embedded in three-dimensional space, and may be instationary (3+1D)) there exists a three-component (3C) velocity-vector:

$$x, y, z; t \rightarrow (u(x,y,z;t), v(x,y,z;t), w(x,y,z;t))^T \quad \text{i.e.} \quad \mathbb{R}^3 \times \mathbb{R} \rightarrow \mathbb{R}^3.$$

Some methods are restricted to time-resolved velocity measurements at points (0+1D), in a line (1+1D) or on a plane (2+1D), or they yield only one or two components of the flow vector (1C/2C). If we deal with *stationary* flows, i.e. the velocity field does not depend on time, we can extend any lower-dimensional method to a 3D method by traversing the sensor in space.

In this section we will have a closer look to some common non-image-based velocity measurement methods, like hot wire anemometry, representing thermoelectric techniques, acoustic Doppler current velocimetry and laser Doppler anemometry, standing for the laser-based optical methods.

3.2.1 Thermoelectric Techniques - Hot-Wire Anemometry

Hot-wire anemometry permits the temporally high-resolved measurement of both mean velocities and fluctuations, so that for the first time it was possible, to capture the turbulent behaviour of flows quantitatively.

Its principle is as follows: A thin metal wire is heated on a constant temperature, which lies significantly above the temperature of the surrounding flow. The required voltage U is used as a measure for the flow's velocity u:

$$U^2 = A + Bu^n, \tag{3.2}$$

where A and B are calibration constants and the velocity exponent n can be set approximately to 0.5. Equation (3.2) serves as a simple calibration rule for hot-wires. Calibration is commonly performed with a pitot-tube as reference.

The time constant of the temperature adaption of a hot-wire depends on its thickness. Typically these wires are very thin (some microns), so that fast sampling is achievable (up to 50 kHz). The precision of hot-wire anemometers is 1% under well-posed conditions. Arrangements of two or more wires in a sensor allow for measuring two or three components of the velocity and other quantities like velocity gradients [Honkan and Andreopoulos, 1997].

Apart from the fact, that hot-wire anemometry is a 0D and intrusive measurement method, its accuracy depends very strongly on correct calibration. Furthermore, this method is suitable to only a limited extend for measurements in water, because the fine sensor is prone to deposits, which may disturb the measurements. For further information see [Lomas, 1986] or [Perry, 1982].
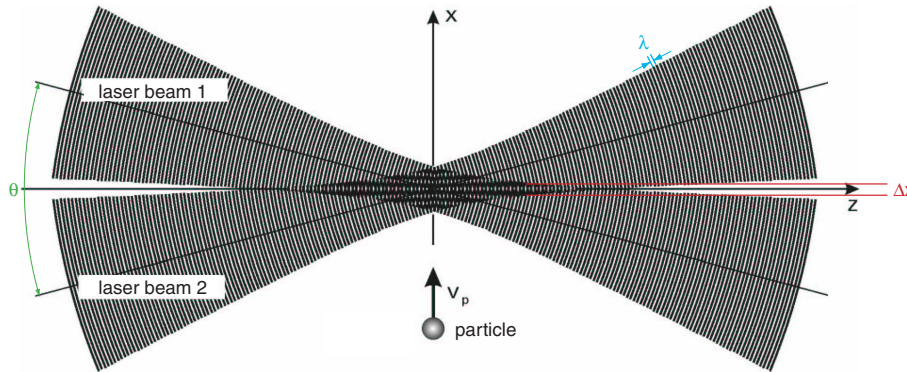
Figure 3.3: *Principle of a dual-beam laser Doppler system. A particle (speed v_p) passes through a region of crossing wave fronts (wave length λ, crossing angle θ), which form a stationary wave (distance of the wave fronts: Δx). Light of frequency f is emitted (from [Albrecht et al., 2003]).*

3.2.2 Optical Methods - Laser Doppler Anemometry

Laser-Doppler anemometry (or Laser-Doppler velocimetry) is based on measurement of the scattered light at particles, advected with the fluid. A moving particle causes a frequency shift of the scattered laser beam, according to the Doppler-effect for light. For further reading we refer to [Durst et al., 1976; Tropea, 1995].

Figure 3.3, left shows the principle of a simple dual-beam laser Doppler system. The light beam, emitted from the laser is divided into two rays and focused in the measurement area. The light, which is being scattered by a traversing particle, is projected onto a photo-detector, which is connected to a signal processing unit.

We can visualise the development of the Doppler signal by a small particle passing through a region of crossing wave fronts, which form a stationary wave. The particle scatters the light, which has a frequency f proportional to the velocity v_p of the particle and antiproportional to the distance Δx of the wave fronts:

$$f = \frac{v_p}{\Delta x} \quad \Rightarrow \quad v_p = f\Delta x = \frac{f\lambda}{2\sin\theta/2}.$$

By using more than one LDA component, i. e. one or two further beam pairs, which are arranged orthogonally to the first beam pair, it is possible to measure 2C or 3C velocity vectors. For the sizing of particles, we have to bear in mind, that the smaller a particle is, the better it follows the fluid, but the worse light is scattered. Beyond a particle size of about $10 \times \lambda$ resp. $1 \times \lambda$, we are in the Mie- resp. Rayleigh-range, where we have a different scattering behaviour than in the range of geometrical optics.

3.2.3 Acoustic Methods - ADV and ADCP

Acoustic Doppler velocimetry (ADV) makes use of the acoustic Doppler effect to measure a three-component velocity vector at a single point in liquids (0D3C). The device sends out a beam of acoustic waves at a fixed frequency from the transmitter probe. These waves bounce off of

moving particles in the liquid and three receiving probes detect the change in frequency of the returned waves. Using this information, the velocity vector of the liquid can be reconstructed [Woodward and Appell, 1986].

An acoustic Doppler current profiler (ADCP) measures how fast liquid is moving across an entire liquid column (1D3C). In addition to the ADV it measures the time it takes for the acoustic waves to bounce back, so that it is able to locate the position of the particle along a line [Voulgaris and Trowbridge, 1998].

3.3 Image Based Methods

Image based methods allow the calculation of 2D2C, 2D3C, 3D2C or 3D3C and/or time-resolved velocity vector fields. They all have in common, that they try to find the *optical flow*, which is the displacement vector field in the image plane, by determining the displacements of image features in a number of successive frames.

All image based methods have in common, that some kind of *tracer* is added to the fluid, which should have two principal qualities: Firstly the tracer's motion should be representative for the motion of the fluid. Secondly the optical properties of the tracer have to be in such a way, that their motion can be detected by the camera and processed by the algorithmics. There are two kinds of tracer, which are commonly used: Small particles suspended in the fluid and continuous tracer, like heat or concentration.

The methods presented in this and in the next section differ in the kind of features, which are used to estimate the optical flow:

Discrete features Here single particles are segmented and tracked. Thus the corresponding technique is called *particle tracking velocimetry* (see section 3.3.2).

Patterns of discrete features Using patterns of particles one can reduce the ambiguity, which one has by tracking single particles. The algorithms generally are based on cross-correlation. This method is known as *particle image velocimetry* (see section 3.3.1).

Continuous features Continuous features, like grey values or intensity gradients, can be used to extract the optical flow. Generally this is done by applying a model like constancy of gray value, as in the *optical-flow based methods* (see chapter 4).

We note, that there are further methods like least squares matching, which has its origin in the field of photogrammetry ([Gruen, 1985]), or that there emerged hybrid methods by combining established techniques.

3.3.1 Particle Image Velocimetry

Particle imaging velocimetry (PIV) has become a standard tool in experimental fluid dynamics since the early nineties ([Adrian, 1991]). The books by [Raffel et al., 1998; Westerweel, 1993] are detailed descriptions of this technique and provide further references to the literature of PIV.

In conventional 2D2C-PIV two subsequent images of the flow, which is provided with small particles, are recorded using a laser-light section and a high-speed CCD-camera (see Fig. 3.4, left). The recordings are fractioned in small subareas, called "interrogation areas", typically of size 16×16 or 32×32 pixels^2. The local displacement vector $(\Delta x, \Delta y)^T$ from one image to the
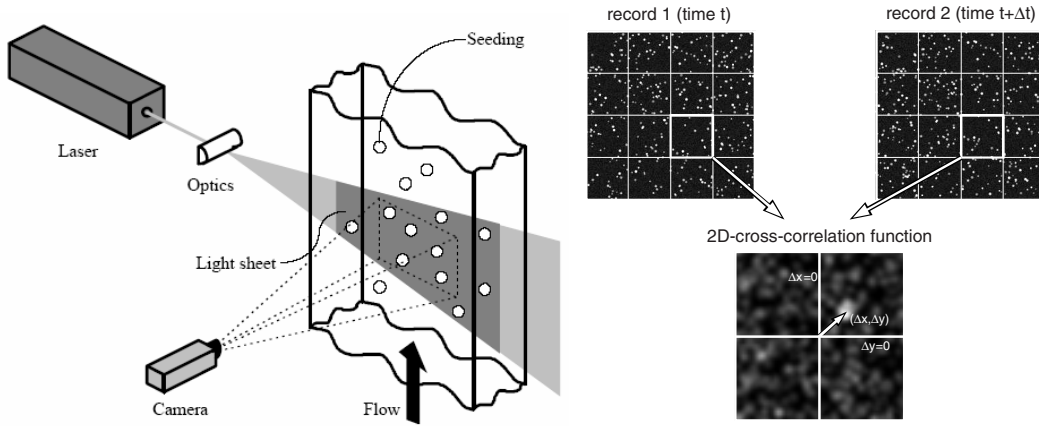
Figure 3.4: *Left: Typical setup of a 2D2C-PIV-system[2]. Right: The images are partitioned into regular interrogation areas. Via cross correlation a displacement vector $(\Delta x, \Delta y)^T$ is estimated.*

next is determined by means of computing the 2D-cross-correlation function

$$R(x,y) = \sum_{i=-K}^{K} \sum_{j=-L}^{L} g_1(i,j) g_2(i+x, j+y), \qquad (3.3)$$

for all possible $(x,y)^T$, and afterwards finding its maximum, where $(x_{R \to \max}, y_{R \to \max})^T \equiv (\Delta x, \Delta y)^T$. Here the interrogation windows are of size $(2K+1) \times (2L+1)$ pixels^2. Because Eq. (3.3) is a *convolution* of the interrogation windows g_1 and g_2, we can use Fourier's theorem to reduce the expression to a pointwise *multiplication* of its Fourier-transforms $\hat{g}_1$ and $\hat{g}_2$:

$$R(x,y) = g_1 * g_2 \quad \circ\!\!-\!\!\bullet \quad \hat{R}(x,y) = \hat{g}_1 \cdot \hat{g}_2.$$

Unfortunately Eq. (3.3) will yield different maximum correlation values for the same degree of matching, because the function is not normalised: Samples with brighter particle images will produce higher correlation peaks than windows with weaker particle images. Thus a normalization procedure is applied as follows:

$$r(x,y) = \frac{\sum_{i=0}^{M} \sum_{j=0}^{N} [g_1(i,j) - \mu_1][g_2(i+x, j+y) - \mu_2(x,y)]}{\sqrt{\sum_{i=0}^{M} \sum_{j=0}^{N} [g_1(i,j) - \mu_1]^2 \sum_{i=0}^{M} \sum_{j=0}^{N} [g_2(i,j) - \mu_2(x,y)]^2}}. \qquad (3.4)$$

Here μ_1 is the average of the template and is computed only once, while $\mu_2(x,y)$ is the average of g_2 coincident to the template g_1 at position (x,y) and has to be computed at every position (x,y). Equation (3.4) cannot be solved in frequency domain easily, so that nowadays normalised cross-correlation is done in spatial domain rather than ordinary cross-correlation is performed in frequency-domain, though it is computational more expensive ([Raffel et al., 1998]).

Problems of PIV

The simple cross correlation scheme, naively implemented, leads to some difficulties, which one tries to overcome:

Spurious vectors Due to the statistical nature of PIV, there may be "false" maxima in the cross correlation function. Using a confidence measure, like the ratio of the tallest to the second tallest correlation peak, one can detect these outliers and remove them.

Velocity gradients Using cross-correlation for motion analysis we assume, that all particles within one interrogation area have moved homogeneously from one frame to the other. If velocity gradients are present in the flow, this is obviously not the case. To overcome this problem iterative *window-deformation* methods have been developed. In each iteration the image area within the interrogation window is deformed according to the displacement field calculated in the previous iteration [Huang et al., 1993a,b].

Out-of-plane loss-of-pairs Applying a 2D-laser laser light section to a 3D flow, particles may enter or leave the light sheet. This is a principle problem of 2D-PIV and can only be overcome by thickening the light sheet or using a 3D-technique.

In-plane loss-of-pairs Due to the fractioning in interrogation windows, there arise imaged particles, which are missing in one of the recordings. By applying a *window shifting* technique, we are able to reduce the resulting bias [Westerweel et al., 1997].

Peak locking When the imaged particles become too small, the displacements tend to be biased toward integer values. Window shifting helps to reduce the effect of "peak locking" [Gui and Wereley, 2002].

We have summarised some "design rules" in table 3.1.

PIV beyond 2D2C

There have been proposed many approaches to overcome the 2D2C restriction of the upper scheme. In the following we will discuss the most important of them:

Time resolved PIV In TR-PIV the analysis does not restrict itself on evaluating an image pair, but by continuously recording images at a high frame rate, evaluation of instationary processes becomes possible. Moreover, by using temporal information a higher accuracy can be achieved [Hain and Kähler, 2004].

Stereoscopic PIV Here two cameras record the same area in a single laser light section, so that for each interrogation windows two 2C vectors can be calculated. Using this information, we can calculate all three components of the velocity vector, if we have acquired knowledge about the system geometry by calibration.

Multiplane stereoscopic PIV Additionally to the 3C vectors, by subsequently scanning the target volume in different depths, a voluminous recording can be achieved [Kähler and Kompenhans, 2000].

Photogrammetric PIV A voluminously illuminated region is recorded by at least three cameras from different directions. This allows for reconstructing the particles' 3D positions. Velocity estimation is performed by cross-correlation of "interrogation volumes" [Schimpf et al., 2003].

Holographic PIV Coherent light stemming from a laser illuminates a 3D target volume. The holograms are recorded on photographic film, which can be read out with coherent light beams [Hinsch, 2002]. Due to its high demands of hardware, the application of holographic

Table 3.1: Design rules for 2D2C-PIV[2].

Particle diameter	2 to 3 pixel
Particle density	greater than 6 per interrogation window
Maximum displacement in-plane	1/4 of the width of an interrogation window
Maximum displacement out-of-plane	1/4 of thickness of the laser light sheet

PIV is limited to relatively simple flow configurations, so far.

PIV with color-coded light-sheets By using two or more color-coded light-sheets [Brücker, 1996; Ruck, 2003], we can illuminate the whole 3D field at once instead of subsequently scanning the volume. This has the advantage, that a higher frame rate can be achieved. Disadvantages are artifacts, which occur at overlappings of particles and wave-length dependent scatter behaviour of particles (Mie-effects). The latter can be avoided by using a non-coherent light-source.

3.3.2 Particle Tracking Velocimetry

In contrast to PIV, particle tracking velocimetry (PTV) does not establish correlations between patterns, but tries to find correspondences between segmented particles. Classical PTV consists of following three tasks:

Segmentation of the particles Generally the particles have to be separated from the background and from each other. The segmentation procedure is addressed in section 7.2 in more detail.

Feature extraction Relevant features are the particle position, which can be estimated by calculating the weighted mean of the coordinates of a segmented particle ("center of mass"), the particle's maximum or mean gray value, the particle's velocity, which can be calculated using the method of optical flow for instance, or shape descriptors like higher moments.

Temporal correspondence analysis Goal is, to establish a unique correspondence between a particle in the first frame and one and the same particle in the next frame.
This can be done using the features of the particles. The simplest thinkable approach is the "nearest neighbour search". [Hering, 1996; Perkins and Hunt, 1989] use the feature of position only, but by incorporating other characteristics it is possible to limit the search range for the corresponding particle [Klar, 2005].
Many algorithms make use of the history of the particle. Some of them implicitly assume smoothness of motion and make use of statistics like the Kalman filter [Welch and Bishop, 1995] or its generalization, the particle filter [Ristic et al., 2004].
A method based on global optimization is variational PTV, proposed by [Ruhnau et al., 2005a]. Here a data term, which incorporates the local information of the nearest-neighbour-solution, is supplemented by a smoothness term, similar to differential global optical flow techniques in section 4.2.1.

---

[2]Figure and rules from http://www.sla.tu-darmstadt.de/lehre/smt.ger.htm/lecture-piv.pdf (Tropea et al.)

Three dimensional PTV

Most of the 3D-PTV approaches work photogrammetrically, i. e. a flow volume is recorded by two, three or more cameras from different viewpoints. One exception is the method proposed by [Willert and Gharib, 1992], where the third spatial dimension is estimated by applying depth from focus in a voluminously illuminated region.

In three dimensions, the problem of correspondence analysis can be tackled in two ways:

- The stereo-correspondence problem (i. e. to identify one and the same particle in the recordings of the various cameras) can be solved making use of the epipolar geometry. Because of the similarity of the imaged particles, classical stereo won't work, so that at least three cameras are needed. Once the 3D-coordinates of the particles are extracted, temporal correspondence analysis is performed using the techniques from above, generalised to 3D [Maas et al., 1993; Malik et al., 1993].

- Standard 2D-PTV is performed to obtain trajectories for each of the different views. In a second step, these trajectories are matched using epipolar geometry. Here two cameras are sufficient, because generally the trajectories contain enough "structure", so that they can be matched unambiguously [Engelmann, 2000; Klar, 2005].

3.3.3 PIV versus PTV

PIV and PTV are two fundamental different approaches. Several different algorithms, both from the PIV and from the PTV type, have been compared to each other in three international "challenges", so far[3] [Stanislas et al., 2003, 2005]. [McKenna and McGillis, 2002] compared PTV and various PIV techniques regarding efficiency and accuracy.

One of the results was, that PTV is clearly complementary to PIV in several aspects:

- To achieve good precision, PIV needs a certain minimum seeding density (see table 3.1). This fact is in contrast to the requirements of PTV, where the probability for mismatches increases with the seeding density.

- PTV yields Lagrangian trajectories, whereas PIV provides an Eulerian vector field. It depends on the application, which output is better suited. Moreover, PTV can deploy its power, when whole image-sequences are present; most PIV-algorithms are designed for image-pairs.

- Generally PTV yields a higher resolution, because a vector is assigned to each particle. Unfortunately, data lies on an irregularly spaced grid, so that interpolating the vector field to a regular grid this advantage is attenuated to a certain extent.

- PTV has clear advantages at locations, where high velocity-gradients are present (for examples at boundary layers). Simple PIV relies on the assumption of a homogeneous displacement of the particles inside the interrogation-window from one image to the next. Thus it cannot resolve these kinds of flows accurately. Sophisticated PIV-algorithms (e. g. containing iterative window-deformation) alleviate but cannot negate this point of criticism [Stanislas et al., 2005].

Attempts have been made to combine the advantages of PIV with the advantages of PTV

---

[3]The results of the third Int. PIV Challenge in Pasadena, USA, haven't been published, so far (2006). For further information, see http://www.pivchallenge.org

[Bastiaans et al., 2002; Cowen and Monismith, 1997; Keane et al., 1995]. These hybrid methods use PIV as an initialization step for a subsequent PTV analysis. The principle procedure of "superresolution PIV" is similar to our approach in section 7.5.

# 4 Optical-Flow Methods in Fluid Flow Analysis

4.1 Introduction

Optical flow can be considered as the distribution of apparent velocities of movement of brightness patterns in an image [Horn and Schunk, 1981]. More precisely the optical flow is an approximation to the *two-dimensional* motion field of an image sequence. We obtain this motion field by projecting the three-dimensional velocities of object points in three-dimensional space onto the two-dimensional image-plane [Barron et al., 1994].

In estimating the optical flow and in determining motion fields from the estimated optical flow, there arise a number of peculiarities and difficulties, which have to be taken into account:

- There may be regions in the images, where no motion can be determined ("black wall problem") or where only the normal velocity component can be determined ("aperture problem"). Figure 4.1 illustrates these situations. In order to obtain a dense flow field an interpolation- or a regularization-technique has to be applied. This is an intrinsic problem in optical-flow computation, and it is addressed throughout the chapter.

- Brightness changes have to be taken into account. Illumination changes lead to a misinterpretation of the optical flow field. This can be nicely demonstrated by considering a rigid sphere with homogeneous surface reflectance, spinning around an axis through the center of the sphere (Fig. 4.2). If the surface is not textured and the illumination stays constant, the optical flow field would be zero over the entire sphere. If a directional light source moves around the same sphere the illumination changes would be falsely attributed to motion of the sphere surface. In many situations we can apply physical models of brightness variations to deal with brightness changes. We address this problem in section 4.3.4.

- There may be regions in the image, where the motion is non-translational. Especially for applications in fluid dynamics the non-rigid behaviour of fluids has to be taken into account. For these situations appropriate models have been developed, explained in section 4.3.1.

- In the presence of motion discontinuities, reflexes or corrupted pixels, parametrised flow field models fail. Using a robust approach described in section 4.3.3 we can determine a correct motion field even in these situations.

- For large displacements the temporal sampling theorem may be violated. Coarse-to-fine techniques applied on bandpass-filtered image-sequences help to cope with this problem. A simple coarse-to-fine algorithm is presented in section 4.3.2.

Optical flow methods can be classified as belonging to one of these groups:

Differential techniques These methods compute image velocity from spatio-temporal intensity derivatives.
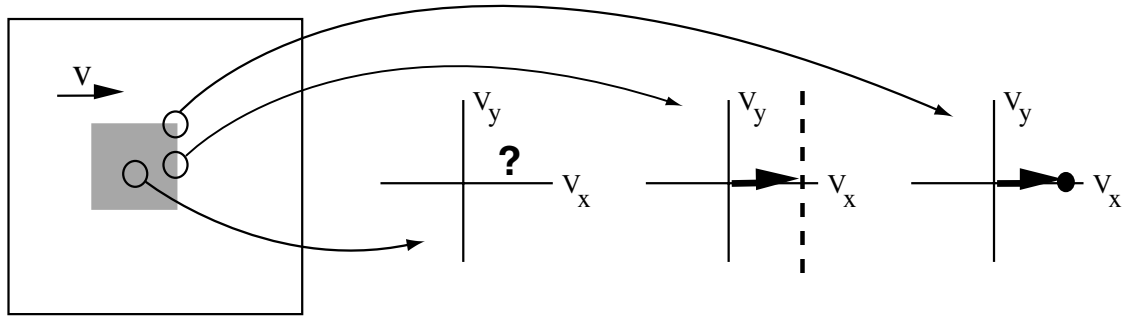
Figure 4.1: *Black wall and aperture problem. At the corners of the moving square, a unique velocity can be estimated. On the edges of the squares only the normal component of the velocity is determinable. In the center the motion is completely unconstrained (from [Simoncelli, 1993]).*

Frequency-based techniques These methods use energy/phase information in the output of velocity tuned filters.

Tensor-based techniques The local image brightness distribution can be represented as a structure-tensor, from which we are able to deduce the motion field.

Though the attempts to estimate optical flow look very different at first glance, all of these approaches are closely related. [Simoncelli, 1993] showed, that differential techniques are equivalent to frequency-based techniques, provided that the derivatives and filters are chosen appropriately. The structure-tensor can be constructed based on operations in the spatio-temporal domain [Jähne, 2002], but it can also be obtained by linear combinations of outputs of filters in frequency-domain [Granlund and H., 1995]. [Jähne et al., 1999] and [Barron et al., 1994] provide a well-founded overview on the field of optical flow estimation, and give a quantitative comparison of the results. Though the method of optical flow is quite common in computer vision, the extent of application in experimental fluid dynamics is relatively small, so far.

In the following we will provide a review of the optical flow methods classified above, and we will show, how to cope with the difficulties listed above. We conclude this chapter with a literature review.
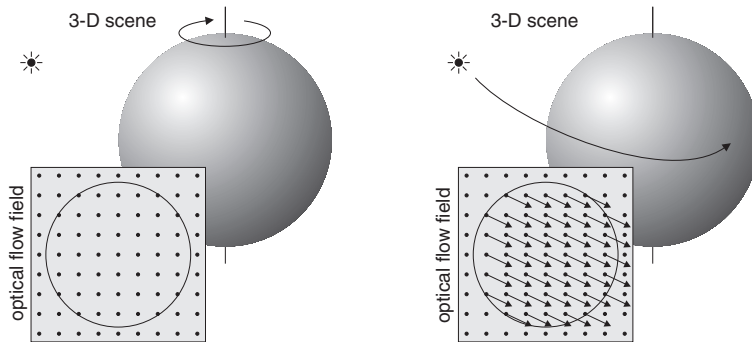
4.2 Optical Flow Methods

4.2.1 Differential Techniques

The general task is to determine the optical flow field $\boldsymbol{f} = (f_1, f_2)^T = (\mathrm{d}x/\mathrm{d}t, \mathrm{d}y/\mathrm{d}t)^T$ from the gray values of an image sequence. In the simplest case it is assumed, that the gray value $g(\boldsymbol{x}, t)$ along a path $\boldsymbol{x}(t)$ remains constant for all times:

$$g(\boldsymbol{x}(t), t) = c. \tag{4.1}$$

By taking the temporal derivative on both sides and applying the chain-rule we get:

$$\frac{\mathrm{d}g}{\mathrm{d}t} = \frac{\partial g}{\partial x}\frac{\mathrm{d}x}{\mathrm{d}t} + \frac{\partial g}{\partial y}\frac{\mathrm{d}y}{\mathrm{d}t} + \frac{\partial g}{\partial t} = 0.$$

Figure 4.2: *Illumination changes and optical flow. Left: Spinning sphere with fixed illumination leads to zero optical flow. Right: Moving illumination source causes apparent optical flow field without motion of the sphere (from [Jähne et al., 1999]).*

Writing down in vector notation using $\nabla g = (\partial g / \partial x, \partial g / \partial y)^T$ this yields the *brightness constancy constraint equation (BCCE)*:

$$(\nabla g)^T \boldsymbol{f} + g_t = 0. \tag{4.2}$$

Because the partial derivatives $g_x = \partial g / \partial x$, $g_y = \partial g / \partial y$ and $g_t = \partial g / \partial t$ are accessible by application of a derivative filter, we obtain one constraint for the two-component flow-field. Dealing with two unknowns in one equation we have an ill-posed problem. Graphically spoken the solution of Eq. (4.2) determines a *line*, containing all vectors, which are possible candidates for the true optical flow vector (Fig. 4.3). Without further assumptions only the flow perpendicular to the constraint line can be estimated. This problem is commonly referred as the *aperture problem* of motion estimation.

Solving Eq. (4.2) for points $\boldsymbol{x}_U$ in a sufficiently large neighbourhood around $\boldsymbol{x}$ we may get other constraint lines, so that we can determine the true optical flow vector by the intersecting point of the constraint lines. But we must not choose the neighbourhood too large, because we can't guarantee, that the motion is constant in a larger area. How large to choose the neighbourhood is referred as the *generalised aperture problem*. One way to weaken the assumption of constant motion is finding a local parametrization of the flow field, so that we demand local coherency instead of local constancy. This leads us to the second constraint of differential optical flow estimation, the *spatial coherence constraint*.

The concept of optical flow originally comes from hydrodynamics. Gray values "flow" over the image plane, like volume elements flow in fluids. In hydrodynamics the principle of conservation of mass is formulated by the continuity-equation, which reads in its differential form (compare Eq. (2.5)):

$$\frac{\partial \rho}{\partial t} + \nabla(\boldsymbol{u}\rho) = \frac{\partial \rho}{\partial t} + \boldsymbol{u}\nabla\rho + \rho\nabla\boldsymbol{u} = 0. \tag{4.3}$$

The three-dimensional velocity $\boldsymbol{u}$ of a fluid element with density ρ in three-dimensional space is apparently analogous to the two-dimensional optical flow $\boldsymbol{f}$ of a gray value g in two-dimensional space. The BCCE Eq. (4.2) corresponds to the continuity-equation Eq. (4.3), if we drop $\rho\nabla\boldsymbol{u}$. Why do we have to drop the last term? Consider an object moving away from the camera. In
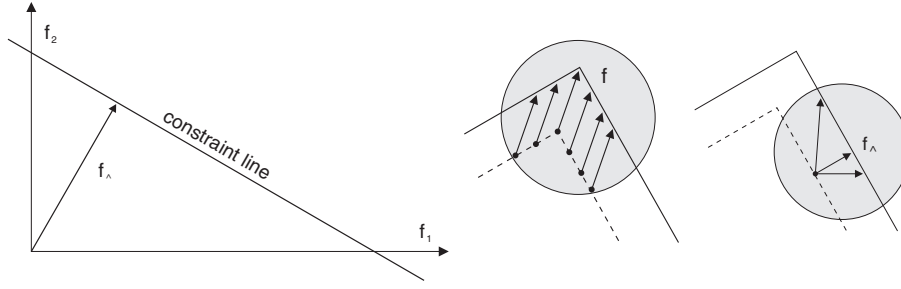
Figure 4.3: *Illustration of the aperture problem: constraint line defined by Eq. (4.2). The normal flow vector $\boldsymbol{f}_\perp$ is pointing perpendicular to the line (from [Jähne et al., 1999]).*

this case the total brightness change $\mathrm{d}g/\mathrm{d}x$ of a gray value on a path $x(t)$ is zero, because the irradiance in the image plane remains the same for an object moving perpendicular to the image plane. Because both g_t and ∇g are zero, we can apply Eq. (4.2). But we cannot apply Eq. (4.3), because the additional term $\rho \nabla \boldsymbol{u}$ resp. $g \nabla \boldsymbol{f}$ is *not* zero, because the motion is not divergence free.

However, under certain conditions the use of a two-dimensional continuity equation instead of the BCCE can be motivated. This is the case, if we have to deal with 2D transmittance images of a 3D fluid flow, so that the 2D (imaged) flow is the density weighted average of the 3D flow [Corpetti et al., 2002; Wildes et al., 2000]. The constraint on the data becomes now

$$g_x f_1 + g_y f_2 + g f_1 + g f_2 + g_t = 0. \tag{4.4}$$

Local weighted least squares

Assuming the optical flow to be constant within a small neighbourhood, [Lucas and Kanade, 1981] proposed a local method to estimate the optical flow. Goal is to minimise the squared left-hand side of the BCCE Eq. (4.2) in a local neighbourhood U around x, which is given by the weighting- (or window-) function $w(\boldsymbol{x} - \boldsymbol{x}')$:

$$\hat{\boldsymbol{f}} = \arg\min_{\boldsymbol{f}} \int_{-\infty}^{\infty} w(\boldsymbol{x} - \boldsymbol{x}') \left[(\nabla g)^T \boldsymbol{f} + g_t \right]^2 \mathrm{d}\boldsymbol{x}'. \tag{4.5}$$

The weighting function is given in the simplest case by a box-filter (all points in the neighbourhood are weighted equally), but better results can be achieved using a binomial filter. Standard least squares minimization (setting the partial derivatives of the functional with respect to f_1 and f_2 to zero) yields the equation system

$$\underbrace{\begin{bmatrix} \langle g_x g_x \rangle & \langle g_x g_y \rangle \\ \langle g_x g_y \rangle & \langle g_y g_y \rangle \end{bmatrix}}_{\boldsymbol{A}} \underbrace{\begin{bmatrix} f_1 \\ f_2 \end{bmatrix}}_{\boldsymbol{f}} = - \underbrace{\begin{bmatrix} \langle g_x g_t \rangle \\ \langle g_y g_t \rangle \end{bmatrix}}_{b} \tag{4.6}$$

with the abbreviation

$$\langle a \rangle = \int_{-\infty}^{\infty} w(\boldsymbol{x} - \boldsymbol{x}') a \, \mathrm{d}\boldsymbol{x}'.$$

The solution of Eq. (4.6) is given by

$$\boldsymbol{f} = \boldsymbol{A}^{-1}\boldsymbol{b},$$

provided the inverse of $\boldsymbol{A}$ exists, i. e. the determinant of $\boldsymbol{A}$ is unequal to zero:

$$\det \boldsymbol{A} = \langle g_x g_x \rangle \langle g_y g_y \rangle - \langle g_x g_y \rangle^2 \neq 0.$$

This is not the case, if all spatial derivatives in the local neighbourhood are zero ("black wall problem"), or if all gradients in the local neighbourhood point into the same direction ("aperture problem").

Global constraints

Instead of assuming local spatial constancy (and therefore coherence) by introducing a window-function we can demand global spatial coherence. One can determine the optical flow by minimizing the BCCE Eq. (4.2) over the entire image Ω. To make the problem well-posed an additional term, the regularizing spatial coherence constraint $\left\| e_S^2 \right\|$, is introduced:

$$\hat{\boldsymbol{f}} = \arg\min_{\boldsymbol{f}} \int_{\Omega} \left[(\nabla g)^T \boldsymbol{f} + g_t \right]^2 \mathrm{d}\boldsymbol{x}' + \lambda^2 \left\| e_S^2 \right\|. \tag{4.7}$$

The parameter λ controls the influence of the spatial coherence term. [Horn and Schunk, 1981] propose global smoothness for the spatial coherence constraint:

$$\left\| e_S^2 \right\| = \int_{\Omega} \left\| \nabla f_1(\boldsymbol{x}') \right\|^2 + \left\| \nabla f_2(\boldsymbol{x}') \right\|^2 \mathrm{d}\boldsymbol{x}' \tag{4.8}$$

There are other suggestions for $\left\| e_S^2 \right\|$, which may be better suited to special kinds of problems (e. g. fluid flow analysis). To solve the minimization problem we use a variational approach. Thus, the integral equation Eq. (4.7) can be solved by a system of Euler-Lagrange-Equations:

$$
\begin{aligned}
L_{f_1} - \frac{\partial}{\partial x} L_{f_{1x}} - \frac{\partial}{\partial y} L_{f_{1y}} &= 0 \\
L_{f_2} - \frac{\partial}{\partial x} L_{f_{2x}} - \frac{\partial}{\partial y} L_{f_{2y}} &= 0
\end{aligned}
$$

The integrand of Eq. (4.7) can be identified with the Lagrange-function:

$$L(f_1, f_2, f_{1x}, f_{1y}, f_{2x}, f_{2y}) = (g_x f_1 + g_y f_2 + g_t)^2 + \lambda^2(f_{1x}^2 + f_{1y}^2 + f_{2x}^2 + f_{2y}^2)$$

L plugged into the Euler-Lagrange-Equations yields

$$
\begin{aligned}
((\nabla g)^T \boldsymbol{f} + g_t)g_x - \lambda^2((f_1)_{xx} + (f_1)_{yy}) &= 0 \\
((\nabla g)^T \boldsymbol{f} + g_t)g_y - \lambda^2((f_2)_{xx} + (f_2)_{yy}) &= 0,
\end{aligned}
$$

which can be combined to one vector-equation:

$$((\nabla g)^T \boldsymbol{f} + g_t)\nabla g - \lambda^2 \nabla^2 \boldsymbol{f} = 0. \tag{4.9}$$

For the case, that we have a high spatial gray value-variation (that means ∇g is large), the first summand dominates in the equation, and the optical flow is calculated using the BCCE. But if we have the case, that we are suffering from a "black wall problem" the optical flow is calculated from the last summand, which states the Laplacian equation $\nabla^2 \boldsymbol{f} = 0$.

The discretisation can be performed using finite differences or finite elements. Once guaranteed, that the problem is well-posed, there exist a number of minimisation schemes like Gauss-Jordan elimination or Gauss-Seidel iteration, which can be applied.

4.2.2 Frequency-Based Techniques

The concept of image sequences as spatio-temporal images allows one to analyse motion in the corresponding spatio-temporal frequency domain (Fourier domain). Let $g(\boldsymbol{x}, t)$ be an image sequence of any pattern moving with constant velocity, causing the optical flow $\boldsymbol{f}$ at any point in the image plane, the resulting spatio-temporal structure can be described by

$$g(\boldsymbol{x}, t) = g(\boldsymbol{x} - \boldsymbol{f}t). \tag{4.10}$$

The spatio-temporal Fourier transform $\hat{g}(\boldsymbol{k}, \omega)$ of equation Eq. (4.10) is given by

$$\hat{g}(\boldsymbol{k}, \omega) = \hat{g}(\boldsymbol{k})\delta(\boldsymbol{k}^T - \omega), \tag{4.11}$$

where $\hat{g}(\boldsymbol{k})$ is the spatial Fourier transform of the pattern, and $\delta(\cdot)$ denotes Dirac's delta distribution. This equation states, that the three-dimensional Fourier spectrum of a pattern moving with constant velocity condenses to a plane in Fourier space. The plane-equation in Fourier domain is given by the argument of the delta-distribution in Eq. (4.11) and can be considered as an alternative formulation of the BCCE Eq. (4.2):

$$\omega(\boldsymbol{k}, \boldsymbol{f}) = \boldsymbol{k}^T \boldsymbol{f}. \tag{4.12}$$

Taking the derivatives of $\omega(\boldsymbol{k}, \boldsymbol{f})$ with respect to k_x and k_y yields both components of the optical flow:

$$\boldsymbol{f} = \nabla_k \omega(\boldsymbol{k}, \boldsymbol{f}).$$

Quadrature-filter-techniques try to estimate the orientation of this plane by using velocity tuned filters in the Fourier-domain. A quadrature-filter-pair is a real frequency selective filter together with its imaginary Hilbert-transform. Its transfer function can be written down in complex notation $\hat{q}(\boldsymbol{k})$.

The most common quadrature-filter-pair is the Gabor filter, which selects a certain spatio-temporal frequency region with a Gaussian window centered at $(\boldsymbol{k}_0, \omega_0)$. Its complex transfer function is

$$\hat{G}(\boldsymbol{k}, \omega) = \exp\left(-\sqrt{(\boldsymbol{k} - \boldsymbol{k}_0)^2 + (\omega - \omega_0)^2}\sigma^2/2\right). \tag{4.13}$$

From this the spatio-temporal filter mask can be computed using the shift-theorem:

$$G(\boldsymbol{x}, t) = \frac{1}{(2\pi)^{3/2}\sigma^3} \exp[i(\boldsymbol{k}_0\boldsymbol{x} + \omega_0 t)] \exp\left[-\left(\frac{x^2 + y^2 + t^2}{2\sigma^2}\right)\right]. \tag{4.14}$$

By applying this filter for different parameter sets $(\boldsymbol{k}, \omega)$ on the original spatio-temporal image we get estimates of the spectral density (or energy) of the corresponding periodic image structure
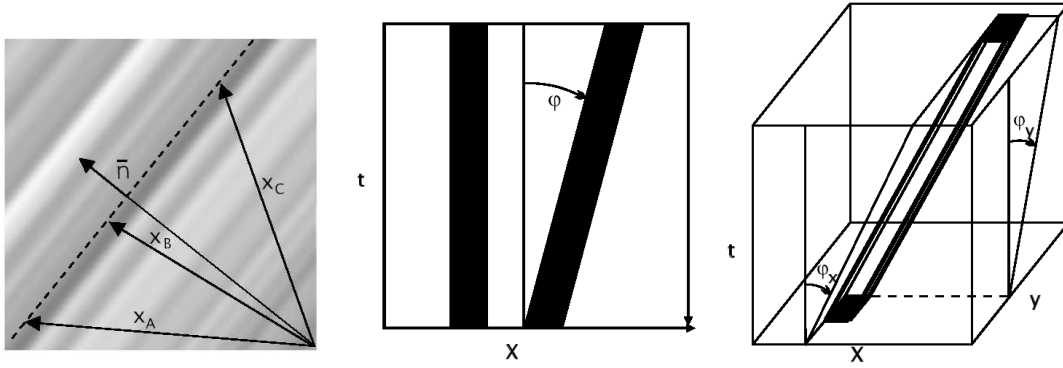
Figure 4.4: *Left: A simple neighbourhood in 2D. The grey values depend on one coordinate in direction of the unit vector $\hat{n}$ only. Space-time diagram with one spatial component (center), with two spatial components respectively (right) (from [Jähne, 2002]).*

belonging to these parameter sets. Ideally, for a single translational motion, the responses of these filters are concentrated about a plane in $(\boldsymbol{k}, \omega)$-space, so that we are able to get the optical flow by a least squares fit to the data. Another way to calculate the optical flow is by constructing a structure tensor composed of the filter outputs ([Larsen, 1998]).

4.2.3 Tensor-Based Techniques

Optical flow estimation can be formulated as orientation analysis in a three-dimensional spatio-temporal image. The concept of orientation analysis of a pattern in 2D (Fig. 4.4, left and center) can be generalised to three dimensions (Fig. 4.4, right). Any moving grey value structure causes inclined patterns. Goal of tensor-based optical flow estimation is to find the orientation of these patterns, provided that there exist any oriented patterns.

Let $\boldsymbol{r} = (r_1, r_2, r_3)^T$ be the vector pointing into the direction of constant brightness within the three-dimensional $\boldsymbol{x}t$-domain. Once estimated $\boldsymbol{r}$ we get for the optical flow:

$$\boldsymbol{f} = (f_1, f_2)^T = \frac{1}{r_3}(r_1, r_2)^T \tag{4.15}$$

$\boldsymbol{r}$ is pointing orthogonal to the spatio-temporal gradient vector $\nabla_{\boldsymbol{x}t} g = (g_x, g_y, g_t)^T$. Therefore the scalar product between $\boldsymbol{r}$ and $\nabla_{\boldsymbol{x}t}$ has to vanish:

$$(g_x, g_y, g_t) \cdot (r_1, r_2, r_3)^T = g_x r_3 f_1 + g_y r_3 f_2 + g_t r_3 = r_3 \left[(\nabla g)^T \boldsymbol{f} + g_t \right] = 0$$

We arrive at the well-known BCCE Eq. (4.2). Instead of the approach of [Lucas and Kanade, 1981], where we minimised the BCCE in a spatial neighbourhood here we minimise $\nabla_{\boldsymbol{x}t} g \cdot \boldsymbol{r}$ in a *spatio-temporal* neighbourhood U, which is characterised by the window-function $w(\boldsymbol{x} - \boldsymbol{x}', t - t')$.

$$\hat{\boldsymbol{r}} = \arg \min_{\boldsymbol{r}} \int_{-\infty}^{\infty} w(\boldsymbol{x} - \boldsymbol{x}', t - t') \left[\nabla_{\boldsymbol{x}t} g(\boldsymbol{x}', t') \cdot \boldsymbol{r} \right]^2 \mathrm{d}\boldsymbol{x}' \mathrm{d}t'. \tag{4.16}$$

Under the assumption of constant $\boldsymbol{r}$ (that is, constant $\boldsymbol{f}$) within U, we can reformulate the minimisation problem to

$$\hat{\boldsymbol{r}} = \arg\min_{\boldsymbol{r}} \left\langle [\nabla_{\boldsymbol{x}t} g \cdot \boldsymbol{r}]^2 \right\rangle = \arg\min_{\boldsymbol{r}} \left[\boldsymbol{r}^T \left\langle \nabla_{\boldsymbol{x}t} g \cdot \nabla_{\boldsymbol{x}t} g^T \right\rangle \boldsymbol{r} \right] = \arg\min_{\boldsymbol{r}} \boldsymbol{r}^T \boldsymbol{J} \boldsymbol{r}, \quad (4.17)$$

using the abbreviation

$$\langle a \rangle = \int_{-\infty}^{\infty} w(\boldsymbol{x} - \boldsymbol{x}', t - t') \, a \, \mathrm{d}\boldsymbol{x}' \mathrm{d}t'. \quad (4.18)$$

$\boldsymbol{J}$ with its components $J_{pq} = \langle g_p g_q \rangle$ is the three-dimensional symmetric *structure tensor* where $g_p, p \in \{x, y, t\}$, denotes the partial derivative along the coordinate p.

The structure tensor can be transformed into diagonal shape by means of rotation. Thus the principal axes of the structure tensor can be found by solving the Eigenvalue problem

$$\boldsymbol{J} \boldsymbol{r} = \lambda \boldsymbol{r}. \quad (4.19)$$

The Eigenvector to the corresponding *minimal* Eigenvalue denotes the direction of constant brightness in the $\boldsymbol{x}t$-domain, from which the optical flow can be calculated according to Eq. (4.15). From the rank of the structure tensor we can deduce the type of motion: Constant brightness resp. "black wall problem" (rank($\boldsymbol{J}$) = 0), spatial orientation and constant motion resp. "aperture problem" (rank($\boldsymbol{J}$) = 1), distributed spatial structures and constant motion (rank($\boldsymbol{J}$) = 2), distributed spatial structures but no coherent motion (rank($\boldsymbol{J}$) = 3). The structure tensor technique is not only able to give an estimate for the optical flow, but is also able to present a confidence measure which states something about the quality of the estimate. For the discussion in table 4.1, we order the Eigenvalues according to $\lambda_1 \geq \lambda_2 \geq \lambda_3 \geq 0$. The corresponding Eigenvectors have the form of $\boldsymbol{r}_i = (r_{ix}, r_{iy}, r_{it})^T$.

A detailed analysis of the structure tensor technique and its practical application to optical flow computation can be found in [Jähne et al., 1999]. The structure tensor technique can be formulated as a solution of the total least squares (TLS) problem in a more general way (see appendix A).

Implementation of the structure tensor

The expression for the structure tensor in Eq. (4.17) is written explicitly:

$$\boldsymbol{J} = \begin{pmatrix} \langle g_x g_x \rangle & \langle g_x g_y \rangle & \langle g_x g_t \rangle \\ \langle g_x g_y \rangle & \langle g_y g_y \rangle & \langle g_y g_t \rangle \\ \langle g_x g_t \rangle & \langle g_y g_t \rangle & \langle g_t g_t \rangle \end{pmatrix},$$

using the abbreviation Eq. (4.18).

The implementation of the structure tensor can be carried out very efficiently by standard image processing operators. Identifying the convolution (Eq. (4.8)) with a smoothing operation (for example the isotropic Binomial operator $\mathcal{B}$), and the derivatives in the pth resp. qth direction with edge detectors (for example the optimised Sobels $\mathcal{D}_p$ and $\mathcal{D}_q$ [Scharr, 2000]), we can construct a structure tensor operator:

$$\mathcal{J}_{pq} = \mathcal{B}(\mathcal{D}_p \cdot \mathcal{D}_q),$$

Table 4.1: *Classification of the Eigenvalues of the structure-tensor in a spatio-temporal neighbourhood*

condition	rank($\boldsymbol{J}$)	comment and calculation of interesting quantities
$\lambda_1 = \lambda_2 = \lambda_3 = 0$	0	There is no variation of the grey values. We are in a constant neighbourhood, where we are not able to reconstruct any kind of optical flow.
$\lambda_1 > 0, \lambda_2 = \lambda_3 = 0$	1	The grey values vary in one direction, which is characterised by the only non-vanishing Eigenvector. Because we suffer from the "aperture problem", we can calculate only the normal optical flow: $\boldsymbol{f}_\perp = -r_{1t}/(r_{1x}^2 + r_{1y}^2)(r_{1x}, r_{1y})^T$.
$\lambda_1, \lambda_2 > 0, \lambda_3 = 0$	2	The grey values vary in two directions, and are constant in a third direction, which is characterised by the Eigenvector belonging to the zero Eigenvalue. Thus the optical flow is here: $\boldsymbol{f} = 1/r_{3t}(r_{3x}, r_{3y})^T$.
$\lambda_1, \lambda_2, \lambda_3 > 0$	3	The grey values vary in all directions. The optical flow cannot be calculated with this simple model.

where $\cdot$ signalises a pixel-wise multiplication.

Because smoothing in general results in a loss of information, the result after applying the structure tensor operator can be stored in a more compact sequence than the original data. In practice this can be handled by downsampling the resulting sequence by a factor of two, for instance. In order to find a procedure to perform the principal axis transformations efficiently, we bear in mind, that we deal with very small, symmetric, matrices. These types of data can be covered by using the numerical method of Jacobi transformations to find the Eigenvalues and Eigenvectors [Press et al., 1992].

4.3 Improvements of Optical Flow Determination

In this section improvements of determining optical flow will be presented. These improvements will help to solve the difficulties mentioned in the introduction. Each improvement can be applied to more than one (but not necessarily to all) methods of determining optical flow.

4.3.1 Parameterisation of 2D-Optical Flow fields

As mentioned in section 4.1 the standard local optical flow methods assume, that the optical flow $\boldsymbol{f}(\boldsymbol{x}, t)$ is constant within the local neighbourhood U around $\boldsymbol{x}$. The optical flow may be expanded to a first order Taylor series in the vicinity of $(\boldsymbol{x}_0, t_0)$ [Farnebäck, 2000]:

$$\boldsymbol{f}(\boldsymbol{x}, t) \approx \boldsymbol{f}(\boldsymbol{x}_0, t_0) + \begin{pmatrix} \partial u/\partial x & \partial u/\partial y \\ \partial v/\partial x & \partial v/\partial y \end{pmatrix} \boldsymbol{x} + \begin{pmatrix} \partial u/\partial t \\ \partial v/\partial t \end{pmatrix} t \equiv \boldsymbol{t} + \boldsymbol{A}\boldsymbol{x} + \boldsymbol{a}t \ .$$

The BCCE supplemented by this parameterisation yields the *extended brightness change constraint equation (EBCCE)*:

$$(\nabla g)^T(\boldsymbol{t} + \boldsymbol{A}\boldsymbol{x} + \boldsymbol{a}t) + g_t = 0 \ . \tag{4.20}$$

Geometric transformations of the local neighbourhood may be computed from the components of the matrix $\boldsymbol{A} = (a_{ij})$, like
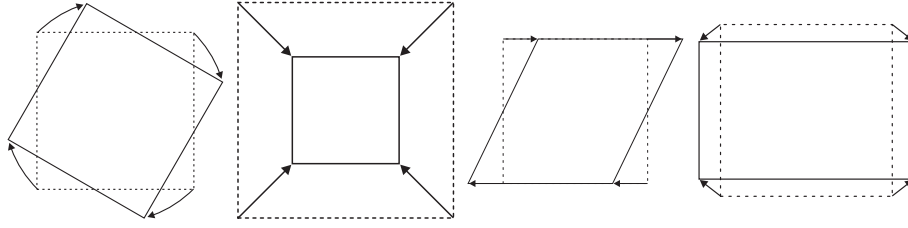
Figure 4.5: *Elementary affine transformations of a rectangular surface element. From left to right: rotation, dilation, shear, stretching (from [Jähne et al., 1999]).*

- rotation: $\operatorname{rot}(\boldsymbol{f}) = \partial u/\partial y - \partial v/\partial x = a_{21} - a_{12}$,
- dilation: $\operatorname{div}(\boldsymbol{f}) = \partial u/\partial x + \partial v/\partial y = a_{11} + a_{22}$,
- shear: $\operatorname{sh}(\boldsymbol{f}) = \partial u/\partial y + \partial v/\partial x = a_{12} + a_{21}$,
- stretching: $\operatorname{str}(\boldsymbol{f}) = \partial u/\partial x - \partial v/\partial y = a_{11} - a_{22}$.

For a graphical illustration of elementary affine transformations see Fig. 4.5. For a more general treatment of parametrization of 2D-optical flow fields in the context of the Lie group of continuous transformations, see appendix B.1.

4.3.2 Coarse-to-Fine Techniques

The temporal sampling theorem states a theoretical upper limit for the magnitude of displacements, which are able to be analysed. Consider a moving sinusoidal pattern of wavelength λ. From Fig. 4.6 it is evident, that only displacements up to the magnitude of $\lambda/2$ are unambiguously determinable. In this case the optical flow can be estimated by the minimal motion, indicated by the solid arrow in Fig. 4.6. Analogue to the spatial sampling theorem $\Delta x < \lambda/2$ we can formulate a temporal sampling theorem:

$$\Delta t < \frac{T}{2} = \frac{\pi}{\omega} = \frac{\pi}{\boldsymbol{k}^T \boldsymbol{f}}. \tag{4.21}$$

ω can be expressed in terms of wave-number $\boldsymbol{k}$ and optical flow $\boldsymbol{f}$ via the plane equation Eq. (4.12). Apparently the maximum determinable displacements are limited by the magnitude of the highest spatial wave-numbers, which are contained in the image.

Coarse-to-fine-techniques help to estimate large motions. By smoothing the image we eliminate the high frequency content of the images, so that we are able to estimate a coarse motion field. Then we "undo" the motion by transforming the image back by means of the estimated coarse motion field. Now we can use the higher frequency content to estimate a finer motion field. Added to the previously coarse motion field the fine motion field provides a more accurate approximation to the real motion field.

This procedure can be improved in several ways:

If an estimation on a coarse level is incorrect, the fine-level estimate has no chance of correcting the errors. To fix this, we must have knowledge of the error in the coarse-level estimates. That suggests working in a probabilistic framework. Indeed, a "state evolution equation" and a "measurement equation" can be proposed similar to Kalman-filtering [Simoncelli, 1993].
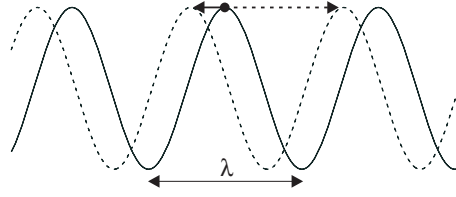
Figure 4.6: *Illustration of the temporal sampling theorem for a sinusoidal pattern of wavelength λ (from [Jähne et al., 1999]).*

For more accurate computation additional filters can be introduced, which slice the bandwidth in smaller pieces than these given by the dyadic pyramid structure. This results in a combined multi-resolution and multi-scale approach [Ruhnau et al., 2005b].

The motion can be distributed very irregularly over the image plane. In these situations a selective multi-resolution approach is suggested [Cohen and Herlin, 1999].

4.3.3 Robust Estimation

There are situations, when parametrised flow field models fail to determine the optical flow correctly: These include the presence of multiple motions, like motion discontinuitities at boundaries (occluded multiple motions) or different motions being overlaid (transparent multiple motions) but also the presence of reflexes or corrupted pixels.

Least squares estimation tries to minimise a quadratic objective function $\rho(x)$ (compare Eq. (4.5)):

$$\hat{\boldsymbol{f}} = \arg\min_{\boldsymbol{f}} \int_{-\infty}^{\infty} w(\boldsymbol{x} - \boldsymbol{x}')\rho\left[(\nabla g)^T \boldsymbol{f} + g_t\right] \mathrm{d}\boldsymbol{x}'. \quad \text{with} \quad \rho(x) = x^2 \qquad (4.22)$$

The influence function $\psi(x)$ of the objective function is defined as the derivative of ρ with respect to x:

$$\psi(x) = \frac{\partial \rho(x)}{\partial x} \qquad (4.23)$$

In the least squares case the influence of data points increases linearly and without bound, so that outliers, which do not fit to the model, like corrupted pixels, have a great influence and distort the estimation of the correct optical flow dramatically. This is due to the fact, that by using a quadratic objective function we inherently assumed, that the residual errors are Gaussian and independently distributed within the neighbourhood U.

To achieve a more robust parameter estimation we have to replace the quadratic objective function by a suitable other function, which is referred to as *M-estimator* in statistics. The influence function of an M-estimator has to be redescending, i. e. it has to approach zero for large residuals after an initial increase for small values. [Geman and McClure, 1984] proposed a commonly used M-estimator (Fig. 4.7), which reads together with its influence function

$$\rho(x, \sigma) = \frac{x^2}{\sigma + x^2}, \quad \psi(x, \sigma) = \frac{2x\sigma}{(\sigma + x^2)^2}, \qquad (4.24)$$

where σ is a scale parameter.
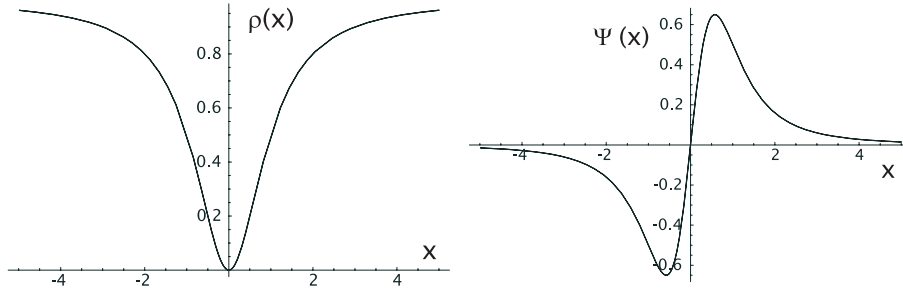
Figure 4.7: *An example for an M-estimator: **a** Geman and McClure-norm. **b** Its derivative (from [Jähne et al., 1999]).*

Given a robust formulation, there are numerous optimization techniques that can be employed to recover the motion estimates and the most appropriate technique will depend on the particular formulation and choice of the ρ-function. For detailed information about robust estimation the reader is referred to [Black and P., 1996].

4.3.4 Dealing with Brightness Changes

In many situations the constraint of brightness constancy Eq. (4.2) is violated. In some cases we are able to find a physical model for the time-dependent brightness variation. So we can estimate both the correct optical flow field $\boldsymbol{f}$ and the parameters $\boldsymbol{a}$ of the underlying physical process. The approach of [Haussecker and Fleet, 2001] constitutes an extension of the brightness change constraint equation to parameterised models of brightness variation, provided that these models are linear in $\boldsymbol{a}$ or can be linearised by a Taylor series expansion.

In section 4.2.1 we have stated that for the case that the brightness $g(\boldsymbol{x}, t)$ is constant along a path $\boldsymbol{x}(t)$ for all times, we are able to derive a constraint on the optical flow. Now we allow, that the brightness along the path may change according to a time-dependent parameterised function $h(g_0, t, \boldsymbol{a})$:

$$g(\boldsymbol{x}(t), t) = h(g_0, t, \boldsymbol{a}), \tag{4.25}$$

where $g_0 = g(\boldsymbol{x}(t_0), t_0)$ denotes the image at time t_0, and $\boldsymbol{a}$ is the Q-dimensional parameter vector for the brightness change model. The total derivative on both sides of Eq. (4.25) yields the *generalised brightness change constraint equation (GBCCE)*,

$$(\nabla g)^T \boldsymbol{f} + g_t = \frac{\mathrm{d}}{\mathrm{d}t} h(g_0, t, \boldsymbol{a}). \tag{4.26}$$

which reduces to the well-known BCCE if h is constant.

Assuming smoothness in the vicinity of $\boldsymbol{a} = 0$, h can be expanded by a Taylor series:

$$h(g_0, t, \boldsymbol{a}) = h(g_0, t, 0) + \sum_{k=1}^{Q} a_k \frac{\partial h}{\partial a_k}. \tag{4.27}$$

Without loss of generality, we choose a parametrization such that $\boldsymbol{a} = 0$ produces the identity transformation: $h(g_0, t, 0) = g_0$. By differentiating Eq. (4.27), and assuming a_k to be constant

through time within local windows of temporal support, we get an expression for the temporal brightness variation:

$$\frac{\mathrm{d}}{\mathrm{d}t}h(g_0, t, \boldsymbol{a}) = \sum_{k=1}^{Q} a_k \frac{\mathrm{d}}{\mathrm{d}t}\frac{\partial h}{\partial a_k} = \sum_{k=1}^{Q} a_k \frac{\partial}{\partial a_k}\frac{\mathrm{d}h}{\mathrm{d}t} = (\nabla_{\boldsymbol{a}}\mathrm{d}h/\mathrm{d}t)^T \boldsymbol{a}.$$

As h is analytic in $\boldsymbol{a}$, we could exchange the order of differentiation. We have reached an expression for $\mathrm{d}h/\mathrm{d}t$, which is basically a scalar product of data vector $\nabla_{\boldsymbol{a}}\mathrm{d}h/\mathrm{d}t$ and parameter vector $\boldsymbol{a}$, so that we can estimate the parameters by using a procedure such as total least squares (see appendix A).

In the following some models of brightness variation are presented:

Linear source terms When sources are present, the brightness depends linearly on time: $h = qt$, where q denotes the source strength. The GBCCE becomes

$$(\nabla g)^T \boldsymbol{f} + g_t = q.$$

Exponential decay In relaxation processes the time-dependent brightness can be modeled by an exponential decay: $h = g_0 \exp(-\kappa t)$, where κ denotes the relaxation constant. By differentiating h with respect to t the exponential function reproduces itself, so that we can write for the GBCCE:

$$(\nabla g)^T \boldsymbol{f} + g_t = -\kappa g. \tag{4.28}$$

Diffusion process: Fick's second law (see Eq. (2.8)), which states, that for isotropic diffusion the time rate of change of the gray value is proportional to its Laplacian tells us, what the GBCCE looks like in this case, where the diffusion constant D is the proportional constant:

$$(\nabla g)^T \boldsymbol{f} + g_t = D\nabla^2 g.$$

You can combine these physical models of brightness variation with all differential or tensor-based techniques: You have to replace the BCCE by the GBCCE, and the minimisation has to be carried out over the optical flow $\boldsymbol{f}$ *and* over the parameters $\boldsymbol{a}$ simultaneously.

4.4 Literature Review

Each of the optical-flow methods (differential, frequency-based or tensor-based) presented in section 4.2 was adapted to evaluation in the field of fluid mechanics. The term "optical flow" suggests its application to image sequences dealing with continuous tracer, like heat or concentration. Indeed, most of the literature addresses continuous tracer. On the other hand, in practice fluid flow analysis is performed to a great extent particle-based (see chapter 3), which does not prevent optical-flow based methods from being applied to. Examples can be found in the literature.

4.4.1 Differential Techniques

[Ruhnau et al., 2005b] applied the method of [Horn and Schunk, 1981] (see Eq. (4.7)) to images recorded with the conventional PIV-technique, described in 3.3.1. They used a coarse-to-fine strategy, as in section 4.3.2. The same authors replaced the global smoothness constraint by a

prior, relying on the Stokes equation ([Ruhnau and Schnörr, 2006]) and on the vorticity transport equation ([Ruhnau et al., 2006]).

Instead of using the BCCE, other authors used the 2D-continuity equation Eq. (4.4) as model. This was justified by the special kind of recording technique (like transmittance imagery in [Wildes et al., 2000]) or data (like satellite imagery in [Corpetti et al., 2002]). The latter used a second-order div-curl-regularisation scheme instead of just assuming global smoothness. Moreover, they applied their scheme to PIV-sequences ([Corpetti et al., 2005]).

4.4.2 Frequency-based Techniques

[Larsen, 1998] applied the local energy distribution to satellite images using the frequency-based techniques presented in 4.2.2. They used the optical-flow estimates together with confidence measures as an input for a regularization method based on the Markovian random field approach.

4.4.3 Tensor-based Techniques

[Jehle et al., 2004] analysed the motion of sand grains in a geotechnical application, recorded using rigid endoscopes. Under certain conditions, the grains can behave like a fluid. [Garbe et al., 2003] estimated both velocity vector field and heat flux simultaneously in image sequences, recorded using infrared thermography. They expanded the structure tensor technique (4.2.3) by a model including brightness changes (4.3.4).

5 Method of Two Wavelengths

In this section we will describe the basic concepts of our measurement technique. It is based on retrieving 3D information from 2D data – the intensity (grey value) being the source of the depth (i. e. the coordinate perpendicular to the image plane). For illustration see Fig. 5.1, left and Fig. 5.2, left. In order to do this, we have to consider two tasks:

1. The intensity distribution provides a depth map, taking into account the medium between illumination source, object and camera (spectral absorbance), the properties of the illumination (spectral characteristics), the attributes of the object (e. g. reflectance, object size), and the camera characteristics (e. g. linearity of the camera sensor, pixel size). Schematically we write:

$$g(x, y) \to z(x, y) \quad \text{i. e.} \quad \mathbb{R}^2 \times \mathbb{R} \to \mathbb{R}^2 \times \mathbb{R}$$

2. Once having obtained a depth map, we don't have the whole 3D-information. This may be because one part of the object may be occluded by another. Unlike in stereo vision, we acquire images of the object only from one perspective, so that we have no chance to reconstruct occlusions directly. But in some appropriate cases, we can infer the 3D-structure from using spatio-temporal information. For example, we assume that the objects move smoothly. We write:

$$z(x, y) \to (x, y, z) \quad \text{i. e.} \quad \mathbb{R}^2 \times \mathbb{R} \to \mathbb{R}^3$$

This chapter deals exclusively with the first task: The reconstruction of a depth map using brightness data. How to incorporate higher level properties of the flow, to reconstruct the whole 3D-information, is addressed in section 7.6.

5.1 Method of One Wavelength

The precursor of our method originally was proposed by [Debaene, 2005] in the context of biofluidmechanics. To distinguish it by our method we will refer to it as the *method of one wavelength*.

Her intention was, to estimate the wall shear rate, which influences the properties of the fluid (for the medical background we refer to section 8.4.1). For the calculation of the wall shear stress, 3D information about the flow field near the wall must be at hand. Therefore a measurement technique, capable to acquire and process 3D-data has to be found.

Like in other tracer-based flow measurement methods, small, reflective, floating particles are supplemented to the fluid. The tracer particles have to be exactly spherical, and their size distribution has to be narrow for reasons explained later. Unlike in particle imaging velocimetry the fluid is illuminated voluminously by light of a specific spectrum. A dye is added to the fluid, which absorbs light of a certain wavelength. The particles are recorded by a camera, which points perpendicularly to the wall.
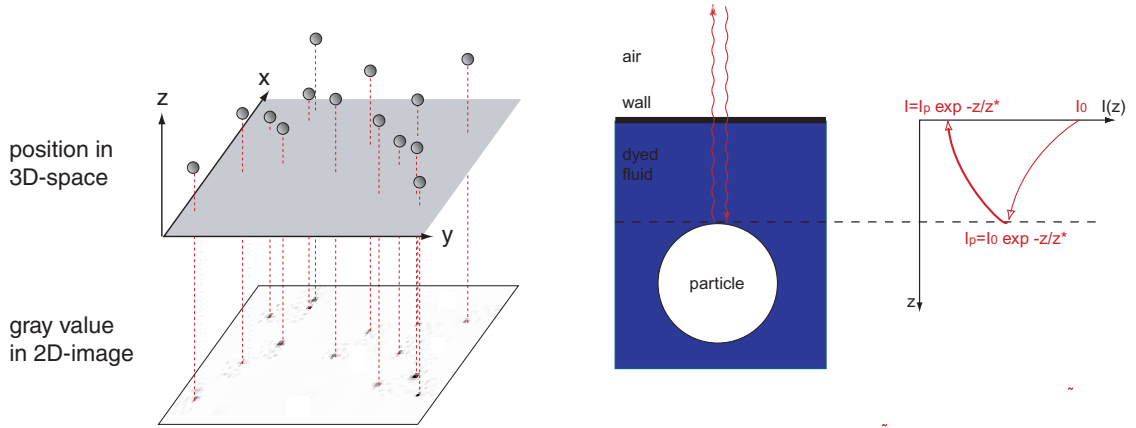
Figure 5.1: *Method of one wavelength. Left: 3D positions in space are obtained by analysing the grey values in a 2D image. Right: A monochromatic beam of light penetrates the dyed fluid with the intensity I_0, and hits the particle with intensity I_p after covering the distance z. After reflecting, it passes through the dye again, and hits the camera sensor with the intensity I. The intensity decrease can be calculated using Beer-Lambert's law.*

The dye limits the penetration depth of the light into the flow according to Beer-Lambert's law. The intensity I_p of the light approaching the particle is

$$I_p(z) = I_0 \exp{-z/\tilde{z}_*}, \tag{5.1}$$

where I_0 is the light's intensity before penetrating into the fluid, z is the distance of the particle's surface from the wall, and $\tilde{z}_*$ is the penetration depth (Fig. 5.1, right). The light is reflected by the particle, and passes the distance z again, before approaching the wall with the intensity

$$I(z) = I_p \exp{-z/\tilde{z}_*} = I_0 \exp{-2z/\tilde{z}_*} = I_0 \exp{-z/z_*}, \tag{5.2}$$

where an effective penetration depth $z_* = \tilde{z}_*/2$ was introduced for convenience. Within the illuminated layer the particles appear more or less bright, depending on their normal distance to the wall: Particles near the wall appear brighter, i.e. they have a higher grey value than particles farther away from the wall. The correlation between the recorded intensity $I(z)$ of a particle and its distance to the wall, which is expressed in terms of the hypothetical intensity I_0 of the particle at the wall and z_*, can be assessed experimentally.
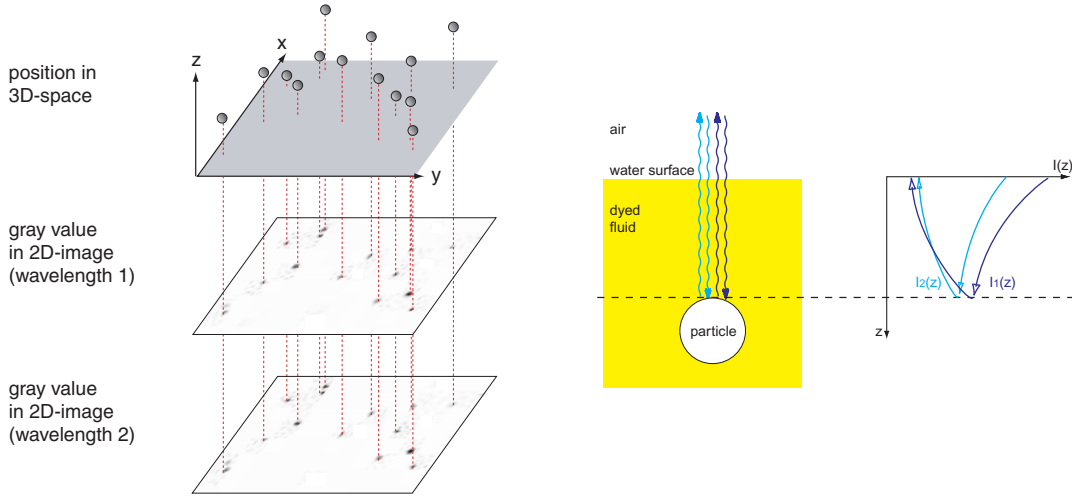
The particle's intensity $I(z)$ is mapped to a grey value $g(I(z))$ by the procedure of imaging. For simplicity, we assume, that the response curve of the camera is linear, i.e. we are allowed to write

$$g(z) = g_0 \exp{-z/z_*}. \tag{5.3}$$

Eq. (5.3) can be solved for the depth z as follows:

$$z = z_*(\ln g_0 - \ln g). \tag{5.4}$$

In order to eliminate the depth z in Eq. (5.3) we have to know:

Figure 5.2: *Method of two wavelengths. Left: 3D positions in space are obtained by analyzing the grey values in two 2D images (one for each wavelength). Right: Two monochromatic beams of light penetrate the dyed fluid. Because their penetration depths differ, their intensities progress differently.*

- The grey value of the particle at the surface $g_0 = g(z = 0)$. Therefore we require, that the particles are exactly spherical, and that they all have to be of the same size. The latter can be loosened by the requirement of a narrow size-distribution.

- The penetration depth z_* of light of a specific wavelength into a certain medium. We have to choose a light source, whose light is as monochromatic as possible, because then we can exclude any hardening effects.

5.2 Method of Two Wavelengths

It turns out, that the greatest restriction of the *method of one wavelength* is the tightness of the size distribution of the tracer particles. In order to use particles variable in size, we have to illuminate with light of two distinct wavelengths (i. e. two different penetration depths: z_{*1} and z_{*2}). We write down Beer-Lambert's law for each wavelength:

$$g_1(z) = g_{01} \exp -z/z_{*1} \quad \text{and} \quad g_2(z) = g_{02} \exp -z/z_{*2}.$$

We solve this equation system for the depth of the particle:

$$z(g_1, g_2) = \frac{z_{*1} z_{*2}}{z_{*1} - z_{*2}} \left(\ln \left(\frac{g_1}{g_2} \right) + \ln \left(\frac{g_{02}}{g_{01}} \right) \right). \tag{5.5}$$

Note, that here the depth of the particle merely depends on the *ratio* of the intensities g_{01}/g_{02}, which is for all particles the same, and which can be calibrated.

Besides its applicability to systems with heterodisperse particles the method of two wavelengths has further benefits compared to the *method of one wavelength*:

- The particles can be imaged as streaks: The particle grey values g_1 and g_2 can be multiplied by a common attenuation factor (depending on the exposure time), which cancels out while calculating the depth according to Eq. (5.5).

Table 5.1: *Comparison of the two methods of depth reconstruction with respect to their advantages and disadvantages.*

Method of one wavelength	Method of two wavelengths
+ easy setup	+ applicable to heterodisperse particles
+ exploits full camera frame rate	+ applicable to higher exposure times
- very high requirements to particles (monodispersity, shape)	- greater relative error in depth-determination

- We can loose the assumption of requiring exactly spherical particles. But we have to take care, that the particles don't rotate significantly from one frame to the other.

The advantages and disadvantages of the two methods of depth reconstruction proposed in this chapter are summarized in table 5.1. Figure 6.9 in section 6.3.2 illustrates the different coverage of the emission spectra of the light sources by the absorption spectrum of the dye.

5.3 Error Analysis

In table 5.1 we have noted, that compared to the *method of one wavelength*, the *method of two wavelengths* has a greater relative error in depth-determination. In this chapter we will address this fact in more detail by applying error propagation to formulas Eq. (5.4) and Eq. (5.5).

Method of one wavelength

First we will consider the more simple case of the *method of one wavelength* (see Eq. (5.4)). We find for the error in depth Δz according to error propagation:

$$\Delta z(g) = \sqrt{\left(\frac{\partial z}{\partial g}\right)^2 \Delta g^2} = \frac{\Delta g}{g}. \tag{5.6}$$

In our model the error in the grey value Δg consists of two parts:

1. $\Delta g = c$, where c is a constant: This is the case, if we have a grey value independent noise on the chip. As a first approximation we can model the chip noise in this way.

2. $\Delta g = k(\sigma)g$, where k is a function of the particle size, expressed by σ: Especially for small σ in comparison to the pixel size the grey value of a particle depends on the position of its centroid relative to the pixel grid. We will call this error *grid error*. The relation $k(\sigma)$ is found using simulations (see section 8.2.4).

Plugging this into Eq. (5.6) we get for the grey value-dependent error of the depth determination using the *method of one wavelength* following expression:

$$\Delta z(g) = z_* \left(\frac{c}{g} + k(\sigma)\right).$$

We define a relative error for the depth $e_z(g)$ by dividing the grey value dependent absolute error by the grey value dependent absolute depth:

$$e_z(g) \equiv \frac{\Delta z(g)}{z(g)} = \frac{c/g + k(\sigma)}{\ln g_0 - \ln g}$$
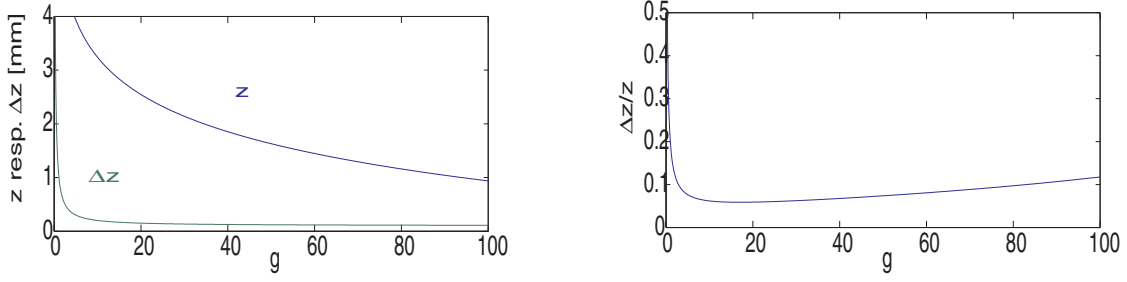
Figure 5.3: *Plot of $z(g)$ resp. $\Delta z(g)$ (left) and $\Delta z(g)/z(g)$ (right) using the one-wavelength method with the parameters $z_* = 1$ mm, $g_0 = 255, c = 1, k(\sigma) = 0.1$.*

This means, that the overall error can be decomposed into two sums: One stemming from the grey value-independent noise, decreasing with increasing g; and one stemming from the grey value dependent grid error. From Fig. 5.3, right, we find, that the relative error for small grey values is very large but approaches a minimum soon. (For demonstration, we have set $c = 1, k(\sigma) = 0.1, z_* = 1, g_0 = 255$.)

Method of two wavelengths

Now we treat the more complicated case of the *method of two wavelengths* (see Eq. (5.5)). Here we find for the error in depth Δz:

$$\Delta z(g_1, g_2) = \sqrt{\left(\frac{\partial z}{\partial g_1}\right)^2 \Delta g_1^2 + \left(\frac{\partial z}{\partial g_2}\right)^2 \Delta g_2^2} = \left|\frac{z_{*1} z_{*2}}{z_{*1} - z_{*2}}\right| \sqrt{\frac{\Delta g_1^2}{g_1^2} + \frac{\Delta g_2^2}{g_2^2}}. \qquad (5.7)$$

After inserting the errors in the grey value $\Delta g_{1,2} = c + k(\sigma)g_{1,2}$, and dividing by the grey value dependent absolute depth we get for the grey value-dependent relative error for the depth $e_z(g_1, g_2)$:

$$e_z(g_1, g_2) \equiv \frac{\Delta z(g_1, g_2)}{z(g_1, g_2)} = \frac{\sqrt{c^2(1/g_1^2 + 1/g_2^2) + 2k^2}}{\ln g_1 - \ln g_2 + \ln(g_{02}/g_{01})}$$

The *absolute error* $\Delta z(g_1, g_2)$ is influenced by the grey value-independent noise for $g_1 \approx 0$ (i. e. for deep particles). With g_1 approaching g_2 (i. e. for particles at the surface), the absolute overall error approximates the grid error. Due to error propagation a grid error of $k = 0.1$ alone causes an absolute error of $\Delta z \approx 0.14$. In Figure 5.4 the absolute errors are plotted for $c = 1$, $k = 0$ (left), for $c = 0$, $k = 0.1$ (center) and for $c = 1$, $k = 0.1$ (right) using $g_{01}/g_{02} = 1$ and requiring $g_2 \geq g_1$.

In Fig. 5.5 we plotted the *relative errors* for the same parameters as in the absolute errors. We find, that the grey value-independent noise contributes to the overall relative error only for $g_1 \approx 0$ and for $g_1 \approx g_2$. In-between, the relative error is determined mainly by the grey value dependent grid error, giving acceptable results for $10 < g_1 < 2/3g_2$.
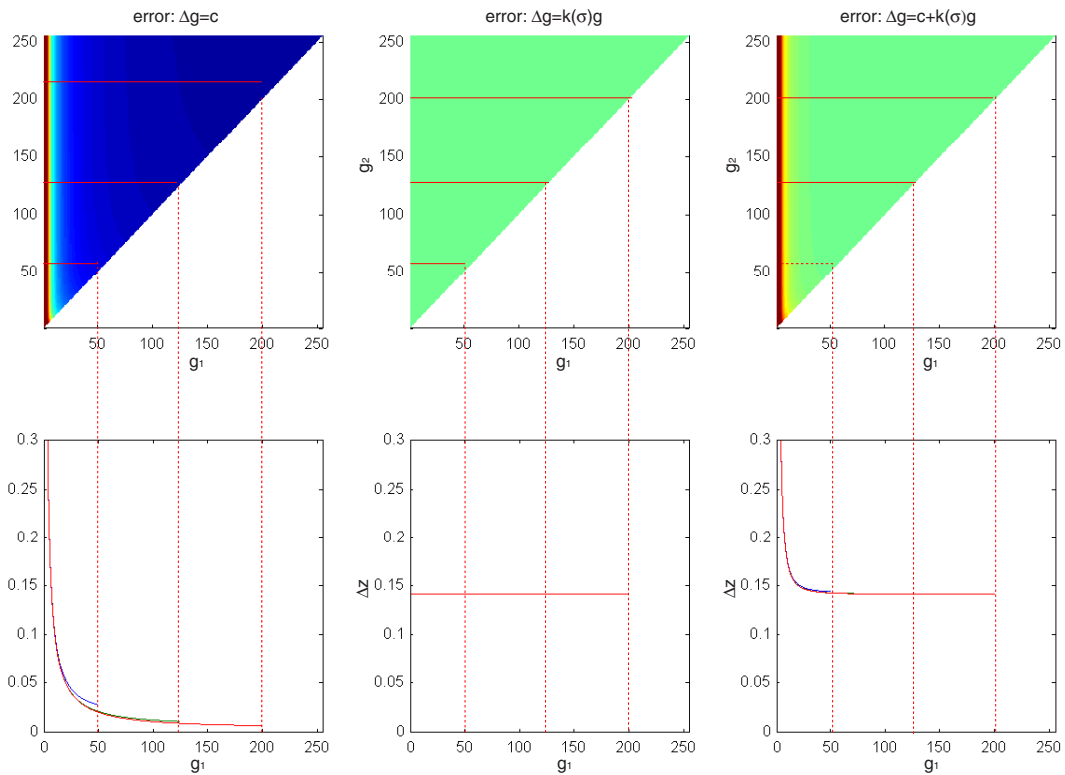
Figure 5.4: *Plot of the absolute error $\Delta z(g_1, g_2)$ using the two-wavelength method with the parameters $g_{01}/g_{02} = 1, c = 1, k(\sigma) = 0.1$. On the left the absolute error stemming from $\Delta g = c$ is plotted; in the middle, the absolute error using $\Delta g = k(\sigma)g$ is given; on the right both errors were combined. The top row shows error maps, where the color map ranges from 0 to 0.3; the bottom row shows sections with $g_1 = 50, g_1 = 125$ and $g_1 = 200$.*
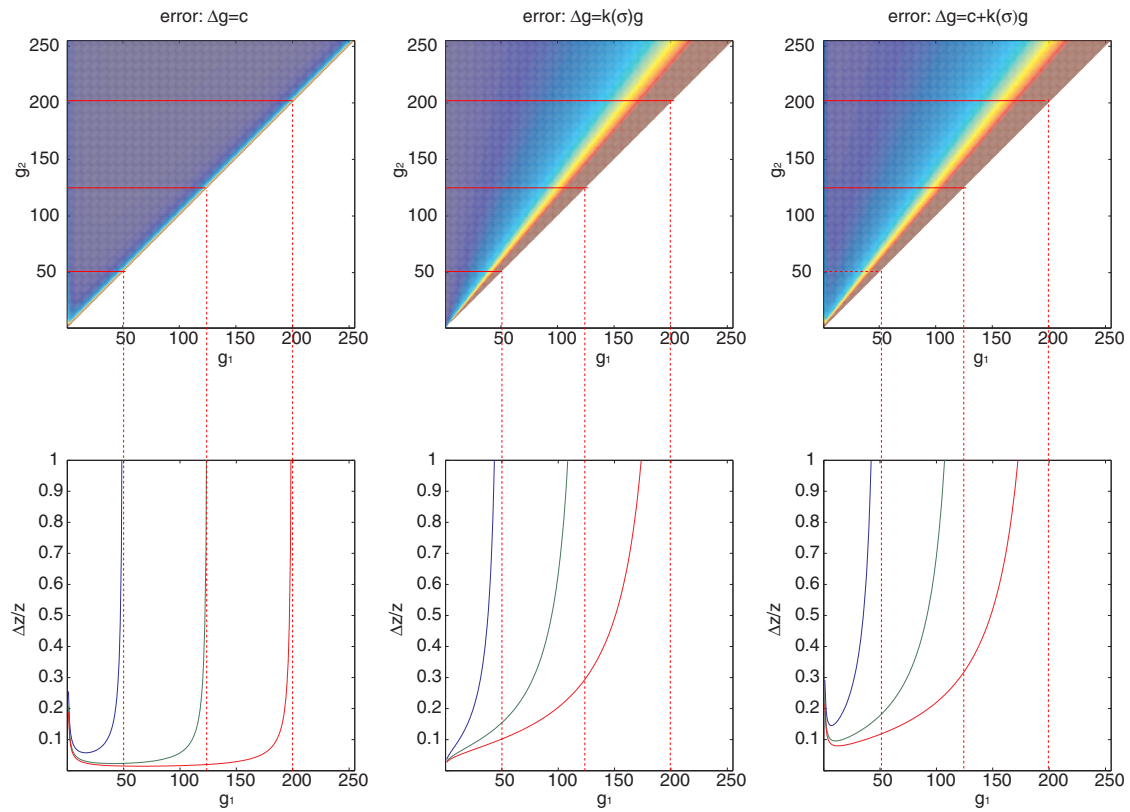
Figure 5.5: *Plot of the relative error $\Delta z(g_1, g_2)/z(g_1, g_2)$ using the two-wavelength method with the parameters $g_{01}/g_{02} = 1, c = 1, k(\sigma) = 0.1$. On the left the relative error stemming from $\Delta g = c$ is plotted; in the middle, the relative error using $\Delta g = k(\sigma)g$ is given; on the right both errors were combined. The top row shows error maps, where the color map ranges from 0 to 0.5; the bottom row shows sections with $g_1 = 50, g_1 = 125$ and $g_1 = 200$.*

6 Hardware Components

In this chapter the various components of the data acquisition hardware used to record image sequences are explained. We will start with the objects of interest, in this case small particles, which are suspended in the fluid (section 6.1). Then we will have a closer look to the medium, the light has to pass on its way to the object (section 6.2). In section 6.3 the light sources are explained, as well as the characteristics of the light itself. The last section is devoted to the optical system, to the CCD-cameras used in the experiments and to the triggering of the individual components.

6.1 Particles as Tracer

Like PIV or PTV (see section 3.3), our method is based on determining position and velocity of small particles, which are added to the fluid. These have to fulfill following requirements:

Flow representation The particles ideally have to be capable to follow the fluid, must not affect the motion of the fluid and must not influence each other. Important parameters are: particle size, specific weight of the particles, hygroscopicity of the particles and particle density. This is a common property, which all particle-based fluid measurement methods have to satisfy.

Visibility The contrast between the particles and the surrounding has to be high. Their imaged grey value has to be significantly over the noise level of the camera. Therefore the particles have to be imaged as brightly as possible. The visibility depends on the reflectance of the particles and on the particle size. Regarding particle size, we have to find a trade-off of flow representation and visibility, which depends on the observed flow and on the experimental setup.

Scattering properties Our method is based on relating the imaged brightness to the position of the particle according to Beer-Lambert's law. A basic requirement to do so, is, that we operate in the geometric scattering range, which provides a requirement for the particle size in relation to the light frequency. Moreover the shape of the particles is affected, which has to be spherical.

6.1.1 Scattering Properties

Light of a certain wavelength is scattered by a spherical particle of a certain diameter. We ask for the differential scattering cross-section which is defined as the scattered intensity per solid angle element.
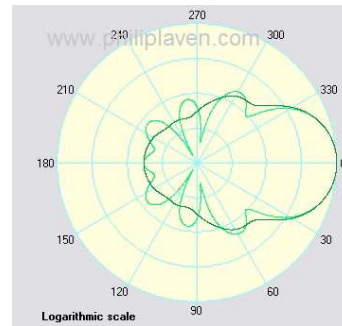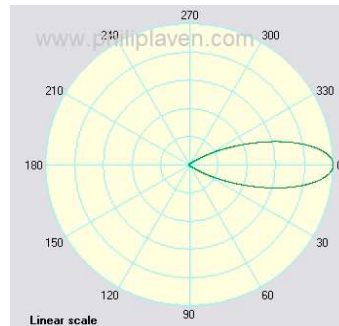

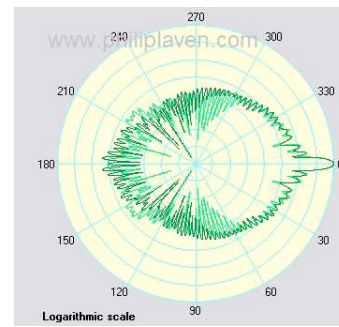[1]Mieplot: A computer program for scattering of light from a sphere using Mie theory and the Debye series; http://philiplaven.com/MiePlot.htm

λ=500nm;
a=40nm;
q=0.5
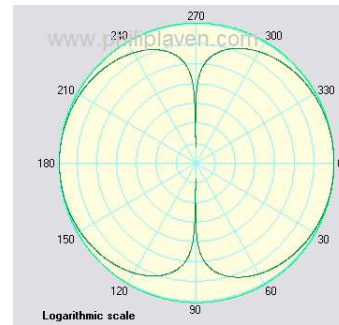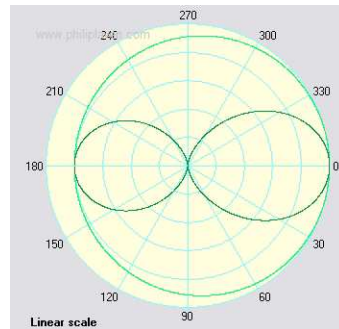
λ=500nm;
a=400nm;
q=5
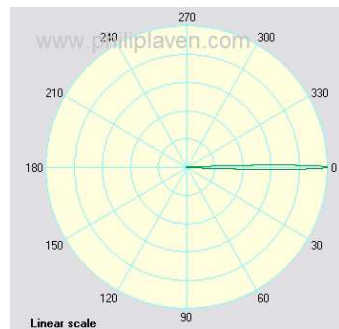
λ=500nm;
a=4μm;
q=50

λ=500nm;
a=40μm;
q=500
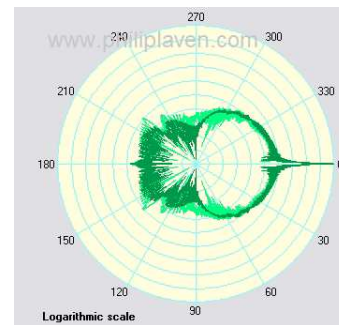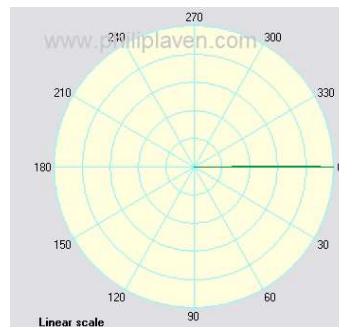
Figure 6.1: *Polar diagrams of the normalized intensities of perpendicular (dark green) and parallel (light green) polarised light, scattered at small, spherical particles according to Mie's theory. The light approaches the particle from the left. The particles have the refractive index of water surrounded by vacuum ($n = 1.3377$). Left column: Linear representation for various q. Right column: Logarithmic representation (plotted using Mieplot [1]).*

Optimage
3M
Potters
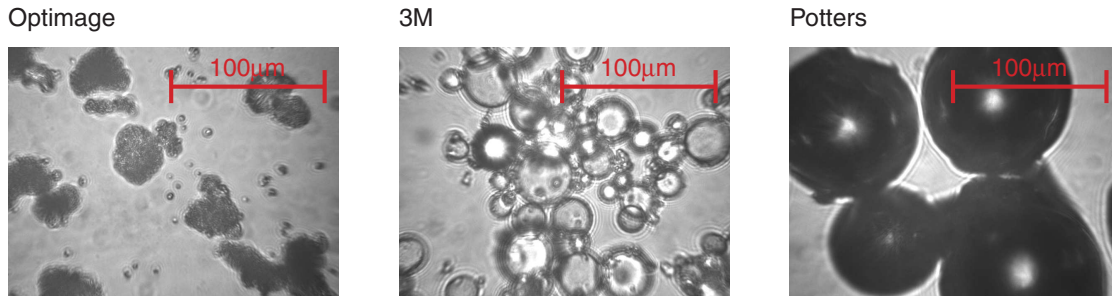
Figure 6.2: *Microscopically taken pictures of the particles, we used in our experiments.*

For solving this problem, we make use of classical electrodynamics, starting with Maxwell's equations. We make the assumptions of a planar wave being scattered at a homogeneous sphere. The general solution was found by [Mie, 1908] for the first time, and is given in [van de Hulst, 1981] in detail. We find, that for a given index of refraction, the angle-dependent scattered intensity is solely a function of normalised diameter q, which is defined as

$$q = \frac{2\pi a}{\lambda},$$

where a is the radius of the particle, and λ is the wavelength of the incoming light. In Fig. 6.1 we printed polar diagrams of the scattered intensity for some selected q. It can be seen, that there is a strong dependence of the scattered light on the angle of observation.

For $q \ll 1$, Mie's solution tends to Rayleigh's approximation: The light scattered by 90°is fully polarized into the direction orthogonal to the image plane, whereas in forward and backward direction (0°resp. 180°) both polarisation directions contribute equally.

With increasing q there are two trends, apparent from the polar diagrams (Fig. 6.1). Firstly, forward scattering develops. Secondly, there are emerging further maxima. Their number increases with rising normalized diameter approximately linearly. Exact measurements of the angular distribution of intensity allow a determination of the size of the spheres.

For $q \gg 1$, Mie's solution tends to the geometric limit: We can abstract parts of the wave (which are of width much larger than λ and yet small compared to the radius a of the sphere) as light rays. The rays can be traced, considering reflection and refraction according to Snell's law and Fresnel's formulas. There are exceptions in or near a focal line (or a focus), where the intensity according geometric optics would tend to infinity. Examples are rainbows and glories.

6.1.2 Particle Characteristics

In table 6.1 at the ending of this chapter we listed the types of particles, we used in our experiments. Because the normalised diameter q is much greater than unity for all particles, we are in the geometric range as a good approximation. That allows to neglect the effects of Mie scattering.

In the introduction to this section we mentioned, that one important characteristic for using particles as tracer is, that they have to follow the fluid optimally. Stokes law of resistance tells us the drag force D, which is exhibited on a sphere of diameter d in a fluid with dynamic viscosity μ:

$$D = 3\pi\mu d U_s,$$
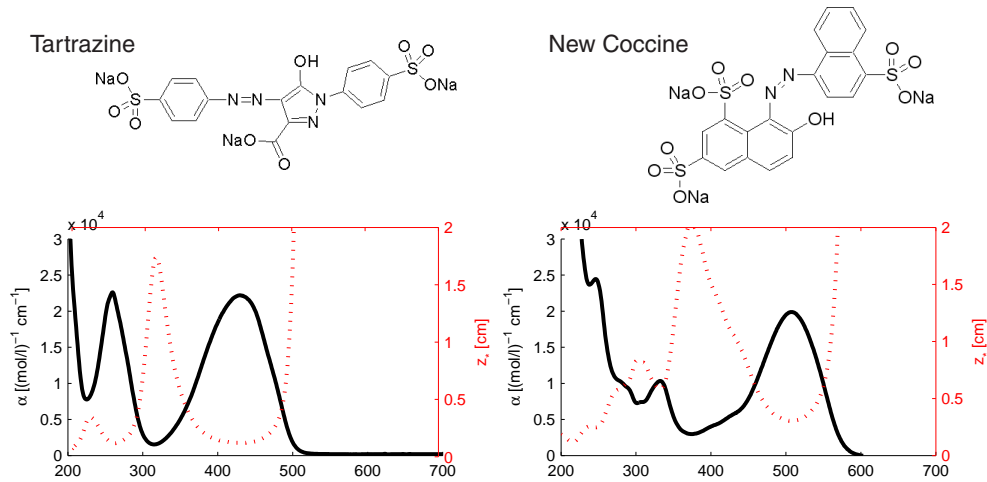
Figure 6.3: *Spectra of tartracine and new coccine. The absorption (black) resp. the penetration depth (red) is plotted against the wavelength (in nm). The penetration depths are calculated from the measured spectra using concentrations $c_{tartracine} = 200mg/l = 374\mu mol/l$ and $c_{new\ coccine} = 100mg/l = 165\mu mol/l$.*

where U_s is the difference of the particle velocity and the fluid velocity, the velocity slip. By equating the drag force with the inertia force $F = 1/6\pi(\rho' - \rho)d^3 a$ of a particle with density ρ' and acceleration a in a fluid with density ρ, we have for the velocity slip:

$$U_s = d^2 \frac{\rho' - \rho}{18\mu} a.$$

The velocity slip is influenced by the particle diameter in a much greater way (quadratically), than by the difference in density (linear). Assuming an acceleration of 10 cm/s, we have a velocity slip for the Optimage particles of about $1\,\mu$m/s, for the 3M particles of about $20\,\mu$m/s and for the Potters particles of about $50\,\mu$m/s.

On the other hand, larger particles appear much brighter to the camera than smaller ones. Again the dependency is quadratic in diameter. This was the reason, why we preferred the spheres by Potters compared to the Optimage particles and spheres by 3M in the convection tank experiments, where we have only slow flows.

Figure 6.2 shows magnified images of the particles. We see, that compared to the spheres by 3M and by Potters, the Optimage particles appear very unshaped. For conventional PIV this is irrelevant, but for our application it might become a serious problem: Because we estimate depth from the apparent intensity, and because intensity depends on the projected size of the particle, we get an error of estimation, if the particles rotate between two recordings. For that reason, we used the 3M spheres in favour of the Optimage particles for the falling film experiments.

6.2 Dye as an Absorber

A dye works as an absorber of light emitting a specific wavelength spectrum. We demand, that the absorption follows Beer-Lambert's law, which is explained in detail in section 6.2.1. Further
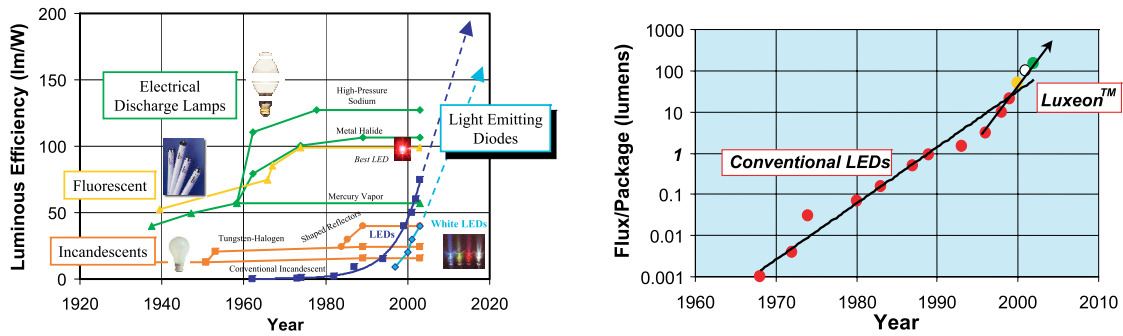
Figure 6.4: *Left: The luminous efficiency (in W/lumen) of LEDs has outperformed several other light sources in the recent past. There exists hope for further improvements. Right: The luminous flux per package for LEDs has increased exponentially in the recent 30 years.*

requirements are, that the dye is not toxic and is not harmful to the environment, that its dosage is simple, that it is soluble in water and that it is inexpensive - at least, if we want to use it in voluminous tanks.

6.2.1 Beer-Lambert's Law

Bougner (1729) and Lambert (1760) found, that the attenuation $\mathrm{d}I$ of light intensity, which traverses a clear medium, is proportional to the particular intensity $I(z)$ and to the traversed layer thickness $\mathrm{d}z$:

$$\mathrm{d}I = k(\lambda)I(z)\mathrm{d}z,$$

with the wavelength-dependent proportionality constant $k(\lambda)$.

This holds for certain conditions only:

- The incoming light has to be monochromatic and collimated.

- The absorbing molecules have to be dispersed homogeneously in the fluid. They must not scatter and must not exhibit any self-interaction.

- Scattering and reflexion on the surface of the probe result in a light attenuation, which masks the effect of absorption, and therefore should be excluded.

Beer showed 1852, that for most solutions of absorbing substances the proportionality constant k on its part is proportional to the concentration c of the particular substance. Beer-Lambert's law follows:

$$\mathrm{d}I = -\alpha(\lambda)cI\mathrm{d}z,$$

where the proportionality constant α is known as the molar absorption-coefficient with dimensions $[\alpha]=(\mathrm{mol/l})^{-1}\mathrm{cm}^{-1}$. We can integrate this to

$$I(z) = I_0 \exp(-\alpha(\lambda)cz) = I_0 \exp(-A(\lambda)),$$

where I_0 is the incoming intensity, and $A(\lambda)$ is called absorbance. The latter is a nondimensional quantity. We arrive at our familiar formulation of Beer-Lambert's law Eq. (5.1), if we introduce
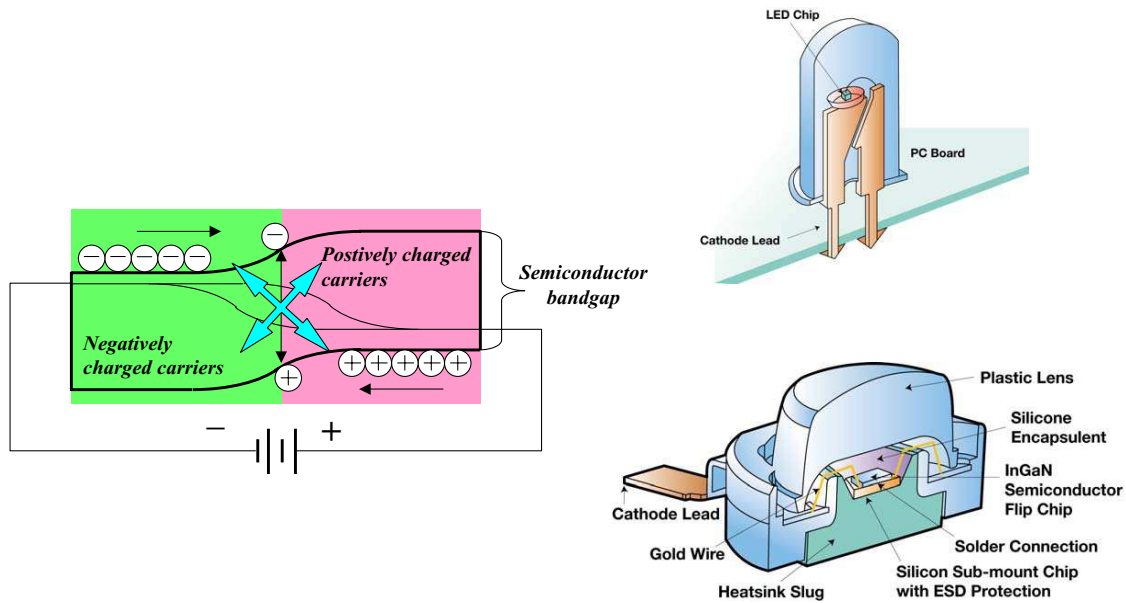
Figure 6.5: *Left: Physical function of a LED. Right: Low power vs. high power LED.*

the penetration depth z_*, defined as

$$z_*(\lambda) = \frac{1}{\alpha(\lambda)c}.$$

Visibly spoken, the penetration depth is the depth, where the intensity is attenuated to 1/e th of its original value.

6.2.2 Example Spectra of Dyes

There are many dyes to choose from. A good overview is given in [Green, 1990]. The most important criterion for our decision was, that the spectrum of the dye should match to the spectra of the light sources (section 6.3). I. e., that the penetration depths with respect to the LED-spectra differ about a factor 2-5, and that the dye exhibits a good absorption in the considered spectral range. Further criteria were solubility, manageability and price of the dye. We found two dyes, which are broadly used in industry (for example to dye textiles and food): The yellow dye Tartracine, which has its peak of absorbance at 425 nm, and the red dye New Coccine, which has its peak of absorbance at 406 nm. An overview over the characteristics is given in table 6.2; the spectra are printed in Fig. 6.3 together with their chemical structure formulas.

6.3 LEDs as Light Sources

In contrast to conventional PIV, in our experiments we cannot illuminate using laser light sections. The reason is, that our measurement method is based on observing particles in a volume, not just in a slice. Light emitting diodes (LEDs) have established themselves as small, reliable, efficient and bright light sources during the last years.
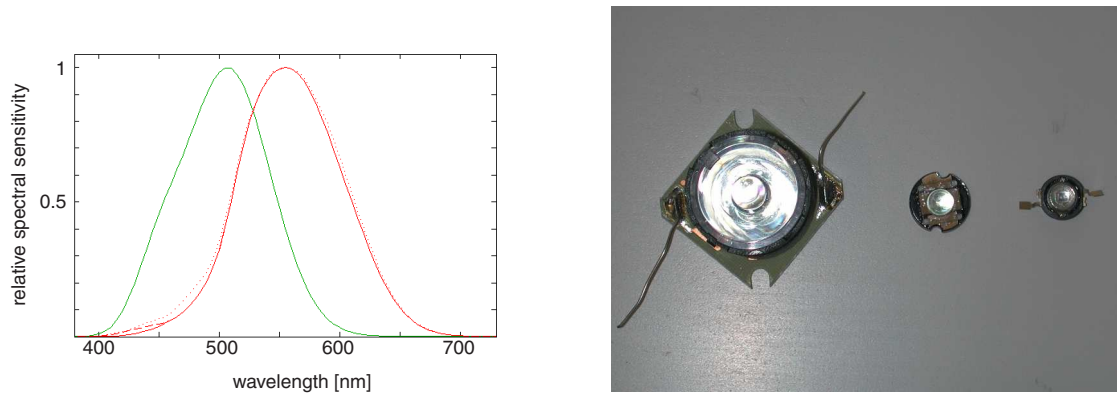
Figure 6.6: *Left: Photopic (vision using the cone-receptors at high intensities, red) and scotopic (vision using the rod-receptors at low intensity, green) luminosity functions. The photopic curves include the CIE 1931 standard (solid), the Judd-Vos 1978 modified data (dashed), and the Sharpe, Stockman, Jagla & Jägle 2005 data (dotted). Right: LEDs we used in our illumination setups. Luxeon III Emitter, C11A1, Luxeon Star O (from left to right)*

There were two developments in technology, which made LEDs feasible for our application: Firstly, LEDs have become more and more powerful over the last decades. The luminous flux per package has doubled every 18 to 24 months over the recent 30 years in accordance with Moore's law. Moreover the luminous efficiency of LEDs has already outperformed that of incandescents and mercury vapor lamps, and is expected to exceed that of fluorescent lamps and electrical discharge lamps, soon (Fig. 6.4). Secondly in the mid-1990s green and blue LEDs became available, which made use of the wide band gap of the semiconductor indium gallium nitride InGaN [Nakamura et al., 1994]. Now lighting in the spectral range beyond 600 nm became possible.

6.3.1 Physical Function of High Power LEDs

Figure 6.5, left, shows a simple sketch of the physical function of a LED. Like a normal semi-conductor diode, a light emitting diode consists of a chip of semiconducting material doped with impurities to create a structure called a p-n-junction. Current flows easily from the p-side (anode) to the n-side (cathode), but not in the reverse direction. When an electron meets a hole, it falls into a lower energy level, and releases energy in the form of a photon. The wavelength of the emitted light depends on the band gap energy of the materials forming the p-n-junction.

Because high power LEDs produce more heat, it was necessary to change their design. Historically, most LEDs have been constructed in a manner similar to the 5 mm type illustrated in Fig. 6.5, top. The base pins serve as both electrical and thermal conduits, which limit how much light can be produced. Fig. 6.5, bottom, represents a standard high power LED (like the Luxeon III Emitter). The large metal slug dramatically improves heat transfer characteristics. This in turn allows for higher current, a larger light emitting surface and proportionally higher light output. The thermal resistance of the high power units is ten times lower than that of a conventional 5 mm LED.
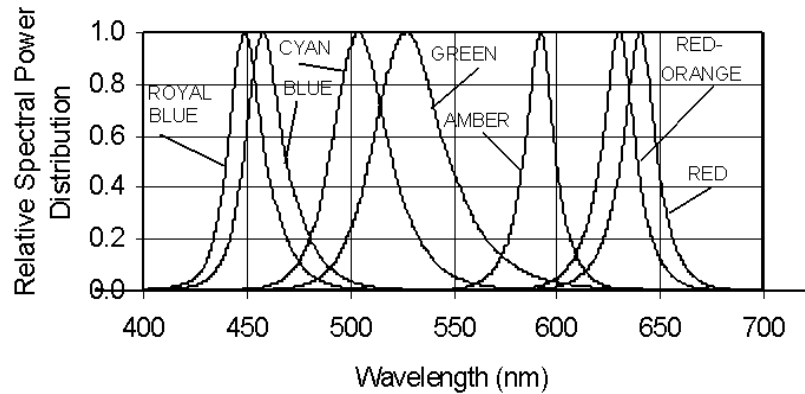
Figure 6.7: *Spectra of the Luxeon III Emitter-family as displayed in the data-sheet (http://www.lumileds/pdfs/DS45.PDF).*
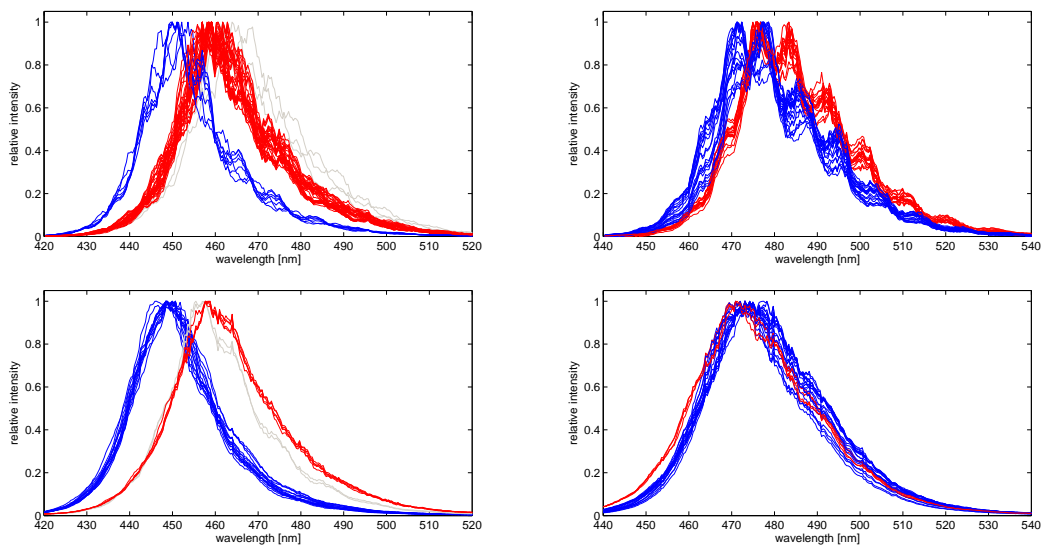
Figure 6.8: *Measured spectra of the LEDs we used for our illumination setups. We grouped the LED-spectra in each case in two major divisions (indicated with blue and red color). Top: Luxeon III Emitter. Bottom: Luxeon Star O. Left: royal blue (455nm). Right: blue (470nm).*

6.3.2 Selection of LEDS, Used in Our Experiments

The LEDs we used in our experiments are listed in table 6.3 and displayed in Fig. 6.6, right. The semiconductor material of all LEDs is gallium indium nitride (InGaN), and we chose four wavelengths, which have arisen as compatible with the selected dyes. In the table we specified the energy flux (photom. luminous flux) Φ, which can be derived by the radiation energy (photom.
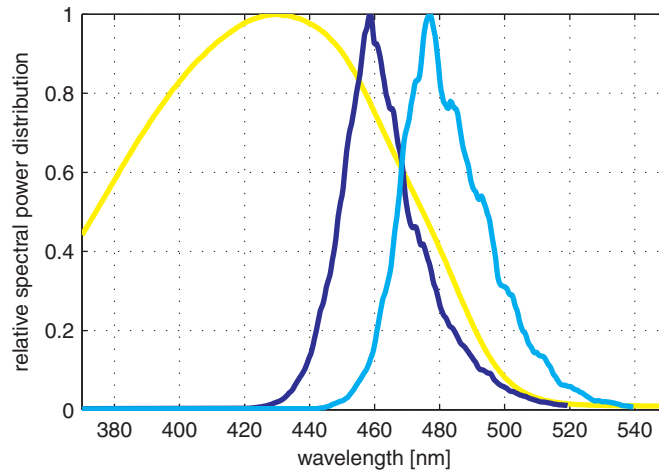
Figure 6.9: *Measured Luxeon III Emitter spectra (royal blue and blue) together with the absorption spectrum of tartracine (yellow).*

quantity of light) Q by:

$$\Phi = \frac{\mathrm{d}Q}{\mathrm{d}t} \quad [Q] = \mathrm{J(radiom.)/lms(photom.)} \quad [\Phi] = \mathrm{W(radiom.)/lm(photom.).}$$

The transition of radiometric to photometric units is made by relating the characteristics of the energy units to their response of the human eye. The response functions are displayed in Fig. 6.6. With their help and the note, that at a wavelength of 555 nm the energy flux of 1 W equals to the luminous flux of 683 lm (specification for photopic vision), the radiometric quantities can be transformed into photometric quantities.

A rough description of the form of the spectra is given in the data-sheet (Fig. 6.7, left). Having a closer look to the spectra of the LEDs using a spectrometer of the type "USB2000", manufactured by Ocean Optics, one will see, that the spectra differ in a significant way. We grouped the spectra of the Luxeon III Emitter LEDs and of the Luxeon Star LEDs (each royal blue and blue) in such a way, that shape of the spectra resemble, and the maxima are roughly the same (Fig. 6.8). We found, that LEDs of the same charge have similar spectra. The heterogeneousness among different charges may be explainable due to variations in manufacturing. From now on we have taken care, that we ordered only LEDs of the same charge, so that it would not be necessary to acquire the spectra of the LEDs and to group them.

Fig. 6.9 shows the absorption spectrum of the Tartracine dye (yellow) together with the measured emission spectra of the Luxeon III Emitter LEDs. The spectrum of the royal blue LEDs have a greater overlap with the dye-spectrum than the blue LEDs. That means, that the penetration depth $z_{*,\mathrm{royal\ blue}}$ of light stemming from the royal blue LEDs is shorter than the one stemming from the blue LEDs $z_{*,\mathrm{blue}}$. Exploiting this property, it is possible to reconstruct the depth of particles variable in size (see section 5.2).
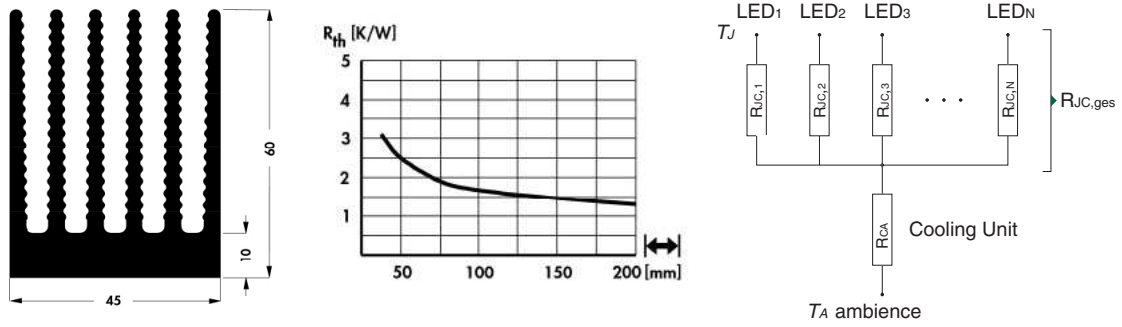
Figure 6.10: *Left: Profile of selected cooling units and diagram: thermal resistance in dependence of length of cooling units[2]. Right: Schematic diagram of thermal resistances occurring in our (simplified) system.*

6.3.3 Cooling of the LEDs

Though the LEDs were designed for operation under high-current-conditions, it is necessary to attach heat sinks to keep the temperature of the p-n-junction constantly below its critical level. To estimate a limit for the minimum length of the cooling units, it is instructive to calculate the thermal resistance of the combined system: light emitting diodes (which can be regarded as connected parallely) and heat sinks.

Generally for the overall thermal resistance R_{JA} holds:

$$R_{JA} = \frac{\Delta T}{P_{\text{ges}}},$$

where $\Delta T = T_J - T_A$ is the temperature drop between junction and ambiance, and P_{ges} is the dissipated power. The overall thermal resistance can be calculated using the same rules as for the computation of an electrical resistance (see the schematic diagram Figure 6.10, right):

$$R_{JA} = \frac{1}{\sum_i^n \frac{1}{R_{JC,i}}} + R_{CA}.$$

Because all the thermal resistances in the LEDs are equal, we let $R_{JC,i} = R_{JC}$. We get for the thermal resistance in the heat sink:

$$R_{CA} = \frac{T_J - T_A}{P} - \frac{R_{JC}}{N}.$$

In the most powerful version of our illumination units (Fig. 6.11, top) we maintain 20 LEDs, each receiving a power of $P_i = 0.6\,\text{A} \times 4\,\text{V} = 2.4\,\text{W}$, so that the overall power to be dissipated becomes approximately $P_{ges} = 45\,\text{W}$, assuming a degree of efficiency of roughly 5%. With a junction temperature of $T_J = 135°\text{C}$, according to manufacturer information, and an ambient temperature of $T_A = 35°\text{C}$, R_{CA} becomes approximately 1.6 K/W, using the vendor's specification of the thermal resistance for each LED: $R_{JC} = 13\,\text{K/W}$[3]. By having a closer look at diagram Fig. 6.10,
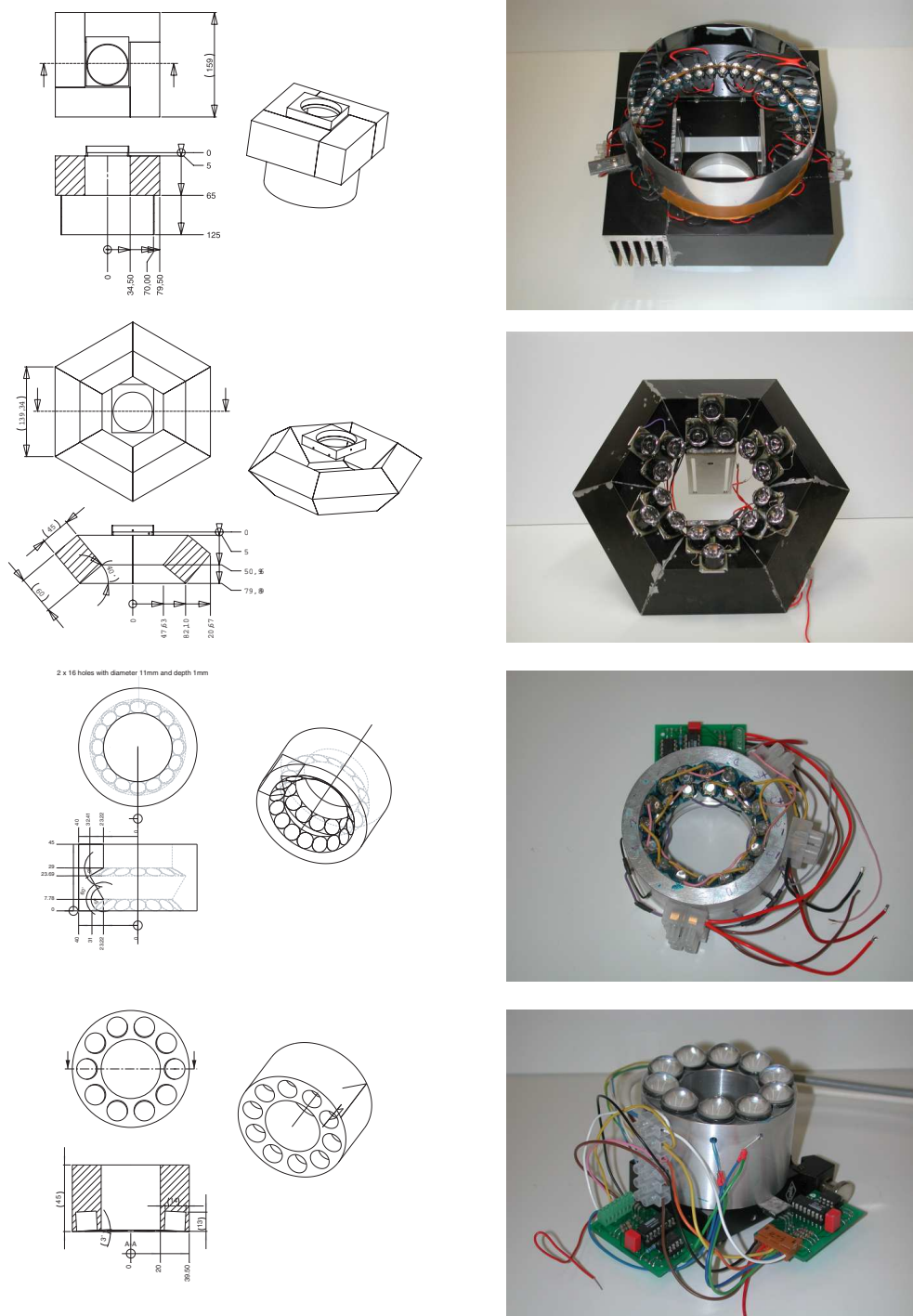
Figure 6.11: *Technical drawings and photographs of the four different illumination-setups which were designed for the experiments. From top to bottom: 1.) Luxeon III Emitter-LEDs (20× royal blue, 20× blue). 2.) Luxeon Star O-LEDs (18× royal blue installed, space for 12× blue). 3.) C11A1-LEDs (16× blue, 16× cyan). 4.) Luxeon III Emitter-LEDs with additional optics (5× blue, 5× cyan).*
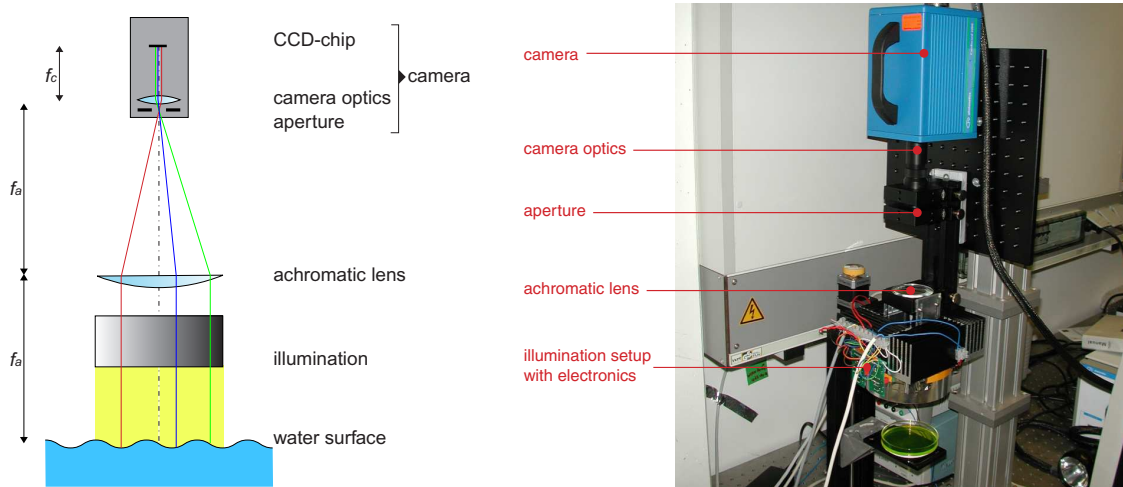
Figure 6.12: *Sketch (left) and photograph (right) of the imaging setup used for the falling-film measurements.*

center, we can estimate the minimum length for the cooling units of about 120 mm. To conclude, passive cooling is possible; but we have to take care, that we choose the heat sinks properly.

6.3.4 Light Sources

Fig. 6.11 shows the various designs of illumination units, that were built for our experiments. We will describe them from top to bottom:

1. The most powerful version contains 2×20 LEDs of type Luxeon III Emitter each being maintained at 2.4 W (only 60% of the maximum possible power). Blue and royal blue LEDs are arranged alternately and circularly on the planar heatsinks. An aluminium mirror is used to yield a flat illumination field, which covers a circular disc of 100 mm in diameter. This light source provides a very homogeneous illumination over a relatively large area. It is used both for the falling film experiment and for the convection tank experiment.

2. In the next illumination unit we wanted to make use of the collimator lens of the Luxeon Star O LEDs. In order to attain high luminance, we had to incline the cooling units about 50°to the optical axis. The useable area is sufficient for 18 royal blue LEDs and 12 blue LEDs (each being maintained at 1 W). The lighting is very inhomogeneous. Homogeneity might be improved using a diffuser.

3. The C11A1-LEDs are not radiating isotropically, but they emit their light in a cone of about 30°. We arranged these light sources in two annuli, each consisting of 2×8 LEDs. Because these LEDs were not available in royal blue, we chose the colour cyan instead. Each LED consumed the power of 0.6 W. Because the area of tolerable homogeneity is relatively small (about 2×2 cm^2), this light source is installed in the falling film experiment only. Its irradiance is considerably higher (factor 2), than the one of source 1.

---

[3]For an exact calculation of the overall thermal resistance the thermo-glue, needed for the attachment of the LEDs, has to be considered. Here we assume, that the glue-layer is very thin.
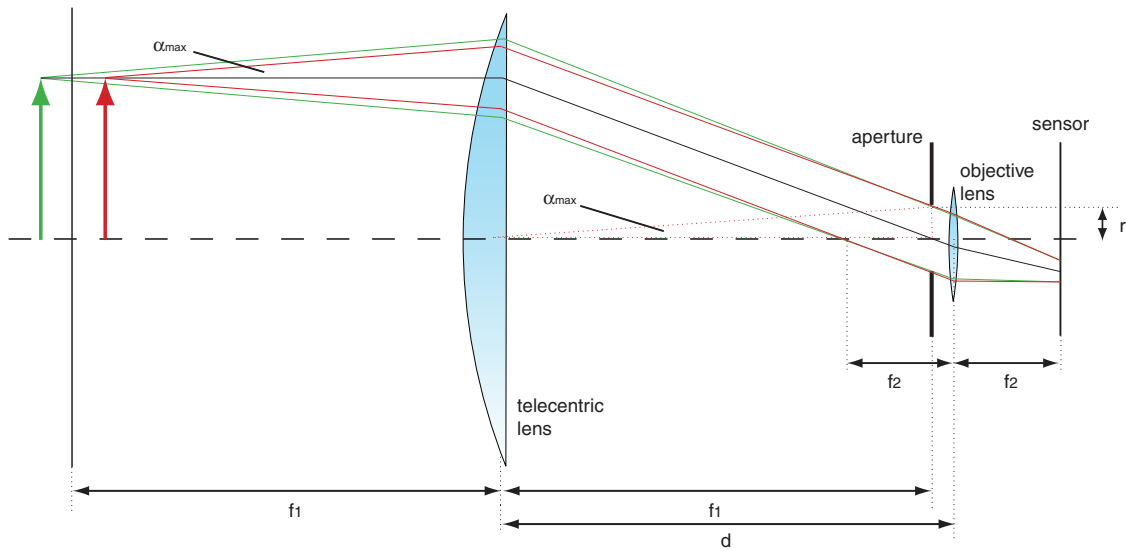
Figure 6.13: *Setup of telecentric optics.* α_{max} *denotes the maximum of the angles enclosing the horizontal and the rays, which leave the object and pass the aperture.*

4. In contrast to the three previous ones, constructing the last one, we wanted to keep a distance of about 60 cm from the illumination setup to the object. This was possible using small planar-convex lenses, which were attached in front of the Luxeon III Emitter diodes. Here we used 2×5 LEDs (royal blue and cyan) each being maintained at 2.4 W. This light source is used in the convection tank. It provides a circular homogeneous area of about 5 cm in diameter.

6.4 Imaging Setup

In the previous chapters we dealt with the objects, the medium and the light, that pervades the medium. Here we will focus our interest onto the recording system, which is responsible for getting 2D image sequences from the 3D world. Like any other conventional digital sequence imaging system, our setup consists of optical components, a digital camera which is connected to the computer hardware, and electronics, which is responsible for synchronizing the individual processes. Figure 6.12 shows the arrangement of the various components used for the falling-film measurements: illumination, telecentric lens, aperture, camera optics and high-speed camera. The image acquisition unit employed in the convection-tank experiment is displayed in Fig. 8.13 in section 8.3.2. Instead of a telecentric optics a conventional objective was used, which was designed for the combination with high resolving cameras.

6.4.1 Telecentric Optics

In the setup for the measurement in a falling film we used telecentric optics. This has the advantage, that the imaged lateral dimensions of the measured object are not dependent on their distance from the camera sensor. The telecentric mapping is a parallel projection.
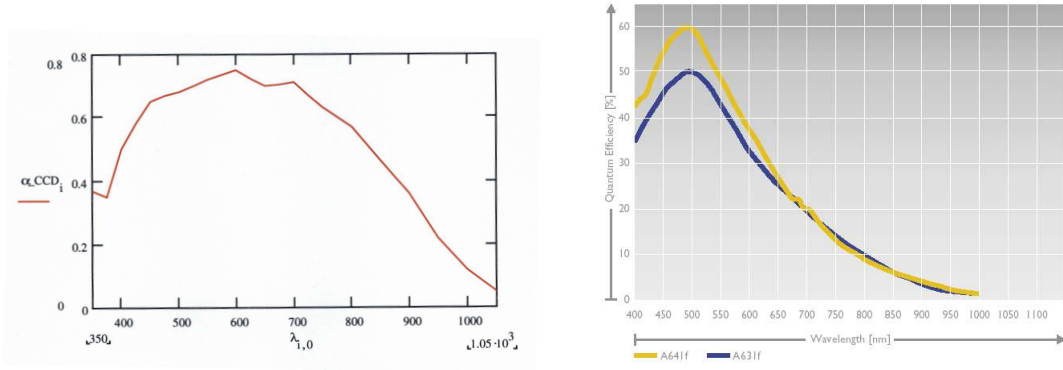
Figure 6.14: *Quantum efficiency curves of the Photonetics CamRecord 2000-camera (left) and of the Basler A641f-camera (right, yellow curve).*

In an *ideal* telecentric system, the infinitesimal narrow aperture is located in the focal plane of the large telecentric lens, so that only parallel principal rays can pass the aperture. The objective lens is adjusted to an infinitesimal object distance, so that the camera sensor lies in the focal plane of the objective. Figure 6.13 shows the setup of the telecentric optics in our system.

In order to obtain an image, the radius r of the aperture is allowed to be finite. Given the focal length of the telecentric lens f_1, we can calculate for the maximum inclination of the rays α_{max} (see also [Rocholz, 2005]):

$$\tan \alpha_{max} = \frac{r}{f_1}.$$

Here we made use of the fact, that parallel rays are focused in the focal planes, so that the two triangles containing α_{max} are congruent. By inserting the definition of the focal ratio of the objective $2k \equiv f_2/r$, we can calculate the angle α_{max} using well-known quantities:

$$\tan \alpha_{max} = \frac{f_2}{2kf_1}.$$

It turns out, that because $f_1 \gg f_2$ and $k = O(10)$ in our system, α_{max} is a very small angle (typically of order $1°$), so that the conditions for telecentricity are met in good approximation.

The focal length of the compound system f_{12} is approximately the focal length of the telecentric lens, because

$$\frac{1}{f_{12}} = \frac{1}{f_1} + \frac{1}{f_2} - \frac{d}{f_1 f_2} \approx \frac{1}{f_1} + \frac{1}{f_2} - \frac{f_1}{f_1} f_2 = \frac{1}{f_1},$$

where we assumed, that the aperture is close to the objective.

6.4.2 CCD- and CMOS-Cameras

Cameras with sensors based on CCD (charge coupled device)-technology or CMOS (complementary metal oxide semiconductor) technologies have become a de facto standard in acquisition of spatio-temporal data. Both image sensors accumulate signal charge in each pixel proportional to the local illumination intensity. When exposure is complete, a CCD transfers each pixel's charge
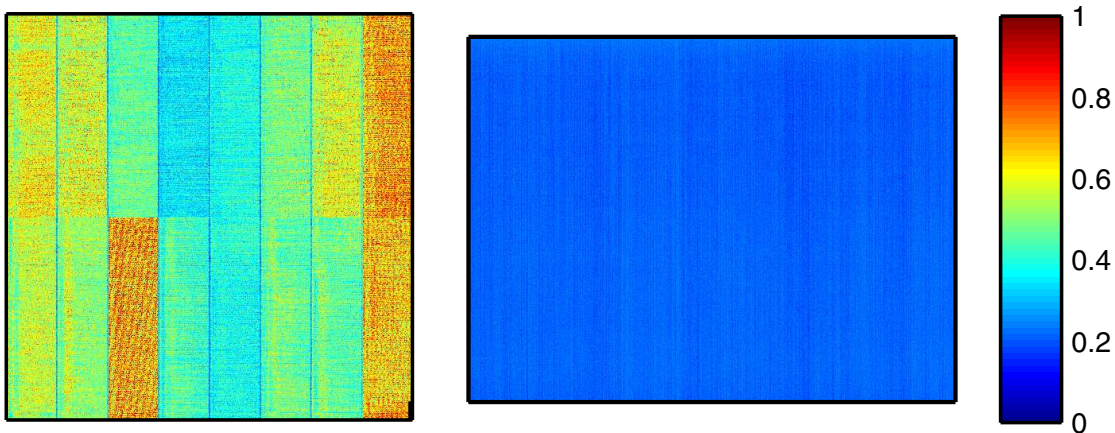
Figure 6.15: *Pixelwise variance in the dark image of the Photonetics CamRecord-chip (left) and of a clipping of the Basler A641f-chip (right).*

packet sequentially to a common output structure, which converts the charge to a voltage, buffers it and sends it off-chip. In a CMOS imager, the charge-to-voltage conversion takes place in each pixel. This difference in readout techniques has significant implications for sensor architecture, capabilities and limitations.

We are mainly interested in an optimal solution regarding speed, resolution, quantum efficiency, fill factor, noise and dark current. In the following we will compare the characteristics of CCD and CMOS regarding those topics:

Speed and resolution Especially for highly turbulent flows it is important to record image sequences using high resolution and high speed. Regarding speed CMOS-sensors have an advantage over CCDs because all camera functions can be placed on the image sensor. Furthermore, it is easily possible to adapt the resolution of a CMOS-chip to ones need by partitioning the pixel-array almost arbitrarily. The product of frame rate and number of pixels remains constant. When you downscale a CCD-camera, you always have a decrease of the product of frame rate and number of pixels. For example the Basler 641f: 14 fps at 1624×1234 but only 30 fps at 640×480 (with CMOS-technology, 90 fps at the small resolution were possible!). Moreover, using CCDs you are restricted to a couple of predefined modes.

Quantum efficiency and fill factor Because of the small exposure times, which occur acquiring high speed images, and the limited brightness of the light sources, we demand a high sensitivity (respectively a high quantum efficiency) of the camera sensors in the interesting spectral range. The quantum efficiency (QE) is a measure of the ratio of collected electrons to incident photons. Here both sensor types are roughly on the same level, whereas the fluctuations of QE among one type may be enormous. This is due to the fact, that not only the base material (in both cases silicon and silicon oxide) is important for the efficiency of the photoelectric effect and for carrier separation, but also the composition and thickness of the top layers are crucial for the QE. The fill factor, defined as the ratio of light-sensitive area to total pixel size, also determines the maximum achievable sensitivity. For example transistors or a lateral anti-blooming drain reduces the photosensitive area of a pixel. This is overcome

by illuminating the chip from behind, or by attaching microlenses on the chip.

Noise and dark current Especially working under poor lighting conditions, noise contributes to the acquired gray values seriously. Because our technique is based on processing the grey values directly or indirectly, special care has to be taken to avoid camera noise. CMOS-sensors generally suffer from fixed pattern noise, because the charge-to-voltage conversion takes place in each pixel there. CCD-sensors don't exhibit fixed pattern noise, at least, if the whole sensor is maintained by the same gain. Other noise sources are electronic noise and dark current noise. Here CCDs are of advantage, too.

For our experiments we have chosen two cameras:

- In the falling film experiment, we deal with comparably high fluid velocities - thus the frame rate has to be sufficiently high, and the sensitivity of the camera has to be sufficient. The Photonetics Cam-Record 2000 camera achieves frame rates up to 1000 fps (at a resolution of 512×512 pixels^2). Its QE is about 60% in the interesting spectral range (Fig. 6.14, left), and because the chip is backside illuminated the fill factor is virtually 100% (more technical data in table 6.4). Though working according to the CCD-principle, the camera sensor is divided into 16 individually controlled segments, which results in a kind of "fixed pattern noise". Moreover the boundaries of the segments exhibit a different noise characteristic in turn (Fig. 6.15, left). The camera works with a proprietary framegrabber board, installed in an extra PC, which is capable to record 2000 images at full resolution. The acquired image sequence can be transfered to mass storage using 100 MByte/s ethernet.

- In the convective tank experiment the fluid velocities are typically two orders of magnitude smaller compared to those in the falling film experiment. Thus, we can choose a camera with an excellent, high resolving sensor, neglecting the high-speed requirement. We chose the Basler A641f camera, because of the high resolution of 1624×1234 pixels^2 and the good chip characteristics (see Fig. 6.14, right and Fig. 6.15, right).

6.5 Triggering Electronics

The illumination setup has to be synchronised with the data acquisition. Both used cameras allow for external triggering via a TTL-signal. Figure 6.16, left, shows, how triggering works: Special hardware, the Data Translation Card[4], triggers the LED-arrays and the camera using one and the same clock. In the upper left corner one possible triggering scheme is shown: The camera-trigger T1 forces the basic frequency. T2 and T3 alternatively trigger the two LED-arrays, so that the frequencies are in each case half of the basic frequency. The duty cycles are chosen to 25%. This is just one example - we can realise every thinkable triggering scheme as long as the frequencies are consistent with the clock frequency (100 MHz).

Figure 6.16, right, shows a schematic circuit diagram, explaining the triggering of the LEDs. The signal of the Data Translation Card is amplified by the op amp LT1211, using an external power supply. Switching is performed by a MOSFET-transistor.

---

[4]Data Translation Inc., Marlboro, Massachusetts; http://www.datex.com

[5]Optimage Ltd., Edinburgh, Scotland, United Kingdom

[6]3M Speciality Materials, Zwijndrecht, Belgium; http://www.3m.com

[7]PQ Potters Europe GmbH, Kirchheimbolanden, Germany; http://www.potterseurope.org
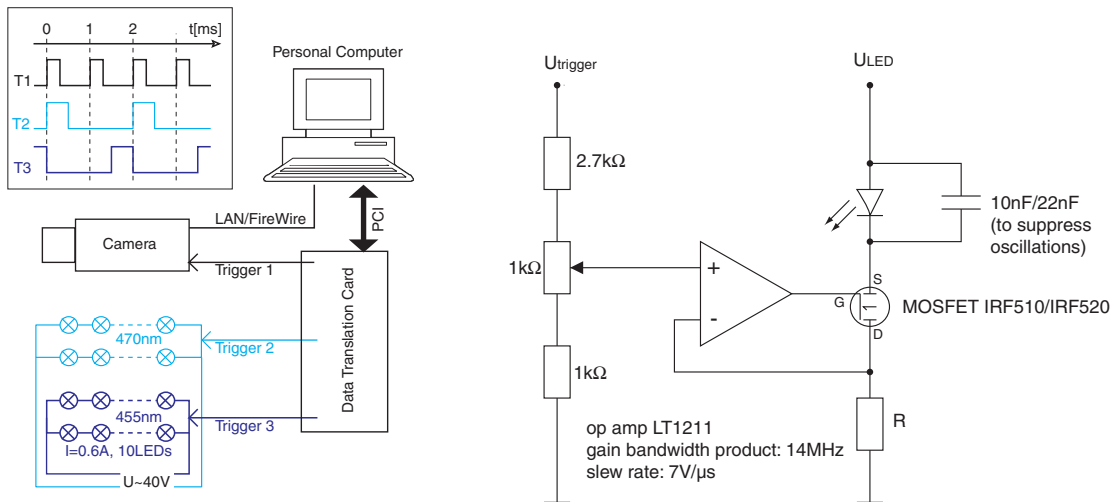
Figure 6.16: *Left: Triggering of the illumination unit and of the camera. In the upper left corner, one possibility of timing is displayed. Right: Schematic circuit diagram. The 5V-signal is amplified using a LT1211 op amp, switching is performed by a MOSFET-transistor*

---

[8]Philips Lumileds Lighting Company, San Jose, California; http://www.lumileds.com

[9]Roithner Lasertechnik GmbH, Vienna, Austria; http://www.roithner-laser.com

[10]Photonetics GmBH, Kehl, Germany; http://www.photonetics.com

[11]Basler AG, Ahrensburg, Germany; http://www.baslerweb.com

Table 6.1: *Different kinds of tracer particles we applied in our experiments. The normalized diameter q was calculated using a wavelength of $\lambda = 500\mu m$.*

vendor	material	ρ [g/cm^3]	d [μm]	q	refr. index	sphericity
Optimage[5]	polystyrene	1.020	30 ± 6	200	1.602	highly aspherical
3M[6]	hollow glass spheres	0.60	30	200	1.471	exactly spherical
Potters[7]	silver-coated hollow ceramic spheres	0.9/1.1	100	500	opaque	roughly spherical

Table 6.2: *Two selected dyes: Tartracine (Acid Yellow 23) and New Coccine (Acid Red 18 or Victoria Scarlet 3R).*

name	chemical formula	mol. weight	appearance	λ_{max}	sol. in water
Tartracine	$C_{20}H_9N_4Na_3O_9S_2$	534.37	orange powder	425 nm	300 mg/ml
New Coccine	$C_{20}H_{11}N_2Na_3O_{10}S_3$	604.48	maroon powder	506 nm	80 mg/ml

Table 6.3: *Different LEDs used for illumination.*

name	material	peak wavelegths	lum. flux	energy flux
Luxeon III Emitter[8]	InGaN	royal blue (455 nm)	20 lm	450 mW
(lambertian, operating at 1000 mA)		blue (470 nm)	30 lm	480 mW
		cyan (520 nm)	80 lm	165 mW
Luxeon Star O[8]	InGaN	royal blue (455 nm)	10 lm	220 mW
(lambertian, with collimator, 350 mA)		blue (470 nm)	16 lm	260 mW
C11A1[9]	InGaN	HB-30 (470 nm)	4.5 lm	70 mW
(viewing angle 30°, 350 mA)		HC-30 (505 nm)	10 lm	35 mW

Table 6.4: *The two cameras, we used in our experiments.*

name	**Camrecord 2000**[10]	**Basler A641f**[11]
Sensor type	CCD frame transfer, backside illuminated	Sony ICX267 AL/AK, progressive scan CCD
Sensor optical size	9.2 mm (100% fill factor)	1/2 inch
Pixel size	$18 \times 18\mu$m	$4.4 \times 4.4\mu$m
Maximum resolution	512×512 pixel	1624×1234 pixel
Maximum frame rate at full resolution	1000 fps	14 fps
Video output type	proprietary/Fast Ethernet	IEEE1394a
Video output format	8 bits/pixel	8 bits/pixel, 12 bits/pixel
Maximum quantum efficiency	70% 600 nm	50% 500 nm
Dimensions	$90 \times 120 \times 140$mm	$75 \times 44 \times 29$mm
Weight	1600 g	110 g

7 Image Processing

Every quantitative image-based measurement technique includes some kind of image processing, fulfilling the tasks of preprocessing, segmentation, feature extraction, motion analysis and postprocessing.

In this chapter we present the image processing in a chronological order, i. e. starting with preprocessing and ending with postprocessing. The input data are the image sequences obtained from the hardware setup, which we already described in chapter 6. Basically these consist of a number of recorded images containing both objects and background. Furthermore, the grey values in the images do not represent necessarily the corresponding light intensities, and the lighting may be inhomogeneous. These topics, which include radiometric calibration, illumination correction and background subtraction, are addressed in the first section of this chapter. In section 7.2 we will extract specific kinds of features, we will use in the further analysis: namely the centers of gravity and the representative grey value[1] of the distinct particles. Another feature is the grey value pattern itself. It has already been "extracted" in the preprocessing procedure. These features work as an input for the estimation of the particles' 3D velocity (section 7.3) and 3D position (section 7.4). Particle trajectories, which are generated using temporal information (section 7.5), work as an input to the task of postprocessing, described in section 7.6, which consists of elongation and smoothing of the trajectories and of the calculation of a dense vector field.

7.1 Preprocessing

The major intention of preprocessing is to prepare the image sequences for the feature extraction step, i. e. to condition the images in such a way, that the later analysis routines do not depend where they are applied in the image *locally*, but that we have to set *global* thresholds only, and that the number of thresholds can be reduced to a minimum. Acquiring real data always accompanies with imperfections of the measurement setup, like non-linearities and fixed-pattern-noise in the camera (section 7.1.1), inhomogeneities in the illumination (section 7.1.2) or objects in the background, which disturb the interesting features (section 7.1.3). We will have a closer look to the problems occurring in our experiments and show approaches to cope with them.

7.1.1 Simultaneous Radiometric Calibration and Illumination Correction

This section deals with the case of the Photonetics Camrecord 2000 high-speed camera; the Basler A641f camera sensor exhibits very good noise and linearity characteristics, so that we can apply the simpler scheme, explained in section 7.1.2.

---

[1]The term "representative grey value" stands for maximum grey value, fitted grey value or integrated grey value. See section 7.2.2
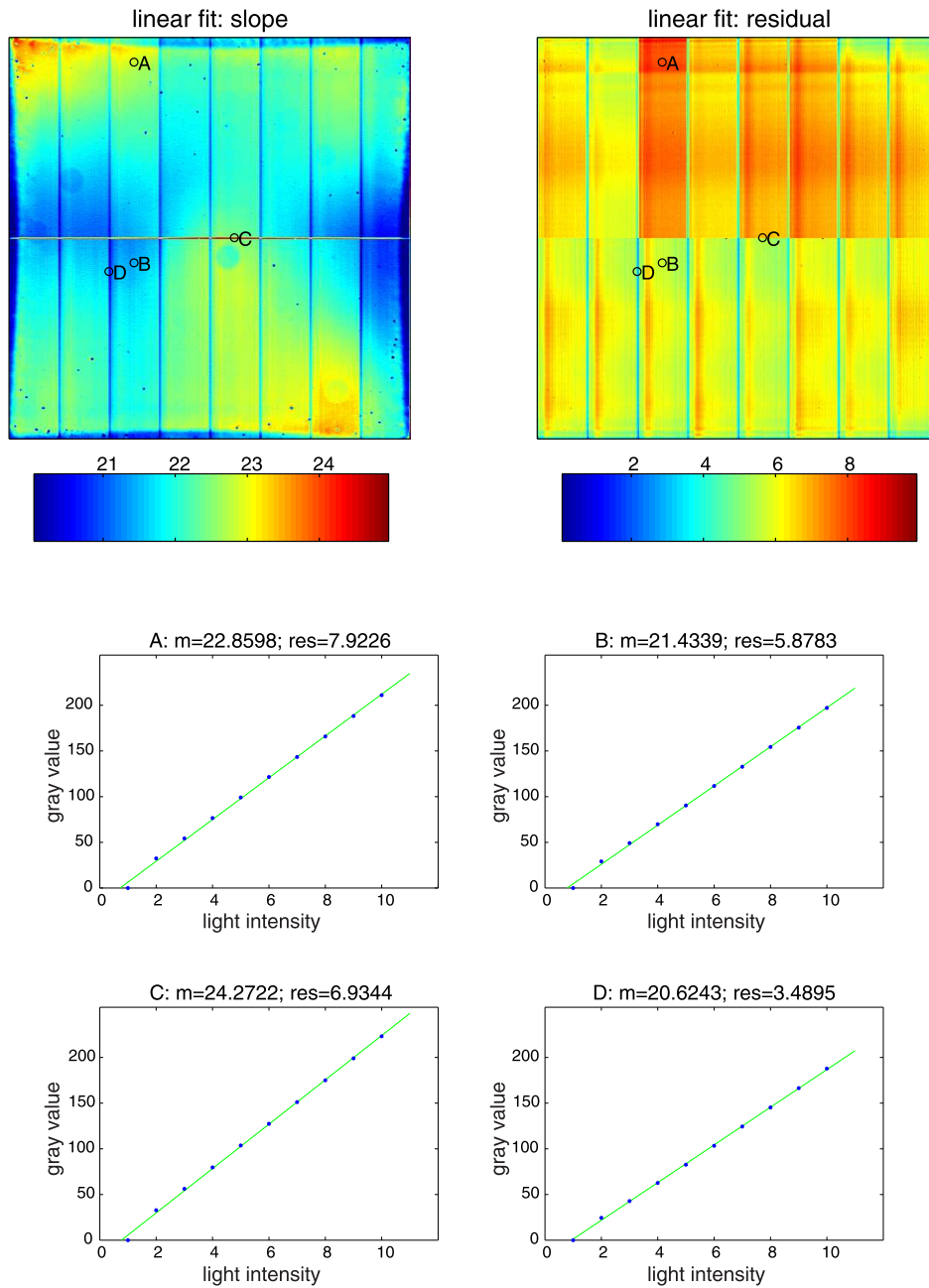
Figure 7.1: *Results of the investigation of the Camrecord 2000-camera sensor. Ten images of the Lambertian calibration standard were taken, gradually expanding the duty cycles of the illuminating LEDs. Top, left: Map of the slopes of the fits to the grey values. Note, that here the effects of variations in gain and illumination inhomogeneity are mixed. Top, right: Map of the residua of the fits. Impressively the irregularity among the sensor segments is demonstrated. The borders of the segments exhibit completely different slopes and residua in turn. Bottom: Samples of data points taken inside the sensor elements (A and B) and at the borders of the sensor elements (C and D).*
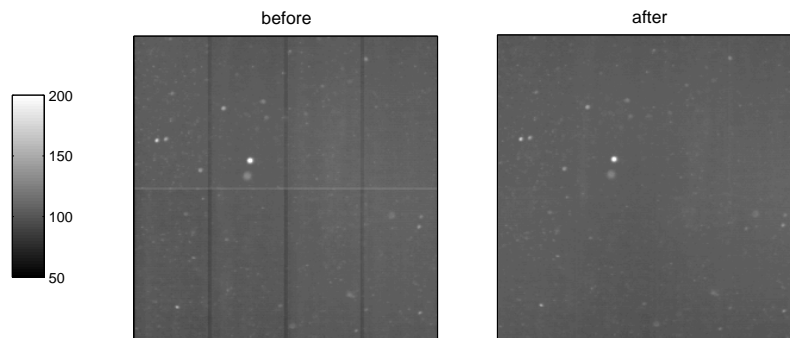
Figure 7.2: *Right: Result of calibration. The image quality has been improved considerably.*

There are two peculiarities of the Photonetics' frame transfer camera sensor, which have to be corrected by means of a radiometric camera calibration:

Gain and noise The sensor is divided into 16 individually controlled segments. Because each segment is adressed by its own amplifier, each segment has its own gain (which can be seen in Fig. 7.1, top, left). The noise, called "electronic noise", can be expressed as the variance of the grey values in the dark image $\sigma_0(i,j)$ and is composed of readout noise, amplifier noise, thermal noise, dark current and quantisation noise. Each segment also has its own noise characteristic, see Fig. 6.15, left.

Linearity Ideal linear camera sensors transform the incoming number of photons (called the "intensity") linearly into a charge, and further linearly into a voltage (called the "grey value"). Real cameras, so the Camrecord 2000, differ from this behaviour, which becomes evident from looking at Fig. 7.1, top, right.

The response of the camera chip to light of varying intensity was investigated. In order to do this, a Lambertian calibration standard was imaged. Starting with a dark image, the duty cycle of the illuminating LEDs was gradually expanded and an image sequence was taken in each case. In order to suppress noise, the image sequences were averaged, yielding a floating point image for a specific duty cycle. So the dependency of the grey value was obtained from the intensity at each pixel $g_I(i,j)$, where the intensities are not continuous, but sampled at ten points only. By applying a linear ordinary least squares fit to the measured data, we obtain a measure for the gain (together with the effect of inhomogeneous illumination), which is the slope of the line of best fit. The goodness of fit, which can be expressed by the residuum, denotes the deviation from linearity. Figure 7.1 shows the result of this procedure.

The approach for a combined radiometric calibration and illumination correction is as follows: By acquiring a sequence of reference images, we have the grey value–intensity dependency at distinct intensities. The goal is now to obtain the true intensity, corresponding to *every* grey value, which may differ from pixel to pixel. The algorithm consists of two steps: First, the gaps between the sampled intensities are filled continuously by piecewise linear interpolation. Then
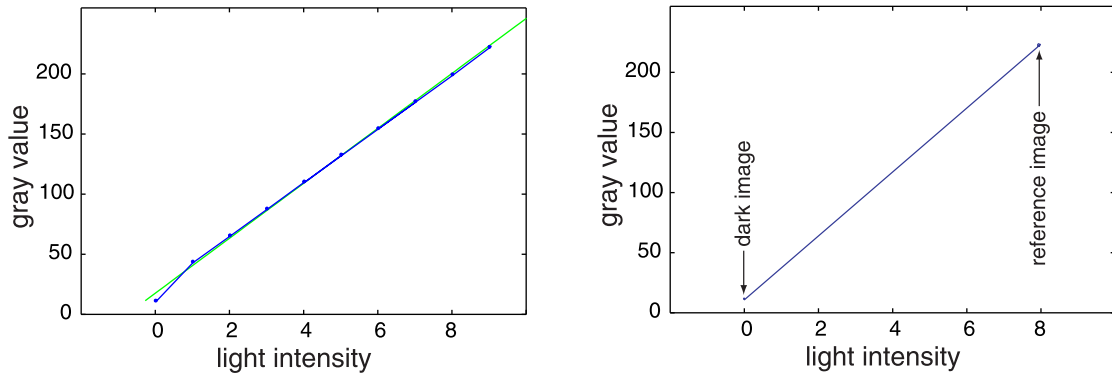
Figure 7.3: *Dependency grey value–intensity $g(I)$ in one selected pixel. Left: Multi-point calibration. Right: Two-point calibration.*

the dependency is inverted, so, that it yields the true intensity, given the grey value.

$$g_I(i,j) \xrightarrow{\text{interpolation}} g(I;i,j) \xrightarrow{\text{inversion}} I(g;i,j)$$

We end up with a data cube of dimensions $256 \times n_x \times n_y$, where n_x and n_y are the numbers of pixels in both directions. This kind of "brute-force" calibration may have the disadvantage of high memory-usage, especially using high-resolution sensors. We note, that using spline interpolation, we could eventually improve the efficiency of this approach.

7.1.2 Illumination Correction

As already mentioned, the Basler A641f camera, which is used in the convection tank experiments, contains a high quality (low temporal noise, no fixed pattern noise, good linearity) sensor. Thus the images, taken by this camera, need not to be corrected radiometrically, but only an illumination correction has to be performed. In order to do this, we a two-point-correction was chosen.

Inhomogeneous illumination affects *multiplicatively* the imaged objects. So we have to *divide* by a reference image, if we want to correct the images with respect to illumination. We have two opportunities to acquire a reference image:

1. A reference image can be recorded using a Lambertian calibration standard from which can be assured, that light is reflected homogeneously and isotropically everywhere in the field of interest.
2. We assume, that our recorded objects, the particles, have - statistically averaged - Lambertian reflection properties. Now we can construct an artificial reference image by calculating an averaged image from the sequence. Note, that this method only works, if we have no background in the image.

Because we have a non-zero dark image, we have to subtract it from both, the image to be corrected, and the reference image. One can write down following formula, in order to get the
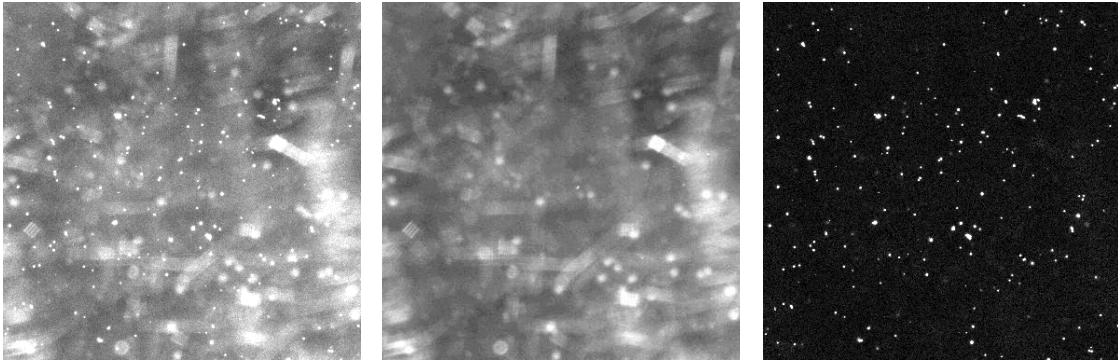
Figure 7.4: *Background subtraction. Left: Sample image from sequence. Center: Minimum image (i. e. background). Right: Subtracted image.*

corrected image $g'(i,j)$ from the original image $g(i,j)$:

$$g'(i,j) = \langle r(i,j) \rangle \frac{g(i,j) - d(i,j)}{\mathcal{B}(r(i,j)) - d(i,j)}.$$

Here $r(i,j)$ is the reference image and $d(i,j)$ is the dark-image. Because the reference image may have a inhomogeneous small-scale structure, it is smoothened with a Gaussian $\mathcal{B}$ of high order. To normalise the resulting image, it is multiplied with a constant, which is chosen to equal the spatially averaged reference image.

Note that this action is just a special case to the more general procedure, described in the previous section: The function $g(I,i,j)$ displayed in Fig. 7.3, left, now is reduced to a straight line, with its endings being grey value in the dark-image and grey value in the reference image, see Fig. 7.3, right.

7.1.3 Background Correction

The recorded image sequences always exhibit some kind of background, which interferes with the feature extraction. In contrast to inhomogeneous illumination, the background does not affect the objects of interest multiplicatively. The background contributes rather *additively* to the overall intensity, so that we have to subtract the background.

There are two ways to obtain a background image:

1. We can record an image, where no particles are added to the fluid, but with the same conditions as in the experiment (same concentration of the absorbing fluid, same position, same water gauge). Sometimes this is not possible.

2. Assuming, that all particles of interest are moving at least about their diameter while the duration of the sequence, the minimum image should equal the background image. One gets the minimum image, if one sorts the grey values of the sequence pixel for pixel, and take the lowest grey value at each pixel:

$$g_{\min}(i,j) = \min(g_1(i,j), g_2(i,j), \dots, g_N(i,j)),$$

where $g_k(i,j)$ denote the grey value at position (i,j) in frame k of an image sequence of length N.

7.2 Segmentation

Segmentation in our context means the separation of the objects of interest, the tracer particles, from the background and from each other. Segmentation can be regarded as one necessary step to the extraction of features like center of gravity or representative grey value of a particle. Input object of the segmentation process is an eight-bit image, which has undergone the preprocessing, described in section 7.1. Output object will be a binary image, in which the object pixels are marked with the value one and the background pixels are marked with the value zero. Starting from this binary image, the particles can be labeled and image features can be extracted.

According to [Jähne, 2002] there are four different approaches for segmentation:

Pixel-based methods This simplest segmentation method is based on grey value thresholding. Pixels with a grey value greater than a certain threshold are assigned to the particle class, otherwise they are assigned to the background class. We will introduce a threshold operator $T_{[t_1,t_2]}$, which acts on the grey-valued image and yields a binary image:

$$T_{[t_1,t_2]}(g(i,j)) = \left\{ \begin{array}{ll} 1: & t_1 < g(i,j) < t_2 \\ 0: & \text{otherwise} \end{array} \right.$$

A lower respectively upper threshold $[t_1, t_2]$ can be determined by the user arbitrarily, or it can be set by the machine based on *a priori* knowledge, like camera noise, or considering the bimodality of the histogram. One problem of grey value thresholding is, that depending on the choice of the threshold, objects may appear more or less large.

Edge-based methods Edges can be detected by first- or second-order derivative operators like the Sobel- or Laplace-filter. Again, we have to apply a threshold to select the edges. Then we have to connect the edges of an object in such a way, that they are unique and closed. One can imagine, that such a contour-tracking algorithm may be very sophisticated, especially, when we have the case, that objects overlap each other. Edges define the borders of an object uniquely, so that we don't suffer from ambiguities concerning the object-size, like using grey value thresholding.

Region-based methods These methods use *a priori* knowledge of the object in such a way, that we demand connectivity of an object. Here connectivity means, that the decision, if one pixel belongs to the object class or to the background class depends on the classification of its neighbours. Section 7.2.2 describes the region-growing algorithm, which is a region-based method containing model-based elements in our implementation.

Model-based methods Here a priori information about the shape of an object is given. For example, we assume, that particles have to look like Gaussians. Because no model fits perfectly to reality, we have to decide on the basis of the residual, a number, which describes the goodness of fit, whether the candidate belongs to the object or to the background class. We will investigate Gaussian fitting further in section 7.2.3.
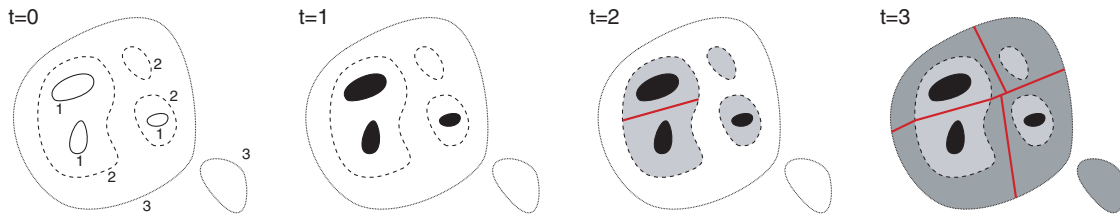
Figure 7.5: *Watershed transformation: Flooding process at different time instants. At time $t = 1$ the lowest basins, marked with the level curve 1, are filled. At time $t = 2$ the water rises to level curve 2. To prevent the lakes stemming from two basins from merging, a dam is built. At time $t = 3$ rising of the water continues and more dams are built.*

7.2.1 The Watershed Transformation

In both employed segmentation approaches, the model-based method and the region-based method, we make use of the watershed transformation, a very valuable tool for segmentation, which has its origins in morphological image processing. So in our application, the watershed transformation is no segmentation procedure on its own, but forms a constituent to both of the selected segmentation techniques, which are region growing (section 7.2.2) and fit of gaussians (section 7.2.3).

We consider an image g as a topographic surface and define the "catchment basins" and the "watershed lines" by means of a flooding process. Imagine, that each minimum of this surface is filled up with a constant vertical speed, so that "lakes" arise. During the process of flooding, two or more lakes coming from different minima may merge at a particular line. By building a "dam" on this line, we prevent the lakes from merging. These dams define the watersheds of the topographic surface, respectively of the image.

Figure 7.5 shows the flooding process at four different time instants $t = \{0, 1, 2, 3\}$. The grey value image is displayed in level curve representation.

The constant vertical speed is chosen in such a way, that every time step the water level rises about the height interval between two adjacent level curves. At $t = 1$ the regional minima at the lowest level are filled. By further rising the water level, we have to build a dam between two of the minima. This dam is the curve, which has exactly the same distance to the adjacent minima. With increasing water level, more and more dams are built.

We can formulate this process mathematically. Here X_t denotes the area, which is already flooded at a time instance t.

1. $X_1 = T_1(g)$
2. $X_{t+1} = R_{t+1}(g) \cup I_{T_{t+1}(g)}(X_t) \quad \text{for} \quad 1 \leq t \leq N$

Here $R_t(g)$ are the regional minima of g at level t, and $I_X(Y)$ are the influence zones of the various sets X within the set Y. T_t is a threshold operator, which yields a binary image consisting of pixels with grey value t.

Finally, the set of the watersheds is defined as the complementary set to X_N, where N is the top level of the topographic surface g. Before applying the watershed transformation to a particle image, it has to be inverted. Results of the watershed transformation are displayed in Fig. 7.9, center.
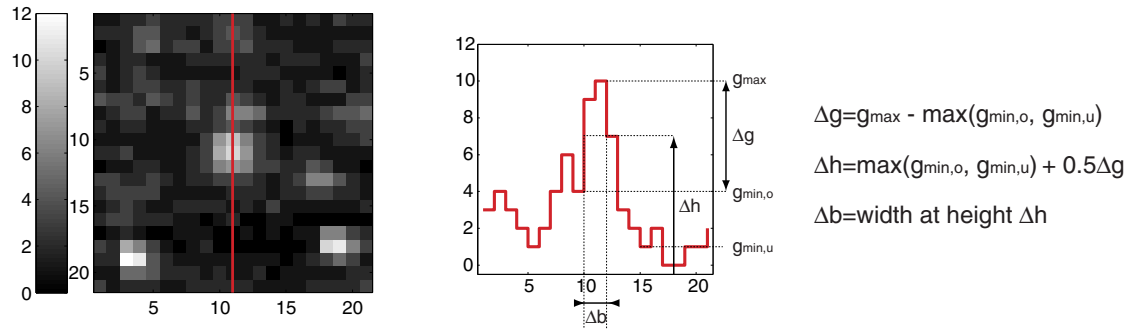
Figure 7.6: *Estimation of the width of a grey value peak Δb and of the grey value contrast Δg: Δb is the difference between the maximum grey value (g_{max}), and the brightest of the adjacent minimal grey values of the particle ($max(g_{min,o}, g_{min,u})$). Δb is the width of the particle at a height Δh, where Δh is defined as the sum of $max(g_{min,o}, g_{min,u})$ and $1/2\Delta g$.*

7.2.2 Region Growing

The watershed transformation exhibits the disadvantage, that images tend to be oversegmented, resulting in many false positives. This occurs mainly because of the presence of noise in the image, which introduces many additional local minima in the topographic surface g. Isotropic presmoothing of the image may reduce the noise, but also it will blur the dams, especially between adjacent particles.

Region growing, in the form presented here introduced by [Hering et al., 1995a], is a somehow more heuristic approach to satisfy the characteristics of particle images:

1. We compute the regional maxima of the image using an 8-connected neighbourhood. I. e. all pixels are selected, which appear maximal in a 3×3-shifted window. These pixels may serve as *candidates* for the regions.
2. Using the minima in the neighbourhood of the candidate, a measure for the width of the grey value peaks Δb and for the contrast of the grey value Δg can be estimated (see Fig. 7.6). A candidate becomes a *seed*, if Δb is in a certain range, and if Δg exceeds a predefined threshold, which may depend on the noise of the image.
3. The seeds serve as markers for the watershed transformation ([Beucher, 1991]): Only the basins become particles, which contain a seed, otherwise they are discarded.

Once we have segmented the particles from the background and from each other, it is easy to extract relevant parameters, like

- Representative grey value of a particle like
  - maximum grey value g_m,
  - fitted grey value g_f (see section 7.2.3) or
  - integral grey value $g_s = \sum_{i \in P} g_i$, where P denotes the pixels in the segmented particle.
- Area of the particle $\sum_{i \in P} 1$.
- Position of the particles, as a result from the fit $(\hat{\mu}_x, \hat{\mu}_y)$, or by calculating the particle's
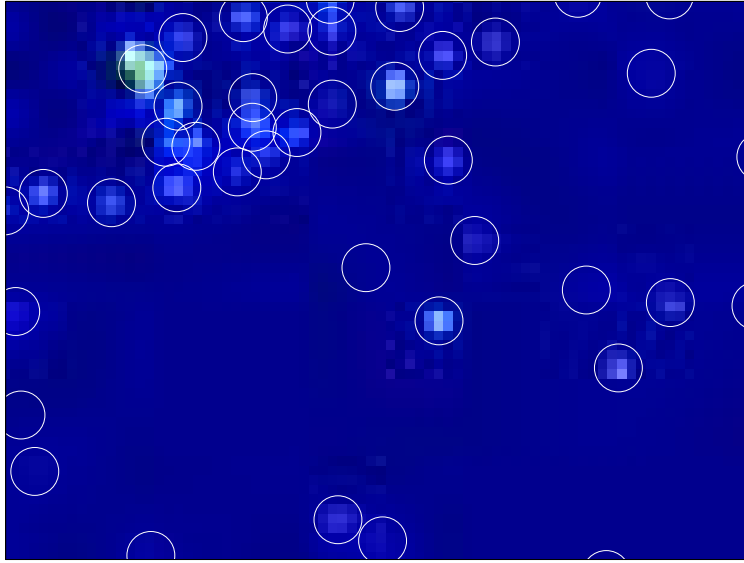
Figure 7.7: *Results of the segmentation process: Every circle indicates a segmented particle. Note, that our algorithm is capable of separating clustered particles*

centroid:
$$(x_c, y_c) = \frac{1}{\sum_{i \in P} g_i} \left(\sum_{i \in P} g_i x_i, \sum_{i \in P} g_i y_i \right)^T.$$

- Second order moments of the particle:
$$\mu_{20} = \sum_{i \in P} (x_i - x_c)^2 g_i, \quad \mu_{02} = \sum_{i \in P} (y_i - y_c)^2 g_i, \quad \mu_{11} = \sum_{i \in P} (x_i - x_c)(y_i - y_c) g_i.$$

The second order moments correspond to the inertia tensor in mechanics and can be consulted in order to get a measure for the eccentricity of an object.

7.2.3 Fit of Gaussians

Tracer particles always exhibit the same shape on the image: small, circular blobs with the maximum grey value in the middle and decreasing intensity to the border. We can benefit from this characteristic by developing a physically motivated model, which has to be fitted to the imaged particles. A similar fit function is applied by [Leue et al., 1996] to segment particle streaks.

According to Babinet's principle, the diffraction of light at a spherical disk exhibits the same pattern on a screen as the diffraction at a spherical aperture, which is the Airy function (assuming Fraunhofer diffraction):
$$I(\rho, \phi) = \left(\frac{2 J_1(ka\rho)}{ka\rho} \right)^2 I_0,$$

where k is the wave number of the light, a is the disk's radius and J_1 denotes Bessel's function of first order (for a plot see Fig. 7.8, red curve). Because of its isotropicity, the two-dimensional Airy function only depends on the radial coordinate ρ, and not on the azimuth ϕ: $I(\rho, \phi) \equiv I(\rho)$.
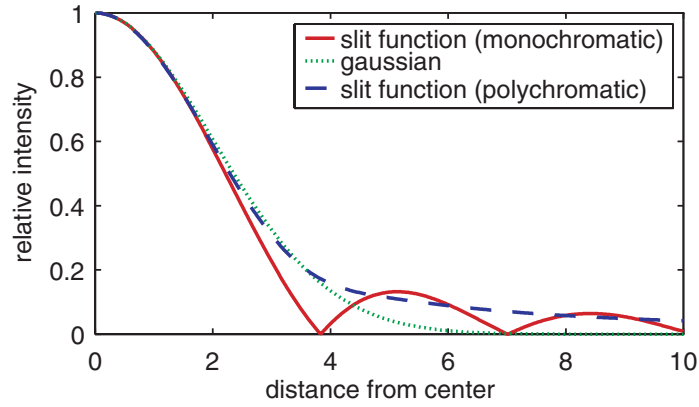
Figure 7.8: *Comparison of the one-dimensional Airy-function (also known as slit-function), using a single wavenumber (monochromatic), a spectrum of wavenumbers (polychromatic), and its Gaussian approximation (from [Leue et al., 1996]).*

Because the diffraction pattern of polychromatic light is a superposition of Airy functions (Fig. 7.8, blue curve), the secondary maxima of the Airy function become irrelevant. A Taylor expansion of $\ln I(\rho)$ yields:

$$\ln I(\rho) = \ln(I_0) - \left(\frac{ka\rho}{2}\right)^2 + O(\rho^4),$$

which legitimates a Gaussian (Fig. 7.8, green curve), as a good approximation of the diffraction pattern of a tracer particle:

$$I_\sigma(\rho) = I_0 \exp\left(-\frac{1}{2}\left(\frac{\rho}{\sigma}\right)^2\right),$$

with $\sigma = \sqrt{2}/(ka)$ being the standard deviation of the Gaussian.

Using Cartesian coordinates and after setting the particle's origin to an arbitrary location (μ_x, μ_y) the Gaussian becomes the final fit function, which reads

$$g_{\mu_x,\mu_y,\sigma}(x,y) = \frac{c}{\sqrt{2\pi}\sigma} \exp\left(-\frac{1}{2\sigma^2}\left((x-\mu_x)^2 + (y-\mu_y)^2\right)\right). \tag{7.1}$$

The segmentation process consists of following steps (see Fig. 7.9):

1. A binary threshold operator $T_{[t_{\min},255]}$ is applied to the grey value image. A low threshold $t_{\min}$ is chosen, to catch as many particles as possible.

2. To identify and separate overlapping particles, the watershed operator is applied to the grey value image. The binary output of the watershed operator is constructed in the way, that one correspondends to basins, and zero correspondends to watersheds. It is multiplied with the result of the threshold operator. The result itself is multiplied with the original grey value image, which serves as input for the optimisation.
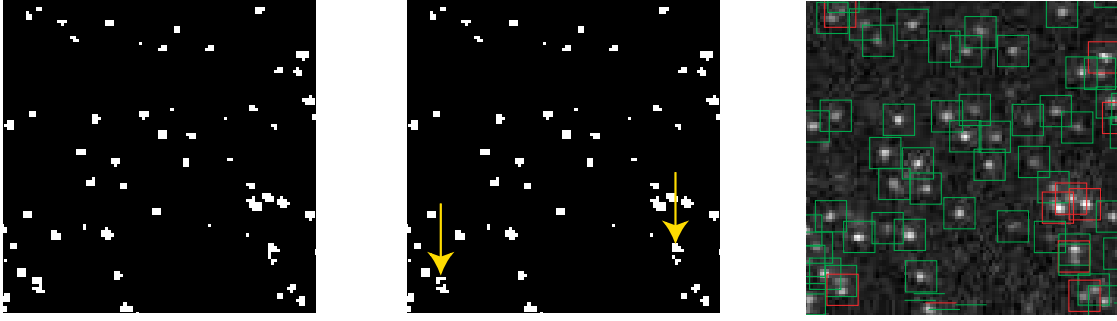
Figure 7.9: *Segmentation by using the model-based Gaussian fit method. Left: Binary image after grey value thresholding. Center: We applied a watershed transformation to the original eight-bit image and multiplied the watershed image with the binary image. Objects divided by watersheds are signalised by the yellow arrows. Right: After applying Gaussian fits to the presegmented objects, we grouped the particle candidates belonging to the particle class (green), or not-particle class (red) by means of the residual of the fit.*

3. The data is fitted to the model function Eq. (7.1). We choose a support of 3×3, 5×5 or 7×7 pixel^2 about the brightest pixel of each presegmented particle. Using the coordinates of the brightest pixel and $\sigma = 1$ as starting parameters, the model function is optimised according to the data. As optimisation routine, we apply the nonlinear Levenberg-Marquardt-fitting algorithm, described in [Press et al., 1992]. c is set to the integral of the presegmented particle, and is held constant during the optimization:

$$\hat{\mu}_x, \hat{\mu}_y, \hat{\sigma} = \min_{\mu_x, \mu_y, \sigma} g_{\mu_x, \mu_y, \sigma}(x, y).$$

Besides of the optimised center of the particle $(\hat{\mu}_x, \hat{\mu}_y)$ and a measure for the width of the particle σ, the optimisation routine yields the residual. We use this criterion to distinguish between particle-class (whose shape is assumed to be approximately Gaussian) and non-particle-class.

We also can estimate a maximum grey value of the particle from the fit parameters by evaluating $g(\hat{\mu}_x, \hat{\mu}_y, \hat{\sigma}) \equiv g_f$. However, the maximum grey value, estimated with this method, seems to be unstable: We fitted a Gaussian to one and the same particle, varying the support from 3×3 up to 7×7 pixel^2. While the optimised center $(\hat{\mu}_x, \hat{\mu}_y)$ does not change a lot there are huge discrepancies in the evaluated maximum grey value. [Marxen et al., 2000] proposes, that – for center estimating – a support of 3×3 pixels would be enough. Addressing the estimation of a maximum grey value, this is definitely not correct, as illustrated in Fig. 7.10.

7.3 Velocity Estimation

In the presented technique, correlation of particle patterns (like in PIV) is not feasible for velocity estimation, because the image sequences typically consist of many layers of particles, each one moving with its own speed. Besides that, particles may move in direction orthogonal to the image plane, commonly referred to as "out-of-plane motion". We make use of an extended optical-flow based approach, in order to obtain the motion of individual particles.
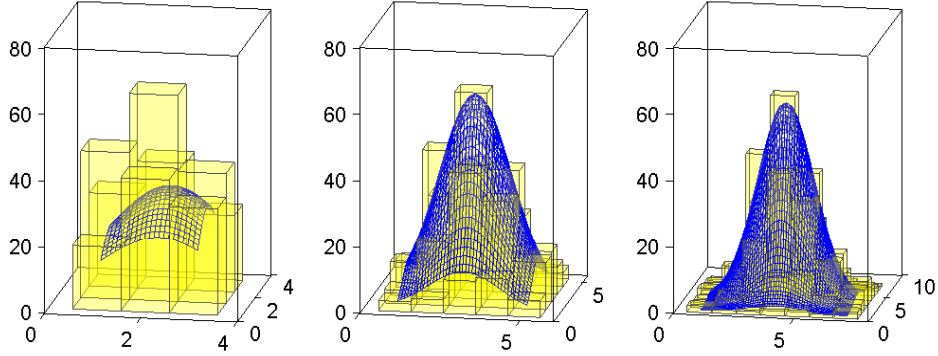
Figure 7.10: *Influence of the support on the the fit-results. Left: Support is $3 \times 3\,pixels^2$, maximum grey value is $g_f = 32.09$. Center: Support is $5 \times 5\,pixels^2$, $g_f = 60.35$. Right: Support is $7 \times 7\,pixels^2$, $g_f = 59.13$.*

In order to estimate a particle's velocity here two cases are considered. First we assume that the suspended particles move parallel to the wall, so that z won't change. The grey value then remains constant for all times, and we can apply the brightness change constraint equation (BCCE) to obtain the optical flow:

$$\frac{\mathrm{d}g}{\mathrm{d}t} = (\nabla g)^T \boldsymbol{f} + g_t = 0 \ .$$

The optical flow represents the components of the particle's velocity parallel to the wall: $\boldsymbol{f} = (u, v)^T$.

Secondly if the particles do not move parallel to the wall, i.e. with z not constant, the grey values will change with time in a Lagrangian frame of reference (see section 2.1.1), according to:

$$\frac{\mathrm{d}g}{\mathrm{d}t} = -g_0 \frac{1}{z_*} \frac{\mathrm{d}z}{\mathrm{d}t} \exp(-z/z_*) = -\frac{1}{z_*} \frac{\mathrm{d}z}{\mathrm{d}t} g = -\frac{w}{z_*} g, \tag{7.2}$$

We find, that, identifying w/z_* with the relaxation constant κ, the brightness change in this special case can be modeled by an exponential decay (see Eq. (4.28)). Note that we expressed the temporal change of the z-coordinate by the out-of-plane velocity-component w. We reformulate Eq. (7.2) in such a way, that it resembles a three dimensional brightness change constraint equation:

$$ug_x + vg_y + wg/z_* + g_t = (\tilde{\nabla} g)^T \boldsymbol{u} + g_t = 0, \tag{7.3}$$

where $\tilde{\nabla} = (\partial/\partial x, \partial/\partial y, 1/z_*)^T$ is an augmented gradient and $\boldsymbol{u} = (u, v, w)^T$ is the three-component flow vector to be estimated. g_x means the partial derivative of the grey value g with respect to x.

This can be written as a product of data matrix $\boldsymbol{D}$ and parameter vector $\boldsymbol{p}$, which expresses some kind of basic TLS-equation (see Eq. (A.1)). The ith row of the data matrix $\boldsymbol{D} = (\boldsymbol{d}_1, \boldsymbol{d}_2, \dots, \boldsymbol{d}_n)$ contains the components:

$$\boldsymbol{d}_i = (g_{xi}, g_{yi}, g_i, g_{ti}/z_*).$$

We construct the structure tensor by applying the left- (see A.3) and right- (see A.4) handed weighting matrices ($\boldsymbol{W}_L$ and $\boldsymbol{W}_R$) to $\boldsymbol{D}$ and computing the product with its transpose:

$$
\begin{aligned}
\boldsymbol{J} &= (\boldsymbol{W}_L \boldsymbol{D} \boldsymbol{W}_R)^T (\boldsymbol{W}_L \boldsymbol{D} \boldsymbol{W}_R) \\
&= \begin{pmatrix}
\langle g_x, g_x \rangle_{11} & \langle g_x, g_y \rangle_{12} & \langle g_x, g \rangle_{13}/z_* & \langle g_x, g_t \rangle_{14} \\
\langle g_x, g_y \rangle_{12} & \langle g_y, g_y \rangle_{22} & \langle g_y, g \rangle_{23}/z_* & \langle g_y, g_t \rangle_{24} \\
\langle g_x, g \rangle_{13}/z_* & \langle g_y, g \rangle_{23}/z_* & \langle g, g \rangle_{33}/z_*^2 & \langle g, g_t \rangle_{34}/z_* \\
\langle g_x, g_t \rangle_{14} & \langle g_y, g_t \rangle_{24} & \langle g, g_t \rangle_{34}/z_* & \langle g_t, g_t \rangle_{44}
\end{pmatrix},
\end{aligned}
$$

using the abbreviation

$$
\langle a, b \rangle_{ij} = \int_{-\infty}^{\infty} w(\boldsymbol{x} - \boldsymbol{x}', t - t') a(\boldsymbol{x}', t') b(\boldsymbol{x}', t')/(\sigma_i \sigma_j) \mathrm{d}\boldsymbol{x}' \mathrm{d}t'. \tag{7.4}
$$

Note, that here we included the multiplications with the entries of the right handed matrix $\boldsymbol{W}_R = \mathrm{diag}(1/\sigma_i)$ for the purpose of equilibration, as stated in A.4. The reason for this is, that in general the noise of the derivatives of the grey values is different from the noise of the grey values themselves.

After constructing the structure tensor and performing Eigenvalue analysis (according to section 4.2.3), the parameter vector is given by the Eigenvector $\boldsymbol{r}_4$ belonging to the smallest Eigenvalue λ_4:

$$
\boldsymbol{p} = (u, v, w, 1) \equiv \frac{1}{r_{44}} (r_{41}, r_{42}, r_{43}). \tag{7.5}
$$

Besides of the parameter vector containing the sought velocities, the presented technique yields confidence measures characterising the structure of the local spatio-temporal neighbourhood, which was used as an input to the structure tensor. There are various types of confidence measures, which can be applied. For a detailed overview see [Jähne, 2002; Spies, 2001]. For our purpose we use following two measures:

Measure of certainty As a measure of the overall changes of the grey values we select the mean square of the spatial gradient, which is the upper left 2×2 part of the structure tensor, derived in this section. According to [Jähne, 2002] this measure is invariant with respect of the determined velocity:

$$
c_c = \langle g_x, g_x \rangle_{11} + \langle g_y, g_y \rangle_{22}.
$$

Total coherence measure An additional measure enquires, whether our model fits to the assumption, that there a local neighbourhood with constant velocity is present. Because for such a motion we require the third Eigenvalue to be approximately zero, a normalised total coherence measure can be defined by

$$
c_t = \left(\frac{\lambda_1 - \lambda_4}{\lambda_1 + \lambda_4} \right).
$$

Due to the structure of the particles (which are circular and of width of only a few pixels), it is guaranteed, that we do not suffer from the aperture problem, mentioned in 4.1. Thus we do not need a coherence measure, which quantifies spatially oriented motions (i.e. the presence of an aperture problem), and we can rely on Eq. (7.5) to be the correct solution for the flow. On the other hand, there may be a motion discontinuity in our neighbourhood (stemming from particle overlappings), which can be detected by applying the total coherence measure.

7.4 3D-Position Estimation

The depth of the particles can be reconstructed according to Eq. (5.4) for the *method of one wavelength*

$$z = z_*(\ln g_0 - \ln g),$$

or according to Eq. (5.5) for the *method of two wavelengths*

$$z(g_1, g_2) = \frac{z_{*1} z_{*2}}{z_{*1} - z_{*2}} \left(\ln \left(\frac{g_1}{g_2} \right) + \ln \left(\frac{g_{02}}{g_{01}} \right) \right).$$

Here g, g_1 and g_2 are the representative grey values of the particle, which can be the maximum grey value, the maximum of a Gaussian fit, or the integral grey value (see 7.2.2).

7.5 Correspondence Analysis and Tracking

From the image sequence we obtain a dense 2D3C velocity vector field $(u(x, y), v(x, y), w(x, y))$, but the reality is in such a way, that the motion vector field is 3D3C $(u(x, y, z), v(x, y, z), w(x, y, z))$. Thus, we have to assign the motions to the particles in various depths.

This procedure ends in a list, where each particle is identified by a number and is attributed by center of mass, representative grey value and velocity. In the *method of one wavelength* we can deduce from the representative grey value to the true depth by means of calibration. This is not possible applying the *method of two wavelengths*. Here we have to find the correspondence of one and the same particle in two temporally neighboured frames. Our approach for this non-trivial task is explained in the next section.

7.5.1 Finding Correspondences

The simplest approach for finding correspondences is the nearest neighbour method, which assigns a particle i in the first frame to the particle j in the second frame, whose Euclidian distance

$$d_{ij} = \sqrt{(x_i - x_j)^2 + (y_i - y_j)^2}, \quad i = 1 \ldots N_1, \quad j = 1 \ldots N_2$$

is minimised, where N_1 and N_2 are the numbers of particles in the first, and in the second frame respectively. In our simple implementation the complexity is of $O(N_1 N_2)$, (i. e. roughly quadratic in the mean number of particles) because for every particle in the first frame the distance to every particle in the second frame has to be calculated in order to find the particle pairs with minimal d.

The nearest neighbour method works well in the case of the displacements from one frame to the next being small compared to the mean particle distance. Nevertheless, because in general the particles are distributed statistically, there may be misassignments: It may happen, that a particle in the second frame does not find any partner (1:0-correspondence), or that it finds more than one partners (1:n-correspondence). To solve this problem, we discard all 1:0- or 1:n-correspondences, so that only 1:1-correspondences survive.

By reducing the average distance between the corresponding particles in the first and second frame, the number of the 1:1-correspondences relative to the misassignments could be enlarged.
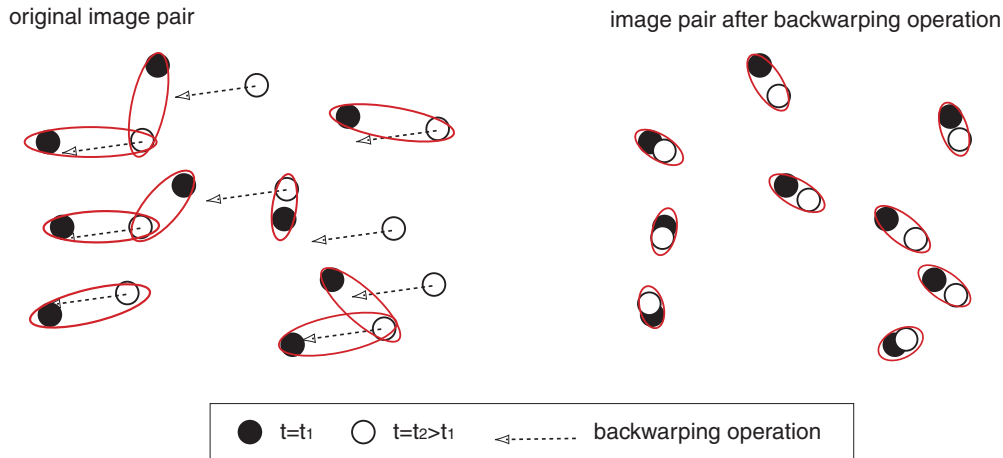
Figure 7.11: *Schematic illustration of the benefits of warping. Left: Unwarped image pair. The nearest neighbour approach yields misalignments and 1:0- or 1:n-correspondences. Right: The second image is warped towards the first image according to the plotted displacement vectors, which are obtained by applying the optical-flow based method.*

In order to do so, prior knowledge about the displacements from one frame to the next could be used, given by the optical-flow based velocity analysis.

Therefore, the particle positions in the second frame (x_j, y_j) are warped towards the positions in the first frame (x_i, y_i) by subtracting the displacements $(u_j(x_j, y_j), v_j(x_j, y_j))$ from (x_j, y_j):

$$(x'_j, y'_j) = (x_j, y_j) - (u_j, v_j).$$

Now the nearest neighbour method is applied, assigning a particle i in the first frame to the particle j in the warped second frame by minimising the Euclidean distance

$$d'_{ij} = \sqrt{(x_i - x'_j)^2 + (y_i - y'_j)^2}$$

between these particles. Additionally we impose an upper threshold for d' to inhibit unlikely 1:1-correspondences.

7.5.2 Particle Tracking

Correspondence analysis can be used for two types of tasks:

Depth estimation As already mentioned in section 7.3, using the *method of two wavelengths*, particles in the first frame (which can be the image, recorded with a wavelength of 455 nm, and which will be denoted as a-frame) have to be assigned to the corresponding particles in the next frame (for instance recorded with 470 nm-wavelength, and called the b-frame further on). Because the velocity vector field is determined using the same type of frames (e. g. a-frames), we have to subtract only *half* of the displacements in order to warp back the particle positions (see Fig. 7.13, green).
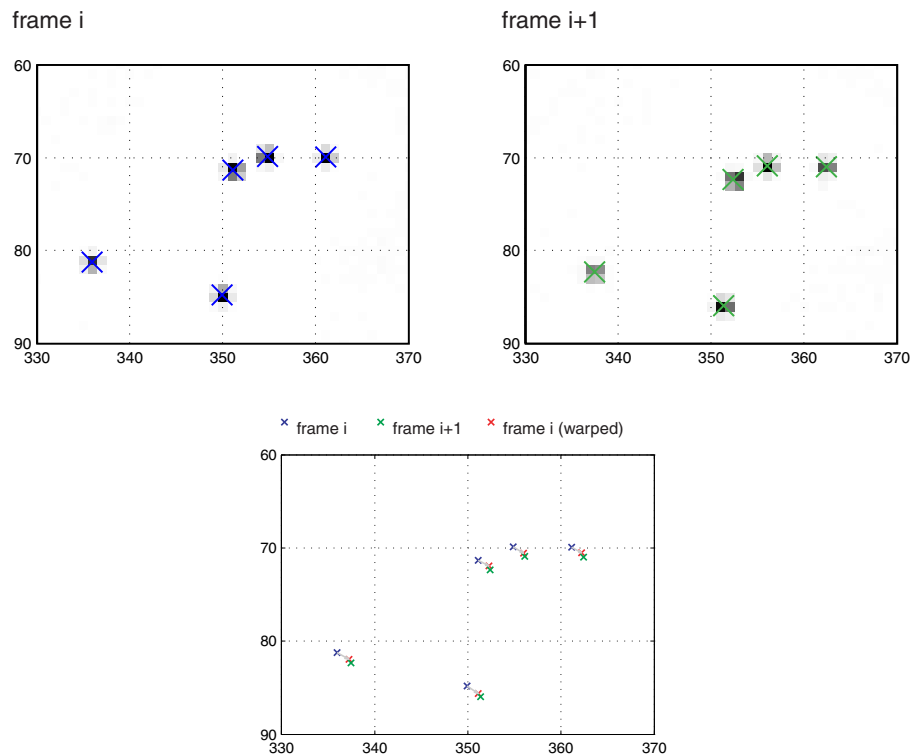
Figure 7.12: *Warping applied to real data. Top left: First frame, with centroids of the particles marked blue. Top right: Second frame, with centroids of the particles marked green. Bottom: The centroids of the first frame (blue) are warped towards the centroids of the second frame (green), yielding the red markers.*

Particle tracking Particle tracking is applied for several reasons: First, by extracting a path line of a moving fluid element (which is represented by a particle in good approximation), we get a Lagrangian representation of the flow. Secondly, we can use the trajectories for postprocessing: For example, we can connect two adjacent trajectories, which may be interrupted by missing frames, using the assumption of continuity of motion, or we can smooth the trajectories. Here a particle in the first frame (a-frame) is assigned to a particle in the next frame but one (again a-frame). Now we have to subtract the full displacements for warping back (see Fig. 7.13, blue).

We note, that a similar approach is made by [Cowen and Monismith, 1997], where information gained by previous cross-correlation was used to obtain a better performance for particle tracking.

7.6 Postprocessing

Once estimated the positions and velocities of the tracer particles, we have acquired an irregularly spaced 3D3C motion vector field. For further analysis we make use of the Lagrangian representation of the flow and of the continuity of the flow field.
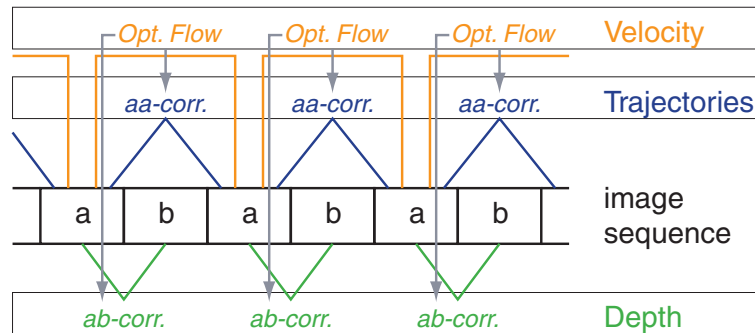
Figure 7.13: *Flow-diagram illustrating the extraction of velocity, depth and trajectories using optical flow and correspondence analysis. In this example, the optical flow (orange) is calculated from the a-frames. The depth (green) is computed from the representative grey values of corresponding particles in both a- and b-frames using the optical flow. The trajectories (blue) are obtained by establishing the correspondences between particles in the a-frames with the help of optical flow.*

7.6.1 Elongation of Trajectories

In the analysis, so far, we acquired information about the depth of a particle by converting grey value into position by means of Beer-Lambert's law. In the introduction of chapter 5 we have already adressed the fact, that this procedure yields only a depth map, i. e., that occluded objects become not visible. In our image sequences, occlusions occur everywhere where particles overlap each other. With increasing particle density overlappings are rather the rule than the exception.

**Detection of overlappings** We have investigated two methods of detection of overlappings. The first one uses the coherence measure, we get by the motion analysis (see section 7.3). Particle overlappings are closely related to discontinuities of motion occuring in the spatio-temporal window, from which the structure tensor is calculated. The second one uses the fact, that in order to do the particle tracking, 1:1-correspondences are required. If two particles overlap in the second frame, one particle in the first frame cannot be assigned to one single particle in the second frame uniquely. Therefore, the trajectory has reached its end.

Finding trajectory candidates Possible candidates for the elongation of a trajectory T_0 with end-particle in frame t are all trajectories $T_i, i = 1 \ldots N$ with start-particles between t and $t + \Delta t$, where Δt is a value for the maximum allowed length of time for a particle-crossing.

Trajectory matching We apply N ordinary least squares fits to the trajectory-pairs $\{T, T_i\}$, regarding the variables x, y and z. The residuals of the fits are measures, how good the trajectories match in the individual variables. By combining these measures to a score, one can give evidence if two trajectories belong to the same particle, or not.

Filling of the gap By adopting the fitted values in the temporal gap between a trajectory pair, two trajectories are merged to a new, long trajectory.

Figure 7.14 shows the process of trajectory elongation. For the sake of simplicity, the y-coordinate has been dropped using 1D sections of the frames. In the $x - t$-image, the spatio-temporal locations of the superpositions become clearly visible. By multiplying the original images with a mask generated from the coherence measure, the positions, where overlappings
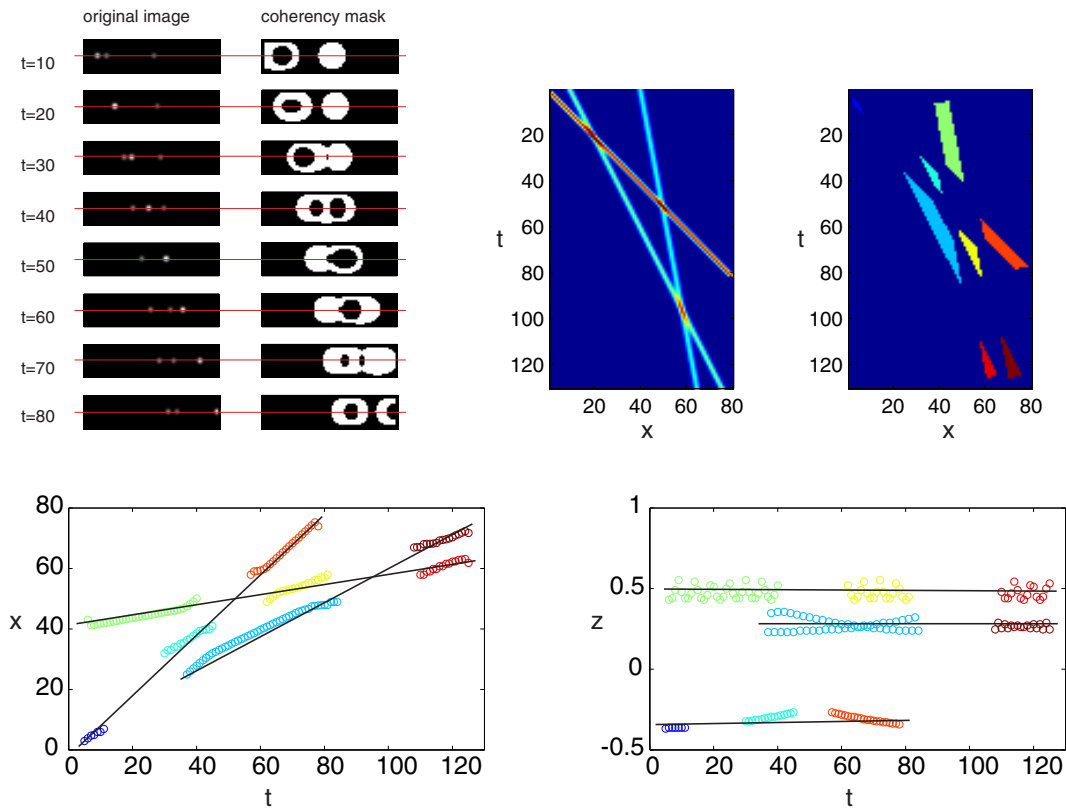
Figure 7.14: *Simple example, demonstrating our procedure to cope with overlappings and to elongate trajectories. Top, left: Some frames of the considered image sequence. A bright and fast particle "overtakes" two slow and dark particles. A horizontal line through the center of the particles was picked as a basis for a spatio-temporal $x - t$-image (top, center). Then a confidence measure from velocity analysis (here the trace of the upper left 2×2-part of the structure tensor) was used to exclude non-constant motion (top, right). Bottom: The sub-trajectories were matched both in $x - t$- and in $z - t$-space. From the residuals of the fits, a score was calculated.*

occur, can be excluded in the further analysis. Figure 7.14, bottom, shows the fits to the particles' x- and z- coordinates. By combining multiple features in a score, a greater stability of the fit can be reached.

Major disadvantage of this method is, that it imposes some thresholds, which have to be set based on empirical knowledge: We have to define a maximum Δt and we have to specify, how the different features are weighted against each other. Moreover, we have to set a limit for the score.

7.6.2 Smoothing of Trajectories

The accuracy of the determination of the z-coordinate suffers from the fact, that there is an error in determining the grey values due to the limited pixel size and the camera noise. This will be investigated in more detail later in section 8.2.4. Figure 7.15, left, shows a typical example how
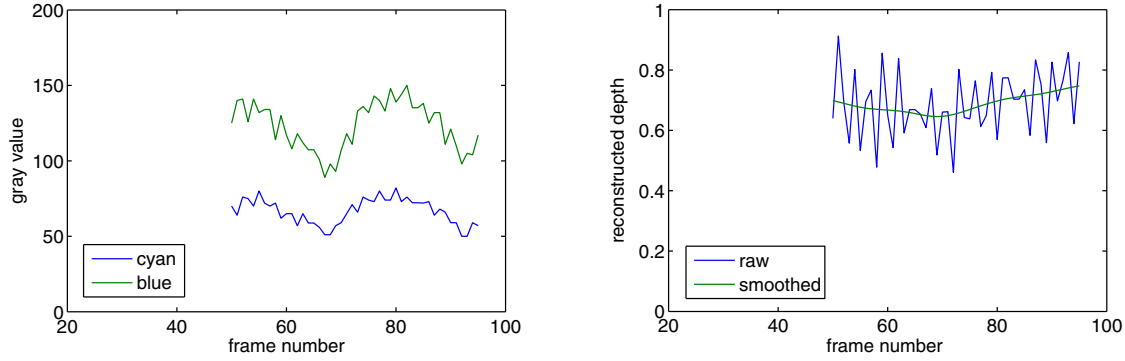
Figure 7.15: *Smoothing of a trajectory. Left: Grey values of one and the same trajectory recorded with cyan and blue light. Right: Directly calculated z-coordinate of this trajectory and smoothed version*

the grey values along a trajectory might look like. Smoothing is able to eliminate this kind of "noise" to a great extent. Therefore we applied a 1D Binomial-filter (e. g. $\mathcal{B}^8$) to the grey value-time series of both wavelengths. The borders of both time series can be zero-padded; this cancels out by division. An exemplary result of smoothing is shown in Fig. 7.15, right.

7.6.3 Calculation of a Dense Vector Field

For some hydrodynamical quantities (like vorticity, shear rate ordissipation rate), we need an equally spaced vector field. Moreover, this might be useful, when we want to compare our algorithms to other methods like classical PIV.

One has to interpolate in some manner to obtain a displacement vector in every point of an equally spaced grid. An overview over the classical methods is given in [Lancaster and Salkauskas, 1986]. A common technique, which is applied in fluid flow analysis, is the adaptive Gaussian windowing method (AGW) presented in [Agüi and Jimenez, 1987], which is a special case of the more general normalised convolution method by [Knutsson and Westin, 1993]. The interpolated vector field $\boldsymbol{v}_i$, $i = \{x, y, z\}$ at the equally spaced positions $\boldsymbol{x}_i$ can be calculated from the irregularly sampled velocities $\boldsymbol{u}_j$ at positions $\boldsymbol{x}_j$ by applying following procedure:

$$\boldsymbol{v}_i(\boldsymbol{x}_i) = \frac{\sum_{j=1}^{N} \boldsymbol{u}_j(\boldsymbol{x}_j) c(\boldsymbol{x}_j) \exp\left(-\frac{|\boldsymbol{x}_i - \boldsymbol{x}_j|}{\sigma^2}\right)}{\sum_{j=1}^{N} c(\boldsymbol{x}_j) \exp\left(-\frac{|\boldsymbol{x}_i - \boldsymbol{x}_j|}{\sigma^2}\right)},$$

where $c(\boldsymbol{x}_j)$ denotes the confidence of the measurement at the position $\boldsymbol{x}_j$, which is given by one of the confidence measures obtained by motion analysis (see section 7.3). Using Monte-Carlo simulations [Agüi and Jimenez, 1987] have shown, that the optimal width of the convolution window, which is given by σ, is directly proportional to the mean spacing between particles δ_2 resp. δ_3:

$$\sigma = \alpha\delta_2 = \alpha\sqrt{\frac{A}{\pi N}} \quad \text{for the 2D, and} \quad \sigma = \alpha\delta_3 = \alpha\sqrt[3]{\frac{V}{\pi N}} \quad \text{for the 3D case,}$$

with the proportionality constant α set to 1.24. Here N is the particle number, contained in the area A or volume V. The results of [Agüi and Jimenez, 1987] for the 2D case could be approved by [Hering, 1996] for the 3D case.

7.7 Estimation of the Wall Shear Rate using 3D Parametric Motion Models

In this section we will generalise the well-known concept of estimating the parameters of an *affine transformation* of the optical flow (see chapter 4.3.1) to the case of 3D. The knowledge of some of the components of the parametric motion model in 3D allows us to estimate the wall shear rate directly, without a previous calculating of the vector fields.

7.7.1 Parameterization of 3D Physical Flow Fields

In the following we consider 3D physical flow fields. We apply the notation $\boldsymbol{u} \equiv (u_1, u_2, u_3)^T \equiv (u, v, w)^T$ for the 3D velocity vector at the 3D position $\boldsymbol{x} \equiv (x_1, x_2, x_3)^T \equiv (x, y, z)^T$. A flow field $\boldsymbol{u}(\boldsymbol{x})$ can be extended to a first order Taylor series in the vicinity of $(\boldsymbol{x}_0, t_0)$:

$$u_i(x_j, t) \approx u_i(x_{j,0}, t_0) + \frac{\partial u_i}{\partial x_j} x_j + \frac{\partial u_i}{\partial t} t.$$

We made use of Einstein's summation convention, and i and j are defined from 1 to 3. In vector-matrix-notation this reads:

$$\boldsymbol{u}(\boldsymbol{x}, t) \approx \boldsymbol{s} + \Gamma \boldsymbol{x} + \boldsymbol{b}t,$$

where $\boldsymbol{s}$ is a 3D translation, $\Gamma = (\gamma_{ij}) = (\partial u_i / \partial x_j)$ is the 3×3-velocity gradient tensor which is essentially the Jacobian, and $\boldsymbol{b}$ is a 3D acceleration.

This 3D parametrization can be incorporated into the 3D-BCCE Eq. (7.3):

$$(\tilde{\nabla} g)^T \cdot (\boldsymbol{s} + \Gamma \boldsymbol{x} + \boldsymbol{b}t) + g_t = 0 \tag{7.6}$$

From the components of the matrix Γ important physical quantities of the local neighbourhood in the flow field can be computed, like

- the vorticity vector: $\omega_k = \epsilon_{ijk} \gamma_{ij}$,
- the strain rate tensor: $s_{ij} = 1/2(\gamma_{ij} + \gamma_{ji})$,
- the dissipation rate: $\epsilon = -2\nu \overline{s_{ij} s_{ij}} = -\nu \overline{(\gamma_{ij} + \gamma_{ji}) \gamma_{ij}}$.

For the interpretation of the velocity gradient tensor, which describes the kinematics of fluid motion up to first order, we also refer to the section concerning the Helmholtz theorem (section 2.1.2).

If we assume that we have pure 2D-flow $u = u(x, y)$, $v = v(x, y)$ and $w = 0$, Eq. (7.6) reduces to the optical flow-parametrization case (4.20).

Like in the case of 2D optical flow fields one can generalise the parametrization of 3D physical flow fields in the context of the Lie group of continuous transformations (see section B.2).
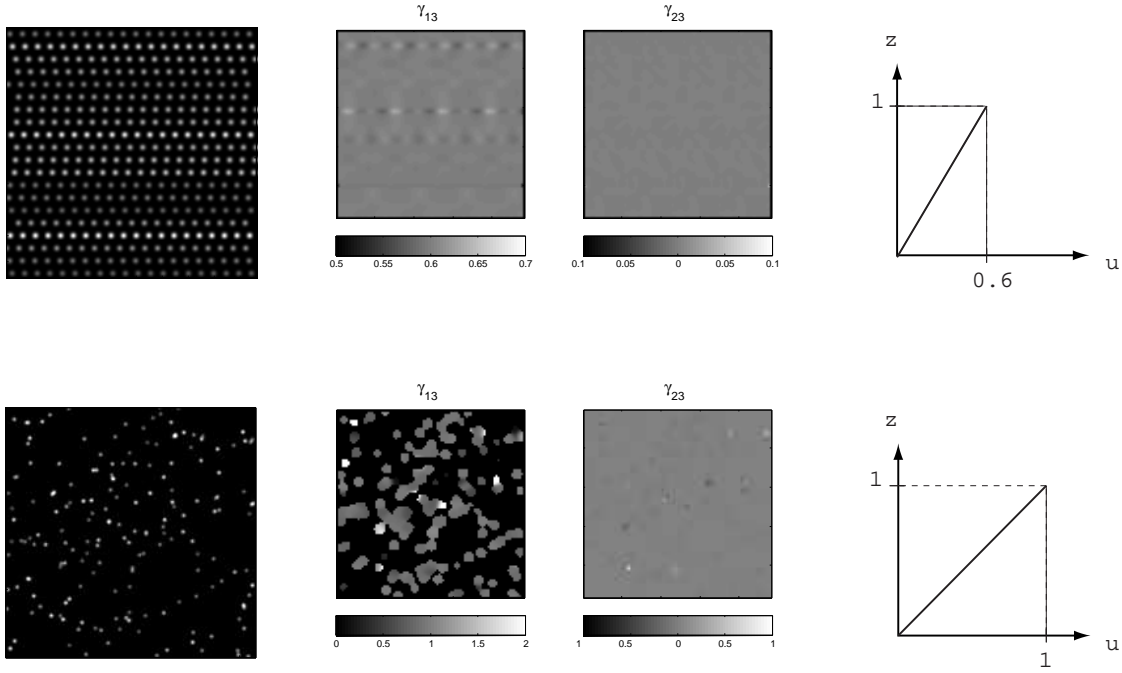
Figure 7.16: *Example images of the synthetic image sequences (left), maps of the wall shear rates estimated with our algorithm (center) and velocity profiles, which deliver the ground truth for the wall shear rates (right). The distinct image sequences are described in the text.*

7.7.2 Estimation of the Wall Shear Rate

In the previous section the parameter estimation of 2D image sequences underlying a 3D affine transformation was discussed. Now we will return to our applications: Besides knowing the velocity fields explicitly, it might be useful to know derived quantities, like vorticity, strain rate or dissipation rate. In particular, the wall shear rate is vitally important to get knowledge about the flow behaviour – e. g. to locate critical points of the flow.

In the following the case of uniform wall parallel shear flow is addressed, i. e. $u = u(z)$, $v = v(z)$ and $w = 0$. The only non-vanishing components of the velocity gradient tensor $\gamma_{ij} = \partial u_i / \partial x_j$ are

$$\frac{\partial u}{\partial z} = \frac{\partial u_1}{\partial x_3} = \gamma_{13} \quad \text{and} \quad \frac{\partial v}{\partial z} = \frac{\partial u_2}{\partial x_3} = \gamma_{23}.$$

Therefore the 3D-EBCCE (4.20) can be rewritten to

$$\widetilde{\nabla} g^T \cdot \left(0 + \begin{pmatrix} 0 & 0 & \gamma_{13} \\ 0 & 0 & \gamma_{23} \\ 0 & 0 & 0 \end{pmatrix} \cdot \begin{pmatrix} x \\ y \\ z \end{pmatrix} + 0 \right) + g_t = 0, \tag{7.7}$$

which can be transformed to a scalar product of the data vector $\boldsymbol{d}$ and the parameter vector $\boldsymbol{p}$ after some simple algebraic manipulations:

$$\boldsymbol{d} \cdot \boldsymbol{p}^T = (g_x z, g_y z, g_t) \cdot (\gamma_{13}, \gamma_{23}, 1)^T = 0 \ .$$

Starting from this scalar product, one can construct an expanded structure tensor, similar to the way presented in section 7.3:

$$\boldsymbol{J} = (\boldsymbol{W}_L \boldsymbol{D} \boldsymbol{W}_R)^T (\boldsymbol{W}_L \boldsymbol{D} \boldsymbol{W}_R) = \begin{pmatrix} \langle g_x z, g_x z \rangle_{11} & \langle g_x z, g_y z \rangle_{12} & \langle g_x z, g_t \rangle_{13} \\ \langle g_x z, g_y z \rangle_{12} & \langle g_y z, g_y z \rangle_{22} & \langle g_y z, g_t \rangle_{23} \\ \langle g_x z, g_t \rangle_{13} & \langle g_y z, g_t \rangle_{23} & \langle g_t, g_t \rangle_{33} \end{pmatrix} .$$

using the abbreviation Eq. (7.4). Again here we used equilibration, in order to weight the entries of the matrix $\boldsymbol{D}$ relative to their noise.

By performing an Eigenvalue decomposition we obtain an estimation for the parameter vector to

$$\boldsymbol{p} \equiv (\gamma_{13}, \gamma_{23}) = \frac{1}{r_{33}} (r_{31}, r_{32}),$$

where $\boldsymbol{r}_3$ is the Eigenvector belonging to the smallest Eigenvalue λ_3.

7.7.3 Application to Synthetical Data

To illustrate the procedure of estimating the wall shear rate directly and to highlight some of its limits, we applied Eq. (7.7) to synthetically generated data, where the ground truth is well known.

The following image sequences are generated by providing a uniform, wall-parallel 3D flow: $u(z) = \gamma_{13}z$, $v = w = 0$. The flow is texturised using Gaussian intensity distributions of equal maximum intensity and equal maximum variance, representing the particles. The z-position of the particles is indicated by attenuating the maximum intensity of the Gaussians according to Beer-Lambert's law Eq. (5.4).

The first synthetic image sequence contains particles, which are distributed in such a way, that they never will overlap each other: The particles are arranged in rows; each particle in one row having the same depth, and therefore the same brightness and the same speed (Figure 7.16, top, left). Here the wall shear rate γ_{13} is exactly 0.6, which is indicated by the profile $u(z)$ (Fig. 7.16, top, right), and the wall shear rate γ_{23} vanishes. Our algorithm yields wall shear rates, which are displayed in Fig. 7.16, top, center. The ground truth is reproduced very well. Slight deviations occur, where there are several particle-rows adjacent, moving with approximately the same speed. The reason for these deviations is the fact that the spatio-temporal neighborhood is of limited size (in this case 65×65 pixels).

In the second synthetic image sequence the particles are randomly distributed (Fig. 7.16, bottom, left), moving so that they follows the wall shear rates $\gamma_{13} = 1$ and $\gamma_{23} = 0$. The estimated wall shear rates are mapped in Fig. 7.16, bottom, middle. As a result of the fact, that overlappings may occur, there are regions, where our algorithm produces significant deviations from the ground truth. This is evidence, that our model fails in the presence of motion discontinuities, which are caused due to overlappings of particles.

7.8 Summary of the Algorithms

In this last section of the chapter we will see, how the distinct techniques can be connected in order to obtain the desired quantities. Here we confine ourselves to the applications presented in chapter 8, namely the estimation of velocity vector fields in Eulerian and Lagrangian representation using the *method of two wavelengths* and the computation of the wall shear rate using the
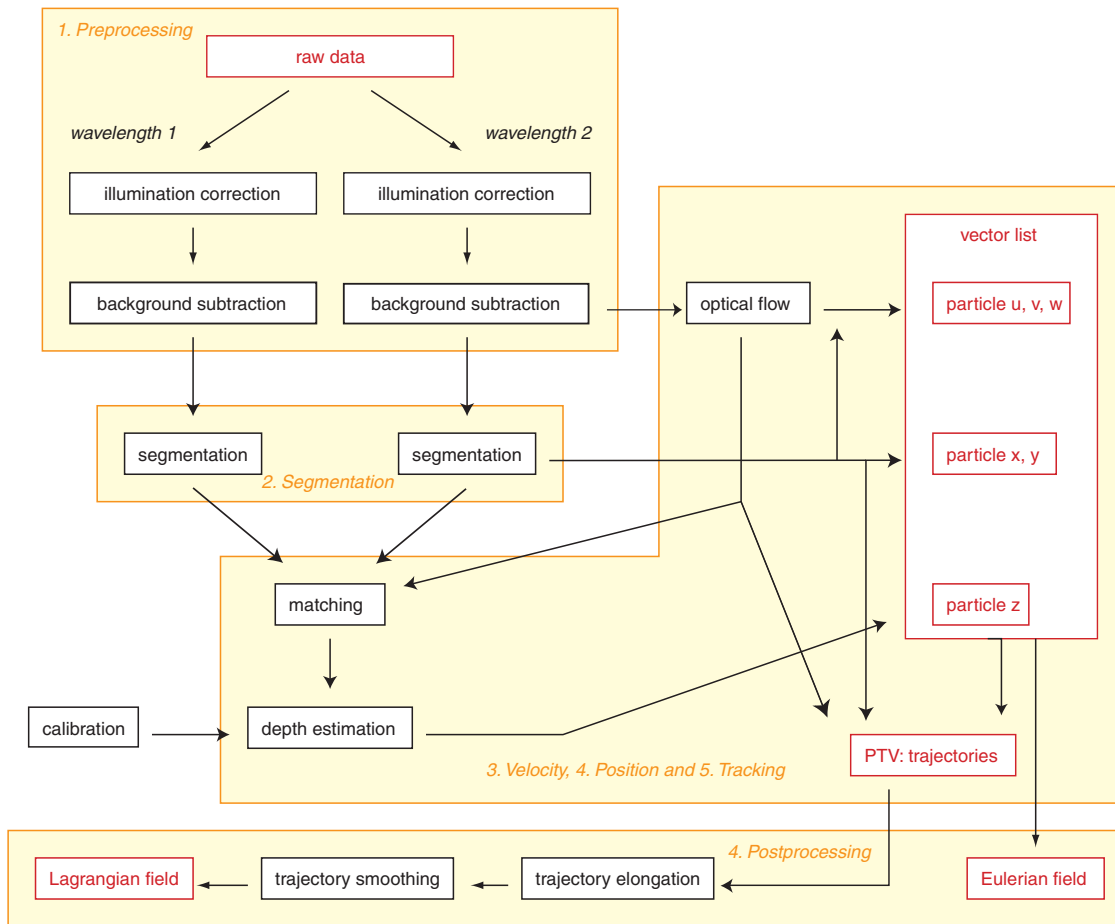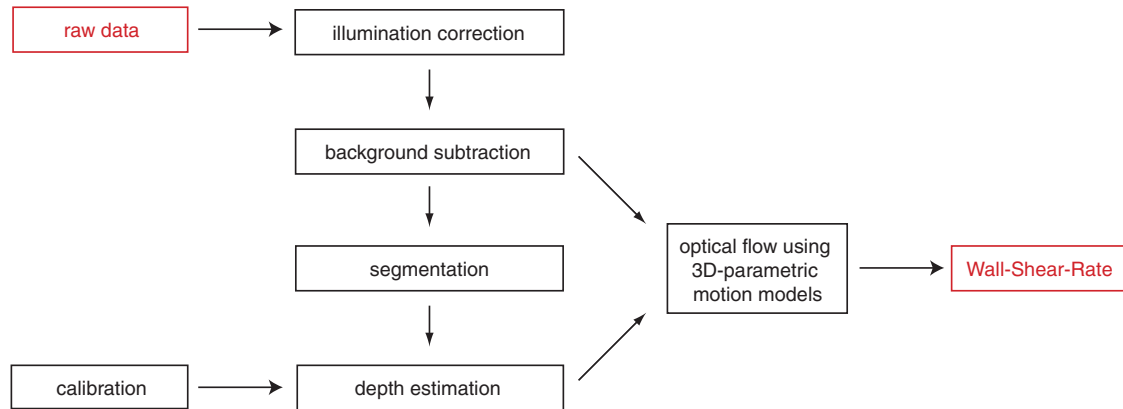
Figure 7.17: *Flowchart of the algorithm to calculate the Eulerian and Lagrangian velocity fields, using raw data generated with the* method of two wavelengths. *The analysis in section 8.2 and section 8.3 is performed in this way.*

method of one wavelength. However, due to its modular setup, one can adapt the algorithmics to one's individual needs.

Estimation of the Velocity Vector Fields

Figure 7.17 shows a view over the different components of our algorithm, and how they are related to each other. The components are grouped in four modules, whose names refer to the headlines of the first six sections in this chapter. In the preprocessing step the raw data is separated into two subsequences (one for the first wavelength, e. g. 455 nm, and one for the second wavelength, e. g. 470 nm). To each of these subsequences the various procedures of preprocessing and segmentation (section 7.1 and section 7.2) are applied. By performing correspondence-analysis (section 7.5.1) two grey values are assigned to one and the same physical particle; thus its depth can be calculated (section 7.4). Using one subsequence (e. g. of 470 nm wavelength), the optical

Figure 7.18: *Flowchart of the algorithm to calculate the wall shear rate distribution using the* method of one wavelength. *The analysis in section 8.4 is performed in this way.*

flow can be estimated according to section 7.3. We have arrived at an unequally spaced 3D3C Eulerian velocity vector field, which can be interpolated to a regularly spaced one, using the technique described in section 7.6.3. On the other hand, the particles can be connected to trajectories (section 7.5.2), so that postprocessing (section 7.6.1 and section 7.6.2) can be applied.

For the quantification of the particles' absolute depths and absolute velocities, a calibration has to be performed. I. e. both, the penetration depths (z_*1, z_*2) and the ratio of the intensities g_{01}/g_{02} has to be extracted using a special calibration technique. In section 8.1 the calibration procedure and its validation are explained.

Estimation of the Wall Shear Rate

Figure 7.18 visualises the various steps, which had to be carried out until the wall shear rate is obtained. In this thesis, the wall shear rate was calculated for image sequences, recorded with the *method of one wavelength*. Thus after preprocessing and segmentation, correspondence analysis is not necessary. Using the preprocessed sequence and a sequence of depth maps $z(x, y)$ as input, the wall shear rate distribution directly can be computed, without previous calculation of the velocity vector fields (section 7.7.2).

8 Experimental Results

In the following some experiments applying our measurement technique and our algorithmics to real flows and to real data will be presented. In section 8.1 the applicability of Beer-Lambert's law to depth estimation is demonstrated. Moreover, we will see, how our system easily can be calibrated regarding the reconstruction of the particles' depth. The main contribution of this work is the "proof-of-concept" of the *method of two wavelengths* applied to real-world flows. A laminar falling film (section 8.2) provides a well-known velocity profile, so that the measurement method can be tested. Convective turbulence (section 8.3) represents a more complex flow. Finally, in section 8.4 the algorithmics is adapted to data, which was recorded using the *method of one wavelength*. Here the focus is set to the direct estimation of the wall shear rate.

8.1 Calibration of Depth-Resolution

In this section procedure and results of the calibration of depth-resolution for the *method of two wavelengths* will be discussed. A possible calibration procedure for the *method of one wavelength* is given in [Debaene, 2005].

In section 5.2 we have found an expression for retrieving the lateral position z of a particle, given its apparent intensities while recording with two distinct wavelengths g_1 and g_2:

$$z(g_1, g_2) = \frac{z_{*1} z_{*2}}{z_{*1} - z_{*2}} \left(\ln\left(\frac{g_1}{g_2} \right) + \ln\left(\frac{g_{02}}{g_{01}} \right) \right).$$

By introducing the abbreviations $\eta = \ln(g_1/g_2)$, $z_{\mathrm{red}} = (z_{*1} z_{*2})/(z_{*1} - z_{*2})$ and $V = \ln(g_{02}/g_{01})$ the former can be rewritten to

$$z(\eta) = z_{\mathrm{red}} \eta + z_{\mathrm{red}} V. \tag{8.1}$$

8.1.1 Calibration via Linear Positioner

Equation (8.1) proposes a linear $z - \eta$ dependency. We can check this, by acquiring η_i at various depths z_i, and subsequently fitting a straight line to the data. The slope turns out to be z_{red} and the intercept yields $z_{\mathrm{red}} V$.

The particles were fixed in a 2 mm thick layer of agarose-gel. The setting up of agarose-gel is described in [Schlosser, 2004]. The gel with the particles was immersed into dyed fluid using a linear positioner (see Fig. 8.1, left). By moving the table the relative change of the width of the covering layer can be controlled. Using thin rods, water-displacement can be neglected, so that the movement of the table equals the relative change in depth.

This procedure is carried out automatically by centrally controlling the motion of the table and image acquisition. Images were taken at 80 measurement points, separated 125 μm, covering a
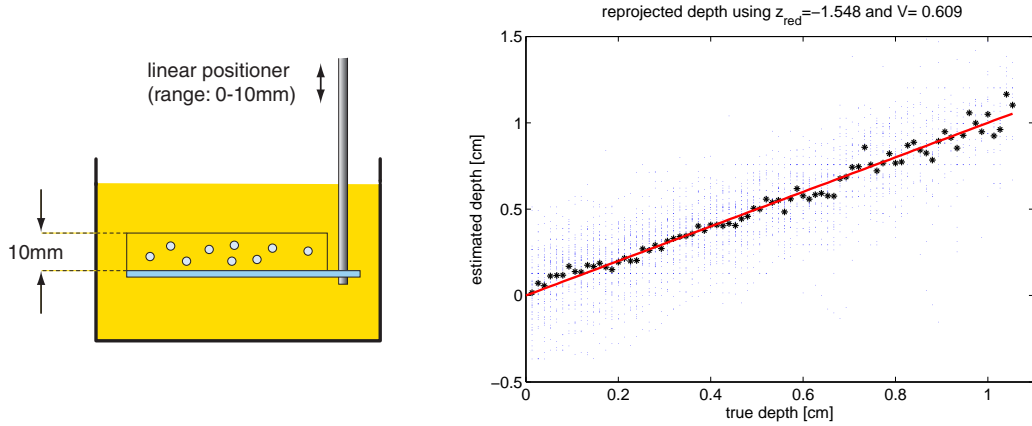
Figure 8.1: *Calibration via linear positioner. Left: Sketch of the experimental setup. Right: Reprojection of the data. The estimated depth using the fitted values for z_{red} and V is plotted against the true depth.*

total distance of 10 mm. Preprocessing (section 7.1) and segmentation (section 7.2) were carried out, and the correspondences between the particles acquired at 455 nm, and those acquired at 470 nm were established (section 7.5.2). Using the maximum gray values of the N distinct particles at the two wavelengths the mean of η, $\langle \eta \rangle = \sum_{i=1}^{N} \eta_i / N$, is calculated in dependency of z. By applying a linear ordinary least squares-fit to the data both z_{red} and V can be extracted.

Figure 8.1, right, shows the reprojection of the data $z_{\text{reproj}}(z)$ using the fit-parameters according to Eq. (8.1). We see a broad variance in the individual data-points, which are marked blue, but the mean values fit very well to the line $z_{\text{reproj}} = z$. Note, that with increasing depth the reprojected data becomes less exact.
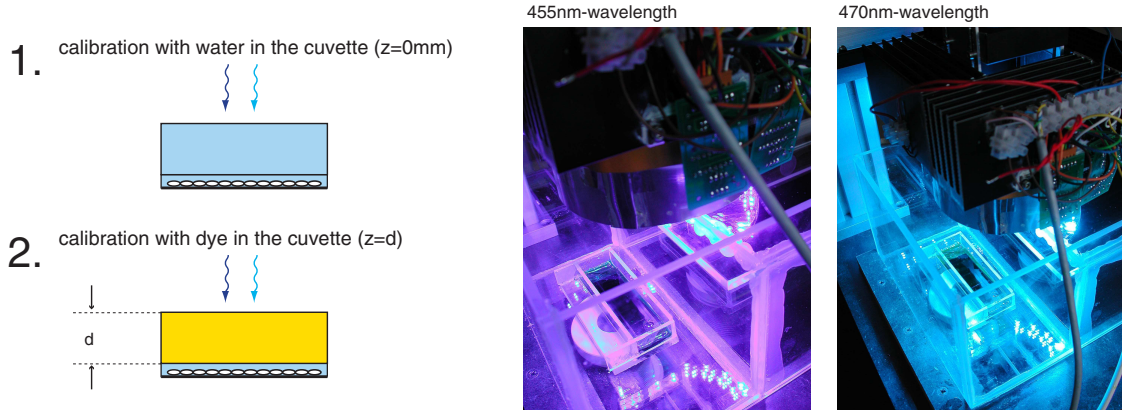
8.1.2 Calibration via a Target

From the previous section we see, that the linear dependency, proposed in Eq. (8.1), is in good agreement to the experiment. Furthermore, we have found a method to obtain the calibration parameters. But this calibration technique has the disadvantage, that it is quite elaborate. Calibration has to be carried out at least once when using a new preparation of dyed fluid. Therefore it would be reasonable to calibrate directly at the measurement place, using the same camera adjustments as in the experiments.

Once linearity is guaranteed it should be sufficient to take images at two measurement points, which are at a defined distance away from each other. Because simultaneously data from many particles were acquired, the statistical measurement error can be reduced. The particles are trapped in a thin cuvette, filled with water. Another cuvette of width d filled with water (or the dyed fluid) is put between particles and camera-optics, working as an absorbing medium. Figure 8.2, left, shows a sketch of the two-step calibration principle.

1. The first image is taken, while the cuvette is filled with water: The absorbing distance is 0 mm, so that Eq. (8.1) becomes

$$0 = z_{\text{red}}(\eta + V).$$

Figure 8.2: Calibration via target. Left: Sketch of the calibration target (filled with (un)dyed fluid). Right: Calibration using light of 455 nm and 470 nm wavelength.

In order to fulfill the equation, the second factor has to be zero, so that a necessary condition for V is:

$$V = -[\eta]_{z=0} = [\ln g_2 - \ln g_1]_{z=0}.$$

2. The second image is taken, while the cuvette is filled with a probe of the dyed fluid used in the experiment: The absorbing distance is d, so that Eq. (8.1) becomes

$$d = z_{\text{red}}(\eta + V),$$

which can be transformed to

$$z_{\text{red}} = \frac{d}{V + \eta} = \left[\frac{d}{V + \ln g_1 - \ln g_2}\right]_{z=d}.$$

Figure 8.3 shows the results of this technique. The calibration parameters $z_{\text{red},i}$ and V_i for each particle are scattered statistically about their mean values. Because there might be outliers (occurring due to swimming particles in the absorber fluid, for instance), the median (instead the mean) of the data is calculated. Reprojection uncovers these outliers.

8.1.3 Discussion: Calibration of Depth-Resolution

Using a linear positioner, on the one hand the applicability of Beer-Lambert's law to the present setup can be tested, on the other hand, we have an instrument to reconstruct the calibration parameters occurring in the linear expression for retrieving the lateral position of a particle Eq. (8.1).

Analogous to radiometric camera-calibration, once being sure, that there is a *linear dependency* at hand, a two-point-calibration should be sufficient. By employing a specially designed target the calibration-procedure has become much simpler, so that the parameters can be extracted directly using the same adjustments as in the experiment. By retrieving the calibration parameters for $O(100)$ individual particles simultaneously and applying the median to find the best estimate, we can be sure, that the error on the parameters is small.
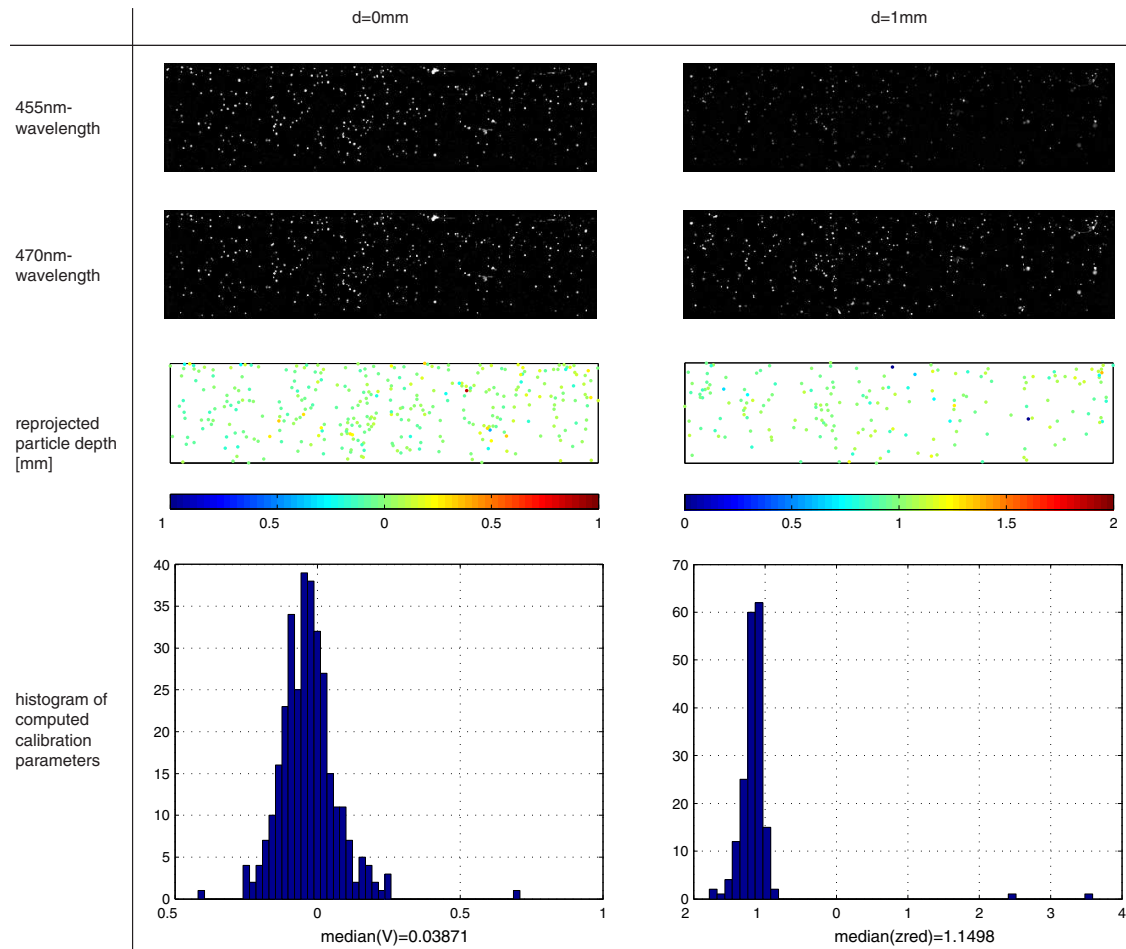
Figure 8.3: *Example of a calibration performed using a target. On the left hand side, results without absorber, on the right hand side, results with dye as an absorber are shown. Top: Acquired images using light of the two wavelengths. Center: Back-projected particles. Except some outliers, their depths scatter about the desired values. Bottom: Histogram of the calibration parameters.*

8.2 Measurements in a Falling Film

One of the most basic laminar flows, which are achievable in the laboratory, is the flow in a falling film on an inclined plane. Flow parameters like film depth, maximum velocity and Reynolds number can easily be varied by changing throughput, inclination angle and viscosity.

Its simplicity and versatility qualifies this flow for a physical reference our technique can be tested at. In this section the hydrodynamics of the flow, its realisation and experiments are addressed.

8.2.1 Laminar Falling Film - Theory

The velocity field results from a solution of the Naviar-Stokes equations (NSE), applying a certain geometry and assuming small Reynolds numbers.

The equations of motion for a flow of a uniform density fluid read (see Eq. (2.6))

$$\frac{\mathrm{d}\boldsymbol{u}}{\mathrm{d}t} = \boldsymbol{g} - \nabla p/\rho + \nu\nabla^2\boldsymbol{u}.$$

We consider the fully developed stage of a two-dimensional ($w = 0$ everywhere), steady ($\partial\boldsymbol{u}/\partial t = 0$) flow running down an inclined plane (the angle to the horizontal is α), which is solely driven by gravity g. Because continuity holds, i.e. $\partial u/\partial x + \partial v/\partial y = 0$, and the flow characteristics are invariant in x-direction (i.e. $\partial u/\partial x = 0$), we have $\partial v/\partial y = 0$ everywhere. Since $v = 0$ at $y = 0$, it follows that $v = 0$ everywhere, which reflects the fact that the flow is parallel to the walls. Therefore the NSE reduce to one equation

$$0 = -g\sin\alpha + \nu\frac{\partial^2 u}{\partial y^2},$$

which can be integrated to

$$\frac{\partial u}{\partial y} = \frac{g\sin\alpha}{\nu}y + A \quad \text{and} \quad u = \frac{g\sin\alpha}{2\nu}y^2 + Ay + B.$$

Because of the boundary conditions $[u]_{y=0} = 0$ (no-slip condition) and $[\partial u/\partial y]_{y=b} = 0$ (no shear stress at surface), we have for the integration constants

$$A = -\frac{gb\sin\alpha}{\nu} \quad \text{and} \quad B = 0,$$

so that the solution becomes

$$u(y) = \frac{g\sin\alpha}{2\nu}(y^2 - 2by).$$

Using a coordinate system, which has its origin on the film-surface, with the ordinate pointing to the wall, we have to replace y by $\tilde{y} = b - y$ and u by $-\tilde{u}$, so that the velocity profile can be written as

$$\tilde{u}(\tilde{y}) = \frac{g\sin\alpha}{2\nu}(b^2 - \tilde{y}^2), \tag{8.2}$$

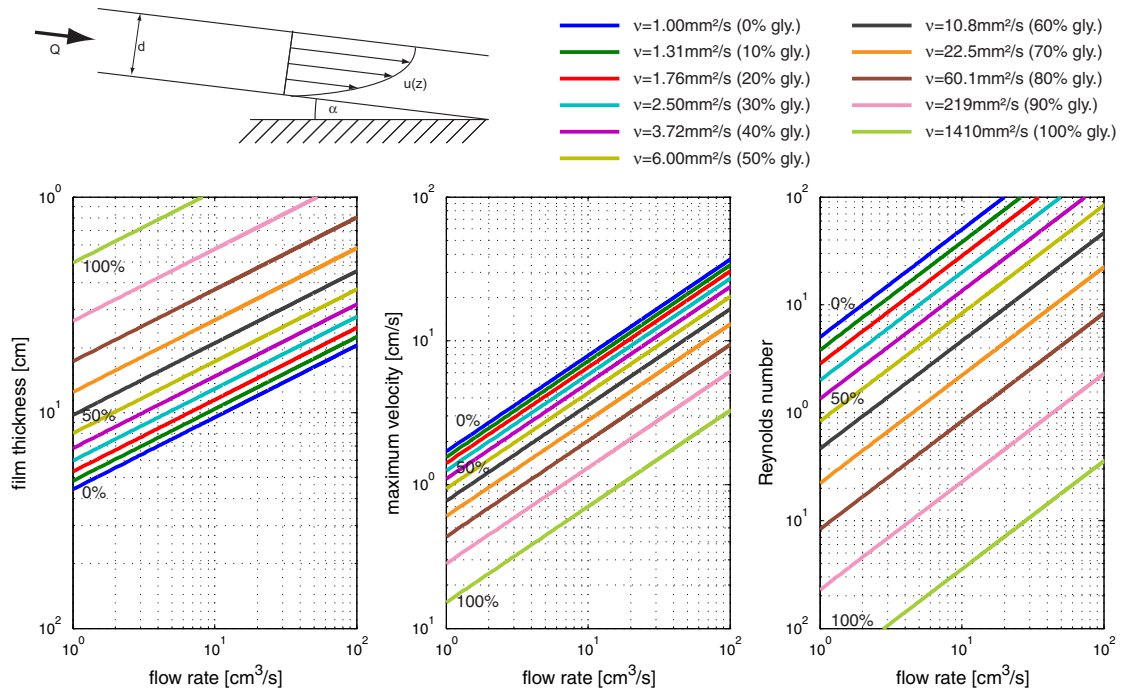which is commonly referred as the *Nusselt solution*. From now on, we omit the tilde in $\tilde{u}$ and $\tilde{y}$.

The velocity, averaged over the depth of the film, is

$$u_m = \frac{1}{b}\int_0^b u(y)\mathrm{d}y = \frac{g\sin\alpha b^2}{3\nu} = \frac{2}{3}u(0),$$

so that we get for the film depth in dependency from the exterior parameters, which are throughput Q, width of the film d, inclination angle α and viscosity of the fluid ν:

$$Q = bdu_m \Rightarrow b = \frac{Q}{du_m} = \sqrt[3]{\frac{3Q\nu}{dg\sin\alpha}}.$$

Figure 8.4: *Diagrams, showing the film depth b, maximum velocity u_{max} and Reynolds number $\textrm{Re}$, given the throughput Q and the viscosity ν. An inclination of $\alpha=1°$and a film width of $b=20\,cm$ are assumed.*

A Reynolds number can be defined to

$$\mathrm{Re} = \frac{bu_m}{\nu} = \frac{Q}{\nu d},$$

which does not depend on the inclination α.

Figure 8.4 shows the interior parameters film depth b, maximum velocity $v(z = 0)$ and Reynolds number in dependency of the exterior parameters throughput Q and viscosity ν, where the inclination angle α and the film width b are held constant. Here a laminar flow is presumed.

According to [Braun, 1969] the flow in a falling film is laminar, as long as Re < 3. In the range $3 < \mathrm{Re} < 45$, small disturbances because of the non-perfect geometry result in pressure fluctuations. In the NSE an additional pressure gradient appears, which makes their solution very complicated. [Chang and Demekhin, 2002] show, that depending on the type of perturbations and on the Reynolds number, various kinds of waves develop, which range from periodic waves to solitary waves.

Above Reynolds numbers of about 45 the flow in the falling film becomes turbulent, because now the inertia forces play a significant role. The wavy flow state becomes instable, and the flow transits to turbulence.
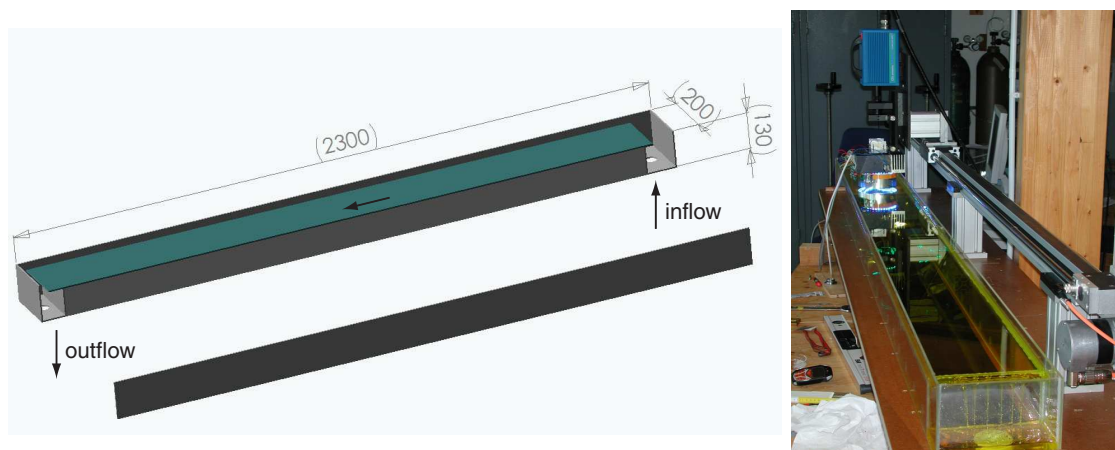
Figure 8.5: *Sketch (left) and photograph (right) of the falling film tank.*

8.2.2 Laminar Falling Film - Setup

A falling film tank of 230 cm length and 20 cm width was constructed (see Fig. 8.5, left). Thread rods are used to adjust the slope of the tank α continuously from 0 to 10°.

The tank was fully made of borosilicate glass[1], which guarantees high resistivity against acids, alkalies and organic substances. Moreover, choosing PP-H[2] (homopolymer polypropylene) as piping material, a safe usability of the tank for the above mentioned substances was assured.

The flow is driven by gravity, pouring from one container, which is located about 2 m above the ground, to the other, residing at the ground. No active elements like pumps were used to avoid contamination of the fluid. By choosing a sophisticated design of the piping using two ball valves, one is able to alternate the positions of the containers without altering the positions of in- and outlet of the tank (see Fig. 8.6). The throughput Q of the flow is measured using a variable area flow meter, being located up-stream of the inlet.

Image acquisition was done using the Camrecord 2000 high-speed camera at a resolution of 512×512 pixels[2] and a frame rate of 125 Hz or 250 Hz. The light sources 1 (royal blue – blue) and 3 (blue – cyan) were installed (see Fig. 6.11). In both cases, the absorption spectra of tartracine acid yellow turned out to be well adapted to the emission spectra of the LEDs. The setup of the recording unit was like that shown in Fig. 6.12. Figure 8.5, right, shows the recording unit mounted on a linear positioner table, which was used to perform measurements with the camera moving relative to the tank.

Both, the Optimage particles and the 3M glass hollow spheres were used. The 3M particles tended to stay at the water surface, or to deposit at the bottom of the tank. This might be explainable due to their hygroscopic properties. The Optimage particles mixed very homogeneously with the fluid. The falling film was operated with both, pure deionized water and water-glycerol-mixtures. The viscosity of the mixtures was measured using a glass tube viscosimeter.

---

[1]Borofloat 33 by Schott AG, Mainz, Germany; http://www.schott.com
[2]Georg Fischer GmbH, Albershausen, Germany; http://www.piping.georgfischer.com
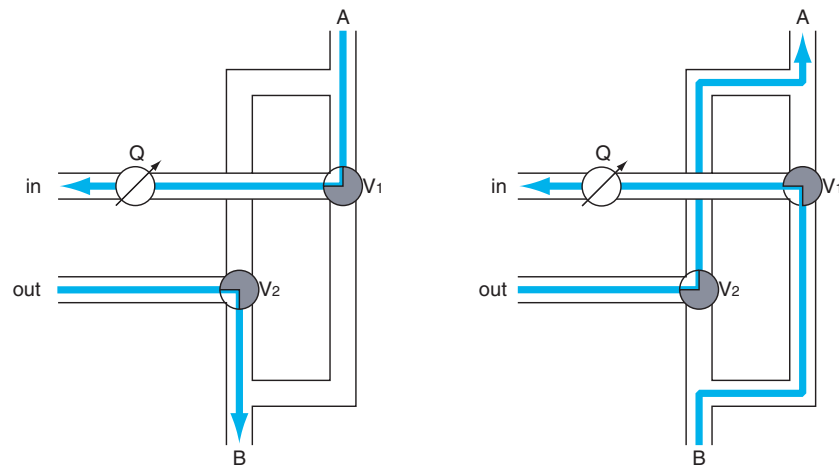
***Figure 8.6:** Schematic drawing of the piping in the falling film tank. The flow is either from container A to B (left), or from container B to A (right), while in- and outlet of the tank stay the same. This behaviour is driven by the two ball valves V_1 and V_2. The throughput Q is measured by a variable area flow meter up-stream of the inlet.*

8.2.3 Laminar Falling Film - Results

In the following results of the measurements in the falling film tank will be shown. The capabilities and the limits of the measurement technique and the algorithms will be demonstrated.

Generally the procedure is as follows:

1. The acquired image sequence undergoes a simultaneous radiometric calibration and illumination correction (section 7.1.1). Then the background, represented by the minimum image, is subtracted (section 7.1.3).

2. The particles were segmented using the region growing procedure (section 7.2.2) or a fit of Gaussians (section 7.2.3). The brightness parameter was either the maximum gray value or the fitted gray value. The performance of these segmentation approaches is discussed later in this section.

3. The velocity vector fields are extracted using the optical flow-based method (section 7.3). The depth coordinate of one particle was obtained using the brightness parameters of two subsequent images (section 7.4). Correspondences between image pairs were found by using the warping technique explained in section 7.5.1.

4. Postprocessing was performed in several ways. Firstly particles with low gray values and thus low expected signal-to-noise-ratio are thrown rejected. Secondly particles were connected to trajectories (section 7.6.1). Afterwards the velocity- and depth-components of a moving particle were smoothed along a trajectory (section 7.6.2). This will be discussed later in this section.

5. Calibration is performed using the technique presented in section 8.1, using a calibration target of width $d = 1\,\mathrm{mm}$.

Use of the linear positioner

The maximum achievable displacements are limited by the temporal sampling theorem. That means, that an upper limit for the measurable velocity of a tracer particle is given by its imaged spatial dimensions. An imaged pixel size of $28\,\mu$m/pixel was chosen. Assuming a slight presmoothing of the particle, this limit is about 4 pixels/frame. Illumination and camera allow a maximum achievable frame rate of about 250 Hz, which has to be divided by two, because only every second recorded image can be consulted for motion analysis (see Fig. 7.13). Using a higher frame rate (theoretically up to 1000 Hz), the dynamic range of the gray values cannot be exploited, because the luminous flux is too low due to the shorter exposure times. With these specifications we have for the maximum velocity:

$$4\,\frac{\text{pixels}}{\text{frame}} = 4\,\frac{28\mu\text{m}}{8\,\text{ms}} = 14\,\frac{\text{mm}}{\text{s}}.$$

One can improve this limit by mounting the imaging setup on a linear positioner, which moves with about half of the expected maximum flow velocity relative to the fluid. In Fig. 8.7, left, averaged velocity profiles without (top) and with (bottom) the use of a linear positioner are shown. Here exactly the same flow conditions (in this case $Q = 30\,$l/h, $\nu = 4.845\,$mm^2/s, $\alpha = 1°$) are applied, so that we can compare the velocity profiles in terms of accuracy. Using a linear positioner the precision of the depths of the deeper particles is much better. This reflects in the fact, that the statistics for deeper particles becomes larger, and the averaged values even in the deeper part of the profile do lie in line with the theoretical parabola (see Eq. (8.2)) very well. Figure 8.7, right, shows the acquired trajectories in this sequence.

### Effects of a Gaussian fit applied to the segmented particles

In the previous experiments the brightest gray value is assumed to be representative for the intensity of a particle. One can also use the outcome of a Gaussian fit to the gray values of a segmented particles as an intensity measure. In the analysis of Fig. 8.8 both kinds of intensity measures were used for the calculation of the depth-coordinates. Every point in the cloud represents a measured particle's velocity assigned to a measured particle's depth (z_i, u_i). Moreover the averages and the standard deviations of the particles' velocities in bins of 50 μm width were calculated. Afterwards the average velocities were fitted to a polynomial of second order. The Gaussian fit does not reduce the statistical errors significantly.

Effects of the trajectory-based postprocessing

The previous analysis has shown, that the theoretical parabolic velocity profile is reproduced by the *averaged* experimental velocity profile in very good agreement. Here averaging is feasible, because of the presence of a *stationary* flow. Provided the absence of systematical errors, one can improve the accuracy of the measurement by elongating the time of the measurement. However, if an *instationary* flow is at hand, averaging does not make sense, if one wants to extract the instantaneous velocity fields, at least, if the time scales of the advection of the flow field are shorter than the time of averaging. For this reason, we apply the postprocessing techniques, described in section 7.6. Figure 8.9 illustrates these methods:
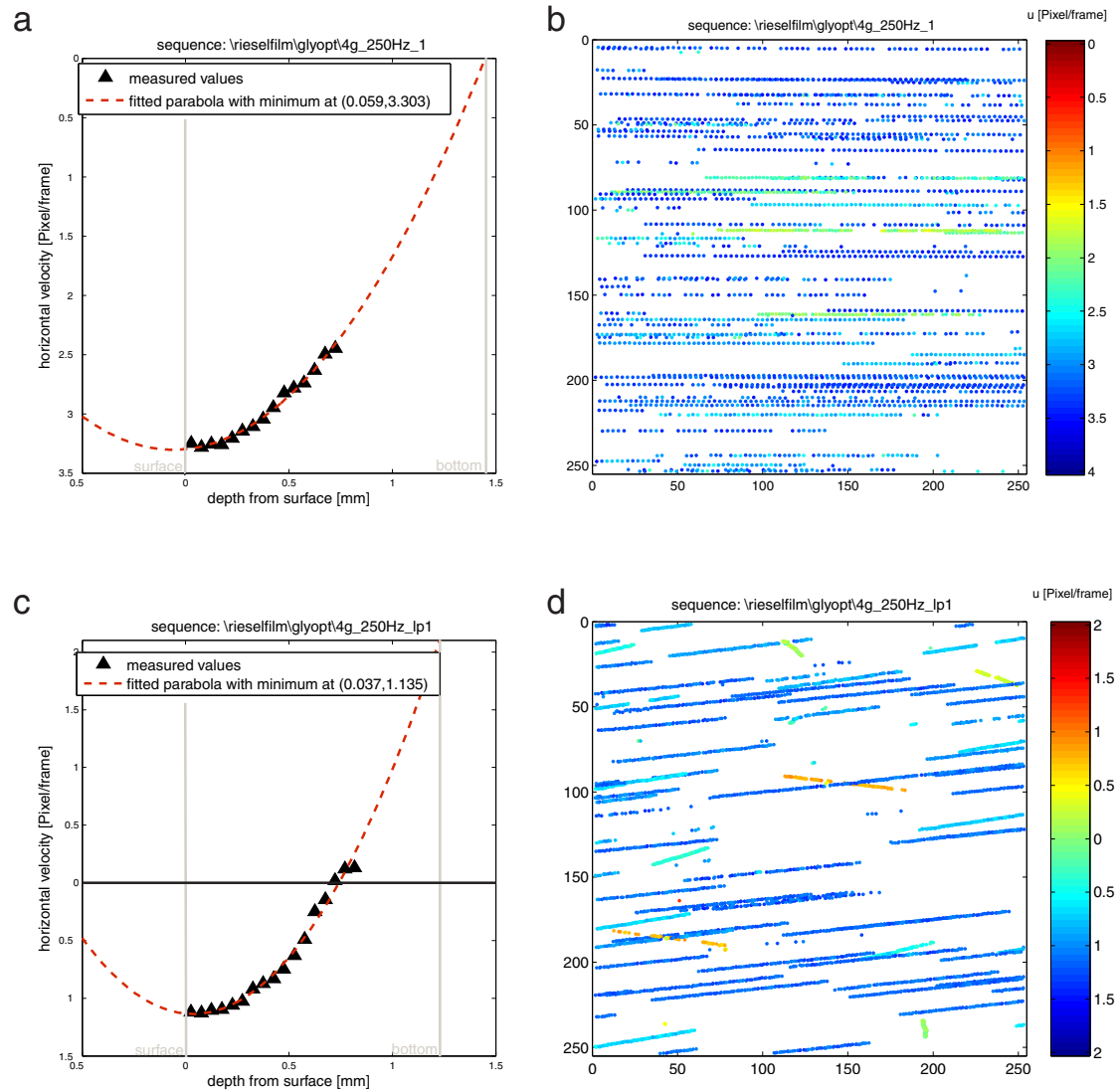
Figure 8.7: *Use of a linear positioner in a falling film experiment ($Q = 30\,l/h$, $\nu = 4.845\,mm^2/s$, $\alpha = 1°$, recorded at 250 Hz, Optimage particles), displayed by means of the velocity profile $u(z)$ and by means of a velocity-map: **a, b** No linear positioner used. **c, d** The recording hardware is mounted on a linear positioner table, which moves at a speed of 7.5 mm/s respectively about 2 Pixels/frame.*
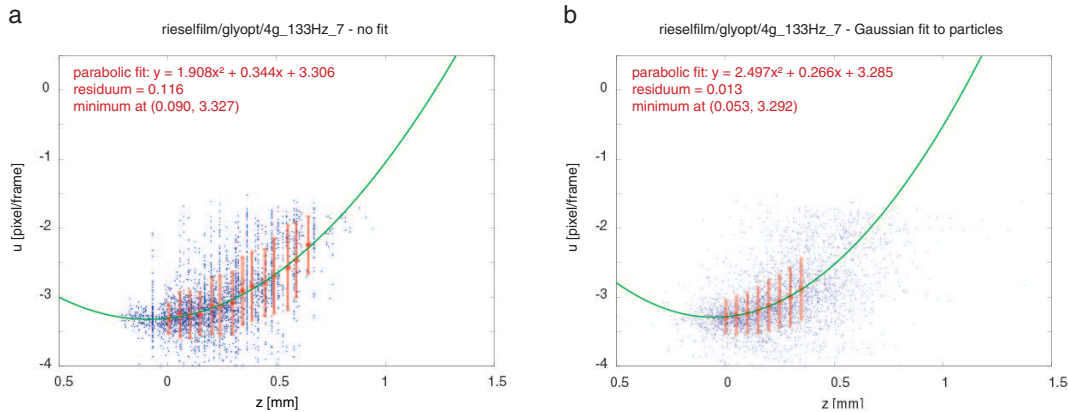
Figure 8.8: *Effects of fitting demonstrated in a falling film experiment ($Q < 15\,l/h$, $\nu =4.845\,mm^2/s$, $\alpha = 1°$, recorded at 133 Hz, Optimage particles), displayed by means of the velocity profile $u(z)$: **a** Maximum gray value taken as characteristic brightness parameter for a particle. **b** Characteristic brightness parameter is the maximum of a Gaussian fit applied to a 5×5-neighborhood of a particle.*

- If we plot all vectors, our measurement gets erroneous. The signal-to-noise-ratio of the low-intensity-particles is very poor. To prevent this, we applied a threshold on the minimum allowed gray value of a particle.

- Smoothing of the z-coordinate or of the u-component helps to reduce the errors significantly.

### 8.2.4 Simulation of a Laminar Falling Film

In the error analysis in section 5.3 it was argued, that the relative error of the maximum gray value $k = \Delta g/g$ is a function of the particle size σ. The oscillations in the gray value, that appear, when a particle moves constantly in one direction (see Fig. 7.15) were conjectured to stem from the effect, that it depends on the position of the particle's centroid relative to the pixel, how much photons one pixel can catch. We quantified $k(\sigma)$ using simulations (see Fig. 8.10).

Further a sequence was simulated, in which the particles move according to a parabolic profile. The particles were textured as Gaussian blobs, being advected with the flow. To this sequence the same algorithms were applied as in the previous section. Figure 8.11 shows impressively, that the oscillations in the gray value are not given by the physics of the flow, but result from the above addressed error.

8.2.5 Discussion: Laminar Falling Film

The velocity profile in a laminar falling film is well known. Moreover, by tuning its parameters (inclination angle, viscosity and throughput) flows in a versatile range of maximum velocity and maximum depth can be generated. Thus it serves well as a physical "ground truth" to test the *method of two wavelengths*.

The present measurements reproduce the predicted parabolic velocity profile Eq. (8.2) very well, if one is allowed to average over "bins" in depth-direction. This procedure is permitted in the presence of a stationary flow or of a flow whose flow field is slowly variable in time.
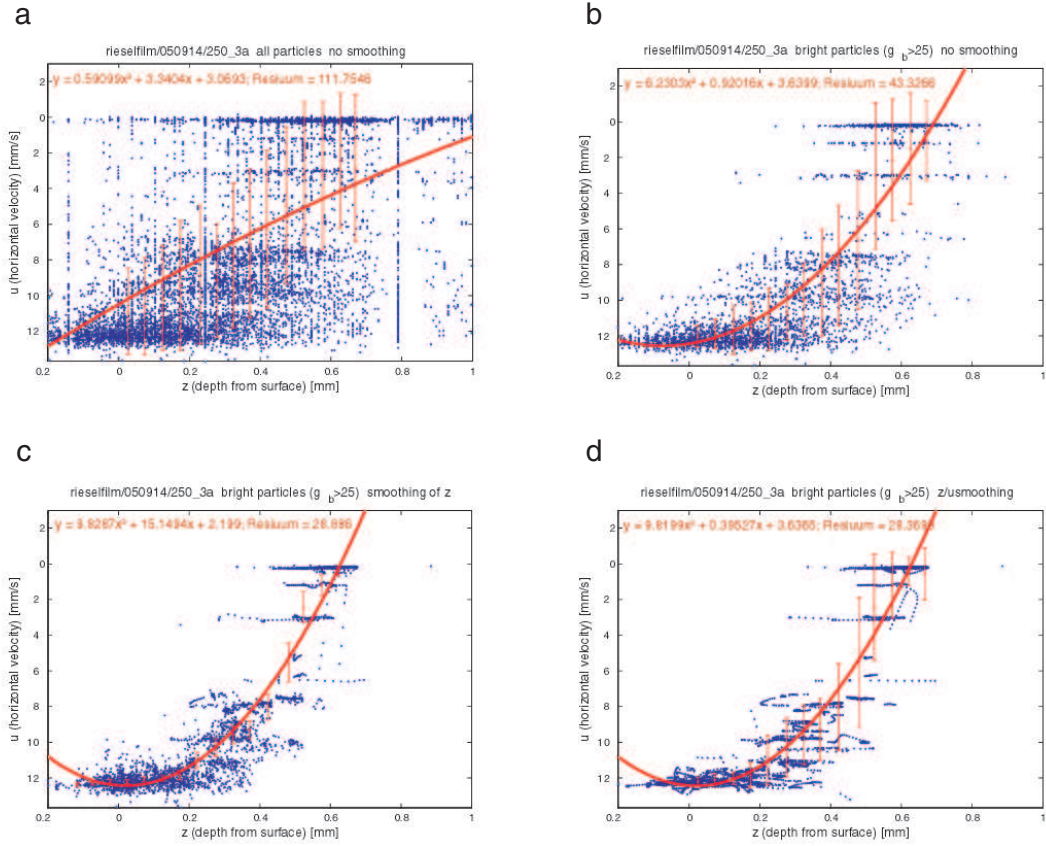
Figure 8.9: *Effects of smoothing demonstrated in a falling film experiment ($Q = 15 \, l/h$, $\nu = 3.676 \, mm^2/s$, $\alpha = 1°$, recorded at 250 Hz, M3-glass hollow spheres), displayed by means of the velocity profile $u(z)$:* ***a*** *All vectors, no smoothing.* ***b*** *Only particles with gray value 470 nm > 25 selected.* ***c*** *The depth coordinate z is smoothed in the trajectories.* ***d*** *Depth coordinate z and velocity component u is smoothed in the trajectories.*

By applying postprocessing-techniques the results could be improved in favour for the applicability to instationary flows. However, the individual (not the averaged) measurement points (which represent measured velocities at measured depths) exhibit considerable scattering.

The measurement setup had two limitations: Firstly, the Camrecord 2000 high-speed camera was of rather poor quality regarding spatial homogeneity of the camera sensor (see section 6.4.2 and section 7.1.1). Secondly, due to the relatively fast moving flow, high frames rates and short exposure times were required, which in turn requests a powerful illumination. The use of a linear positioner, moving with about half of the flow's maximum velocity, helped to attenuate the second limitation.

Simulations show, that the measurement error depends strongly on the particle size, which in turn affords a camera-sensor with a high resolution.
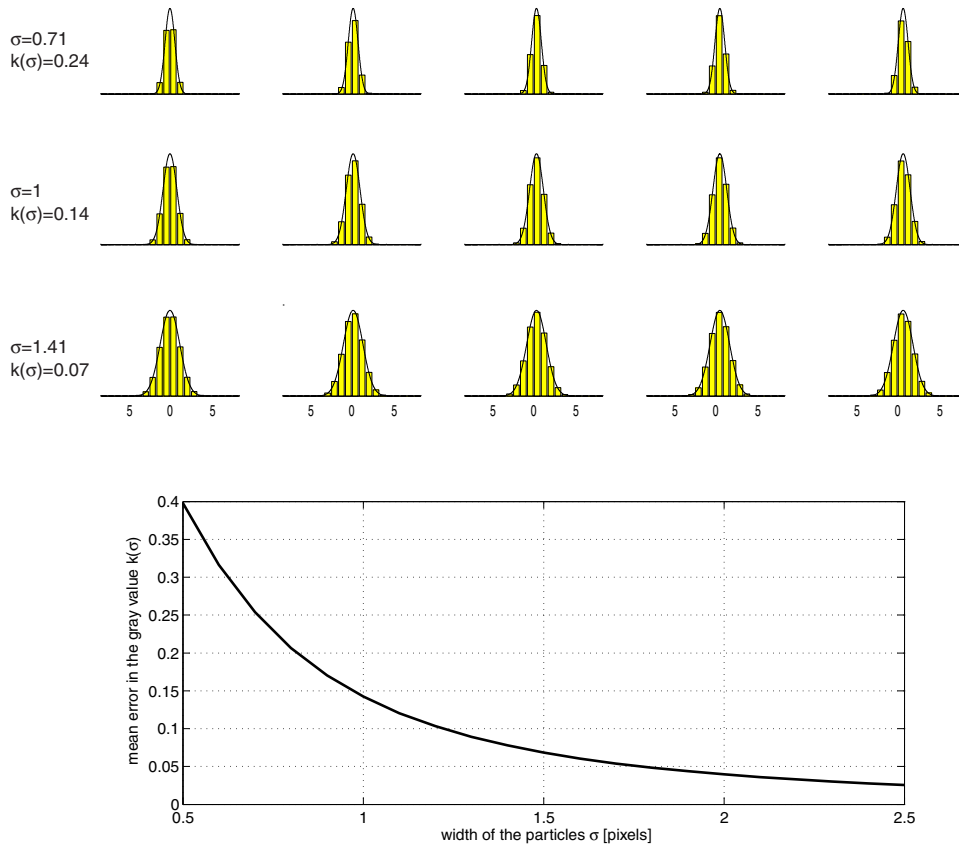
Figure 8.10: *Quantification of the relative error of the maximum gray value $k = \Delta g/g$ in dependency of σ. Top: Examples of three particles (having the widths σ=0.71, 1 and 1.41) "flowing" over the pixel lattice. Bottom: For each σ a mean error is calculated and plotted, resulting in the function $k(\sigma)$.*

8.3 Measurements in a Convection Tank

The measurements in the falling film showed, that the technique is capable to reproduce the exact flow fields (here in form of a 1D-profile), as long as the flow is stationary. In contrast, convective turbulence represents a flow, which is intrinsically 3D and instationary.

Compared to a falling film, convection is a slow process, so we can use high-quality hardware. In this section, we will introduce to the theoretical aspects of turbulent convection, address the measurement setup and show results.

8.3.1 Turbulent Convection - Theory

We are concerned about convection which is driven by buoyancy and by evaporation. For rigorous mathematical treatment see [Kundu, 1990] and [Koschmieder, 1993].

Buoyancy is realised by heating the fluid in a tank from below [Kundu, 1990]. Small disturbances (which occur because of the inhomogeneity of the boundary conditions) may cause a high-temperature fluid packet at the bottom to move upward. While raising, the difference of its
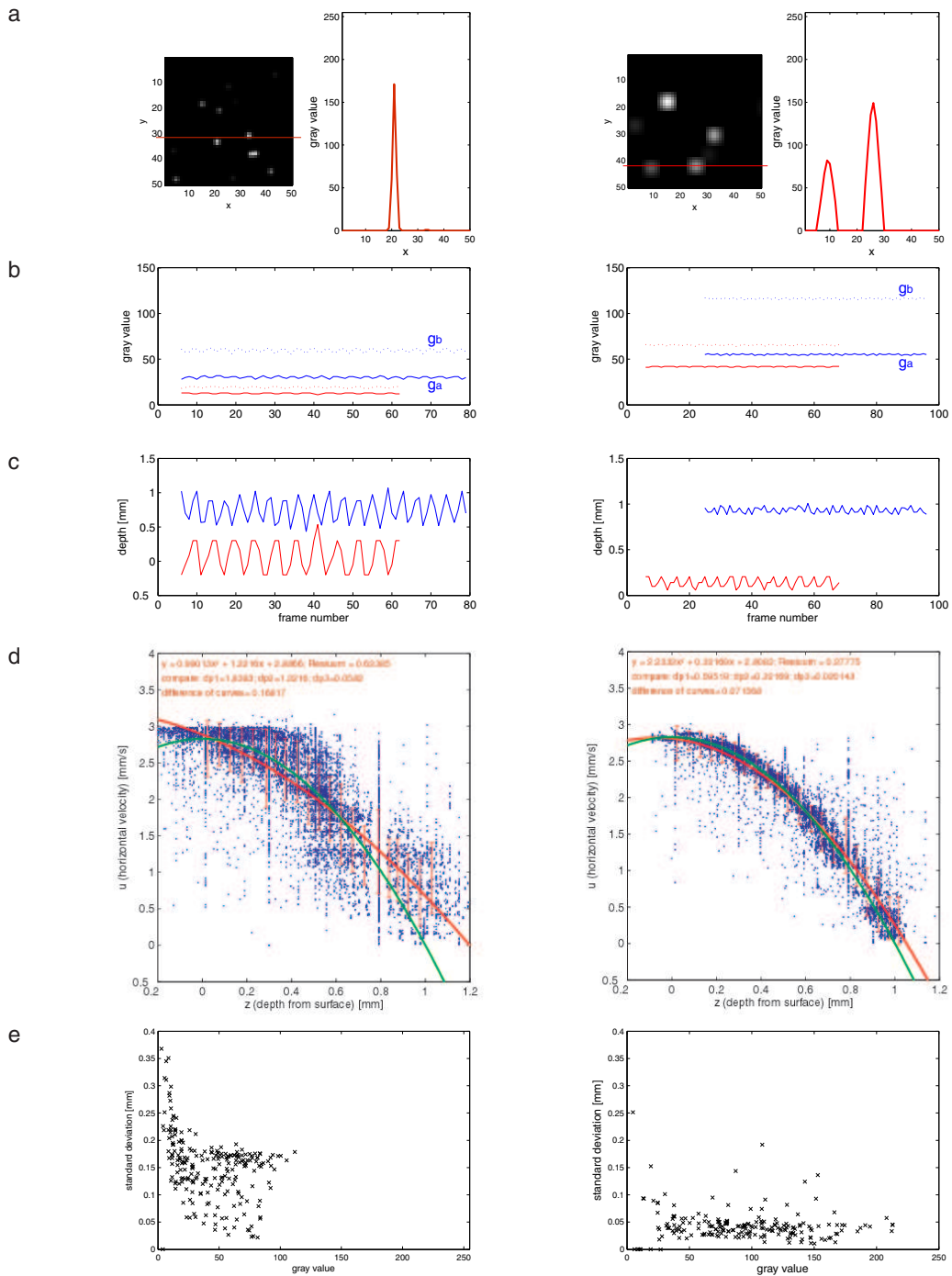
Figure 8.11: *Results of simulation of falling film experiments (width of particles 0.71 (left) resp. 2 (right)).* ***a*** *2D-image and 1D-profile.* ***b*** *Gray-values of two trajectories.* ***c*** z-*coordinate of two trajectories.* ***d*** *Velocity-profile* $u(z)$ *with fitted parabola (red) and ground truth (green).* ***e*** *standard deviations of the* z-*coordinate of the trajectories in dependence of their maximum gray-values.*
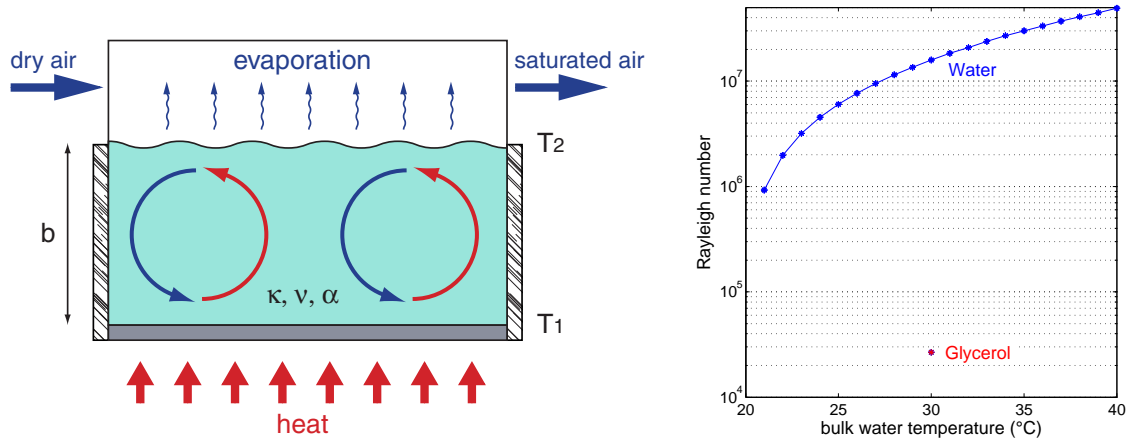
Figure 8.12: *Left: Sketch of buoyant evaporative convection: The water in the isolated tank is heated from below. Evaporation at the upper surface causes a transfer of latent heat. The vapour is transported by "dry air". Right: Diagram showing the Rayleigh number for water in dependence of temperature (d=4 cm, T_2=20°C). For comparison Ra for glycerol is plotted also.*

density to the density of the colder surrounding increases, which accelerates the upward motion (positive feedback). Vice versa a low-temperature fluid packet from the top may get in slighter higher-temperature regions because of random fluctuations. Because now it is heavier than the surrounding its downward-motion will accelerate. Originally hot and originally cold fluid elements exchange their places; the final result is a continuous circulation.

[Rayleigh, 1916] derived the theoretical requirement of buoyant convection in a layer of fluid with two free surfaces. He showed that the instability would occur when the ratio

$$\text{Ra} = \frac{\text{buoyancy force}}{\text{viscous force}} = \frac{g\alpha d^3 \Delta T}{D_H \nu},$$

which is known as Rayleigh number, exceeds a certain critical value. This number depends on the geometry of the fluid layer, which is expressed by its vertical dimension d (its horizontal dimension is assumed infinite), on the temperature difference from top to bottom surface $\Delta T = T_1 - T_2$ and on material properties of the fluid: kinematic viscosity ν, thermal diffusivity D_H and thermal expansion coefficient α. The critical Rayleigh number, which marks the onset of buoyant convection for a free upper surface and a rigid bottom wall, is about 1100. Here the flow forms regular patterns like regular polygons, depending on the boundary conditions. As Ra is further increased, the cell structure becomes more chaotic, and the flow becomes turbulent when Ra > 54000 [Kundu, 1990].

The heat transfer from water to air occurs via two modes: Firstly the difference in temperature of air and water causes sensible heat transfer, secondly evaporation causes latent heat transfer. The cool and thus dense water parcels at the interface plunge into the deep water; the warm and
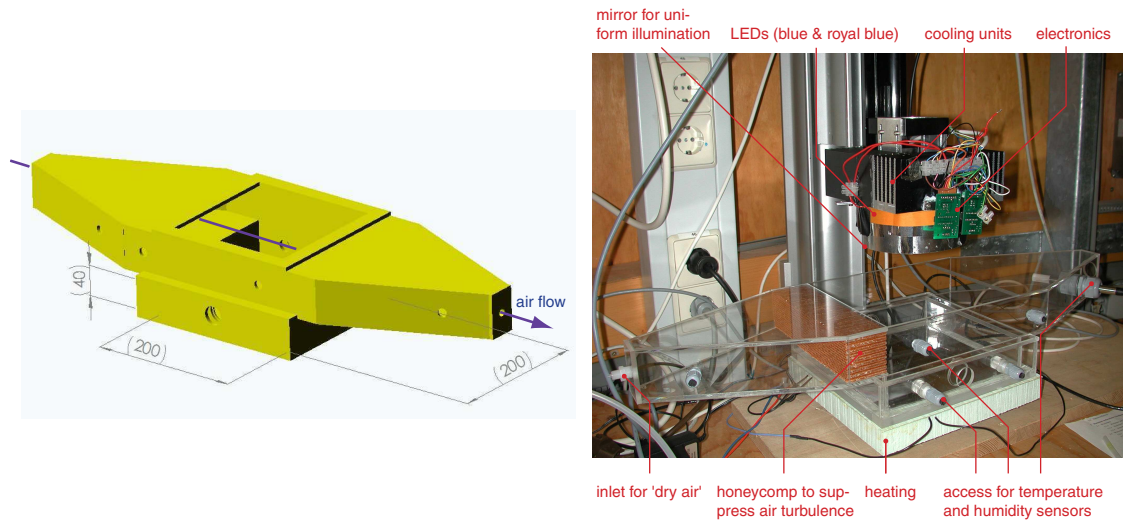
**Figure 8.13:** *Left: Drawing of the convection tank. Right: Convection tank with image acquisition unit.*

light ones rise and penetrate into the cool air above. The transition of water from liquid to gaseous state requires a certain heat volume, which is known as the evaporation heat.

Figure 8.12 shows a schematical sketch of the conditions in our experiments. The Rayleigh numbers of water for different temperatures in the water-bulk were calculated, where the temperature of the top is set to air temperature: $T_2=20$°C. Both, thermal expansion coefficient and viscosity depend strongly on temperature, whereas the thermal diffusivity is assumed to be constant: $D_{H,\text{water}} = 1.5 \times 10^{-7} \, \text{m}^2/\text{s}$. For water the Rayleigh numbers are in the highly turbulent range. Due to the much greater viscosity, the Rayleigh number of glycerol is of orders of magnitude lower ($\text{Ra}_{\text{glycerol}}(\Delta T = 10$°C$) = 27000$. Because we use water-glycerol mixtures, we are nevertheless in the turbulent range in our experiments.

8.3.2 Turbulent Convection - Setup

For the turbulent convection measurements a tank of dimensions $20 \times 20 \times 4 \, \text{cm}^3$ was constructed. The tank was fully made out of acrylic glass, the walls being double-glazed for the purpose of insulation. It is equipped with sensors for the bulk- and air-temperature and for the relative air humidity. Two quartz glass windows allow measurements using UV-spectroscopy. Heating was realized by warming an aluminum plate, which was located under the bottom of the tank, using attached heat foils.

The image sequences were acquired by a Basler 641f-camera, which has a resolution of $640 \times 480 \, \text{pixels}^2$ at 30 fps. $55 \, \mu$m were imaged to one pixel, so that the displayed window was about $3.5 \times 2.6 \, \text{cm}^2$. The distance between camera and object was about $60 \, \text{cm}$, so that the aperture angle of the objective was only about $3°$. Therefore lateral variations of size in the imaged volume can be neglected, so that this experiment was done without telecentric optics. The light sources 1 and 4 (both royal blue – blue) were installed (see Fig. 6.12). Using light source 4, one can simultaneously apply a second camera (like an infrared camera). Figure 8.13 shows a drawing
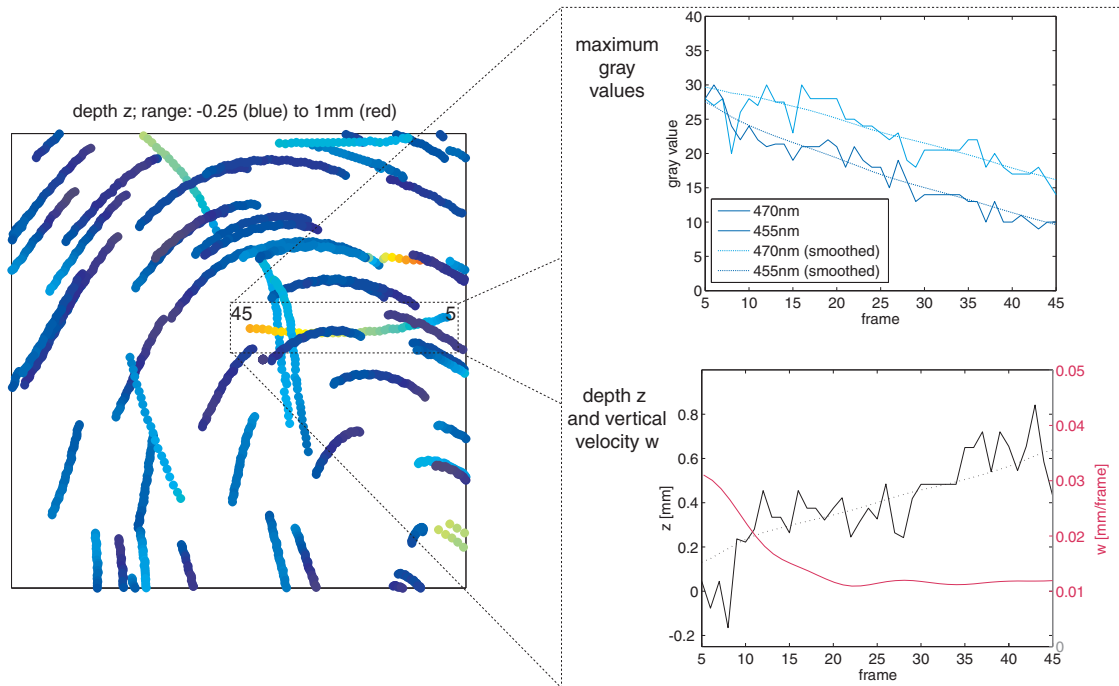
Figure 8.14: *Clipping of an example image sequence. Left: depth map of trajectories. Right: The (smoothed) maximum gray values, (smoothed) depth and vertical velocity of a selected particle moving along its trajectory are shown.*

and a photograph of our tank.

Because an imaged particle should cover about 2 to 5 pixels and for increasing the reflected intensity, we selected the Potters-particles (see section 6.1.2) to trace the fluid. Goal was to illuminate a volume of about 1 cm depth, so that their mean size of $100 \, \mu$m was appropriate. We used pure deionized water and a water-glycerol-mixture (ratio about 1:1) as fluid.

8.3.3 Turbulent Convection - Results

Experimental results, obtained by measurements in our convection tank are presented. It is shown, that the technique can be applied to highly complex, full 3D and instationary flows.

Here is an overview of the overall procedure:

1. The acquired image sequence was corrected for illumination inhomogeneity (section 7.1.2) and background (section 7.1.3).

2. The particles were segmented using the region growing procedure (section 7.2.2). The brightness parameter was the maximum gray value.

3. Like in the falling film experiments 3C-velocities and 3D-positions of the particles were extracted.

4. Postprocessing included connecting the particles to trajectories (Lagrangian representation), and elongation and smoothing of them (see section 7.6). Moreover by applying the adaptive

Table 8.1: *Experiment 060831 performed while constantly heating. The heating was started at 6:02 pm.*

Figure	Time	T_{water}	T_{air}	relative humidity
Figure 8.16	6:06 pm	22.98°C	25.15°C	32%
Figure 8.17	18:39 pm	26.50°C	25.37°C	62%
Figure 8.18	19:07 pm	29.00°C	25.89°C	81%

Gaussian windowing scheme, regularly spaced Eulerian velocity vector fields were obtained.

5. Calibration is performed using the technique presented in section 8.1, now using a calibration target with a cuvette of d=10 mm width.

Motion perpendicular to the image plane

Figure 8.14 shows a clipping of an example image sequence. Most of the tracer particles swim at the surface, but some of them are transported in deeper fluid regions and move in other directions. The vertical velocities, obtained by the optical-flow based technique, fits to the z-coordinates, as this is demonstrated by following the trajectory of a selected particle.

Turbulent convection varying the temperature difference

The image sequences outlined in table 8.1 are recorded under identical conditions; merely the temperature difference was varied by heating constantly with a power of 20.8 W. The arising vapour was transported by dry air, which streamed with constantly five liters per minute through the tank. Tartracine dye (about 25 mg/liter) and tracer particles (Potters, mean density 1.1 g/cm^3) were added to the fluid, consisting of a water-glycerol-mixture. Light source 4 (blue–cyan) illuminated a fluid volume of about $3.5 \times 2.6 \times 1.5$ cm^3, operating at a maximum power of 12 W.

The figures, referred to in table 6.4, show:

- Top: The trajectories as seen by the camera, where the colour-information represents the depth z and the horizontal velocity u.

- Center: Velocity vector fields obtained by the adaptive Gaussian windowing technique starting from the deepest layer (distance from the surface $z = 9.5$ cm) moving upwards. The colour code is the same as in the velocity-map of the particles (top, right), but showing the w-component of the velocity here.

- Bottom: Vertical profiles of the mean and rms velocities (red: u, blue: v, black w).

Figure 8.16 shows the situation four minutes after the heating was turned on. The seeding particles in the deeper layers move with a maximum speed of about 1 pixel/frame ($\approx$1.5 mm/s). There is almost no motion in the upper layers. This behaviour is reflected in the vertical profiles.

In Fig. 8.17, where we have heated 37 minutes, the convective motion has become faster (up to 2 pixels/frame, which is 3 mm/s) and more chaotic. Looking at the interpolated vector fields, upward and downward moving cells can be identified. The vertical motions tend to neutralize themselves, i. e. w_{mean} equals zero for all measurable depths, but w_{rms} increases with increasing depth.

After heating of 63 minutes (see Fig. 8.18) we recognize, that turbulence has further developed, which is evident looking at the velocity profiles. The fluctuations in horizontal velocity u_{rms} and
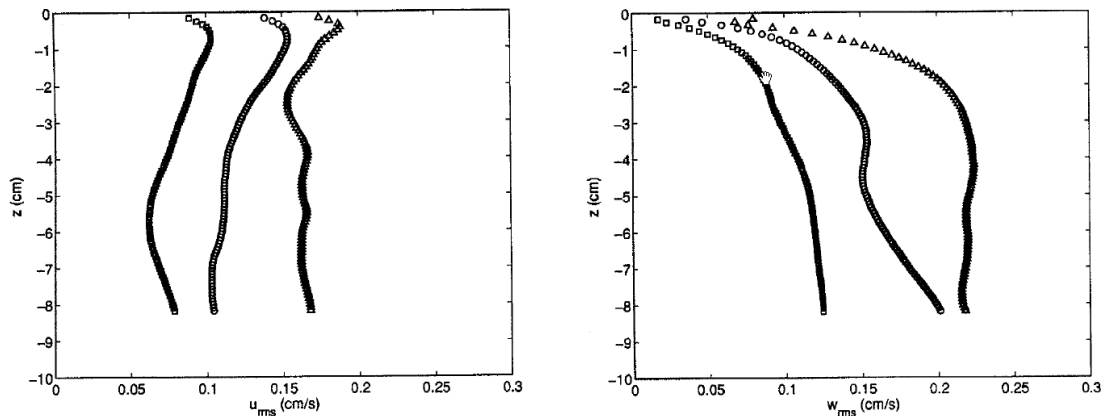
Figure 8.15: *Vertical profiles of the rms turbulent velocities. Left: Horizontal. Right: Vertical. The three distinct profiles in each figure refer to different heat fluxes applied.*

v_{rms} start near zero at the surface and reach a maximum in a depth of about 5 to 7 mm, then they are damped. The fluctuations in vertical velocity u_{rms} show a different behaviour: They rise with increasingly depth almost monotonously.

Qualitative comparison with experiments done by other researchers

The phenomenon of *natural convection* was investigated by other researchers. [Volino and Smith, 1999] simultaneously measured the surface temperature and two-dimensional subsurface velocity fields using infrared thermography and PIV (see section 3.3.1). They found, that the water surface is cooled by evaporation and the cooler water plunges into the warmer bulk below. [Flack et al., 2001] measured the surface temperature of water undergoing evaporative convection using infrared imagery. The subsurface turbulence was measured using two-component LDA. They conducted the experiments both with a clean surface (absence of shear) and with a surfactant monolayer present. They observed fundamental differences of the flow fields between the two cases.

[Bukhari and Siddiqui, 2006] investigated the two-dimensional velocity field beneath the surface in a plane perpendicular to the surface using 2D-PIV. They also measured the vertical profiles of the velocity fluctuations (see Fig. 8.15). Though they used water instead of a water-glycerol-mixture, and the dimensions of their tank was very different compared to ours, a qualitatively similar behaviour of the profiles can be observed. Their u_{rms} exhibits a maximum some millimeters below the surface and declines to greater depths. Their w_{rms} is ascending monotonously with increasing depth.

8.3.4 Discussion: Turbulent Convection

The measurements in a convection tank differ in two ways from the measurements in the falling film: Firstly, the motions of the flow are slower, so that a camera with a higher-quality camera sensor and a higher resolution can be employed. Secondly, the turbulent flow is intrinsically 3D and instationary.
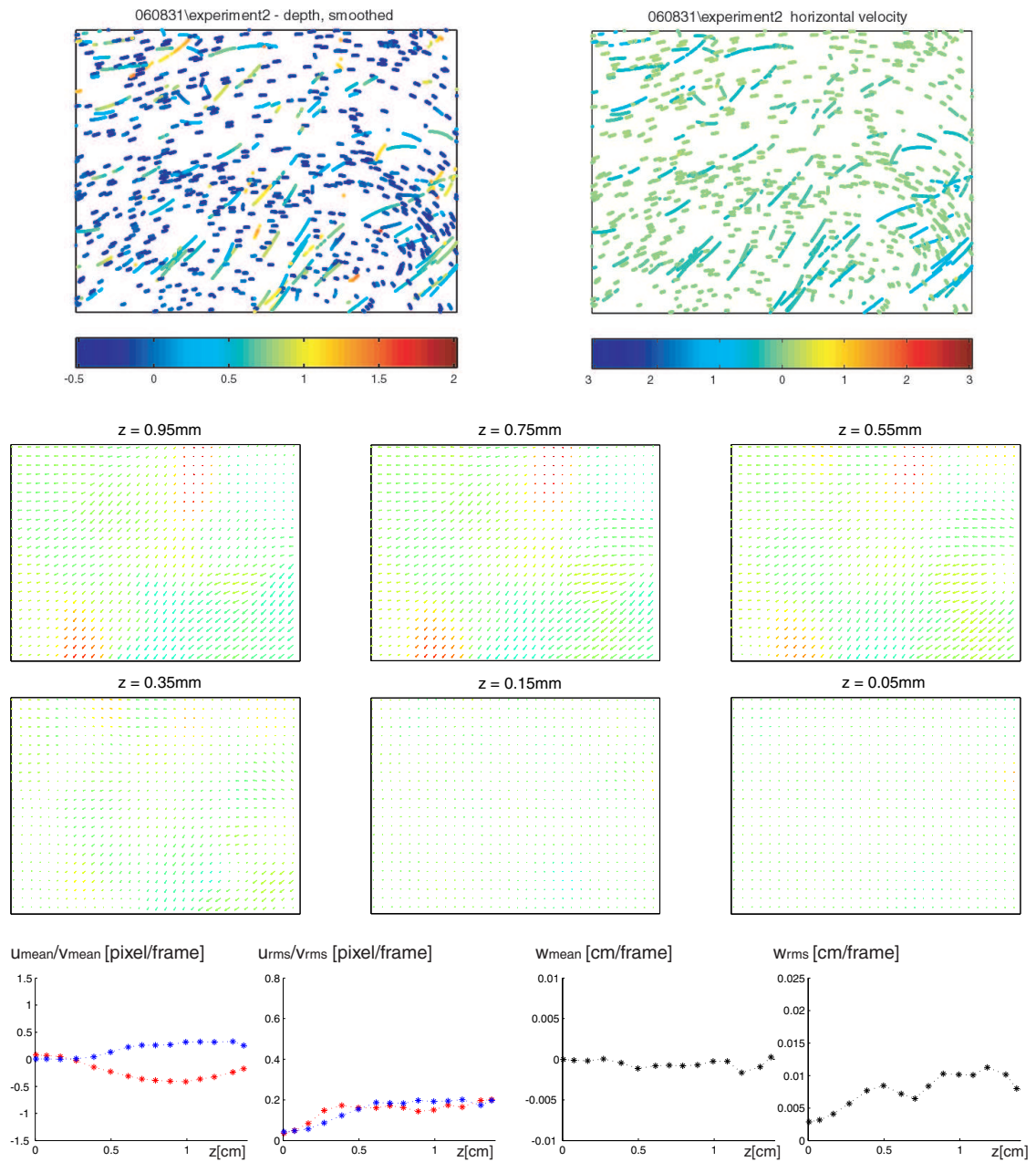
Figure 8.16: *Experiment 060831.* $\Delta T = -2.17°C$. *For details see section 8.3.3.*
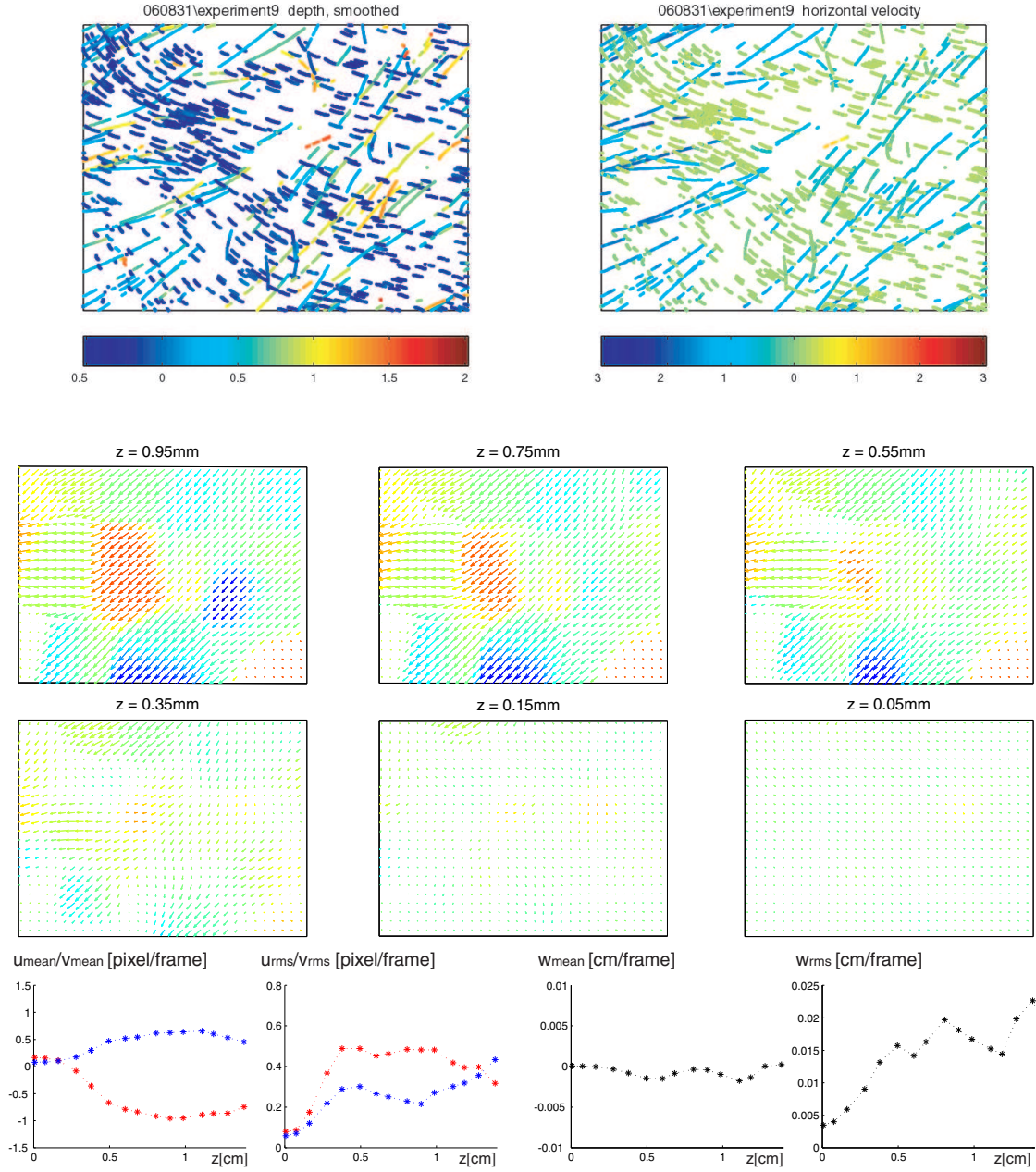
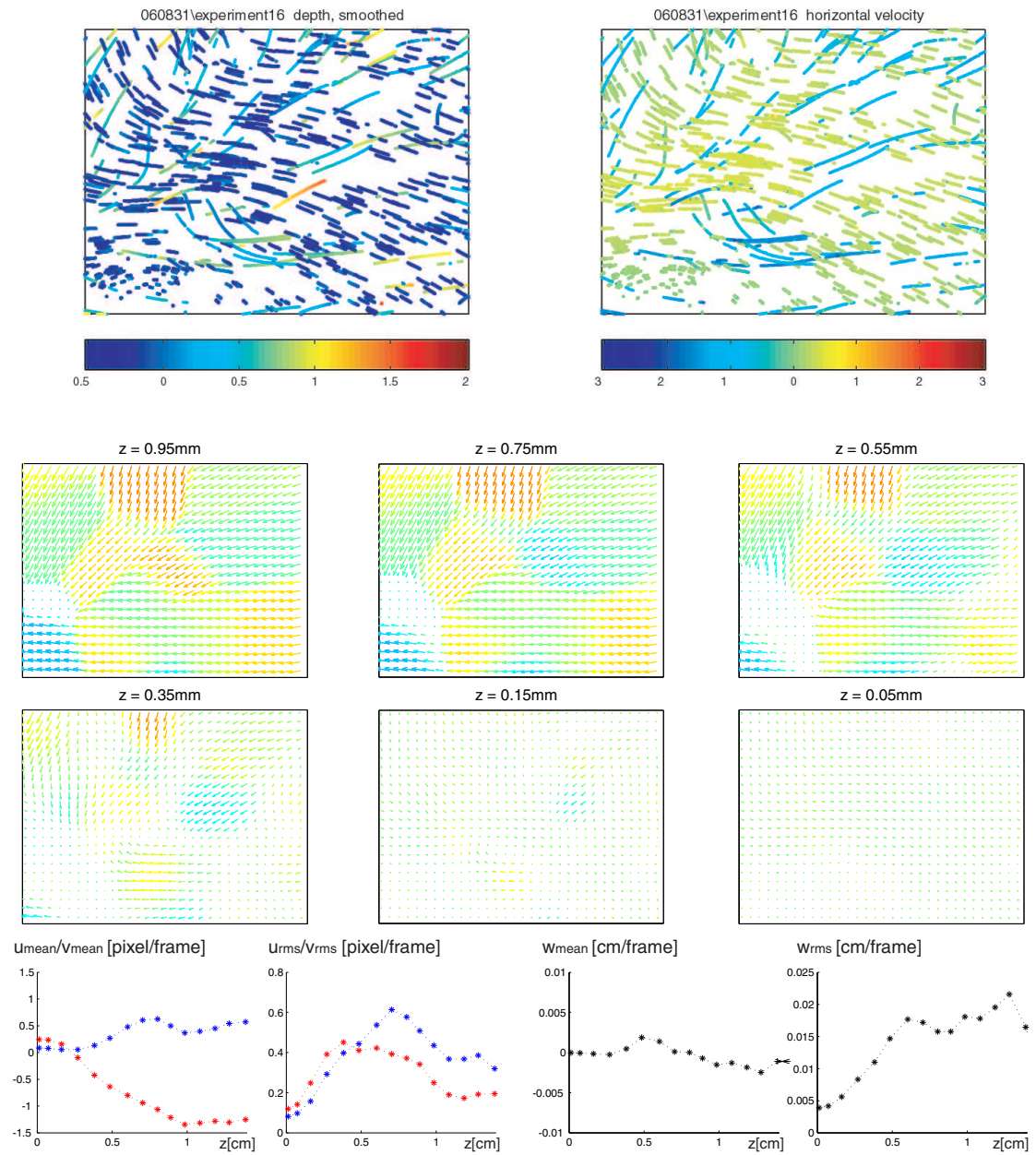**Figure 8.17:** *Experiment 060831.* $\Delta T = 1.13°C$. *For details see section 8.3.3.*

119

Figure 8.18: *Experiment060831 $\Delta T = 3.11°C$. For details see section 8.3.3.*

The drawback of this kind of flow is, that there is no analytic solution at hand. In this case we are restricted to qualitative evaluation and to comparative measurements by other researchers. Looking at the vertical profiles of the rms velocities, we indeed find a qualitatively similar behaviour of our results and the results of [Bukhari and Siddiqui, 2006].

Applying simultaneously an established technique (like thermography), we should be able to test our method quantitatively. This is under investigation.

8.4 Application to Sequences acquired in Context of Biofluidmechanics

In section 5.1 it was already mentioned, that the *method of one wavelength* was developed in the field of biofluidmechanics by [Debaene, 2005]. The biofluidmechanics lab[3], a department of the Charité, a clinical center in Berlin, Germany, is concerned about the application of engineering methods to problems encountered in medicine, where the emphasis is on fluid mechanics.

After resuming the medical background of the analysed experiments, the measurement setup will be sketched. Finally some results of our analysis will be presented, consisting of the determination both of the velocity and of the wall shear rate.

8.4.1 Medical Background and Motivation

The investigation of the flow near the wall of a blood vessel or an artificial organ is of great interest, since a close relationship is known between the characteristics of the flow such as magnitude and direction of the wall shear stress and biological phenomena such as thrombus formation or atherosclerotic events. The wall shear stress influences structure and function of endothelial cells as well as the behaviour of platelets.

Blood is a non-Newtonian, shear-thinning fluid, i.e. the viscosity changes with the wall shear rate in such a way, that the viscosity decreases with increasing wall shear rate. Reason for this is, that at low shear rates the blood platelets join in aggregates, which form a high resistance against the shear forces. While the shear forces increase, these structures dissolve and the viscosity decreases. Moreover, the platelets change their orientation and their form, while the shear forces rise, which results in an additional loss of internal friction. At high shear rates (above $100\,\mathrm{s}^{-1}$) blood can be approximated by a Newtonian fluid with a viscosity of $\eta \approx 3.5 \times 10^{-3}\,\mathrm{Pa \cdot s}$.

Together with the non-Newtonian characteristics of blood, the flow in blood vessels has an impact on blood-clotting. Other factors for intravascular blood-clotting might be a damaged endothelian layer or the contact with a foreign surface. Therefore in 1856, Robert Virchow postulated the interaction of blood flow, vessel wall and blood properties, today known as *'Virchow's Triad''*, which is largely confirmed by clinical experience. A precise measurement of the wall shear stress should help to quantify the complex interrelations.

8.4.2 Measurement Setup at the Charité

Ultimate goal for the Charité group is to develop a versatile method to measure the spatial distribution of the wall shear rate in models of blood vessels or artificial organs. Occurring difficulties include the instationary, pulsatile flow and curved and moving walls. The Charité group used exactly spherical, monodisperse particles, which are of $300\,\mu\mathrm{m}$ in diameter. Thus it is sufficient

---

[3]http://www.charite.de/biofluidmechanik/
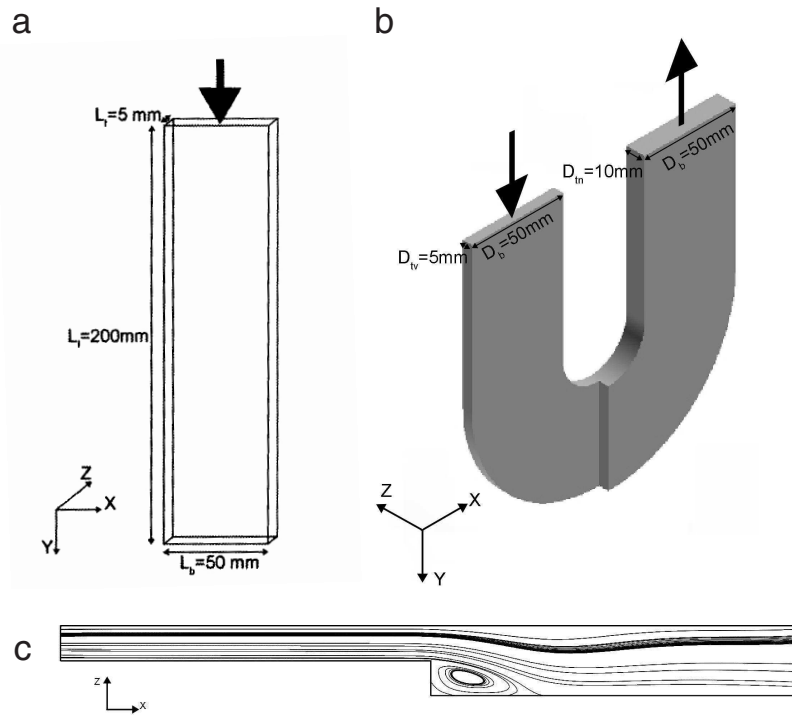
Figure 8.19: *a Linear glass tank with a rectangular cross-section. **b** U-shaped channel with rectangular step. **c** Computed path lines in a parallel cut to the $x - y$-plane at $y = D_b/2$ in the U-shaped channel with step (from [Debaene, 2005]).*

to illuminate using one wavelength, which improves accuracy and simplifies both measurement setup and analysis. The Berlin group chose a blue dye (patent blue V) and an illumination setup, consisting of LEDs emitting in the red spectral range (peak wavelength 639 nm). [Debaene, 2005] separated the near-wall flow in two layers by means of gray-value thresholding. For each layer, which is characterized by a distinct distance from the wall, the motion of the particles was determined with a conventional PIV algorithm (for PIV see section 3.3.1. This resulted in a vector field $u(x)$ for each layer.

We applied our algorithmics to two sequences, each one dealing with flow in a distinct geometry.

Spatially homogeneous and stationary flow

A mixture of water and glycerol ($\nu = 10.96 \times 10^{-6}\,\mathrm{m^2 s^{-1}}$) flows through a linear glass tank with a rectangular cross-section (see Fig. 8.19, **a**). This results in following velocity profile in the $y - z$-plane (for its derivation see [Debaene, 2005]):

$$v(z) = 6v_{\mathrm{mean}} \left(\frac{z}{L_t} - \frac{z^2}{L_t^2} \right),$$
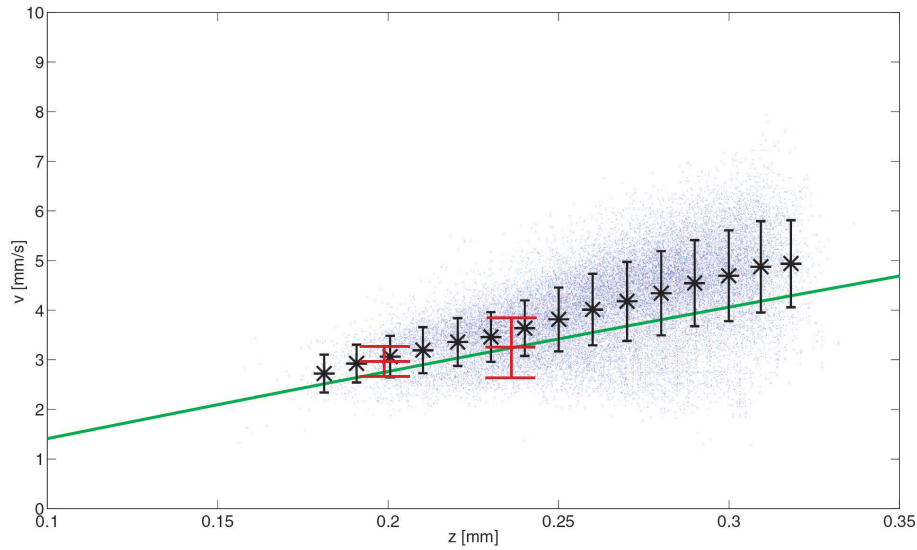
Figure 8.20: *Velocity profile of an image sequence (marked as "STA3" in [Debaene, 2005]). Both, the output of our optical-flow-based computation (black) and the PIV-analysis of the Charité-group (red) are in line with the analytical profile (green) within their statistical errors.*

with the mean vertical velocity $v_{\text{mean}} = 11.96$ mm/s and the channel depth $L_t = 5$ mm. In contrast, the flow field in the $x - y$-plane is nearly homogeneous, which was verified conducting a conventional PIV-measurement.

The experiment was conducted by illuminating the glass tank frontally using diffuse light. A high speed camera recorded the scene running at 125 frames/s at a resolution of 512×480 pixel^2.

Stationary, complex flow in a U-shaped channel

A water-glycerol mixture ($\nu = 8.372 \times 10^{-6}$ m^{2}s^{-1}) flows through a U-shaped channel with a rectangular cross-section and a step (see Fig. 8.19, **b**). In combination with the bending, the step in the cross-section generates a complex flow which detaches from the wall (see Figure 8.19, **c**). Figure 8.23, left shows a sample image of the recorded sequence.

8.4.3 Results of our Analysis

Spatially homogeneous and stationary flow: velocity profile

First results concerning the flow in the linear glass tank are shown. Because we deal with a spatially homogeneous and stationary flow, we are mainly interested in the velocity profile. The image sequence was already corrected for illumination and background by the Charité-group. The procedure of the image analysis was as follows:

1. The particles were segmented using a fit of Gaussians (section 7.2.3. The characteristic brightness parameter of a particle was its maximum gray value. Further we calculated a depth map assigning every particle to a z-coordinate, which can be directly calculated from the maximum
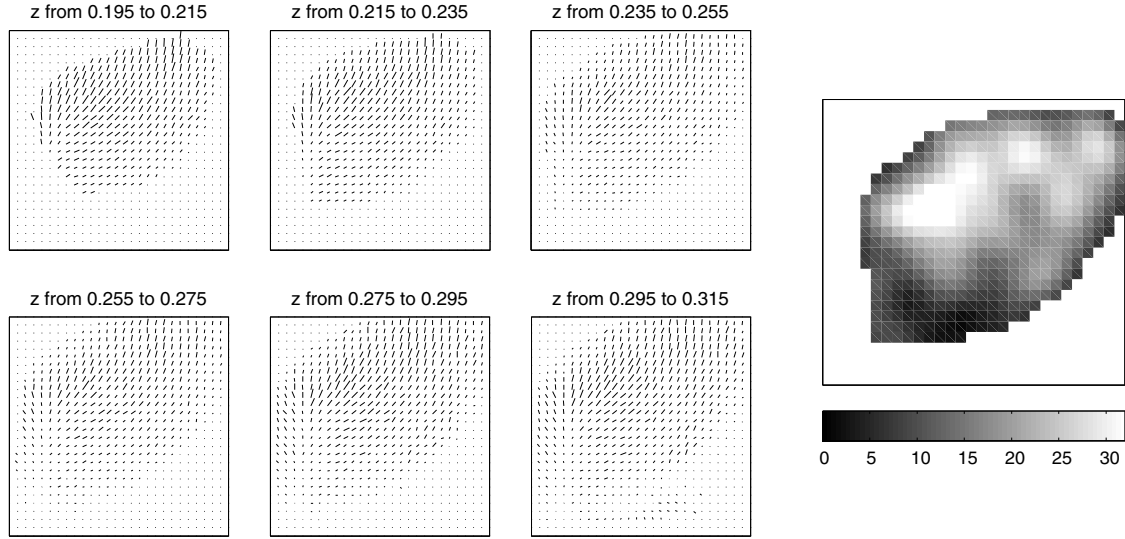
Figure 8.21: *Left: Velocity vector fields in various depths. Right: Distribution of the wall shear rate using the velocity data.*

gray value via the inversion of Beer-Lambert's law (Eq. (5.4)). The calibration parameters g_0 and z_* are provided by the Charité-group.

2. The velocity vector fields are extracted using the method of optical flow. Because wall-parallel motion is assumed, the simple optical flow-constraint without brightness-variations was used (Eq. (4.2)).

Figure 8.20 shows the results of this analysis. Each point in the cloud represents a single flow vector in the sequence. Moreover the averages over $10\,\mu$m wide bins were calculated and displayed together with their error bars. The averaged values lie about 10 to 15% above the analytical solution, which is marked by a solid line. [Debaene, 2005] averaged spatially the vector fields they obtained by applying PIV to the thresholded layers. These are indicated as red horizontal bars.

Stationary, complex flow in a U-shaped channel: 3D2C velocity field

Using the same procedure as in the previous paragraph the velocity vector fields were estimated, given an image sequence recorded by the Charité-group. In Fig. 8.21, left, the velocity vector fields of various depths were plotted.

Stationary, complex flow in a U-shaped channel: Wall shear rate

Using the vector fields, the field of the wall-shear rate $(\gamma_x(x, y), \gamma_y(x, y))$ was estimated. Therefore, ordinary least squares-fits to the local velocity vector profiles were applied, followed by calculating the magnitude of the resulting wall shear rate-vectors $\gamma_m(x, y)$:

$$(u(x, y, z), v(x, y, z))^T \overset{\text{OLS-fit}}{\to} (\gamma_x(x, y), \gamma_y(x, y))^T \to \gamma_m(x, y) = \sqrt{\gamma_x^2 + \gamma_y^2}.$$
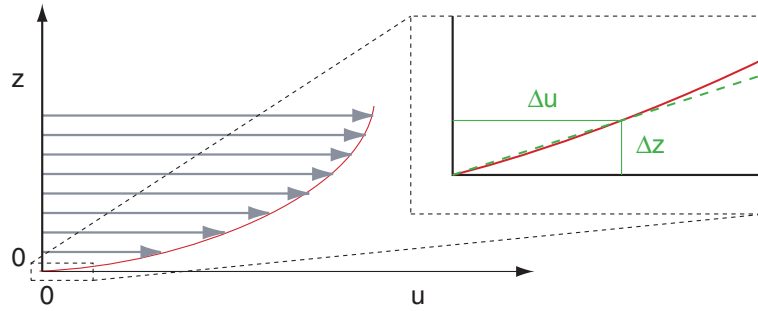
Figure 8.22: *Estimation of the wall shear rate: In the vicinity of the wall the tangent to the velocity profile ($\partial u/\partial z$) can be approximated by a line, which intersects the origin (no-slip-condition) and has a slope, which equals the difference quotient ($\Delta u/\Delta z$).*

Here "local" means, that the input to the fit were blocks of 33×33 pixels^2. We implicitly assumed, that we can replace the differential quotients by the difference quotients in the definition of the wall shear rate (see Fig. 8.22). This is allowed, because the visible particles fall within a region, where the velocity distribution is considered to be proportional to the wall distance:

$$(\gamma_x, \gamma_y) = \left[\frac{\partial u}{\partial z}, \frac{\partial v}{\partial z} \right]_{z=0} \approx \frac{\Delta u}{\Delta z}.$$

In Section 7.7.1 the parametrization of three dimensional physical flow fields. was addressed. We already saw, that the wall shear rate can be regarded as components of the more general velocity gradient tensor: $(\gamma_x, \gamma_y) = (\gamma_{13}, \gamma_{23})$. Therefore Eq. (7.6) could be applied to the data. Since the diameter of the spheres is significantly larger than the penetration-depth, only the particles close to the wall are imaged and no overlapping particles are recorded. Therefore, the problem of multiple-motions does not occur in this situation. Though not having a uniform flow, (7.7) could be applied since the components of the velocity gradient tensor containing the derivatives w. r. t. z are large compared to the components containing the derivatives w. r. t. x and y.

The components γ_{13} and γ_{23} of the wall shear rate are mapped in Fig. 8.23, right. Since the examined flow is stationary, the shear rate is averaged over 300 frames. The gaps in the otherwise dense flow field indicate the spots, where the confidence measure, which is provided by the structure-tensor-technique, was to low for providing a reliable result.

Figure 8.24 displays the magnitude of the wall shear rate, obtained with different techniques, and compares the methods to each other. To establish some kind of "ground truth" [Debaene, 2005] computed the flow numerically with the solver FLUENT6[4], which is shown in Fig. 8.24, top, left. The analysis of the flow using the PIV-technique and subsequent derivation of the wall shear rate, as carried out by [Debaene, 2005] is shown in Fig. 8.24, top, center. Our result is mapped in Fig. 8.24, top, right. In order to compare the techniques with each other, the gaps were filled by means of interpolation, and the result was smoothed afterwards smoothed using a 2D-anisotropic diffusion.

[4]Fluent Inc., Lebanon, USA; http://www.fluent.com/
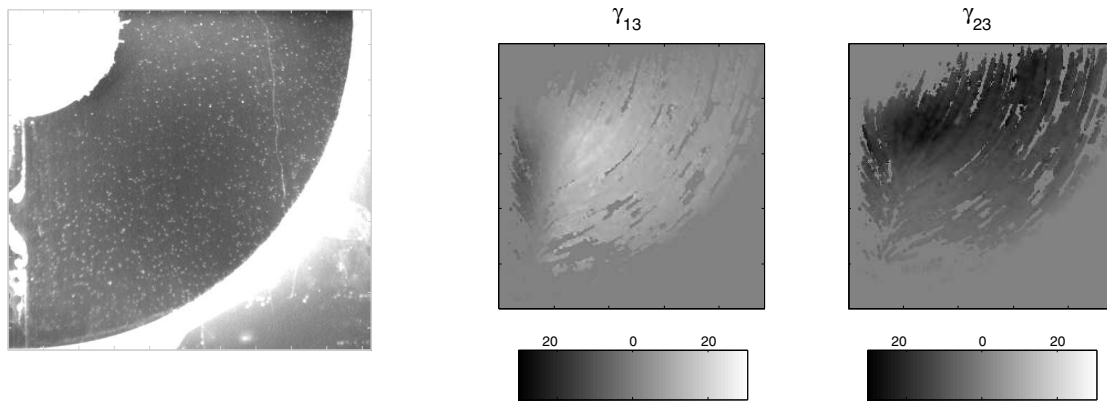
Figure 8.23: *Left: Example image of the recorded image sequence. Right: Maps of the wall shear rates estimated with our algorithm.*

Our optical-flow-based method provides a dense, highly resolved vector field of the wall shear rate, which is capable of estimating this quantity at positions where the PIV-method fails. The flow-detachment in the lower left corner can, for instance, be reproduced very well. Both techniques, optical flow and PIV, show a deficit of the wall shear rate in the upper left corner, and a surplus in the upper right corner, compared to the analysis provided by computational fluid dynamics. These systematical deviations may occur as a result of the fact, that the particles, which are of a comparable large size, cannot follow the fluid ideally, or influence the fluid. To provide a measure of how much the results of the experimental methods are apart from the numerical solution, we added up the magnitudes of the differences on each pixel. Optical flow resulted in about 10% better results, than PIV, when the CFD-solution was regarded as the "ground truth". Besides that, the optical flow analysis yielded a much better spatial resolution, and the area, where a reliable estimate of the wall shear rate is possible, is about 30% greater compared to the area, obtained using the PIV analysis.

8.4.4 Discussion: Biofluidmechanics

Both, the reconstruction of the velocity fields and the direct estimation of the wall shear rates, were applied to the image sequences provided by [Debaene, 2005] and underwent a quantitative evaluation. The stationary flow through a tank with a rectangular cross-section can be solved analytically - our results lie 10 to 15% above the predictions. The Charité group has computed the more complex flow in a U-shaped channel with a rectangular cross-section numerically, which serves as reference in order to evaluate our reconstruction of the wall shear rate. Compared to the PIV-analysis, the method, proposed in this thesis, provides a higher resolution and a greater coverage, so that the essential features of the flow become clearly visible.
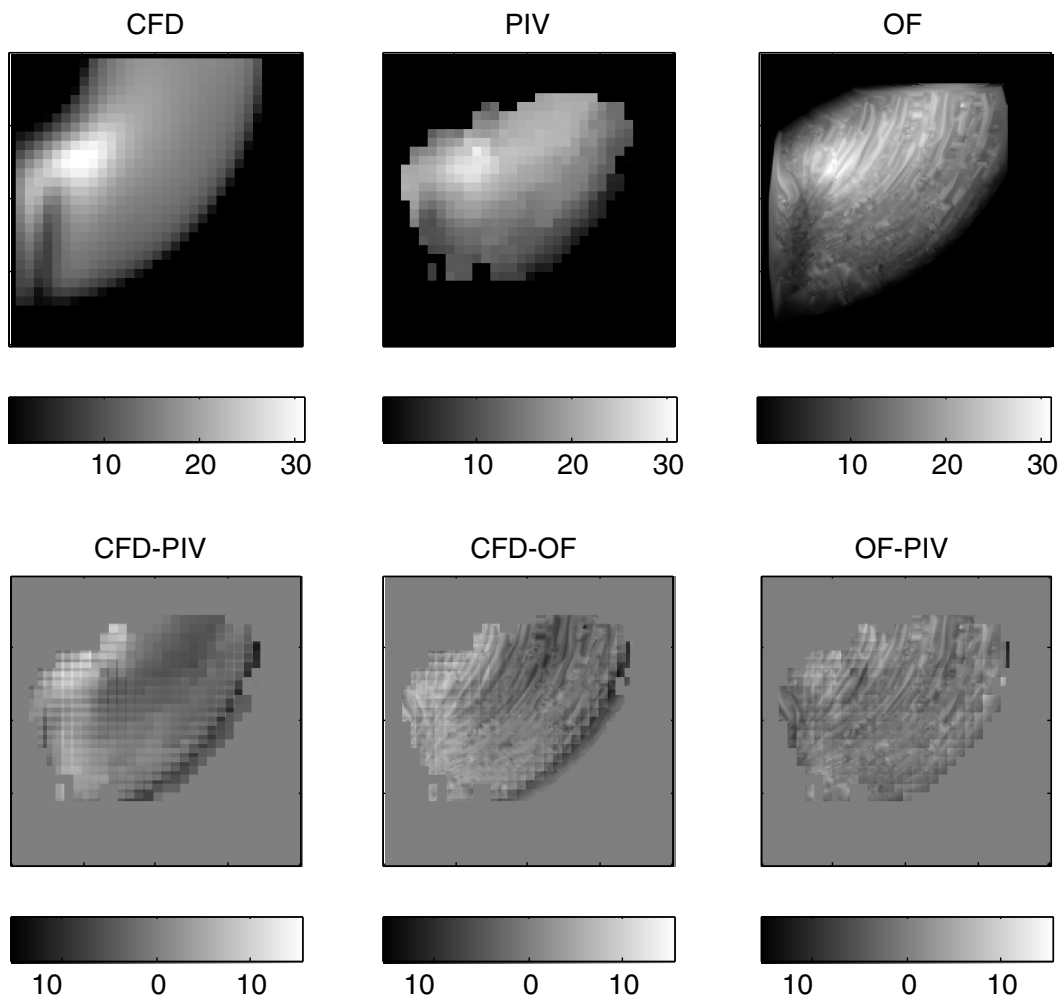
Figure 8.24: *Top: Wall shear rates determined by computational fluid dynamics (left), PIV-technique (center) and our optical-flow-based method (right). Bottom: Pointwise Differences between CFD and PIV (left), CFD and optical flow (center), optical flow and PIV (right).*

9 Summary and Outlook

The aim of this thesis has been the development and testing of a technique for the spatio-temporal analysis of flows close to free water surfaces. Knowledge about the 3D-flow fields within and beneath the water-side viscous boundary layer is vitally important for our understanding of the transport of momentum and mass. Previous methods applied to this question commonly rely on 2D laser light sections followed by velocity reconstruction based on cross correlation. The new method overcomes the restriction of planar dimensionality by both a sophisticated experimental setup and data analysis based on contemporary image processing techniques.

9.1 Summary

A fluid volume is illuminated by light emitting diodes. Small spherical particles are added to the fluid, functioning as a tracer. A camera pointing to the water surface from above records the image sequences. A dye is added to the fluid, which limits the penetration depth of the light into the flow according to Beer-Lambert's law. Within the illuminated layer the particles appear more or less bright, depending on their normal distance to the wall: Particles near the wall appear brighter, i.e. have a higher gray value than particles farther away from the wall. Illuminating the fluid alternatively with LEDs of two different emission spectra, which overlap with the absorption spectrum of the dye unequally, the size of a particle has not to be known, so that the size distribution of the spheres is allowed to be broad. A proper selection of tracer particles, dye and LEDs is essentially for the presented method. Like in all quantitative flow visualisation techniques, optics and camera have to be adjusted to the experiment.

Information about the 3D position of the particles in the fluid is retrieved by 2D grey value data. Special care has to be taken concerning the preprocessing of the image sequences and segmentation of the particles. The three components of a particle's velocity are obtained applying an extended optical-flow based approach. The information gained by previous optical-flow computation was used to obtain a better performance for particle tracking. Thus both, the Eulerian velocity field and the Lagrangian flow-representation can be extracted. Postprocessing tackles the problem of overlapping particles and enhances the length of the trajectories. In order to determine the wall shear stress, the wall shear rate can be estimated directly without previous computation of the velocity vector field using parametric modeling of 3D affine flow fields.

Both, measurement setup and algorithmics are tested in several ways:

1. For correct depth-reconstruction an easy-to-handle two-point-calibration technique was employed. The applicability of Beer-Lambert's law was validated by measurements using a linear positioner.
2. A laminar falling film serves as reference flow. The theoretical parabolic profile of this stationary flow could be reproduced by measurements very well.

3. Buoyant convective turbulence acts as an example for an instationary, inherently three dimensional flow. Qualitative investigations and comparisons with the appropriate literature show, that the results are physically plausible.

4. The direct estimation of the wall shear rate was applied to sequences recorded in the field of biofluidmechanics. Our results are in good agreement with the "ground truth" and outperform the analysis based on PIV which is a standard method in experimental fluid mechanics.

9.2 Outlook

The technique described in this thesis constitutes the first part of a comprehensive research project embedded in the priority program 1147 of the German Research Foundation. Ultimate goal of the project is the voluminetric analysis of flows close to moving and wave-driven curved interfaces. Further steps to achieve this ambitious aim are:

- By performing simultaneous measurements using other techniques, like infrared thermography, we can test the applicability of the current setup and algorithmics to instationary 3D-flows like turbulent convection quantitatively.

- Surface divergences and convergences are related to the transport of momentum and mass. Modeling of 3D affine flow fields can be used for a direct estimation of these important quantities. Testing can be accomplished using the convection tank designed in the scope of this thesis.

- The measurement setup will be installed in a linear wind-wave tank. Using this facility, we can generate a shear flow. At flows with moderate speeds or applying surfactants, i. e. without waves present, the velocity profile obeys the universal wall law discussed in section 2.3.2. This yields a method to validate the computation of the wall shear stress.

- The analysis of wavy flows is a great challenge, due to refraction and geometrical distortions at the curved surface. In order to get knowledge of the geometry of moving boundary conditions, flow measurement has to be supplemented by simultaneous recording of the wave slope.

A Total Least Squares

An excellent overview on the TLS-Problem is given by [van Huffel and Vandewalle, 1991]. The term "total least squares" was introduced by [Golub and van Loan C. F., 1980], though it was known in statistical literature as orthogonal regression or errors-in-variables regression since the 19th century. [Naya et al., 2006] give a critical overview on the errors of OLS (ordinary least squares), TLS and equilibrated TLS, addressing the estimation of a 2D homography as a reference problem.

For our purpose we will merely summarize the key aspects of data regression using an analysis based on OLS, TLS, weighted TLS and equilibrated TLS. Fitting a straight light serves as simple example to illustrate the benefits of error-in-variables regression. The last section of this chapter presents the TLS estimation from normal equations. We will see, that diagonalising the structure tensor $\boldsymbol{J} = \boldsymbol{D}^T \boldsymbol{D}$ is equivalent to a TLS fit to the data matrix $\boldsymbol{D}$.

A.1 Ordinary Least Squares

To introduce into the subject of TLS, we will treat the case of ordinary least squares (OLS) firstly. A regression problem can be summarised in the matrix-vector-equation:

$$\boldsymbol{A}\boldsymbol{m} = \boldsymbol{b},$$

where $\boldsymbol{A} \in \mathbb{R}^{m \times n}$ is the data matrix, $\boldsymbol{m} \in \mathbb{R}^m$ is the parameter vector and $\boldsymbol{b} \in \mathbb{R}^n$ is the observation vector. Fitting n points in the $x-y$-plane to a straight line for example, $\boldsymbol{A} = (x_i, 1)$ is a $2 \times n$-matrix, containing the points, $\boldsymbol{m}$ is the two-dimensional parameter vector, and $\boldsymbol{b}$ contains the corresponding y-values. The task, to be performed, can be expressed as a minimisation problem:

$$\left\| \boldsymbol{b} - \hat{\boldsymbol{b}} \right\|_2 \to \min,$$

where $\hat{\boldsymbol{b}}$ denotes the optimised observation vector. In the example above, $\hat{\boldsymbol{b}}$ would be part of the line, which can be expressed by the parameters $\boldsymbol{m}$. The optimal solution in an OLS-sense is given by applying the Moore-Penrose Inverse $(\boldsymbol{A}^T \boldsymbol{A})^{-1} \boldsymbol{A}^T$ to the observation vector:

$$\boldsymbol{m} = (\boldsymbol{A}^T \boldsymbol{A})^{-1} \boldsymbol{A}^T \boldsymbol{b}.$$

[Gauss, 1823] showed, that the estimate $\boldsymbol{m}$ has the smallest variance in the class of estimation methods, which display no systematic error in the estimates and whose estimates are linear functions of $\boldsymbol{b}$. One kind of differential optical flow technique is based on OLS: the local weighted least squares-method originally proposed by [Lucas and Kanade, 1981].

A.2 Total Least Squares

Now we allow, that besides the data matrix $\boldsymbol{A}$, the observation vector $\boldsymbol{b}$ also contains errors. Here it is assumed, that the noise is the same for the data matrix and for the observation vector. Now we arrive at a slightly different minimisation problem:

$$\left\|(\boldsymbol{A}, \boldsymbol{b}) - (\hat{\boldsymbol{A}}, \hat{\boldsymbol{b}})\right\|_F \to \min, \quad (\boldsymbol{A}, \boldsymbol{b}), (\hat{\boldsymbol{A}}, \hat{\boldsymbol{b}}) \in \mathbb{R}^{m \times (n+1)},$$

where $\|\cdot\|_F$ denotes the Frobenius norm, that is $\|\boldsymbol{A}\| = \sqrt{\sum_i \sum_j |a_{ij}|^2}$.

This can be transformed to

$$(\boldsymbol{D}^T \boldsymbol{p})^2 \to \min \quad \text{subject to} \quad \boldsymbol{p}^T \boldsymbol{p} = 1,$$

where $\boldsymbol{D} = (\boldsymbol{A}^T, -\boldsymbol{b})^T \in \mathbb{R}^{m \times (n+1)}$ is a matrix, composed of the data matrix $\boldsymbol{A}$ and the observation vector $\boldsymbol{b}$, and $\boldsymbol{p}$ is a new parameter vector of dimension $n + 1$. In order to avoid the trivial solution, we require the norm of the parameter vector to be unity. This formulation of the TLS-problem is also known as the orthogonal L_2 approximation problem. The sought model parameters $\boldsymbol{m}$ can be estimated from the parameter vector $\boldsymbol{p}$, by dividing the first n components by the $(n + 1)$th component:

$$m_i = p_i / p_{n+1} \quad \text{for} \quad i = 1, \ldots, n - 1.$$

In the following we will address the equation

$$\boldsymbol{D}^T \boldsymbol{p} = 0 \tag{A.1}$$

as the basic TLS-equation. The minimization problem can be written in integral form as follows:

$$\int_U (\boldsymbol{D}^T(\boldsymbol{x}', t') \boldsymbol{p})^2 \mathrm{d}\boldsymbol{x}' \mathrm{d}t' \to \min \quad \text{subject to} \quad \boldsymbol{p}^T \boldsymbol{p} = 1,$$

where $\boldsymbol{d}(\boldsymbol{x}, t)$ are the rows of the data matrix $\boldsymbol{D}$, and the integration is performed over a neighbourhood U, to sufficiently constrain the problem.

A.3 Weighted Total Least Squares

In the formulation of the TLS problem from the previous section, the rows in the data matrix $\boldsymbol{D}$ were treated equal. But, because in optical-flow-based motion estimation for example, it is the case, that the observations are weighted differently depending on their relative location in a local neighbourhood, we have to reformulate our minimisation problem to:

$$\int_{-\infty}^{\infty} w(\boldsymbol{x} - \boldsymbol{x}', t - t')(\boldsymbol{D}^T(\boldsymbol{x}', t') \boldsymbol{p})^2 \mathrm{d}\boldsymbol{x}' \mathrm{d}t' \to \min \quad \text{subject to} \quad \boldsymbol{p}^T \boldsymbol{p} = 1. \tag{A.2}$$

We have introduced a weighting function w, which weighs the point in the spatio-temporal neighbourhood differently, according to their relative significance. We arrive at another representation of the WTLS-Problem by multiplying the data matrix $\boldsymbol{D}$ with a left hand weighting matrix $\boldsymbol{W}_L$:

$$(\boldsymbol{W}_L \boldsymbol{D}) \boldsymbol{p} \to \min$$

A.4 Equilibrated Total Least Squares

In the previous section we have addressed the problem of weighting each data point individually. Now we arrive at the question: What has to be done, if the errors of the variables haven't to be treated equally? Consider for example the OLS-case: Here we have no errors in the observations, so it is not feasible to apply a TLS-solver to such a problem. This is an extreme case, but you can imagine other situations, where for example the errors in the observations ("y-axis") are half of the errors in the data ("x-axis"). [Mühlich and Mester, 1999] have developed a framework, how to incorporate this problem, and we will summarise it here shortly.

The key is introducing a diagonal right hand weighting matrix $\boldsymbol{W}_R = \mathrm{diag}(1/\sigma_i)$, which contains the errors in the parameters. Our minimisation problem reads now:

$$(\boldsymbol{W}_L \boldsymbol{D} \boldsymbol{W}_R)\boldsymbol{p} \to \min$$

Applying diagonal equilbration matrices can be interpreted as row and column *scaling* of the data matrix $\boldsymbol{D}$. This procedure is well known and is often used to obtain numerically stable results [Golub and van Loan, 1996].

A.5 Example: Fitting a Straight Line

In this section we will summarise the content presented in this section by applying OLS, TLS and equilibrated TLS (E-TLS) to the simple problem of fitting a straight line to the data (x_i, y_i). The line can be described by the equation

$$y = mx + b,$$

where m is the slope, and b is the intercept.

Reformulating the problem in OLS-notation yields

$$\boldsymbol{A}\boldsymbol{m} = \boldsymbol{b}, \quad \text{with} \quad \boldsymbol{A} = (x_i, 1), \ \boldsymbol{m} = (m, b)^T, \ \boldsymbol{b} = (y_i).$$

We get the optimal parameters of the line in OLS-sense by applying the Moore-Penrose-Inverse: $\boldsymbol{m} = (\boldsymbol{A}^T \boldsymbol{A})^{-1} \boldsymbol{A}^T$ to $\boldsymbol{b}$. OLS is optimal, if we have Gaussian noise in the x-coordinates only.

We are better off using a TLS-solver, if we have the same degree of noise in both x- and y-coordinates. In TLS we use a slightly different notation:

$$\boldsymbol{D}\boldsymbol{p} = 0, \quad \text{with} \quad D = (A^T, -\boldsymbol{b})^T = (x_i, 1, -y_i), \ \boldsymbol{p} = (m, b, 1).$$

This normal equation can be solved by means of a Lagrange multiplier, which will be explained in the next section.

Finally we will take advantage of the benefits of equilibration. Therefore we assume, that for instance the noise in the x-coordinate is $\sigma_x = 1$ and in the y-coordinate it is $\sigma_y = 0.5$. Starting from this, we can construct a right hand weighting matrix:

$$\boldsymbol{W}_R = \mathrm{diag}(1/\sigma_i) = \begin{pmatrix} 1/\sigma_x & 0 & 0 \\ 0 & 1 & 0 \\ 0 & 0 & 1/\sigma_y \end{pmatrix} = \begin{pmatrix} 1 & 0 & 0 \\ 0 & 1 & 0 \\ 0 & 0 & 2 \end{pmatrix}.$$
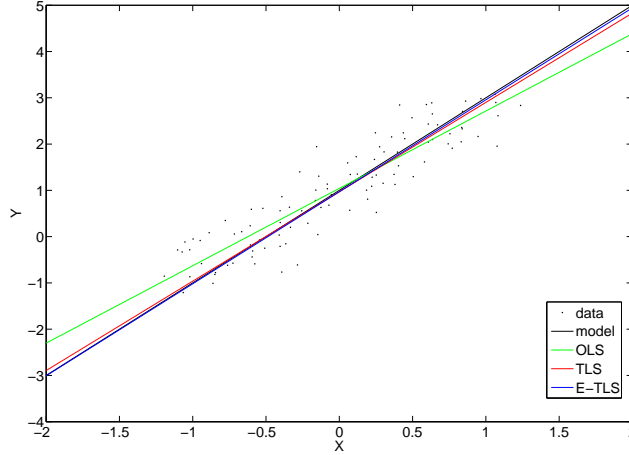
Figure A.1: *Numerical example of fitting a straight line: The model is $y = 2x + 1$. The noise is $\sigma_x = 1$ and $\sigma_y = 0.5$ The results of OLS, TLS and equilibrated TLS are displayed for one selected experiment. It is evident, that E-TLS performs best, while TLS is slightly worse and OLS is the worst.*

Our E-TLS-Problem now becomes:

$$(\boldsymbol{DW}_R)\boldsymbol{p} = (x_i, 1, -2y_i)(m, b, 1)^T = 0.$$

It is evident, that equilibration is nothing else, than column scaling of the data matrix $\boldsymbol{D}$. A numerical example of fitting a straight line is given in Figure A.1.

A.6 TLS Estimates from Normal Equations

In this section we will derive the structure tensor starting from the examinations made in the previous chapters. Our starting point is Eq. (A.2): The weighted total least squares problem together with the necessary requirement $\|\boldsymbol{p}\| = 1$, applied to spatio-temporal data $\boldsymbol{d}(\boldsymbol{x}, t)$ in a weighted spatio-temporal neighbourhood. We have to solve a minimisation problem. It would be a good idea, to incorporate this requirement into the functional to be minimised. This can be done by means of introducing a Lagrangian multiplier:

$$E = \int_{-\infty}^{\infty} w(\boldsymbol{x} - \boldsymbol{x}', t - t') \left[(\boldsymbol{d}^T(\boldsymbol{x}', t')\boldsymbol{p})^2 + \lambda \left(1 - \sum_{i=1}^{n} p_i^2 \right) \right] \mathrm{d}\boldsymbol{x}' \mathrm{d}t' \to \min$$

The energy functional E reaches a minimum, when the derivatives with respect to all variables vanish. These derivatives are:

$$\frac{\partial E_i}{\partial p_i} = 2 \int_{-\infty}^{\infty} w(\boldsymbol{x} - \boldsymbol{x}', t - t') \left[d_i(\boldsymbol{d}^T(\boldsymbol{x}', t')\boldsymbol{p}) - \lambda p_i \right] \mathrm{d}\boldsymbol{x}' \mathrm{d}t' \quad \text{for} \quad i = 1 \dots n.$$

If we require a constant parameter field $\boldsymbol{p}$ in our local neighbourhood U, then the p_i can be taken out of the integral:

$$p_1 \int_U d_i d_1 \mathrm{d}\boldsymbol{x}' \mathrm{d}t' + \ldots + p_n \int_U d_i d_n \mathrm{d}\boldsymbol{x}' \mathrm{d}t' = \lambda p_i \quad \text{for} \quad i = 1 \ldots n,$$

where we assumed the weight function to be normalised for the right hand side: $\int w \mathrm{d}\boldsymbol{x}' \mathrm{d}t' = 1$. These n equations can be written in vector-matrix-form, introducing the *structure tensor* $\boldsymbol{J}$:

$$\boldsymbol{J}\boldsymbol{p} = \lambda\boldsymbol{p} \quad \text{with} \quad \boldsymbol{J} = \int_{-\infty}^{\infty} w(\boldsymbol{x} - \boldsymbol{x}', t - t')\boldsymbol{d}(\boldsymbol{x}', t')\boldsymbol{d}(\boldsymbol{x}', t')^T \mathrm{d}\boldsymbol{x}' \mathrm{d}t'. \tag{A.3}$$

It follows, that Eq. (A.2) is minimized by the Eigenvector $\boldsymbol{p}_n$ to the smallest Eigenvalue λ_n of $\boldsymbol{J}$. We have arrived at an equation, which is similar to the Eigenvalue equation Eq. (4.19). The difference is, that now the *parameter vector* $\boldsymbol{p}$ represents the Eigenvectors. So Eq. (A.3) is a generalization of the former Eigenvalue problems. It can be transformed to Eq. (4.19), if we consider a spatio-temporal problem, where $n = 3$:

$$\boldsymbol{p} = (p_x, p_y, p_t)^T \equiv \boldsymbol{r}_3 = (r_{3x}, r_{3y}, r_{3t}).$$

By deducing this TLS solution mathematically rigorously instead of inducing it intuitively, we have laid the foundations for solving more complicated TLS-problems.

B The Lie Group of Continuous Transformations

B.1 Generalization of the Affine Subgroup in 2D

The affine group is a subgroup of the *Lie group of continuous transformations*. An excellent overview over the mathematical prerequisites is given in [Olver, 1986]. [Bluman and Kumei, 1989] present this topic from the view of applied mathematicians. In [Kanatani, 1990] some applications of the Lie group of continuous transformations to computer vision are presented.

In section 4.3.1 we have taken a look at affine transformations of the kind $\boldsymbol{f} = \boldsymbol{t} + \boldsymbol{A}\boldsymbol{x} + \boldsymbol{a}t$. Now we will replace the flow vector $\boldsymbol{f}$ by a generalised transformation $\boldsymbol{r} = \boldsymbol{S}(\boldsymbol{r}', \boldsymbol{a})$, where $\boldsymbol{a}$ is a parameter vector ($\boldsymbol{r}, \boldsymbol{r}' \in \mathbb{R}^N, \boldsymbol{a} \in \mathbb{R}^P$). $\boldsymbol{S}$ forms a one-parameter Lie group of continuous transformations if following properties hold (amongst others):

1. There exists an identity element of the group: $\boldsymbol{r} = \boldsymbol{S}(\boldsymbol{r}, 0)$.
2. There exists the inverse transformation: $\boldsymbol{r}' = \boldsymbol{S}^{-1}(\boldsymbol{r}, \boldsymbol{a})$.
3. $\boldsymbol{a}$ is a continuous parameter in a given interval in $\mathbb{R}^P$.
4. $\boldsymbol{r} = \boldsymbol{S}(\boldsymbol{r}', \boldsymbol{a})$ is infinitely differentiable in $\boldsymbol{r}$ and analytical in $\boldsymbol{a}$. A real function is analytical, if it can be expressed by a power series locally.

From the last property, it follows, that we can expand the vector $\boldsymbol{r}$ in a Taylor series about $\boldsymbol{a} = 0$:

$$r_j = S_j(r_j', \boldsymbol{a}) \approx S_j(r_j', 0) + \sum_{i=1}^{P} a_i \frac{\partial S_j(r_j', \boldsymbol{a})}{\partial a_i} = r_j' + \sum_{i=1}^{P} a_i \frac{\partial r_j}{\partial a_i} \quad \text{for} \quad j = 0 \ldots N. \quad \text{(B.1)}$$

Now we expand the brightness function $g(\boldsymbol{r})$ about $\boldsymbol{r}'$ with respect to the parameters a_i:

$$g(\boldsymbol{r}) \approx g(\boldsymbol{r}') + \sum_{i=1}^{P} a_i \frac{\partial g(\boldsymbol{r})}{\partial a_i}, \quad \text{(B.2)}$$

using following expressions for the brightness function's dependence of the transformation parameters (together with Equation (B.1)):

$$\frac{\partial g(\boldsymbol{r})}{\partial a_i} = \sum_{j=0}^{N} \frac{\partial g}{\partial r_j} \frac{\partial r_j}{\partial a_i} = \sum_{j=0}^{N} \frac{\partial g}{\partial r_j} \frac{\partial S_j(r_j, \boldsymbol{a})}{\partial a_i} \equiv \mathfrak{L}_i g(\boldsymbol{r}),$$

where $\mathfrak{L}_i, i \in \{1, \ldots, P\}$ is the infinitesimal generator of the Lie group. With the assumption of brightness conservation $g(\boldsymbol{r}) = g(\boldsymbol{r}')$ along the trajectory, Eq. (B.2) becomes

$$\sum_{i=1}^{P} a_i \frac{\partial g(\boldsymbol{r}')}{\partial a_i} = \sum_{i=1}^{P} a_i \mathfrak{L}_i g(\boldsymbol{r}') \equiv (\mathfrak{L}g)^T \boldsymbol{a} = 0, \quad \text{(B.3)}$$

137

which is a more general version of the EBCCE (see Eq. (4.20)).

Example: Translation. The corresponding coordinate transformation reads

$$\boldsymbol{r}' = \boldsymbol{S}(\boldsymbol{r}, \boldsymbol{a} = (\boldsymbol{t}, 1)^T) = (x, y)^T + \boldsymbol{t},$$

where $\boldsymbol{t} = (t_1, t_2)^T$ denotes the translation vector, and $\boldsymbol{r} = (x, y, t)$ denotes a point in the 2+1 dimensional space. The infinitesimal generators are calculated to:

$$\mathfrak{L}_1 = \frac{\partial S_1}{\partial a_1} \frac{\partial}{\partial r_1} + \frac{\partial S_2}{\partial a_1} \frac{\partial}{\partial r_2} + \frac{\partial S_3}{\partial a_1} \frac{\partial}{\partial r_3} = 1 \frac{\partial}{\partial x} + 0 + 0, \quad \mathfrak{L}_2 = \frac{\partial}{\partial y}, \quad \text{and} \quad \mathfrak{L}_3 = \frac{\partial}{\partial t},$$

so that the EBCCE Eq. (B.3) becomes

$$\sum_{i=1}^{3} a_i \mathfrak{L}_i g(\boldsymbol{r}') = t_1 \frac{\partial}{\partial x} g + t_2 \frac{\partial}{\partial y} g + 1 \frac{\partial}{\partial t} g = 0,$$

which can be identified as the BCCE.

Example: Affine Transformation. The corresponding coordinate transformation reads

$$\boldsymbol{r}' = \boldsymbol{S}(\boldsymbol{r}, \boldsymbol{a} = (\boldsymbol{t}, \boldsymbol{A}, 1)^T) = \boldsymbol{A}(x, y)^T + \boldsymbol{t},$$

where $\boldsymbol{A} = (a_{ij})$ is a 2×2 matrix, and $\boldsymbol{t} = (t_1, t_2)^T$ denotes the translation vector. Again $\boldsymbol{r} = (x, y, t)$ is a point in the 2+1 dimensional space. The infinitesimal generators are in this case:

$$\mathfrak{L}_1 = \frac{\partial S_1}{\partial a_1} \frac{\partial}{\partial r_1} + \frac{\partial S_2}{\partial a_1} \frac{\partial}{\partial r_2} + \frac{\partial S_3}{\partial a_1} \frac{\partial}{\partial r_3} = x \frac{\partial}{\partial x} + 0 + 0, \quad \mathfrak{L}_2 = y \frac{\partial}{\partial y}, \quad \mathfrak{L}_3 = x \frac{\partial}{\partial y}$$

$$\mathfrak{L}_4 = y \frac{\partial}{\partial y}, \quad \mathfrak{L}_5 = \frac{\partial}{\partial x}, \quad \mathfrak{L}_6 = \frac{\partial}{\partial y}, \quad \text{and} \quad \mathfrak{L}_7 = \frac{\partial}{\partial t}.$$

so that the EBCCE reads in this case

$$\sum_{i=7}^{P} a_i \mathfrak{L}_i g(\boldsymbol{r}') = a_{11} x \frac{\partial}{\partial x} g + a_{22} y \frac{\partial}{\partial y} g + a_{12} x \frac{\partial}{\partial y} g + a_{21} y \frac{\partial}{\partial x} g + t_1 \frac{\partial}{\partial x} g + t_2 \frac{\partial}{\partial y} g + \frac{\partial}{\partial t} g.$$

B.2 Generalization of the Affine Subgroup in 3D

Again, we loose the assumption of having an affine transformation, and replace the vector $\boldsymbol{u}$ by a generalised transformation $\boldsymbol{r} = S(\boldsymbol{r}', \boldsymbol{a})$, like we did in the previous section. Amongst others, Eq. (B.3) holds for the 3D-case, too.

Example: Rotation About the x-Axis. The rotation about the x-axis, which is essentially the first component of the vorticity vector, is given by

$$\omega_1 = \epsilon_{ij1} \gamma_{ij} = \gamma_{23} - \gamma_{32} = \frac{\partial u_2}{\partial x_3} - \frac{\partial u3}{\partial x2}.$$

The corresponding coordinate transformation reads

$$\boldsymbol{r}' = S(\boldsymbol{r}, \boldsymbol{a} = (\gamma_{23}, \gamma_{32}, 1)^T) = (0, \gamma_{23}z, -\gamma_{32}y, 0)^T,$$

where $\boldsymbol{r} = (x, y, z, t)^T$ denotes a point in the 3+1 dimensional space. The infinitesimal generators are calculated to:

$$\mathfrak{L}_1 = \frac{\partial S_1}{\partial a_1}\frac{\partial}{\partial r_1} + \frac{\partial S_2}{\partial a_1}\frac{\partial}{\partial r_2} + \frac{\partial S_3}{\partial a_1}\frac{\partial}{\partial r_3} + \frac{\partial S_4}{\partial a_1}\frac{\partial}{\partial r_4} = 0 + z\frac{\partial}{\partial y} + 0 + 0, \quad \mathfrak{L}_2 = -y/z_*, \quad \mathfrak{L}_3 = \frac{\partial}{\partial t},$$

so, that the three dimensional extension of the EBCCE Eq. (B.3) reads in this case

$$\sum_{i=1}^{3} a_i \mathfrak{L}_i g(\boldsymbol{r}') = \gamma_{23}z\frac{\partial}{\partial y}g - \gamma_{32}y\frac{g}{z_*} + \frac{\partial}{\partial t}.$$

Note, that for building the derivatives we used an extension of the augmented gradient: $\partial/\partial r_i = (\tilde{\nabla}^T, \partial/\partial t) = (\partial/\partial x, \partial/\partial y, 1/z_*, \partial/\partial t)$.

Bibliography

R. J. Adrian. Particle-imaging techniques for experimental fluid mechanics. *Annu. Rev. Fluid Mech.*, 23:261–304, 1991. 28

J. C. Agüi and J. Jimenez. On the performance of particle tracking. *Journal of Fluid Mechanics*, 185:261–304, 1987. 93, 94

H.-E. Albrecht, M. Borys, N. Damaschke, and C. Tropea. *Laser Doppler and phase Doppler measurement techniques*. Springer Verlag, Berlin, Heidelberg, 2003. 27

G. Balschbach, J. Klinke, and B. Jähne. Multichannel shape from shading techniques for moving specular surfaces. In *Computer Vision - ECCV'98*. Springer, Berlin, 2001. 17

M. L. Banner. The influence of wave breaking on the surface pressure distribution in wind-wave interactions. *J. Fluid Mech.*, 211:463–495, 1990. 21

M. L. Banner and W. L. Peirson. Tangential stress beneath wind-driven air-water interfaces. *Journal of Fluid Mechanics*, 364:115–145, 1998. 21, 22

M. L. Banner and O. M. Phillips. On the incipient breaking of small scale waves. *J. Fluid Mech.*, 65:647–656, 1974. 18

J. L. Barron, D. J. Fleet, and S. S. Beauchemin. Performance of optical flow techniques. *Intern. J. Comput. Vis.*, 12(1):43–77, 1994. 35, 36

R. J. M. Bastiaans, G. A. J. van der Plas, and R. N. Kieft. The performance of a new PTV algorithm applied in super-resolution PIV. *Experiments in Fluids*, 32:346–356, 2002. 33

S. Beucher. The watershed transformation applied to image segmentation. In *Conference on Signal and Image Processing in Microscopy and Microanalysis*, pp. 299–314, 1991. 82

M. J. Black and A. P. The robust estimation of multiple motions: parametric and piecewise-smooth flow fields. *Computer Vision and Image Understanding*, 63:75–104, 1996. 46

G. W. Bluman and S. Kumei. *Symmetries and differential equations*. Springer Verlag, Berlin, Heidelberg, New York, 1989. 137

D. Braun. *Die effektive Diffusion im welligen Rieselfilm*. Phd thesis, Rheinisch-Westfälisch Technische Hochschule Aachen, 1969. 104

C. Brücker. 3-D PIV via spatial correlation in a color-coded light-sheet. *Experiments in Fluids*, 21:312–314, 1996. 31

S. J. K. Bukhari and M. H. K. Siddiqui. Turbulent structure beneath air-water interfaces during natural convection. *Physics of Fluids*, 18(035106), 2006. 117, 121

H.-C. Chang and E. A. Demekhin. *Complex wave dynamics on thin films*. Elsevier, 2002. 104

M. Coantic. A model of gas transfer across air-water interfaces with capillary waves. *Journal of Geophysical Research*, 91:3925–3943, 1986. 14

I. Cohen and I. Herlin. Non uniform multiresolution method for optical flow and phase portrait models: environmental applications. *International Journal of Computer Vision*, 33(1):24–49, 1999. 45

E. D. Cokelet. Breaking waves. *Nature*, 267:769–774, 1977. 18

T. Corpetti, E. Memin, and P. Perez. Dense estimation of fluid flows. *IEEE Trans. on Pattern Analysis and Machine Intelligence*, 24(3):365–380, 2002. 38, 48

T. Corpetti, D. Heitz, G. Arroyo, E. Memin, and A. Santa-Cruz. Fluid experimental flow estimation based on an optical-flow scheme. *Exp. Fluids*, 40(1):80–97, 2005. 48

E. Cowen and S. Monismith. A hybrid digital particle tracking velocimetry technique. *Experiments in Fluids*, 22:199–211, 1997. 33, 90

G. T. Csanady. The role of breaking wavelets in air-sea gas transfer. *J. Geophs. Res.*, 95:749–759, 1990. 17, 20

P. V. Danckwerts. Significance of liquid-film coefficients in gas absorption. *Industrial and Engineering Chemistry*, 43:1460–1467, 1951. 13

E. L. Deacon. Gas transfer to and across an air-water interface. *Tellus*, 29:363–374, 1977. 16

P. Debaene. *Neuartige Messmethode zur zeitlichen und örtlichen Erfassung der wandnahen Strömung in der Biofluidmechanik*. Phd thesis, TU Berlin, 2005. 3, 49, 99, 121, 122, 123, 124, 125, 126

K. Degreif. *Untersuchungen zum Gasaustausch: Entwicklung und Applikation eines zeitlich aufgelösten Massenbilanzverfahrens*. Phd thesis, Universität Heidelberg, 2006. 14

M. Detert, G. H. Jirka, M. Jehle, M. Klar, B. Jähne, H.-J. Köhler, and T. Wenka. Pressure fluctuations within subsurface gravel bed caused by turbulent open-channel flow. In *Proc. of River Flow 2004*, pp. 695–701. A. A. Balkema Publishers, 2004. 24

J. Dieter and B. Jähne. Flow Measurements close to the free air/sea interface. In Dieter, J. and Jähne, B., eds., *Proceedings of the 7th International Symposium on Applications of Laser Techniques to Fluid Mechanics*. Lisbon, July 1994. 21

F. Durst, A. Melling, and J. H. Whitelaw. Principles and practise of laser-Doppler anemometry. *NASA STI/Recon Technical Report A*, 76:47019–+, 1976. 27

H. Eckelmann. *Einführung in die Strömungsmesstechnik*. Teubner, Stuttgart, 1997. 24

D. Engelmann. *3D-flow measurement by stereo imaging*. PhD thesis, University of Heidelberg, 2000. 32

G. Farnebäck. Fast and accurate motion estimation using orientation tensors and parametric motion models. In *Proc. ICPR*, vol. 1, pp. 135–139. Barcelona, Spain, 2000. 43

H. H. Fernholz, G. Janke, M. Schober, P. M. Wagner, and D. Warnack. New developments and applications for skin-friction measuring techniques. *Meas. Sci. Technol.*, 7:1396–1409, 1996. 24

K. A. Flack, J. R. Saylor, and G. B. Smith. Near-surface turbulence for evaporative convection at an air/water interface. *Physics of Fluids*, 13(11):529, 2001. 117

C. Garbe, H. Spies, and B. Jähne. Estimation of surface flow and net heat flux from infrared image sequences. *Journal of Mathematical Imaging and Vision*, 19:159–174, 2003. 24, 48

C. F. Gauss. Theoria combinationis observationum erroribus minimis obnoxiae. *Comment. Soc. Reg. Sci. Gotten. Recent.*, 5:33–90, 1823. 131

S. Geman and D. E. McClure. Bayesian image analysis: An application to single photon emission tomography. In *Proc. Amer. Statist. Assoc. Statistical Computing Section*, pp. 12–18, 1984. 45

G. H. Golub and C. F. van Loan, eds. *Matrix computations*. The John Hopkins University Press, Baltimore and London, 1996. 133

G. H. Golub and van Loan C. F. An analysis of the total least squares problem. *SIAM Journal on Numerical Analysis*, 17(6):883–893, 1980. 131

G. H. Granlund and K. H. *Signal processing for computer vision*. Kluwer, 1995. 36

F. J. Green. *The Sigma-Aldrich handbook of stains, dyes and indicators*. Aldrich Chemical Company Inc., Milwaukee, Wisconsin, 1990. 62

A. W. Gruen. Adaptive least squares correlation: a powerful image matching technique. *S Afr J of Photogrammetry, Remote Sensing and Cartography*, 14(3):175–187, 1985. 28

L. Gui and S. T. Wereley. A correlation based continuous window-shift technique to reduce the peak-locking effect in digital PIV evaluation. *Experiments in Fluids*, 32:506–517, 2002. 30

R. Hain and C. J. Kähler. Dynamisches Auswerteverfahren für zeitaufgelöste PIV-Bildsequenzen. In *12. Fachtagung "Lasermethoden in der Strömungsmesstechnik"*. Universität Karlsruhe, 2004. 30

H. Haussecker, S. Reinelt, and B. Jähne. Heat as a proxy tracer for gas exchange measurements in the field: principles and technical realization. In *Selected Papers from the 3rd International Symposium on Air-Water Gas Transfer*, pp. 405–413, 1995. 21

H. W. Haussecker and D. J. Fleet. Computing optical flow with physical models of brightness variation. *PAMI*, 23(6):661–673, 2001. 46

H. Helmholtz. Über die Integrale der hydrodynamischen Gleichungen, welche den Wirbelbewegungen entsprechen. *Crelles J.*, 55:25, 1858. 6

F. Hering. *Lagrangesche Untersuchungen des Strömungsfeldes unterhalb der wellenbewegten Wasseroberfläche mittels Bildfolgenanalyse*. PhD thesis, University of Heidelberg, 1996. 31, 94

F. Hering, M. Merle, D. Wierzimok, and B. Jähne. A robust technique for tracking particles over long image sequences. In *Proc. of ISPRS Intercommission Workshop 'From Pixels to Sequences', Int'l Arch. of Photog. and Rem. Sens.*, 1995a. 82

F. Hering, D. Wierzimok, and B. Jähne. Measurements of enhanced turbulence in short wind-induced water waves. In *Selected Papers from the 3rd International Symposium on Air-Water Gas Transfer*, pp. 125–134, 1995b. 21

R. Higbie. The rate of absorption of a pure gas into a still liquid during short periods of exposure. *Trans. Am. Inst. Chem. Eng.*, 31:365–389, 1935. 13

W. J. Hiller, S. Koch, T. A. Kowalewski, and F. Stella. Onset of natural convection in a cube. *Int. J. Heat Mass Transfer*, 13:3251–3263, 1993. 24

K. D. Hinsch. Holographic particle image velocimetry. *Meas. Sci. Technol.*, 13:R61–R72, 2002. 30

A. Honkan and Andreopoulos. Vorticity, strain-rate and dissipation characteristics in the near-wall region of turbulent boundary layers. *J. Fluid Mech.*, 350:29–96, 1997. 26

B. K. P. Horn and B. G. Schunk. Determining optical flow. *Artificial Intelligence*, 17:185–204, 1981. 35, 39, 47

H. T. Huang, H. F. Fielder, and J. J. Wang. Limitation and improvement of PIV, part I. Limitation of conventional techniques due to deformation of particle image patterns. *Experiments in Fluids*, 15:168–174, 1993a. 30

H. T. Huang, H. F. Fielder, and J. J. Wang. Limitation and improvement of PIV, part II. Particle image distortion, a novel technique. *Experiments in Fluids*, 15:263–273, 1993b. 30

IPCC. Third assessment report: Climate change. Technical report, International Panel on Climate Change, 2001. 1

B. Jähne. *Digital image processing*. Springer-Verlag, Berlin, Heidelberg, 5th edn., 2002. 36, 41, 80, 87

B. Jähne, H. Haussecker, and P. Geissler, eds. *Handbook of computer vision and applications*. Academic Press, San Diego, CA, USA, 1999. 36, 37, 38, 42, 44, 45, 46

M. Jehle and B. Jähne. Direct estimation of the wall shear rate using parametric motion models in 3D. In *Pattern Recognition, 28th DAGM*, 2006a. 3

M. Jehle and B. Jähne. Eine neuartige Methode zur raumzeitlichen Analyse von Strömungen in Grenzschichten. In *Frühjahrstagung 2006 der Deutschen Physikalischen Gesellschaft*. Heidelberg, Germany, 2006b. 3

M. Jehle and B. Jähne. A novel method for spatiotemporal analysis of flows within the water-side viscous boundary layer. In *12th International Symposium of Flow Visualisation*. Göttingen, Germany, 2006c. 3

M. Jehle, M. Klar, and B. Jähne. Optical-Flow based velocity analysis. In C. Tropea, J. Foss, and A. Yarin, eds., *Springer Handbook of Experimental Fluid Dynamics*. Springer, Berlin, Heidelberg, in preparation. 4

M. Jehle, M. Klar, H.-J. Köhler, and M. Heibaum. Bewegungsdetektion und Geschwindigkeitsanalyse in Bildfolgen zur Untersuchung von Sedimentverlagerungen. In *Mitteilungen des Instituts für Grundbau und Bodenmechanik*, vol. 77, pp. 371–392. Braunschweig, Germany, 2004. 48

B. Jähne. *Transfer processes across the free water surface*. Professorial dissertation, University of Heidelberg, 1985. 2

B. Jähne, P. Libner, R. Fischer, T. Billen, and E. Plate. Investigating the transfer processes across the free aqueous viscous boundary layer by the controlled flux method. *Tellus*, 41B:177–195, 1989. 21

B. Jähne, K. O. Münnich, R. Bösinger, A. Dutzi, W. Huber, and P. Libner. On the parameters influencing air-water gas exchange. *J. Geophys. Res.*, 92:1937–1949, 1987. 19, 21

B. Jähne, M. Schmidt, and R. Rocholz. Combined optical slope/height measurements of short wind waves: principles and calibration. *Meas. Sci. Technol.*, 16:1937–1944, 2005. 17

K. Kanatani. *Group-theoretical methods in image understanding*. Springer Verlag, Berlin, Heidelberg, New York, 1990. 137

R. Keane, R. J. Adrian, and Y. Zhang. Super-resolution particle imaging velocimetry. *Meas. Sci. Technol.*, 6:754–768, 1995. 33

C. Kähler and J. Kompenhans. Fundamentals of multiple plane stereo particle image velocimetry. *Experiments in Fluids*, 29:70–77, 2000. 30

M. Klar. *Design of an endoscopic 3-D Particle-Tracking Velocimetry system and its application in flow measurements within a gravel layer*. Diss., Univ. Heidelberg, 2005. 31, 32

H. Knutsson and C.-F. Westin. Normalized and diffrential convolution. In *IEEE Conf. Computer Vision & Pattern Recognition*, pp. 515–523, 1993. 93

E. L. Koschmieder. *Bénard Cells and Taylor Vortices*. Cambridge University Press, 1993. 111

E. B. Kraus and J. A. Businger. *Atmosphere-ocean interaction*. Oxford University Press, 1994. 17

P. K. Kundu. *Fluid mechanics*. Academic Press, San Diego, USA, 1990. 8, 13, 111, 113

P. Lancaster and K. Salkauskas. *Curve and surface fitting. An introduction*. Acadamic Press, 1986. 93

R. Larsen. Estimation of dense image flow fields in fluids. *IEEE Transactions on Geoscience and Remote Sensing*, 36(1):256–264, January 1998. 41, 48

C. Le Quéré, O. Aumont, L. Bopp, P. Pousquet, P. Ciais, R. Francey, M. Heimann, C. D. Keeling, R. F. Keeling, H. Kheshgi, P. Peylin, S. C. Piper, I. C. Prentice, and P. J. Rayner. Two decades of ocean CO_2 sink and variability. *Tellus*, 55B:649–656, 2003. 1

C. Leue, P. Geissler, F. Hering, and B. Jähne. Segmentierung von Partikelbildern in der Strömungsvisualisierung. In *Proceedings of 18th DAGM-Symposium Mustererkennung, Informatik Aktuell*, pp. 118–129, 1996. 83, 84

P. S. Liss and P. G. Slater. Flux of gases across the air-sea interface. *Nature*, 247:181–184, 1974. 12

C. G. Lomas. *Fundamentals of hot wire anenometry*. Cambridge University Press, Cambridge, London, New York, Melbourne, 1986. 26

M. S. Longuet-Higgins. Capillary rollers and bores. *J. Fluid Mech.*, 240:659–679, 1992. 19

B. Lucas and T. Kanade. An iterative image registration technique with an application to stereo vision. In *DARPA Image Understanding Workshop*, pp. 121–130, 1981. 38, 41, 131

H. G. Maas, A. Gruen, and D. Papantoniou. Particle tracking velocimetry in three-dimensional flows, Part I: Photogrammetric determination of particle coordinates. *Experiments in Fluids*, 15:133–146, 1993. 32

N. A. Malik, T. Dracos, and D. Papantoniou. Particle tracking velocimetry in three-dimensional flows, Part II: Particle tracking. *Experiments in Fluids*, 15:279–294, 1993. 32

M. Marxen, P. E. Sullivan, M. R. Loewen, and B. Jähne. Comparison of Gaussian particle center estimators and the achievable measurement density for particle tracking velocimetry. *Experiments in Fluids*, 29:145–153, 2000. 85

R. Mayer, R. A. W. M. Henkes, and J. L. van Ingen. Quantitative infrared-thermography for wall-shear stress measurements in laminar flow. *Int. Journal of Heat and Mass Transfer*, 41 (15):2347–2356, 1998. 25

S. P. McKenna and W. R. McGillis. Performance of digital image velocimetry processing techniques. *Experiments in Fluids*, 32:2, 2002. 32

B. G. McLachlan and J. H. Bell. Pressure-sensitive paint in aerodynamic testing. *Experimental Thermal and Fluid Science*, 10:470–485, 1995. 24

W. K. Melville, R. Shear, and F. Veron. Laboratory measurements of the generation and evolution of Langmuir circulations. *Journal of Fluid Mechanics*, 364:31–58, 1998. 19, 20

M. Mühlich and R. Mester. Subspace methods and equilibration in computer vision. Technical report, Institute for Applied Physics, Goethe-Universität, Frankfurt, Germany, 1999. 133

G. Mie. Beiträge zur Optik trüber Medien, speziell kolloidaler Metallösungen. *Ann. Physik*, 25: 377–445, 1908. 59

D. Monson, G. Mateer, and F. Menter. Boundary-layer transition and global skin friction measurement with an oil-fringe imaging technique. *SAE Tech Paper Series*, 932550, 1993. 25

S. Nakamura, T. Mukai, and M. Senoh. Candela-class high-brightness InGaN/AlGaN double-heterostructure blue-light-emitting diodes. *Appl. Phys. Lett.*, 64:1687–1689, 1994. 63

A. Naya, E. Trucco, and N. E. Thacker. When are simple LS estimators enough? An empirical study of LS, TLS, and GTLS. *Intern. J. Comput. Vis.*, 68(2):203–216, 2006. 131

W. Nitsche. *Strömungsmesstechnik*. Springer, Berlin, Heidelberg, 1994. 24

K. Okuda. Internal flow structure of short wind waves, part I-IV. *Journal of the Oceanographical Society of Japan*, 38, 40, 1982. 19, 20, 21, 22

P. J. Olver. *Applications of Lie groups to differential equations*. Springer Verlag, Berlin, Heidelberg, New York, 1986. 137

W. L. Peirson and M. L. Banner. Aqueous surface layer flows induced by microscale breaking wind waves. *Journal of Fluid Mechanics*, 479:1–38, 2003. 21, 22

R. J. Perkins and J. C. R. Hunt. Particle tracking in turbulent flows. In *Advances in Turbulence 2*, pp. 286–291. Springer, 1989. 31

A. E. Perry. *Hot-wire-anenometry*. Oxford university press, Oxford, New York, 1982. 26

O. M. Phillips. *The dynamics of the upper ocean*. Cambridge University Press, 1969. 17

W. H. Press, S. A. Teukolsky, W. Vetterling, and B. Flannery. *Numerical recipes in C: The art of scientific computing*. Cambridge University Press, New York, 1992. 43, 85

M. Raffel, C. Willert, and J. Kompenhans. *Particle Image Velocimetry. A practical guide.* Springer, Berlin, Heidelberg, New York, 1998. 28, 29

L. Rayleigh. On convection currents in a horizontal layer of fluid, when the higher temperature is on the under side. *Phil. Mag*, 32:529, 1916. 113

H. Reichardt. Vollständige Darstellung der turbulenten Geschwindigkeitsverteilung in glatten Leitungen. *Z. angewandt. Math. und Mech.*, 31:208–219, 1951. 16

B. Ristic, S. Arulampalam, and N. Gordon. *Particle filters for tracking applications*. Artech House, 2004. 31

R. Rocholz. Bildgebendes System zur simultanen Neigungs- und Höhenmessung an kleinskaligen Wind-Wasserwellen. Diploma thesis, University of Heidelberg, 2005. 70

B. Ruck. Color-coded tomography. In *Proc. 7th Int. Symp. on Fluid Control, Measurement and Visualization*, pp. 25–28, 2003. 31

P. Ruhnau, C. Gütter, and C. Schnörr. A variational aproach for particle tracking velocimetry. *Meas. Sci. Technol.*, 16(7):1449–1458, 2005a. 31

P. Ruhnau, T. Kohlberger, C. Schnörr, and H. Nobach. Variational optical flow estimation for particle image velocimetry. *Experiments in Fluids*, 38:21–32, 2005b. 45, 47

P. Ruhnau and C. Schnörr. Optical Stokes flow. In *13th International Symposium. Applications of Laser Techniques to Fluid Mechanics, Lisbon, Portugal*, 2006. 48

P. Ruhnau, A. Stahl, and C. Schnörr. On-line variational estimation of dynamical fluid flows with physics-based spatio-temporal regularization. In *Pattern Recognition, Proc. 26th DAGM Symposium*, 2006. 48

C. L. Sabine, R. A. Feely, N. Gruber, R. M. Key, K. Lee, J. L. Bullister, R. Wanninkhof, C. S. Wong, D. W. R. Wallace, B. Tilbrook, F. J. Millero, T.-H. Peng, A. Kozyr, T. Ono, and A. F. Rios. The ocean sink for anthropogenic CO_2. *Science*, 305:367–372, 2004. 1

H. Scharr. *Optimal operators in digital image processing*. PhD thesis, University of Heidelberg, 2000. 42

A. Schimpf, S. Kallweit, and J. B. Richon. Photogrammetric Particle Image Velocimetry. In *Proc. 5th Int. Symp. on Particle Image Velocimetry*, 2003. 30

H. Schlichting. *Boundary layer theory*. McGraw Hill, New York, 1960. 17

C. Schlosser. Messung von Diffusionskonstanten. Diploma thesis, University of Heidelberg, 2004. 99

M. Siddiqui, M. R. Loewen, W. E. Asher, and A. T. Jessup. Coherent structures beneath wind waves and their influence on air-water gas transfer. *J. Geophys. Res.*, 109:C03024, 2004. 22

M. Siddiqui, M. R. Loewen, C. Richardson, W. E. Asher, and A. T. Jessup. Simultaneous particle image velocimetry and infrared imagery of microscale breaking waves. *Physics of Fluids*, 13 (7):1891–1903, 2001. 21

E. P. Simoncelli. *Distributed representation and analysis of visual motion*. Phd thesis, MIT, 1993. 36, 44

H. Spies. *Range flow estimation: The movement of deformable surfaces*. PhD thesis, University of Heidelberg, 2001. 87

M. Stanislas, M. Okamoto, and C. Kähler. Main results of the First International PIV Challenge. *Meas. Sci. Technol.*, 14:63–89, 2003. 32

M. Stanislas, M. Okamoto, C. Kähler, and J. Westerweel. Main results of the Second International PIV Challenge. *Exp. Fluids.*, 39(2):170–191, 2005. 32

G. G. Stokes. On the theory of oscillatory waves. *Trans. Camb. Philos. Soc.*, 8:441, 1847. 18

C. Tropea. Laser Doppler anemometry: recent developments and future challenges. *Meas. Sci. Technol.*, 6:605–619, 1995. 27

C. Tropea, J. Foss, and A. Yarin. *Springer Handbook of Experimental Fluid Dynamics*. Springer, Berlin, Heidelberg, in preparation. 24

H. C. van de Hulst, ed. *Light scattering by small particles*. Dover Publications, New York, 1981. 59

S. van Huffel and J. Vandewalle. *The total least squares problem: Computational aspects and analysis*. SIAM (Society for Industrial and Applied Mathematics), Philadelphia, 1991. 131

F. Veron and W. K. Melville. Experiments on the stability and transition of wind-driven water surfaces. *J. Fluid Mech.*, 446:25–65, 2001. 19

R. J. Volino and G. B. Smith. Use of simultaneous IR temperature measurements and DPIV to investigate thermal plumes in a thick layer cooled from above. *Experiments in Fluids*, 27: 70–78, 1999. 117

G. Voulgaris and J. H. Trowbridge. Evaluation of the accoustic velocimeter (ADV) for turbulence measurements. *Journal of Atmospheric and Oceanic Technology*, 15(1):272–289, 1998. 28

G. Welch and G. Bishop. An introduction to the Kalman-filter. Technical Report TR 95-041, University of North Carolina at Chapel Hill, Department of Computer Science, 1995. 31

J. Westerweel. *Digital Particle Image Velocimetry - Theory and application*. Delft University Press, Delft, 1993. 28

J. Westerweel, D. Dabiri, and M. Gharib. The effect of a discrete window offset on the accuracy of cross-correlation analysis of digital PIV recordings. *Experiments in Fluids*, 23:20–28, 1997. 30

R. Wildes, M. Amabile, A.-M. Lanziletto, and T.-S. Leu. Recovering estimates of fluid flows from image sequence data. *Computer Vision and Image Understanding*, 80:246–266, 2000. 38, 48

C. E. Willert and M. Gharib. Three-dimensional particle imaging with a single camera. *Experiments in Fluids*, 12:353–358, 1992. 32

J. Wolfrum, T. Dreier, V. Ebert, and C. Schulz. Laser-based combustion diagnostics. In R. A. Meyers, ed., *Encyclopedia of Analytical Chemistry*, pp. 2118–2148. John Wiley and Sons Ltd., Chinchester, 2000. 24

W. Woodward and G. Appell. Current velocity measurements using acoustic Doppler backscatter: A review. *IEEE Journal of Oceanic Engineering*, 11(1):3–6, 1986. 28

C. J. Zappa, W. E. Asher, A. T. Jessup, J. Klinke, and S. R. Long. Microbreaking and the enhancement of air-water transfer velocity. *J. Geophys. Res.*, 109:C08S16, 2004. 21

Danksagung